Forschungsbericht 2025-23

Preliminary Aerodynamic Design and Assessment of Boundary Layer Ingesting Fans

Maximilian Mennicken

Deutsches Zentrum für Luft- und Raumfahrt
Institut für Antriebstechnik
Köln

DLR Deutsches Zentrum für Luft- und Raumfahrt

Forschungsbericht 2025-23

Preliminary Aerodynamic Design and Assessment of Boundary Layer Ingesting Fans

Maximilian Mennicken

Deutsches Zentrum für Luft- und Raumfahrt
Institut für Antriebstechnik
Köln

183 Seiten
122 Bilder
17 Tabellen
122 Literaturstellen

Deutsches Zentrum
DLR für Luft- und Raumfahrt

Herausgeber:

Deutsches Zentrum
für Luft- und Raumfahrt e. V.
Wissenschaftliche Information
Linder Höhe
D-51147 Köln

ISSN 1434-8454
ISRN DLR-FB-2025-23
Erscheinungsjahr 2025
DOI: 10.57676/evq8-4k74

Rumpfgrenzschichteinsaugung, Störungstoleranter Fan, Aerodynamische Fanauslegung, Totaldruckstörung, Drallstörung

Maximilian MENNICKEN
DLR, Institut für Antriebstechnik, Köln

Aerodynamische Vorauslegung und Bewertung grenzschichteinsaugender Fans
Universität der Bundeswehr München

Grenzschichteinsaugung (engl. boundary layer ingestion, BLI) ist eine Technologie, die zur Reduzierung des Treibstoffverbrauchs beitragen kann und damit potentiell die Umweltbelastung der zivilen Luftfahrt reduziert. Dabei werden die Fanstufen infolge der inhomogenen Totaldruckverteilung in Umfangsrichtung variierenden Anströmbedingungen ausgesetzt. Die Berücksichtigung der Inhomogenitäten ist insbesondere in der aerodynamischen Vorauslegung eine Herausforderung, da die Berechnung der BLI-Strömung entweder sehr zeitaufwendig ist oder die Methoden lediglich globale Leistungsdaten statt detaillierter Strömungsfelder liefern und damit den umfangreichen Einsatz im Vorentwurf limitieren.

In dieser Arbeit wird eine numerisch effiziente aerodynamische Vorentwurfs- und Bewertungsmethodik für grenzschichteinsaugende Schuberzeuger entwickelt. Innerhalb der Methodik werden ein Reynolds-averaged Navier-Stokes-Ansatz (RANS) und ein Stromlinienkrümmungsverfahren miteinander gekoppelt. Der RANS-Ansatz wird für die Berechnung der Strömungsumverteilung im Einlauf verwendet, wohingegen das Stromlinienkrümmungsverfahren um ein Modell zur Erfassung der infolge BLI auftretenden Strömungsumverteilung erweitert und zur Berechnung der lokalen Fanbetriebspunkte am Umfang verwendet wird. Während der Entwicklung der Methodik werden die Strömungsfelder und die sich daraus ergebenden lokalen Betriebspunkte durch instationäre RANS (uRANS) Berechnungen umfassend verifiziert, die instationären Effekte des Leistungseintrages und der Verlustgenerierung diskutiert und die Grenzen der Methodik erläutert. Insgesamt ist die Methodik in der Lage, den numerischen Aufwand für eine BLI-Bewertung von 10000 CPUh für detaillierte uRANS-Berechnungen auf etwa 3 CPUh zu reduzieren und gleichzeitig eine hohe Güte der Betriebspunktberechnung zu erzielen.

Die Methodik wird dann auf zwei verschiedene Fanintegrationen angewandt. Für das Integrationsszenario rumpfeingebetteter Turbofans werden drei radiale Verteilungen des Fan-Totaldruckverhältnisses im Vorentwurf untersucht und wiederum durch uRANS-Berechnungen verifiziert. In einem weiteren Schritt werden 32 einzelne Fans betrachtet, die sich in der Meridionalmachzahl und der Schaufelspitzengeschwindigkeit unterscheiden. Basierend auf den Ergebnissen dieser Studie haben einlaufstörungstolerante, in den Rumpf eingebettete Fans ein höheres Totaldruckverhältnis als konventionelle Fans. Die radiale Totaldruckverteilung erfordert ein ausreichend hohes Totaldruckverhältnis innerhalb der Totaldruckstörung, um den Impuls des Grenzschichtfluids zu erhöhen, und der Blattspitzenbereich des Rotors sollte leicht entlastet werden, um hohe Spaltverluste zu vermeiden.

Das zweite Integrationsszenario ist ein heckintegrierter Fan, der über den gesamten Rumpfumfang Grenzschichtfluid einsaugt. Der Schuberzeuger verfügt über ein radial abfallendes Totaldruckverhältnis, mit dem Ziel die Totaldruckstörung am Fanaustritt zu reduzieren. Die neue Methodik wird verwendet, um die Fanstufe auszulegen und eine BLIBewertung vorzunehmen. Instationäre RANS-Rechnungen verifizieren die Vorentwurfsergebnisse und zeigen die Anwendbarkeit der Methodik auf dieses Integrationsszenario. In einem weiteren Schritt wird die Auswirkung der überlagerten Drallstörung untersucht. Dabei zeigt der einlaufstörungstolerante Fan nur geringe Variationen des Betriebspunktes und die Fähigkeit die Störung abzumildern ist weitgehend unbeeinflusst. Daher ist es im aerodynamischen Vorentwurf ausreichend lediglich die Totaldruckstörung zu berücksichtigen. Schließlich wird der effiziente Einsatz der Methodik demonstriert, indem verschiedene BLI-Betriebspunkte innerhalb des Fankennfelds berechnet und diskutiert werden.

Boundary Layer Ingestion, Distortion tolerant fan, Aerodynamic fan design, Stagnation pressure distortion, Swirl distortion

(Published in English)

Maximilian MENNICKEN
German Aerospace Center (DLR), Institute of Propulsion Technology, Cologne

Preliminary Aerodynamic Design and Assessment of Boundary Layer Ingesting Fans

University of the Bundeswehr Munich

Boundary Layer Ingestion (BLI) is a promising technology for reducing fuel burn and environmental impact in civil aviation. With BLI, the fan is exposed to circumferentially and radially varying inflow conditions. The consideration of BLI during preliminary aerodynamic design is challenging as the calculation of BLI flow is either very time consuming or the methods provide simplified performance data instead of detailed information about the flow. Therefore, both types of approaches are not suitable for the application within the preliminary aerodynamic design.

In this thesis a preliminary design and assessment methodology for boundary layer ingesting fans is developed. Within the methodology, a Reynolds-averaged Navier-Stokes (RANS) approach and a streamline curvature approach are coupled. The former is dedicated to the calculation of flow redistribution. The latter is extended by a stream tube contraction model and accounts for the local fan operation around the circumference. During the development of the methodology, the flow redistribution and local performance data are comprehensively verified by unsteady RANS (uRANS) calculations, the unsteady effects related to work input and loss generation are discussed and the limitations of the methodology are presented. Overall, the methodology is able to reduce the numerical effort for a BLI assessment from 10000 CPUh for state-of-the-art uRANS calculations to approximately 3 CPUh.

The methodology is then applied to two different integration scenarios. Fuselage embedded turbofans are dealing with a once per revolution distortion. In this integration scenario, three spanwise fan pressure ratio distributions are investigated with the preliminary design methodology and the data is again verified by uRANS calculations. In a subsequent step, 32 individual fans differing in meridional Mach number and blade tip speed are evaluated. Based on the findings of this study, distortion tolerant fuselage embedded fans have a higher fan pressure ratio than conventional fans, the spanwise fan pressure distribution requires a reasonably high fan pressure ratio within the distortion to re-energise the low momentum fluid, and the tip section needs to be slightly unloaded to avoid high tip gap related losses.

The second integration scenario is an aft-propulsor that ingests boundary layer fluid over the entire circumference of a fuselage. The propulsor has a descending spanwise fan pressure ratio to mitigate distortion. The new methodology is again used to assess the fan stage at a preliminary design level and the performance is verified by uRANS calculations. The results demonstrate the applicability of the methodology to this integration scenario. In a subsequent step, the effect of superimposed swirl distortion is investigated. The distortion tolerant fan shows only slightly lower fan efficiencies due to swirl distortion. The (corrected) mass flow and the fan pressure ratio, as well as the fans ability to attenuate the distortion, are mainly unaffected by the swirl distortion. Therefore, it is sufficient to consider only the stagnation pressure distortion in the preliminary design. Finally, a fan assessment along an iso speed line is performed to demonstrate the efficient applicability of the methodology to assess various off-design conditions.

Preliminary Aerodynamic Design and Assessment of Boundary Layer Ingesting Fans

Maximilian Peter Mennicken

Vollständiger Abdruck der von der Fakultät für Luft- und Raumfahrttechnik der Universität der Bundeswehr München zur Erlangung des akademischen Grades eines

Doktor-Ingenieurs (Dr.-Ing.)

angenommenen Dissertation.

Gutachter:

1. Univ.-Prof. Dr.-Ing. Dragan Kožulović
2. Univ.-Prof. Dr.-Ing. Jens Friedrichs

Die Dissertation wurde am 30.10.2023 bei der Universität der Bundeswehr eingereicht und durch die Fakultät für Luft- und Raumfahrttechnik am 16.01.2025 angenommen. Die mündliche Prüfung fand am 20.02.2025 statt.

Abstract

Boundary Layer Ingestion (BLI) is a promising technology for reducing fuel burn and environmental impact in civil aviation. With BLI, the fan is exposed to circumferentially and radially varying inflow conditions. The consideration of BLI during preliminary aerodynamic design is challenging as the calculation of BLI flow is either very time consuming or the methods provide simplified performance data instead of detailed information about the flow. Therefore, both types of approaches are not suitable for the application within the preliminary aerodynamic design.

In this thesis a preliminary design and assessment methodology for boundary layer ingesting fans is developed. Within the methodology, a Reynolds-averaged Navier-Stokes (RANS) approach and a streamline curvature approach are coupled. The former is dedicated to the calculation of flow redistribution. The latter is extended by a stream tube contraction model and accounts for the local fan operation around the circumference. During the development of the methodology, the flow redistribution and local performance data are comprehensively verified by unsteady RANS (uRANS) calculations, the unsteady effects related to work input and loss generation are discussed and the limitations of the methodology are presented. Overall, the methodology is able to reduce the numerical effort for a BLI assessment from 10000 CPUh for state-of-the-art uRANS calculations to approximately 3 CPUh.

The methodology is then applied to two different integration scenarios. Fuselage embedded turbofans are dealing with a once per revolution distortion. In this integration scenario, three spanwise fan pressure ratio distributions are investigated with the preliminary design methodology and the data is again verified by uRANS calculations. In a subsequent step, 32 individual fans differing in meridional Mach number and blade tip speed are evaluated. Based on the findings of this study, distortion tolerant fuselage embedded fans have a higher fan pressure ratio than conventional fans, the spanwise fan pressure distribution requires a reasonably high fan pressure ratio within the distortion to re-energise the low momentum fluid, and the tip section needs to be slightly unloaded to avoid high tip gap related losses.

The second integration scenario is an aft-propulsor that ingests boundary layer fluid over the entire circumference of a fuselage. The propulsor has a descending spanwise fan pressure ratio to mitigate distortion. The new methodology is again used to assess the fan stage at a preliminary design level and the performance is verified by uRANS calculations. The results demonstrate the applicability of the methodology to this integration scenario. In a subsequent step, the effect of superimposed swirl distortion is investigated. The distortion tolerant fan shows only slightly lower fan efficiencies due to swirl distortion. The (corrected) mass flow and the fan pressure ratio, as well as the fans ability to attenuate the distortion, are mainly unaffected by the swirl distortion. Therefore, it is sufficient to consider only the stagnation pressure distortion in the preliminary design. Finally, a fan assessment along an iso speed line is performed to demonstrate the efficient applicability of the methodology to assess various off-design conditions.

Kurzfassung

Grenzschichteinsaugung (engl. boundary layer ingestion, BLI) ist eine Technologie, die zur Reduzierung des Treibstoffverbrauchs beitragen kann und damit potentiell die Umweltbelastung der zivilen Luftfahrt reduziert. Dabei werden die Fanstufen infolge der inhomogenen Totaldruckverteilung in Umfangsrichtung variierenden Anströmbedingungen ausgesetzt. Die Berücksichtigung der Inhomogenitäten ist insbesondere in der aerodynamischen Vorauslegung eine Herausforderung, da die Berechnung der BLI-Strömung entweder sehr zeitaufwendig ist oder die Methoden lediglich globale Leistungsdaten statt detaillierter Strömungsfelder liefern und damit den umfangreichen Einsatz im Vorentwurf limitieren.

In dieser Arbeit wird eine numerisch effiziente aerodynamische Vorentwurfs- und Bewertungsmethodik für grenzschichteinsaugende Schuberzeuger entwickelt. Innerhalb der Methodik werden ein Reynolds-averaged Navier-Stokes-Ansatz (RANS) und ein Stromlinienkrümmungsverfahren miteinander gekoppelt. Der RANS-Ansatz wird für die Berechnung der Strömungsumverteilung im Einlauf verwendet, wohingegen das Stromlinienkrümmungsverfahren um ein Modell zur Erfassung der infolge BLI auftretenden Strömungsumverteilung erweitert und zur Berechnung der lokalen Fanbetriebspunkte am Umfang verwendet wird. Während der Entwicklung der Methodik werden die Strömungsfelder und die sich daraus ergebenden lokalen Betriebspunkte durch instationäre RANS (uRANS) Berechnungen umfassend verifiziert, die instationären Effekte des Leistungseintrages und der Verlustgenerierung diskutiert und die Grenzen der Methodik erläutert. Insgesamt ist die Methodik in der Lage, den numerischen Aufwand für eine BLI-Bewertung von 10000 CPUh für detaillierte uRANS-Berechnungen auf etwa 3 CPUh zu reduzieren und gleichzeitig eine hohe Güte der Betriebspunktberechnung zu erzielen.

Die Methodik wird dann auf zwei verschiedene Fanintegrationen angewandt. Für das Integrationsszenario rumpfeingebetteter Turbofans werden drei radiale Verteilungen des Fan-Totaldruckverhältnisses im Vorentwurf untersucht und wiederum durch uRANS-Berechnungen verifiziert. In einem weiteren Schritt werden 32 einzelne Fans betrachtet, die sich in der Meridionalmachzahl und der Schaufelspitzengeschwindigkeit unterscheiden. Basierend auf den Ergebnissen dieser Studie haben einlaufstörungstolerante, in den Rumpf eingebettete Fans ein höheres Totaldruckverhältnis als konventionelle Fans. Die radiale Totaldruckverteilung erfordert ein ausreichend hohes Totaldruckverhältnis innerhalb der Totaldruckstörung, um den Impuls des Grenzschichtfluids zu erhöhen, und der Blattspitzenbereich des Rotors sollte leicht entlastet werden, um hohe Spaltverluste zu vermeiden.

Das zweite Integrationsszenario ist ein heckintegrierter Fan, der über den gesamten Rumpfumfang Grenzschichtfluid einsaugt. Der Schuberzeuger verfügt über ein radial abfallendes Totaldruckverhältnis, mit dem Ziel die Totaldruckstörung am Fanaustritt zu reduzieren. Die neue Methodik wird verwendet, um die Fanstufe auszulegen und eine BLI-Bewertung vorzunehmen. Instationäre RANS-Rechnungen verifizieren die Vorentwurfsergebnisse und zeigen die Anwendbarkeit der Methodik auf dieses Integrationsszenario. In einem weiteren Schritt wird die Auswirkung der überlagerten Drallstörung untersucht. Dabei zeigt der einlaufstörungstolerante Fan nur geringe Variationen des Betriebspunktes und die Fähigkeit die Störung abzumildern ist weitgehend unbeeinflusst. Daher ist es im aerodynamischen Vorentwurf ausreichend lediglich die Totaldruckstörung zu berücksichtigen. Schließlich wird der effiziente Einsatz der Methodik demonstriert, indem verschiedene BLI-Betriebspunkte innerhalb des Fankennfelds berechnet und diskutiert werden.

Preface

This monograph was written as part of my research work at the German Aerospace Center, Institute of Propulsion Technology in Cologne. During the course of my doctorate, there were many people who contributed significantly to the success of this undertaking.

Firstly, I would like to express my sincere gratitude to my doctoral supervisor, Univ.-Prof. Dr.-Ing. Dragan Kožulović. Through the many intensive technical discussions, you contributed significantly to the success and finalisation of this thesis. Thank you so much! Furthermore, I would like to thank Univ.-Prof. Dr.-Ing. Jens Friedrichs for taking on the role of second reviewer and Univ.-Prof. Dr.-Ing. Christian Mundt for chairing my doctoral examination.

My department heads, Dr.-Ing. Eberhard Nicke and Dr.-Ing. Christian Tiedemann, have supported and enabled this work in many ways. I would like to thank you both for your support and your interest in my research.

My group lead Dr.-Ing. Rainer Schnell has supported and mentored me along the way. This work would not have been possible without your invaluable support and guidance throughout my research, as reflected in our many discussions over the past few years. Likewise, it would not have been possible without the freedom you gave me, when finalising the monograph. I would also like to thank you for your trust and for the opportunities to develop and realise my own ideas. I do not take this for granted, and I am very grateful for it!

I would like to thank my colleagues at the Institute of Propulsion Technology, particularly those in the Fan and Compressor Department. Your friendly, collegial cooperation and openness create an engaging working atmosphere, that makes our institute such a wonderful place to work at. I have had countless inspiring discussions with my colleagues. If I tried to name them all, I would either end up with an extensive list of names or miss out important people. That is why I decided to make life easier for myself and focus just on the essentials - the conversations. They have been invaluable in broadening and deepening my knowledge of aerodynamic flows, particularly those involving distortion, flow modelling, especially two-dimensional modelling in a three-dimensional world, as well as performance and loss analysis.

Even though research has been a big part of my life in the last few years, life is far more than just that. To my friends at DLR and beyond: I am happy to have you on my side. I remember many good times and you provided a welcome distraction, when times were challenging. This allowed me to achieve a more focused state of mind after spending time with you. Thank you so much!

Last but certainly not least, I would like to express my deepest gratitude to my family. Without your unconditional love, support and understanding, I would never have been able to embark on this long educational journey.

Contents

List of Figures

List of Tables

Nomenclature

Latin letters

A	cross-section area	m^2
a	polynomial coefficient static pressure approximation	-
a	specific work	J/kg
a/c^2	dimensionless cross-section area of an airfoil	-
b	axial length diffusor in chapter 2	m
b	blockage	-
b	boundary layer width	m
b	polynomial coefficient static pressure approximation	-
c	chord length	m
c	polynomial coefficient static pressure approximation	-
c	velocity in absolute reference frame	m/s
c_p	isobaric heat capacity	J/(kg·K)
D	diameter	m
d	polynomial coefficient static pressure approximation	-
DC	distortion coefficient	-
DF	diffusion factor	-
DH	DeHaller number	-
DI	distortion intensity	-
E	power	W
e	polynomial coefficient static pressure approximation	-
F	blade or thrust force	N
f	polynomial coefficient static pressure approximation	-
g	polynomial coefficient static pressure approximation	-
h	specific enthalpy	J/kg
$h_{rel.}$	relative channel height	-

httr	hub-to-tip-ratio	-
i	incidence	°
L	intake length	m
Ma	Mach number	-
MVDR	meridional-velocity-density-ratio $(\rho_{out} \cdot c_{m,out})/(\rho_{in} \cdot c_{m,in})$	-
$\dot{m}$	mass flow	kg/s
$\dot{m}_{corrected}$	ISA corrected mass flow $\dot{m}_{corrected} = \dot{m} \cdot \frac{p_{ISA}}{p_t} \cdot \sqrt{\frac{T_t}{T_{ISA}}}$	kg/s
N	rotational speed	1/min
P	power	W
p	pressure	Pa
q	dynamic pressure	Pa
q	heat flux	W
q	streamwise station in streamline curvature	-
R	radius at the casing	m
R	specific gas constant	J/(kg·K)
r	coordinate r	m
Re	Reynolds number	-
s	pitch	m
Δs	specific entropy $\Delta s = s - s_{ref.} = c_p \cdot ln(\frac{T}{T_{ref.}}) - R \cdot ln(\frac{p}{p_{ref.}})$	J/(kg·K)
$\dot{s}$	time derivative of the entropy	J/(kg·K·s)
s/c	pitch-chord-ratio	-
SM	surge margin	-
stc	stream tube contraction	-
T	temperature	K
t	time	s
u	blade velocity and fluid velocity	m/s
w	velocity in relative reference frame	m/s
x	axial position of engine integration	m
x	coordinate x	m
y	coordinate y	m

y^+	dimensionless wall distance	-
Greek letters		
α	swirl angle	°
δ	boundary layer thickness	m
δ	deviation	°
η	efficiency	-
η	kinematic viscosity	m²/s
γ	stagger angle	°
ν	dynamic viscosity	Pa·s
ω	angular speed	1/s
ω	blade/vane stagnation pressure loss coefficient $= \frac{p_{t,in} - p_{t,out}}{q_{in}}$	-
ω	fan cycle stagnation pressure loss coefficient $= \frac{p_{t,in} - p_{t,out}}{p_{t,in}}$	-
Φ	energy loss	W
Φ	flow coefficient $c_{ax,mean}/u_{mean}$	-
Π_{t-s}	stagnation to static pressure ratio $p_{out}/p_{t,in}$	-
Π_t	stagnation pressure ratio $p_{t,out}/p_{t,in}$	-
Ψ	work coefficient $\Delta h_t/u_{mean}^2$	-
ρ	density	kg/m³
σ	standard deviation	-
σ_a	stress of a fan blade	Pa
τ	shear stress	Pa
τ	temperature ratio	-
Θ	coordinate in the circumferential direction	°
Superscripts		
$\vec{}$	vector	
$'$	fluctuation of a quantity	
-	area average	
ADP	aerodynamic design point	
Subscripts		
∞	free stream conditions	

Θ	circumferential direction
1	time 1
2	time 2
60°	segment with circumferential extent of 60°
abs	absolute reference frame
ADP	aerodynamic design point
avg.	average
ax.	axial direction
BLI	averaged value due to BLI
c	curvature
corrected	ISA-corrected conditions
distortion	inside of the boundary layer
external	external
high	high value of a quantity
hub	hub section of a blade
i,j	running index
in	inlet
intake	intake
is.	isentropic
jet	jet
kin.	kinetic
L,N	maximum index
LE	leading edge
low	low value of a quantity
m	meridional
mean	mean flow in static pressure approximation
mean	radius at which the half of the cross sectional area is
mid	half way between mean flow and extrema in static pressure approximation
midspan	50% span

min.	minimum or worst
net	netto
nozzle	quantity at nozzle exit
out	outlet
prop.	propulsive
ref.	reference
rel	relative frame of reference
res	vector length
surface	surface of the aircraft
surge	operating point at the stability limit
t	stagnation quantity
t	tip
t-s	stagnation-to-static
thrust	thrust
tip	tip section of a blade
trans.	transfer
w	wall
wake	wake of the aircraft
working	operating point for the surge margin evaluation

Abbreviations

ACDC	Advanced Compressor Design Code
ADP	aerodynamic design point
AIP	aerodynamic interface plane
AoA	angle-of-attack
BL	boundary layer
BLI	boundary layer ingestion
CFD	computational fluid dynamics
CIP	compressors in parallel
CO_2	carbon dioxid
CPU	central processing unit

DLR	German Aerospace Center
FPR	fan pressure ratio
ISA	International Standard Atmosphere
MIT	Massachusetts Institute of Technology
NACA	National Advisory Committee for Aeronautics
NASA	National Aeronautics and Space Administration
NO_x	nitrogen oxid
OGV	outlet guide vane
RANS	Reynolds-averaged Navier-Stokes
rpm	rounds per minute
SAE	Society of Automotive Engineers
SLC	streamline curvature
u	unsteady
UHBR	ultra high bypass ratio
uRANS	unsteady Reynolds Averaged Navier Stokes
VTP	vertical tail plane

1. Benefits and challenges of highly integrated fan stages during preliminary design

1.1. Motivation for the use of boundary layer ingesting propulsion units

Civil aviation is aiming for climate neutrality to reduce the environmental impact of the aviation industry. The European Commission wants the aviation industry to reduce carbon dioxide (CO_2) emissions by 75%, nitrogen oxides (NO_x) by 90% and noise emissions per passenger-kilometre by 65% by 2050 compared with the technology in place in 2000 (see Comission (2011)). This will require technological improvements to state-of-the-art aircraft and engines. In addition, sustainable aviation fuels are expected to further reduce greenhouse gas emissions from the current and future aircraft fleet.

In the medium to long term, another promising path towards more sustainable aviation is the exploration of highly embedded propulsion units that take advantage of fuselage boundary layer ingestion (BLI). This results in a highly coupled propulsion and airframe system. The top row of fig. 1.1 shows a conventional aircraft with underwing mounted engines and the bottom row shows an aircraft concept with highly integrated engines. In underwing integration scenarios, the analysis of the airframe and the engine can be decoupled. Classically, the balance of momentum is considered in the overall system analysis to investigate steady-state flight conditions. Then the thrust of the engine balances the drag of the airframe according to eq. (1.1). Assuming a constant mass flow through the engine and neglecting the core section, the net thrust F_{net} is equal to the product of the mass flow $\dot{m}$ and the velocity difference between the flight velocity c_∞ and the nozzle velocity c_{nozzle}. When the nozzle is choked, the static pressure within the nozzle p_{nozzle} exceeds the ambient pressure p_∞ and the net thrust increases according to the pressure force given by the product of the nozzle area A_{nozzle} and the pressure difference $p_{nozzle} - p_\infty$.

$$F_{net} = \dot{m} \cdot (c_{nozzle} - c_\infty) + A_{nozzle} \cdot (p_{nozzle} - p_\infty) \tag{1.1}$$

In the top row of fig. 1.1 this is shown by the momentum deficit in the aircraft wake, which is balanced by the engine jet. Both the jet and the wake velocities are different from the airspeed and therefore dissipation occurs.
The accounting of drag and thrust is a more complex challenge for BLI integration scenarios. Because the airframe and engine are closely coupled, the split between the airframe and engine domains can be arbitrary. Smith (1993) uses momentum balance analysis to investigate such an integration scenario. Within this analysis, Smith (1993) simplifies the net thrust equation by averaging the inlet and outlet velocities and neglecting the pressure terms. Then eq. (1.1) is simplified to

$$F_{net} = \dot{m} \cdot (c_{nozzle} - c_{avg.,in}) \tag{1.2}$$

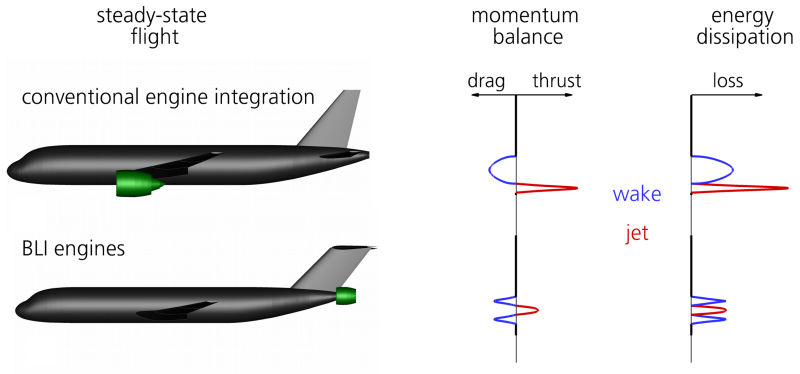

Figure 1.1.: Comparison of conventional under-the-wing-mounted engines with a BLI propulsion unit. Adapted from Drela (2009) and Hall (2015).

where only the difference in momentum at the inlet and outlet is taken into account. The improvement of the BLI engines can then be seen in the propulsion efficiency equation, which relates the propulsive power (thrust power) $c_\infty \cdot F_{net}$ to the power associated with the kinetic energy P_{kin}.

$$\eta_{prop} = \frac{c_\infty \cdot F_{net}}{P_{kin}} = \frac{c_\infty \cdot \dot{m} \cdot (c_{nozzle} - c_{avg.,in})}{\frac{1}{2} \cdot \dot{m} \cdot (c_{nozzle}^2 - c_{avg.,in}^2)} \tag{1.3}$$

If a constant thrust requirement and a constant mass flow through the fan stage is assumed, the following changes of a BLI propulsion unit can be observed in comparison to a propulsor with homogeneous inflow. Due to BLI, the lower averaged velocity $c_{avg.,in}$ entering the propulsor leads to a lower velocity in the nozzle c_{nozzle} while maintaining a specific thrust level. Furthermore, the kinetic energy, which is added to the flow P_{kin}, declines because of its quadratic dependency on the velocities. Consequently, the propulsive efficiency of BLI propulsion units is higher compared to conventional engine integration.

Plas (2006) addresses the issue of neglecting static pressure due to the upstream effect of engine integration. The engine installation is expected to cause a non-homogeneous static pressure field at the domain inlet. Therefore, Plas (2006) extends the control volume of the engine flow upstream of the aircraft and includes parts of the fuselage in this control volume. The assumptions of Smith (1993) can then be applied at the inlet of the control volume, but this underlines the ambiguity of defining the split between the aircraft and the engine.

A more precise analysis is given in the study by Habermann et al. (2020). In their study, a number of control volumes are coupled to achieve a clear division between the airframe and the engine, while maintaining the momentum balance analysis.

Drela (2009) introduces a different approach that considers the power balance instead

of the momentum balance.

$$P_{prop} - \Phi_{jet} = \Phi_{surface} + \Phi_{wake} \tag{1.4}$$

Equation 1.4 shows that the propulsive power added to the flow P_{prop} minus the jet losses Φ_{jet} equals the surface losses $\Phi_{surface}$ and the wake losses Φ_{wake}. The advantage of the power balance method is that it is independent of the static pressure field (see Sato (2012)).

Regardless of which balance is used, the benefit of BLI engines is visualised in the bottom row of fig. 1.1. In terms of momentum balance, the aircraft wake is partially filled by the propulsor. In addition, the jet speed is lower compared to conventional engine integration. Consequently, the engine jet and aircraft wake losses are lower than in the conventional scenario.

In the literature, a number of different overall aircraft design studies address the fuel burn benefit of BLI engines. Depending on the aircraft type, different efficiency gains are reported. Silberhorn et al. (2019) examines a fuselage-and-wing aircraft with turbofan engines embedded in the tail. In this study, the block fuel of the BLI configuration is 1.1% lower than the baseline. Hall (2015) examines the MIT D8 "double-bubble", which is comparable to a tube-and-wing aircraft but has a more elliptical fuselage. Most important is

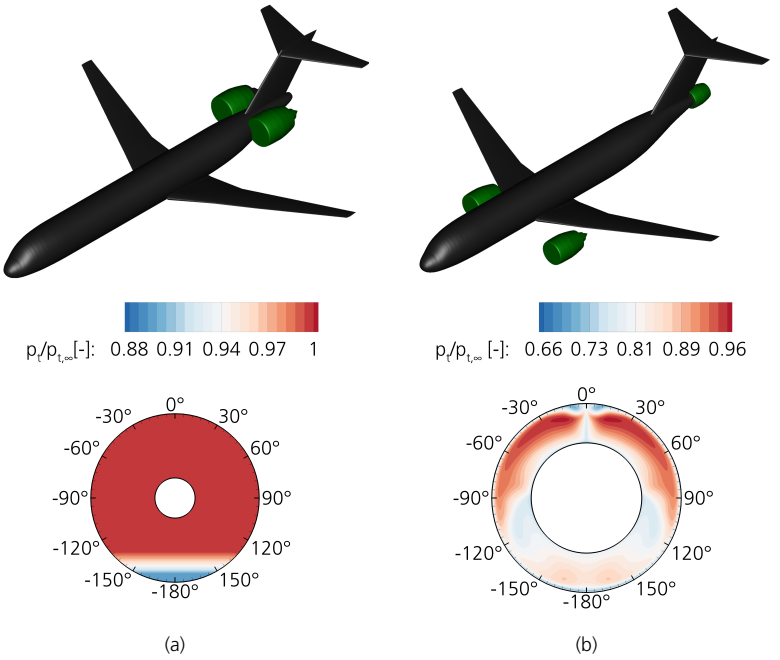

Figure 1.2.: Embedded turbofan engines in the rear part of the fuselage (a). The distortion pattern shows the impact of the fuselage at 180°. A rear integrated fan that ingests boundary layer fluid around the entire fuselage is shown in (b).

the reduced flight Mach number of 0.72. The resulting aircraft consumes 14% less fuel than the reference aircraft with podded engines.

Another way forward for BLI propulsion is the hybrid-electric fan, which uses boundary layer fluid around the entire fuselage. The electric fan is driven by the underwing engines. Figure 1.2 (b) shows such an aircraft concept. In the literature the benefit for such a concept varies from 1.9% reported by Silberhorn et al. (2020), over 4.7% shown by Seitz et al. (2021) to 7-12% found by Welstead and Felder (2016).

1.2. Challenges for boundary layer ingesting fans

In contrast to the system-level improvements, BLI fans are exposed to challenging and varying flow conditions along the circumference and span, even in steady-state flight. At the same time, the fan is required to maintain high levels of fan efficiency and sufficient margin to the stability limit. This leads to various challenges in the disciplines of aerodynamics, aeromechanics, aeroelasticity and aeroacoustics. Furthermore, there are interdependencies between propulsion and aircraft design that need to be considered in a design study. In this study, the focus is on fan aerodynamics.

Figure 1.2 shows two different aircraft concepts incorporating boundary layer ingesting fan stages and the corresponding inhomogeneous inlet conditions. Both show characteristic distortion patterns showing radial and circumferential stagnation pressure variations. However, there are differences between the two integration scenarios.

Figure 1.2 (a) shows embedded engines facing a distortion in an approximately 120° sector near the casing, which originates from the fuselage boundary layer. The rotor blades pass through this sector once per revolution with low momentum fluid. Outside of the distortion, the fan operates close to freestream conditions (high stagnation pressure).

The aircraft in 1.2 (b) has a hybrid-electric propulsion unit consisting of underwing turbofan engines and an electrically driven propulsor at the rear of the fuselage. This propulsor ingests a part of the boundary layer around the entire circumference of the fuselage. The stagnation pressure distribution shows a pronounced radial variation around the entire circumference at the inlet. The distortion also shows a circumferential variation due to the geometry of the fuselage.

The literature provides a comprehensive understanding of the interaction effects between fans and compressors and non-homogeneous inlet stagnation pressure. The approaches used to account for the fan/compressor interaction are either too imprecise for preliminary aerodynamic design (i.e. compressors in parallel approach) or already require very detailed input and are numerically expensive (i.e. 3D body force approach or unsteady Reynolds Averaged Navier Stokes (uRANS) calculations). As a result, aerodynamicists tend to design fans for clean inflow conditions and subject these designs to stagnation pressure distortions in later stages of the design process.

1.3. Ambition of this thesis

There is the necessity to close this gap and enable fan designers to quickly assess fan stages in BLI flow at an early stage of the design process. This enables fan designers to explore large parameter spaces to identify promising design parameters for distortion tolerant fan designs. Therefore, the objective of this thesis is to develop a preliminary design and assessment methodology for fan stages dedicated to non-homogeneous inflow. The methodology is intended to be characterised by low numerical effort, which directly translates into short turnaround times. In addition, the design capabilities include annulus design as well as blade and vane design.

The preliminary fan assessment is required to cover the BLI related flow physics, which is extensively reported in the literature. The previous work of the community on this specific topic is addressed in chapter 2. Based on these results, the considered approaches need to be extended and coupled to cover the main BLI flow characteristics. Furthermore, the resulting flow fields from the preliminary fan assessment need to be verified by time-resolved calculations. Chapter 3 deals comprehensively with the development and verification of the methodology.

In the following chapter 4, the integration scenario used in the methodology development is further investigated. In this context, the new methodology is used to analyse the impact of different fan design philosophies in terms of spanwise fan pressure ratio on distortion tolerance. Again, time-resolved calculations are used to verify the results of the preliminary design methodology. Demonstration of rapid fan assessment in BLI flows is aimed at by investigating a wide parameter space in terms of meridional Mach number and blade speed. The consideration of a comparable number of individuals would not be suitable to be covered by conventional design and assessment approaches.

Another important requirement for the methodology is the versatility to cover a different integration scenario. Therefore, chapter 5 deals with the integration of a fan stage in the rear part of the fuselage as shown in fig. 1.2 (b). In this chapter, conceptual design considerations are followed by a preliminary design of the fan stage. Again, the preliminary assessment of fan performance in a two-dimensional distortion pattern is verified by time-resolved calculations. A subsequent analysis looks at the effect of twist distortion on fan performance and loss generation. A further application of the preliminary fan assessment is then presented by assessing the fan performance along an iso speed line. Finally, a conclusion is drawn and suggestions are made for future BLI-related studies.

2. Fan aerodynamics in distorted inflow

In general, fan stages are required to generate the thrust that propels aircraft. The fan rotor therefore adds power and hence swirl to the flow (see Cumpsty (2004)). Downstream of the fan, the flow splits into a bypass flow and a core flow. The latter is very small in Ultra High Bypass Ratio (UHBR) engines and produces only a small fraction of the overall thrust. The bypass flow, which is associated with the majority of the engine thrust, passes through the outlet guide vane (OGV), which removes the swirl from the flow. The bypass flow then passes through the bypass section and exits the engine at the bypass nozzle. This task is shown in the enthalpy-entropy diagram in fig. 2.1 (a). The enthalpy increase is related to the work input into the fan blade. According to Euler's work equation 2.1, the specific work input into the flow is achieved by adding swirl to the flow in the absolute frame of reference (Cumpsty (2004)).

$$a = u_{out} \cdot c_{\Theta,out} - u_{in} \cdot c_{\Theta,in} \tag{2.1}$$

Two simplifications can help evaluating the work equation. In case of a constant radius the blade velocity reduces to $u_{out} = u_{in} = u$ and the work input reads $u \cdot \Delta c_\Theta$. Another simplification is the assumption of axial inflow, which reduces the work input to be only dependent on the velocity triangle at the rotor outlet. Then, equation 2.1 is simplified to $a = u_{out} \cdot c_{\Theta,out}$.

Figure 2.1(b) shows a section of a rotor blade with the corresponding velocity triangles at the inlet and outlet. The definition of velocity triangles and flow angles is given in appendix A. In general, fan and compressor blades are required to add work to the flow at the same time as they decelerate the flow (see Cumpsty (2004)). The added swirl in the absolute frame of reference is also marked in the velocity triangle. The flow deceleration in the relative frame of reference can be seen as the velocity w_{out} is less than w_{in}. Exceptions are fan and compressor sections with high work input and low blade speed, i.e. fan hub sections. In these areas the flow can be accelerated in the relative frame of reference to achieve the high work input as shown by Schnell et al. (2019). In addition, the added swirl can lead to absolute Mach number levels of unity near the fan blade root outlet (see Gummer and Wenger (2000)).

The flow kinematics and work input are directly translated into the non-dimensional parameters flow coefficient and work coefficient. The flow coefficient

$$\Phi = \frac{c_{ax}}{u_{mean}} \tag{2.2}$$

relates the axial velocity c_{ax} to the blade velocity u_{mean}. Another dimensionless quantity is the work coefficient, which relates the enthalpy increase Δh_t to the square of the blade velocity.

$$\Psi = \Delta h_t / u_{mean}^2 \tag{2.3}$$

Assuming incompressible flow and perfectly aligned flow with the blade geometry over the entire operating range, the flow kinematics can be translated into the work coefficient

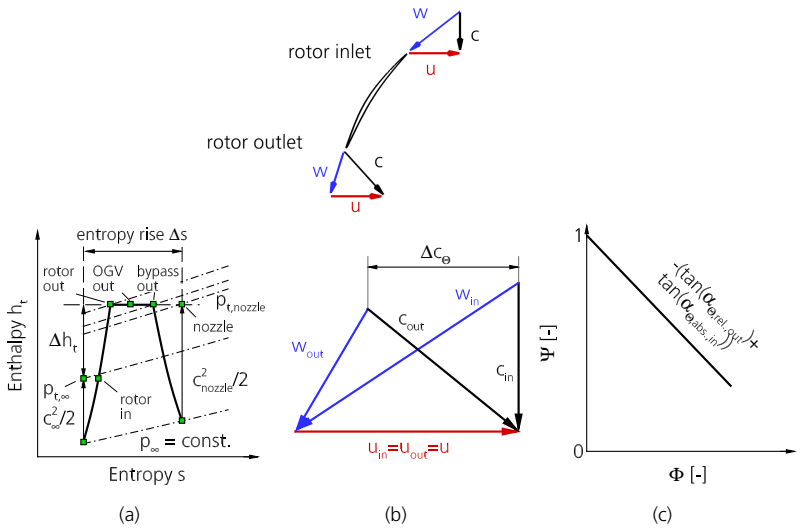

Figure 2.1.: Fan cycle (a), velocity triangles in (b) and simplified characteristic (c). Adapted from Cumpsty (2004).

according to Cumpsty (2004). The slope of the characteristic then depends only on the flow angles (metal angles) in the work coefficient and flow coefficient diagram. This is shown in fig. 2.1 (c).

As discussed in chapter 1, the assessment of fans with distorted inflow is more challenging in terms of physical and numerical complexity than for homogeneous inflow. Understanding fan aerodynamics under distorted inflow conditions is crucial to the design of highly integrated distortion tolerant fans. Distortion tolerant fans maintain high levels of efficiency combined with a sufficient margin to the stability limit over a wide range of operating conditions. It is therefore important to identify different types and patterns of distortion. In addition, their effects on fan operation in terms of changes in flow kinematics, work input, loss generation and influence on fan stability are discussed in the following subsections.

2.1. Characterisation of distortion types and patterns

SAE International deals primarily with three different types of distortion that affect engine performance. Associated Aerospace Information Reports and Aerospace Recommended Practice Reports deal with these topics:

1. stagnation pressure distortion SAE (2011)
2. stagnation temperature distortion SAE (2017)
3. swirl distortion SAE (2022)

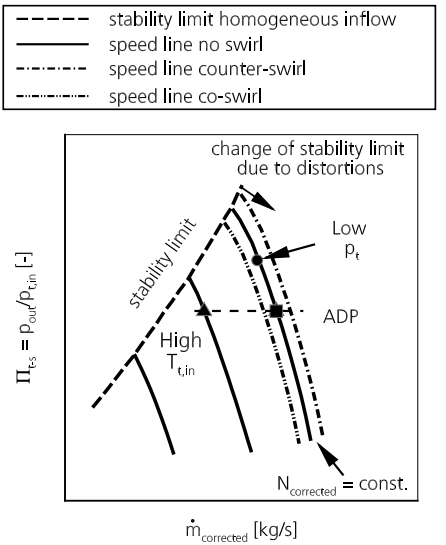

Figure 2.2.: Fan map in terms of stagnation-to-static fan pressure ratio and corrected mass flow. Adapted from Greitzer and Griswold (1976), Cumpsty (2004) and SAE (2022).

In general, these distortions can be composed of complex patterns with radial and circumferential components. In addition, superimposed distortions consisting of the above types of distortion occur in realistic engine integration. Nevertheless, it is useful to analyse the different distortions separately using the simple compressors-in-parallel (CIP) approach. Because of its simplicity and its ability to capture distortion-related performance variations, it is often used to analyse distorted inflow (Longley and Greitzer (1992), Greitzer and Griswold (1976) and Lecht (1987)). The basic idea of the CIP is to evaluate the performance of two stream tubes with different inflow conditions. Both stream tubes are coupled by a common back pressure, but all interactions upstream of the compressor outlet are neglected (i.e. mixing). The assumption of uniform static pressure is valid in the case of uniform swirl at the outlet and the presence of a constant area duct (see Greitzer and Griswold (1976) and Longley and Greitzer (1992)). It is also assumed that the compressor performance determined for homogeneous inflow is maintained for both stream tubes.

Due to its simplicity, CIP is applied in this subsection to explain the effect of the different distortions on fan and compressor performance. Figure 2.2 shows a generic fan map in terms of stagnation-to-static fan pressure ratio ($\Pi_{t-s} = \frac{p_{out}}{p_{t,in}}$) and corrected mass flow. The solid lines represent the corrected speed lines and the dashed line marks the stability limit at homogeneous inflow. The aerodynamic design point (ADP, black square) is used as a baseline and all operating point variations due to the specific distortions are compared to the ADP. In addition, the isolated effect of the three types of distortion mentioned above is considered. Therefore, only the distortion related inflow changes, while the others remain

unchanged. However, distortion related flow changes are allowed.

Firstly, a stagnation pressure distortion is considered. A decrease in stagnation pressure leads to a decrease in (corrected) mass flow. According to the assumptions, the stagnation temperature remains constant and the operating point of the low momentum steam tube remains on the same corrected speed line. Therefore, the operating point is on the upper left side compared to ADP. In addition, the stability limit line moves to the right with distorted inflow and therefore the lower inflow stagnation pressure operating point is closer to the stability limit. Stagnation pressure distortions occur in conventional aero-engines during off-design conditions such as crosswind operation or high angle-of-attack flight and associated flow separation at the inner nacelle (see Peters et al. (2015) or Cao et al. (2017)). In addition, this type of distortion occurs in highly embedded s-shaped ducts, which are likely to be used in military engines (see Williams (1986), Migliorini et al. (2022) or Max et al. (2022)). Another source is aircraft boundary layers, which are intentionally introduced into BLI engines to improve efficiency, as discussed in chapter 1.

Secondly, the change in operating point in the case of stagnation temperature distortion is taken into account. This type of distortion also changes the amount of mass flow taken in (corrected). Figure 2.2 illustrates a hot gas ingestion. Due to the increased (stagnation) temperature, the (corrected) mass flow decreases. In addition, the mechanical shaft speed remains constant, but the corrected shaft speed changes due to the distortion. The resulting operating point is therefore on the left of ADP. As the stagnation pressure at the inlet and the static pressure at the outlet remain unchanged, their ratio also remains the same. Hot gas ingestion at the fan inlet is mainly associated with military engines, i.e. after a cruise missile launch (see SAE (2017)). However, stagnation temperature distortions also occur in civil engines. In the case of a non-homogeneous work input within an upstream component (i.e. fan), the downstream components (i.e. low-pressure compressor) are subject to stagnation pressure and stagnation temperature distortions (compare Longley and Greitzer (1992)).

Finally, the effect of swirl angle distortions on fan operating points is considered. Flow angle distortions can mainly be divided into radial and circumferential components. The presence of radially homogeneous, circumferential swirl changes the position of the corrected speed lines within the fan map (compare SAE (2022)). The dash-dotted lines in fig. 2.2 represent co-swirl and counter-swirl characteristics. For a fixed corrected mass flow, a given speed line is shifted upwards in the case of counter-swirl and downwards in the case of co-swirl. Such conditions can be found around the entire circumference if an inlet guide vane is present. In crosswind or high angle-of-attack operation, the fan operates in swirl distortion (compare Thollet et al. (2016)). In addition, swirl angle distortions occur due to ground vortex ingestion (see Schönweitz et al. (2013)) or in S-shaped ducts of highly integrated aero-engines (compare Migliorini et al. (2022)). These swirl distortions consist of three-dimensional vortices and the flow is more complex than allowed by the above assumptions. Consequently, fan performance variations are more complex.

The current study examines highly integrated fan stages, as introduced in chapter 1. The associated boundary layer mainly causes stagnation pressure distortion to which the fan is subjected, and therefore the following section focuses on this type of distortion.

In the previous explanations, two individual stream tubes are evaluated to explain their

effect on the overall fan and compressor performance. This study is therefore more related to circumferential distortions. However, radial distortions can also occur. When purely radial distortions are present, the distortion leads to spanwise variations in blade incidence and therefore blade performance. Mennicken et al. (2022) show the above inflow conditions for the BLI propulsor discussed in chapter 5. If the blade is operating at positive incidence over a large part of the blade, the work input will increase and the fan pressure ratio is likely to increase as well. If the blade operates mainly at negative incidence, the fan pressure ratio is likely to decrease compared to undistorted inflow. Furthermore, the fan characteristic is likely to change its slope (see Abbasi et al. (2018)). Consequently, the overall fan characteristic is different from that obtained with undistorted inflow. Nevertheless, conventional numerical approaches can be applied to analyse purely radial distortions due to the circumferential periodicity of the flow. Furthermore, the flow characteristics of circumferential distortions are more complex. Therefore, the following section is mainly focused on circumferentially non-homogeneous flow.

2.2. Stagnation pressure distortion

This subsection deals with boundary layer specific flow features and performance variations. Highly integrated propulsion units are subject to stagnation pressure distortions which have a large characteristic length scale in the circumferential direction compared to the rotor pitch. The equations 2.4 and 2.5 give two commonly used metrics to characterise stagnation pressure distortions. The numerator of both metrics is the difference between the average stagnation pressure over the entire circumference and the minimum stagnation pressure in a 60° segment. The denominator is different for both metrics. The distortion coefficient $DC_{60°}$ in eq. (2.4) uses the dynamic pressure in the case of incompressible flow (Longley and Greitzer (1992)).

$$DC_{60°} = \frac{\overline{p}_{t,360°} - \overline{p}_{t,min,60°}}{\frac{1}{2}\rho c_{ax}^2} \tag{2.4}$$

The denominator of the distortion intensity $DI_{60°}$ in eq. (2.5) is the average stagnation pressure (SAE (2011)).

$$DI_{60°} = \frac{\overline{p}_{t,360°} - \overline{p}_{t,min,60°}}{\overline{p}_{t,360°}} \tag{2.5}$$

2.2.1. Flow redistribution upstream of the fan stage

In flows with non-homogeneous stagnation pressure, there is an interaction between the distortion and the compression system. A CIP approach is used, corresponding to the explanations in section 2.1. One stream tube contains high momentum fluid, the other low momentum fluid. In the far upstream position, the stagnation pressure distortion is fully allocated to the dynamic pressure and therefore translates into an axial velocity distortion. Consequently, the static pressure and the swirl velocity are homogeneous. The solid lines in fig. 2.3 (a) and (b) show these flow conditions. At the rotor inlet, the stagnation pressure profile remains the same as in the far upstream position as shown in fig. 2.3 (a), but the distortion allocation between dynamic and static pressure changes. In the low momentum region, the static pressure decreases and the axial velocity increases. The stream tube associated with high stagnation pressure shows the opposite change. In addition, flow redistribution is directly related to swirling flow. This behaviour is extensively

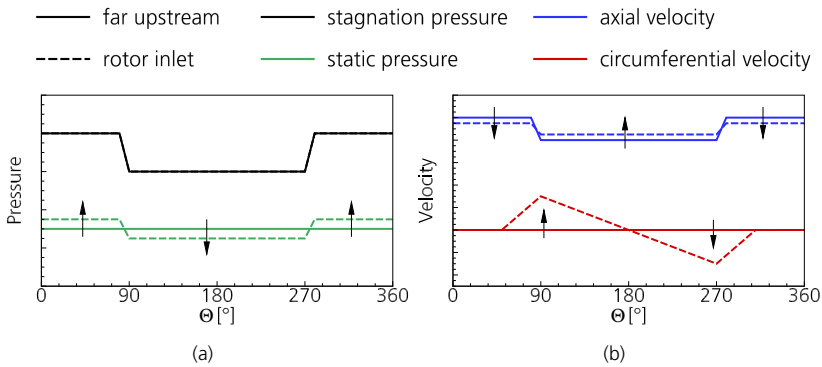

Figure 2.3.: Stagnation and static pressure as well as axial and circumferential velocities far upstream and at the rotor inlet. Figure adapted from Longley and Greitzer (1992).

reported in the literature and can be found in Longley and Greitzer (1992), Greitzer and Griswold (1976), Fidalgo et al. (2012), Schoenweitz et al. (2015) or Gunn and Hall (2014). The flow redistribution is not discrete in nature, but is related to a spatial extent in the upstream flow path. Figure 2.4 (a) shows the dividing streamlines between the high and low stagnation pressure fluid in an "unrolled" compressor. The high stagnation pressure stream tube expands as it approaches the compressor and contracts the low stagnation pressure stream tube (see Mazzawy (1977)). Figure 2.4 (b) shows the axial distribution of the static and stagnation pressure distributions. Stenning (1980) compares experimental data represented by squares and diamonds with theoretical results (solid lines). The axial coordinate is non-dimensionalised by the compressor radius and the compressor inlet is located at x/R=0. Upstream of the compressor, the stagnation pressure distortion is independent of the axial position. In contrast, the static pressure distortion increases as the flow approaches the compressor. Additionally, fig. 2.4 (b) depicts the distortion attenuation within the compressor due to higher work input within the distorted sector.

The flow redistribution described above takes place mainly in the intake. Similar to conventional intakes, the purpose of the intake in BLI configurations is to decelerate the flow while maintaining almost the same stagnation pressure. The intake is also required to straighten the flow. In BLI cases, the geometry of the intake also determines the amount of boundary layer fluid ingested. Therefore, there is a need for special intake designs to deal with boundary layer ingestion.

Intake designs of embedded turbofans are mainly non-axisymmetric at the inlet transitioning to a rotationally symmetric cross-section at the rotor inlet (see Plas (2006) and Florea et al. (2015)). The inlet design of Florea et al. (2015) is mainly driven by the non-dimensional inlet length L/D and the embedding degree $\Delta R/L$, which defines the radial offset of the inlet and outlet planes of the inlet. The application of these design parameters results in an S-shaped inlet geometry. Florea et al. (2015) find the optimum design parameters to be L/D between 0.6 and 0.8 while $\Delta R/L$ is between 0.2 and 0.3. In this region of the parameter space the compromise between low stagnation pressure losses, low

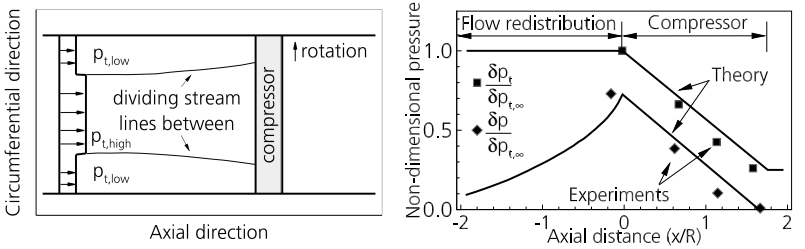

Figure 2.4.: The left part (a) shows the dividing stream lines between the high and low stagnation pressure stream tubes according to Mazzawy (1977). The right part (b) shows the change in static and stagnation pressure upstream, within and downstream of the compressor. Adapted from Stenning (1980).

amplitude of the first two harmonics of the stagnation pressure distortion and a tolerable mass flow variation around the circumference is found.

Ordaz et al. (2017) simultaneously design the rear part of an aircraft and the intake geometry of an aft-propulsor. The $DC_{60°}$ of the optimal design has a value of 0.0182 and is 95.6% lower compared to the baseline. The fan therefore receives a more homogeneous inflow in the circumferential direction than in the baseline design. However, the improved inflow distribution is achieved over an area of slightly increased drag across the entire rear of the aircraft.

2.2.2. Fan performance in distorted inflow

Flow kinematics at rotor inlet

In section 2.2.1 the flow redistribution in the inlet is introduced. This results in different velocity triangles as shown in fig. 2.5. Figure 2.5 (a) shows the rotor velocity triangles at the aerodynamic design point. Typically, ADP performance aims for minimised losses while considering other design constraints (i.e. stability). Throughout this study, incidence and

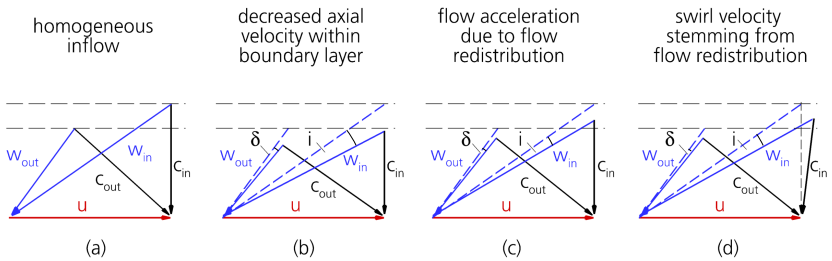

Figure 2.5.: Superposition of BLI specific flow features on velocity triangles. Adapted from Mennicken et al. (2019).

deviation angles are measured between the aerodynamic design point and the flow angle at a specific operating point. As shown in eq. (2.6), incidence accounts for the difference in relative flow angles (see Hergt et al. (2011)).

$$i = \alpha_{\Theta,in,OP} - \alpha_{\Theta,in,ADP} \tag{2.6}$$

Positive incidence is associated with a stagnation point shifted to the pressure side, whereas negative incidence shows a stagnation point located on the suction side of the blade. According to this definition, the incidence angle in fig. 2.5 (a) is equal to zero. The deviation is calculated according to eq. (2.7) and takes into account the difference in the relative flow angle at the trailing edge. The deviation is therefore zero for ADP. Ignoring the effects of the downstream flow path between the rotor and stator, the velocity triangle at the rotor outlet represents the stator inlet conditions. At ADP, the design intent is to align the vanes with the flow and the stator incidence is, by definition, zero.

$$\delta = \alpha_{\Theta,out,OP} - \alpha_{\Theta,out,ADP} \tag{2.7}$$

In addition, fig. 2.5 decomposes the BLI related changes in the velocity triangles into individual effects. As seen in section 2.2.1, boundary layer ingestion is associated with a decrease in axial velocity. Figure 2.5 (b) shows velocity triangles in the case where no flow redistribution would take place. The rotor receives a positive inflow due to the axial velocity deficit. At the rotor outlet, these inflow conditions can lead to a deviation. The incidence at the rotor inlet combined with the deviation leads to changes in the velocity triangle at the rotor outlet. Firstly, the work input increases due to an increased circumferential velocity component $c_{\Theta,out}$. Secondly, the stator inflow velocity triangle changes towards positive incidence conditions for the stator. This can be seen from the difference between the black and grey (ADP) velocity vector c in fig. 2.5 (b). As introduced in section 2.2.1, the circumferential flow redistribution leads to an acceleration of the boundary layer fluid. Therefore, the rotor incidence decreases compared to the case without flow redistribution, as can be seen in 2.5 (c). These conditions are representative of the middle of the distortion. However, the deviation remains at the trailing edge of the rotor. Gunn et al. (2013) quantify the deviation to be less than 3°. According to the velocity triangles in fig. 2.5 (c), the work input remains higher than with ADP. In line with the explanation above, the downstream stator is exposed to positive incidence. Figure 2.5 (d) shows a velocity triangle in counter-swirl conditions. Swirl is present due to static pressure gradients at the rotor inlet. When the swirl and blade rotation are aligned, it is called co-swirl and tends to reduce blade incidence and work input. The opposite is called counter-swirl and is associated with an increase in the angle of incidence and therefore work input. Another important aspect of flow redistribution is the decoupling of corrected mass flow and blade incidence due to BLI related flow acceleration and deceleration. At undistorted inflow conditions, the fan map provides Mach and incidence similarity independent of ambient conditions. In the case of BLI, the incidence is changed due to flow redistribution and therefore conventional fan map considerations are misleading. This needs to be considered when assessing local operating conditions.

Figure 2.6 shows a counter-clockwise rotating fan and a BLI related stagnation pressure pattern. Over the entire circumference, the inflow velocity triangles and therefore the fan performance can change compared to a homogeneous inflow. At 0° the fan stage is barely affected. In the study of Yang et al. (2021) a positive incidence is reported while Gunn and Hall (2014) observes a negative incidence. In the region where the low momentum fluid is

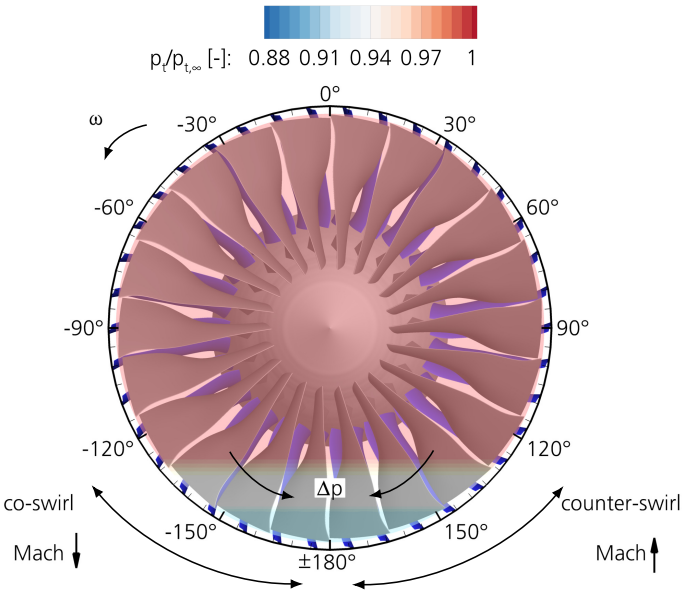

Figure 2.6.: Fan stage and boundary layer distribution.

located, flow redistribution takes place. In the region of -120° there is a co-swirl, while near 120° there is a counter-swirl. In the middle of the distortion (±180°) the static pressure minimum is located and both swirl regimes cancel each other out. No swirl is observed. These results are reported in detail, e.g. by Fidalgo et al. (2012), Gunn et al. (2013), Gunn and Hall (2014) or Schoenweitz et al. (2015). Due to the different flow kinematics, the rotor incidence varies along this part of the circumference. In BLI distortion patterns, the decreasing axial velocity has the main influence on the incidence angles, while the swirl has only a small contribution. Therefore, the rotor is mainly exposed to positive incidence in the distorted region (see Gunn and Hall (2014) Yang et al. (2021)). In addition, Yang et al. (2021) observed an inflow Mach number variation with lower Mach number values near -120° and higher Mach number values at 120°.

Tip leakage flow and entropy generation

According to the experiments of Storer and Cumpsty (1991), under clean inflow conditions the tip leakage flow has almost the same stagnation and static pressure distribution as the blade section near the tip gap. In addition, the inflow Mach number and blade incidence are the main parameters affecting the static pressure distribution on the blade (see Weingold and Behlke (1987)). As the tip gap flow is mainly driven by the pressure force between the pressure and suction sides, Yang et al. (2021) find lower tip gap related loss generation at co-swirl (-120°) and amplified flow through the tip gap at counter-swirl (120°) with increased tip flow related losses. In the study of Yang et al. (2021) 54% of the additional entropy generation in the case of BLI is associated with this flow feature. Gunn

and Hall (2014) find that two-thirds of the additional BLI-related loss generation occurs in the rotor. Based on their study, tip gap flow in the counter-swirl regime is also a major source of loss. In addition, Gunn and Hall (2014) find a counter-intuitive behaviour of the rotor efficiency in the middle of the distortion (-180° position in fig. 2.6). At this point, one would expect a reduction in fan efficiency due to positive incidence. However, Gunn and Hall (2014) finds high efficiencies in this region. This is due to radial flow migration within the rotor, higher work input due to incidence and flow acceleration rather than flow deceleration.

Unsteady flow features due to BLI

In addition to the varying inflow conditions at the rotor inlet, unsteady flow features affect the flow field and fan performance. Even with homogeneous inflow unsteady flow features are present in turbomachinery due to blade row interactions, as reported in detail by Sanders et al. (2001), Sanders and Fleeter (2001) and Mailach (2010). Depending on the Mach number level, different flow features are present. By definition, at low Mach numbers the flow velocity is less than the speed of sound. Since the propagation of static pressure perturbations is linked to the speed of sound, they move faster than particles transported at the convective speed in subsonic flows. In rotor-stator interaction, the wake of a rotor subjects the downstream stator to an instantaneous change in incidence. This causes an instantaneous change in the stator pressure distribution and therefore the circulation changes over the entire chord length as reported by Sanders et al. (2001) and Mailach (2010). In addition, the difference between the rotor wake and the free stream velocity (slip velocity) leads to flow migration of the low momentum wake fluid from the suction side to the pressure side within the stator passage. This flow migration is known as the negative jet effect. At subsonic conditions, the negative jet effect slightly changes the stator pressure distribution.

At transonic flow conditions, the convective transport is of the same order of magnitude or even exceeds the speed of sound. In such conditions, the negative jet effect caused by the rotor wake is the main driver of blade performance variations, as shown by Sanders and Fleeter (2001). The flow migration to the pressure side increases as the velocity ratio between the rotor wake and the free stream within the stator passage increases. In addition, an upstream pressure wave is created at the trailing edge of the blade due to the interaction between the rotor wake and the blade. The superposition of the pressure wave with the variation of the stator circulation changes the static pressure distribution along the suction side.

In BLI flows, the unsteadiness is due to the relative motion between the rotor and the stationary distortion. The incidence-affected inflow combined with the decreasing static pressure in the distorted sector leads to results similar to the rotor-stator interaction effects discussed above. Mazzawy (1977) considers the static pressure path and the convective path, both of which are shifted circumferentially by the rotor. In subsonic flow, the circumferential displacement of a particle is greater than that of the static pressure. Consequently, the static pressure and the particle path are decoupled. Mazzawy discusses the effects of decoupling by considering a simplified representation of realistic rotor flow. The rotor blade passage is modelled by a diffuser with a linear increase in cross-sectional area. Within the relative frame of reference, a one-dimensional, inviscid and incompressible flow is assumed and eq. (2.8) shows the corresponding axial momentum equation.

The time derivative of the velocity in eq. (2.8) accounts for the time dependent changes in the velocity field and reveals the unsteady nature of the rotor flow.

$$-\frac{1}{\rho}\frac{\partial p}{\partial x} = w\frac{\partial w}{\partial x} + \frac{\partial w}{\partial t} \tag{2.8}$$

Including the assumptions about the flow field and geometry, Mazzawy performs the spatial integration over the diffuser. This leads to eq. (2.9), which shows the two terms influencing the static pressure rise. The first one only considers the spatial variations, while the second one is transient as it includes the time derivative of the disturbance velocity w'.

$$\Delta p = -\int_0^b \rho w\frac{\partial w}{\partial x}dx - \int_0^b \rho\frac{\partial w'}{\partial t}\frac{1}{1+\frac{A_{out}-A_{in}}{A_{in}b}x}dx \tag{2.9}$$

Thus, the static pressure rise depends on the chord length b, the cross-sectional area at the inlet and outlet of the diffuser and the time derivative of the flow velocity.

There is also a time-dependent increase in the stagnation enthalpy. Using the formula of *Gibbs*, the change in entropy depends on the enthalpy and pressure gradient.

$$Tds = dh - \frac{1}{\rho}dp \tag{2.10}$$

Applying the definition of stagnation enthalpy, rearranging the equation taking into account the momentum eq. (2.8) and performing the spatial integration leads to eq. (2.11).

$$\int_0^b \frac{\partial h_t}{\partial x}dx = -\int_0^b \rho\frac{\partial w'}{\partial t}\frac{1}{1+\frac{A_{out}-A_{in}}{A_{in}b}x}dx + \int_0^b T\frac{\partial s}{\partial x}dx \tag{2.11}$$

The first summand on the right-hand side of this equation is equal to the one discussed above. So the stagnation temperature rise also depends on the geometry of the blade and the time derivative of the velocity perturbation. In addition, the stagnation enthalpy rise depends on the entropy variation.

The underlying mechanisms of this summand can be explained by considering fig. 2.7. On the left-hand side, the circumferential entropy distribution is shown. High entropy fluids are associated with low stagnation pressures. At time t_1 the low momentum particle A enters the rotor passage. This is shown in the upper part of fig. 2.7. For a time interval, the rotor continues to move in the circumferential direction and the particle passes through the passage. At time t_2 particle A, which entered the passage at t_1, reaches the trailing edge of the rotor and particle B enters the passage. Particle B has a higher momentum and a lower entropy level than particle A. Thus, the distortion related entropy variation leads to an unsteady stagnation entropy increase. The reduced frequency, which relates the particle residence time in the passage to the characteristic time of the rotor rotation, is an indicator of how pronounced this effect is. Reduced frequencies below 0.1 indicate quasi-steady behaviour Hall et al. (2017), while higher values indicate the relevance of unsteady flow characteristics.

The varying work input due to the flow kinematics combined with the unsteady work input (see above) and three-dimensional flow features within the rotor passage (i.e. shock systems in transonic rotors) leads to varying rotor performance around the circumference.

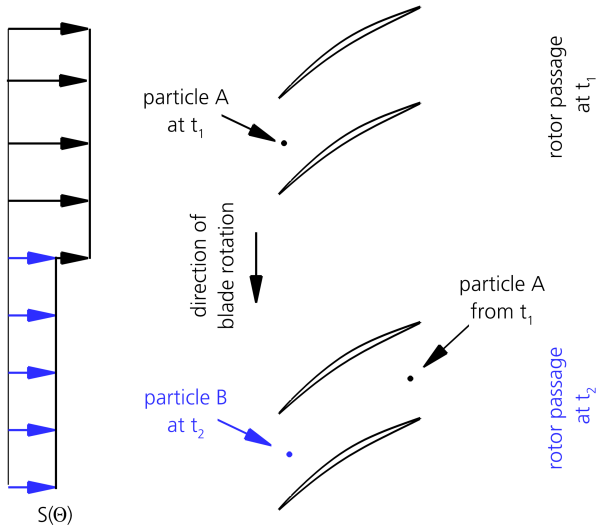

Figure 2.7.: Stagnation pressure related entropy distribution along the circumference and convective particle tracking through the rotor at two times. Figure adapted from Mazzawy (1977).

In addition, the rotor shifts the flow in the circumferential direction. Accordingly, the flow field at the rotor outlet exhibits non-homogeneous stagnation pressure and temperature distributions that are not at the same spatial location as the incoming flow. In addition, both distortions can be out of phase as reported by Yao et al. (2008) or Reutter et al. (2020). This effect seems to be more pronounced in multistage compressors than in fans, as there is no significant shift in the published data of Fidalgo et al. (2012) and Gunn et al. (2013). Especially in highly transonic rotors, the impact on the shock system can lead to significant shock oscillations of 20% chord length at each pass through the distortion (see Hah et al. (1998)). All these effects also lead to rotor force variations. Schoenweitz et al. (2015) examine fan stages with a high fan pressure ratio ($\Pi_t = 1.7$) and a low fan pressure ratio ($\Pi_t = 1.35$). The fans are exposed to a distorted sector with a constant stagnation pressure drop, located close to the casing. The fan with the high fan pressure ratio has a peak-to-peak rotor force variation of 63.8%, while the fan with the low fan pressure ratio has a blade force variation of 130.3%.

Stator performance

In contrast to the rotor, the stagnation pressure distortion and the stator are clocked. Therefore, the stator vanes are exposed to varying inflow conditions around the circumference. In the case of axisymmetric stators, flow separations can occur within stators operated with low momentum fluids (see Gunn et al. (2013) and Gunn and Hall (2014)). As the stator and distortion are clocked, there is an opportunity to improve flow conditions by using non-axisymmetric stators. In the studies of Hall et al. (2017) and Hall et al. (2022)

individual stator geometries are incorporated and swirl is allowed at the fan stage exit. Individual stators have an upstream effect and can therefore positively influence the performance of the rotor. Therefore Hall et al. (2017) aims to reduce the rotor blade loading by staggering the stators around the circumference. By varying the stator stagger angle by 3°, smaller variations in the diffusion factor in the rotor tip area can be achieved. Hall et al. (2022) are minimising the circumferential variations of the rotor incidence and the rotor blade force. Both metrics can be improved within their study by applying moderate changes in stator blade angles ($\pm$7° in stator exit angle) at the expense of a less homogeneous flow field at the fan stage exit. Gunn and Hall (2017) design a three-dimensional non-axisymmetric stator. The stators clocked with the distortion have an increased chord length near the tip and an increased chamber. In addition, these stators are more leaned than the baseline stators. In contrast to the vanes within the distortion, the vanes operating in the high momentum fluid are less chambered and the vane chord is reduced. All in all, the redesigned stator has less flow separation and therefore lower losses.

Stage performance

The observation of flow redistribution in section 2.2.1 raises the question of why it occurs. Figure 2.8 shows a stagnation-to-static (inlet-to-outlet) pressure rise characteristic of a fan/compressor. If the stagnation pressure distribution at the inlet and the static pressure at the outlet of the fan stage are known, the stagnation-to-static pressure ratios are given. Knowing the shaft speed and axial velocity gives the flow coefficient $\Phi = \frac{c_{ax}}{u}$. Far upstream, the axial velocity deficit leads to the operating point L'. As the CIP approach requires all local operating points to be on the characteristic, the flow redistribution shifts the operating point L' towards L. A simplified approach to obtaining an averaged operating point is to linearly weight the local operating points by mass or area. The averaged operating point is then found to be below the characteristic. The margin between the operating point and the characteristic is due to additional losses in the case of BLI. As explained above, the stagnation-to-static pressure ratio defines the operating point of the low stagnation pressure stream tube. Therefore, the shape of the rotor characteristic influences the variation of the flow coefficient at the rotor inlet. Figure 2.8 (b) shows two different rotor designs, one with a steep and one with a flat characteristic. Both compressors are subjected to a similar inlet distortion. Therefore, the difference in pressure rise between the low and high stagnation pressure stream tubes is the same for both rotors, but the variation in the flow coefficient is not. The steep characteristic shows less variation than the flat characteristic.

Similar results can be found in recent studies by Hall et al. (2017), Godard et al. (2019) or Schönweitz et al. (2017). The fan efficiency degradation varies between 1-2% (see Gunn and Hall (2014) or Mennicken et al. (2021)) and 10% (see Giesecke and Friedrichs (2019)). A dedicated design for a boundary layer ingesting turbofan as well as the experimental assessment can be found in Cousins et al. (2017) and Arend et al. (2017). The fan rig diameter has a 22 inches fan diameter, a fan pressure ratio of 1.34 and achieves an isentropic efficiency of 87.9% at ADP.

Rear integrated and mostly electrically driven fans are designed in the studies of Castillo Pardo and Hall (2019), Mårtensson et al. (2019) or Mennicken et al. (2020). The design stagnation pressure distribution is purely radial in all studies. However, the realistic distortion pattern is the superposition of radial and circumferential components as shown in Mårtensson and Laban (2020). Their design philosophy is to design a fan rotor with a

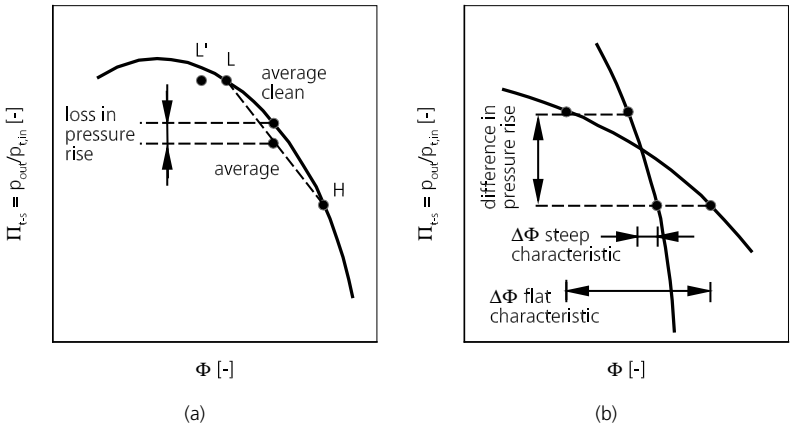

Figure 2.8.: Fan map including the operating points of the low momentum (L) and high momentum stream tube (H) and the averaged operating points with the associated loss in pressure rise on the left (a). On the right-hand side (b) the impact of different characteristics is shown. Figure adapted from Greitzer and Griswold (1976).

radially constant fan pressure ratio. Mårtensson et al. (2022) shows the deduction of a rig scale model. The rig-scale fan stage is part of a high-altitude test facility. Rasimarzabadi et al. (2022) show the ability to modify the stagnation pressure profiles within their facility, allowing the testing of different boundary layer distortion patterns. Castillo Pardo and Hall (2019) numerically and experimentally compare a free vortex design with a design dedicated to BLI flow. The latter is characterised by a reduced work input in the hub and tip sections, while the work input in the midspan is increased. In addition to the adjusted work input, the blade loading is limited by individually adjusting the chord length in the spanwise direction. The fan is also evaluated at take-off conditions. Here the boundary layer profile changes significantly and the fan operates with complex incidence distributions varying from negative to positive incidence in the spanwise direction. Similar results and mitigation strategies are detailed in the study by Mennicken et al. (2022). The fan stage used in this study has a radially decreasing fan pressure ratio and is discussed further in chapter 5.

2.2.3. Impact of downstream components on fan performance

In most cases, a homogeneous static back pressure is assumed for distorted inflow conditions, and the conditions under which this is true are already explained in section 2.1. However, Sulam et al. (1970) published experimental data where distorted inflow leads to a non-homogeneous static pressure at the fan stage outlet. The static pressure field shows an inhomogeneity of the same order of magnitude as the stagnation pressure distortion at the fan inlet. The distinctive feature of this experimental setup is the implementation of a diffuser downstream of the fan. Therefore, Greitzer and Griswold (1976) investigate the influence of downstream components to study the static pressure field at the

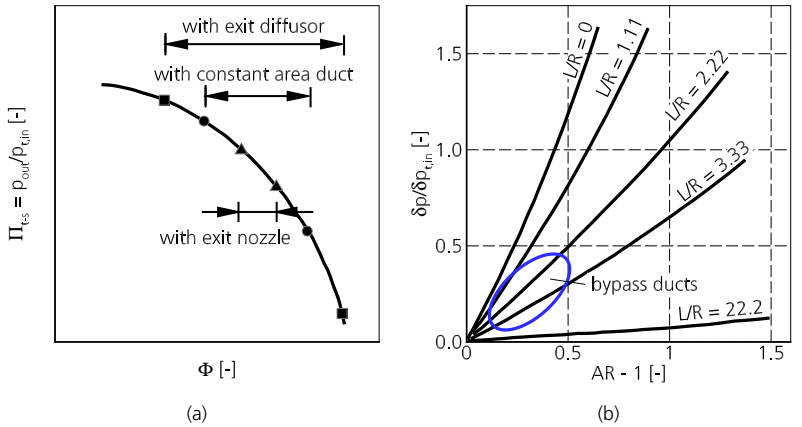

Figure 2.9.: Impact of downstream components on local operating points on the left in (a) and the impact of diffuser geometry on the static pressure field at compressor outlet in (b). Figure adapted from Greitzer and Griswold (1976)

.

compressor outlet. Taking advantage of a quasi-two-dimensional flow field, as discussed in section 2.3.2, they find that the static pressure distortion and therefore the operating points depend on the downstream component. Figure 2.9 (a) shows the effect of different downstream components on these operating points. Typically, CIP approaches assume a constant area duct downstream of the compressor and use this set of operating points as a reference. A diffuser increases the operating point variation, whereas a nozzle has the opposite effect. Focusing on diffusers, Greitzer and Griswold (1976) find that the static pressure distortion depends on the diffuser length and the diffuser area ratio. Figure 2.9 (b) shows this dependence. Low static pressure distortions are obtained for long diffusers with respect to their radius (high values of L/R) and small variations in the diffuser area ratio, which can be found near the origin of the graph. Typical bypass duct designs are characterised by small variations in the area ratio, and the length to radius ratio is expected to be between 1-3 (see Goulos et al. (2018)). Therefore, the static pressure distortion at the fan outlet is expected to be low.

Furthermore, the remaining stagnation pressure distortion can change the velocity distribution and therefore the efficiency of thrust generation. Kožulović (2010) investigates the effect of a non-homogeneous velocity distribution within the nozzle on the propulsive efficiency. With increasing non-uniformity of the nozzle velocity distribution, the efficiency degradation increases and the constant velocity distribution is identified as the optimum. Small variations in the peak velocity compared to the free stream velocity cause only small reductions in propulsion efficiency. For example, a velocity peak 1.05 times higher than the freestream results in an efficiency degradation of 1%. If the peak velocity is five times higher than the freestream velocity, the propulsion efficiency is reduced by about 20%. The location of the peak velocity within the nozzle is also found to affect the performance degradation. Peak velocities near the centreline of the nozzle result in greater propulsive

efficiency degradation than peak velocities near the casing.

2.2.4. Fan stability in stagnation pressure distortions

Stability over a wide range of operating conditions is an inevitable requirement for aero-engines and their components. Overall stability is related to both aerodynamic and mechanical stability. Aerodynamic stability is addressed first, followed by mechanical integrity.

Aerodynamic stability

Aerodynamic stability is associated with the terms surge and stall, which describe flow conditions beyond the attached flow (see Day (2016)). On the one hand, surge is characterised by fluctuating flow in the axial direction. Thus, the mass flow pulsates during surge operation (see Iura and Rannie (1954)). On the other hand, stall cells rotate along the circumference, leading to the common term rotating stall (see Huppert and Benser (1953)). Consequently, stall cells are characterised by higher circumferential than axial velocities. Stall can be divided into part span and full span stall (see Cumpsty (2004)). In full span stall one or a number of passages are completely blocked, whereas in part span stall only a fraction of one or more blade passages are blocked. However, both types of stall result in stalled and unstalled rotor passages around the circumference (see Iura and Rannie (1954)). Therefore, the average mass flow in stall operation remains largely constant (see Iura and Rannie (1954)). There are different stall mechanisms in turbomachinery acting on different length scales. Modal perturbations are a long length scale mechanism and can lead to stall as well as the presence of spikes associated with short length scales (see Day (1991)). Both types of stall move around the circumference at a circumferential velocity less than the rotor speed, but they differ in speed. Modal perturbations rotate at about 50% of the shaft speed and spike cells at about 70% (Day (2016)). Spike induced stall occurs in the tip region of the rotor due to increasing incidence (see Day (1991)). More recent research has provided a deeper insight into the flow pattern of spike stall cells. Inoue et al. (2004) observes vortex formation at the rotor leading edge. Vo et al. (2008) explains stall initiation by the combination of two effects. The forward spillage effect causes tip clearance fluid to enter the adjacent blade upstream of the leading edge. Tip clearance backflow occurs when tip clearance fluid enters the adjacent blade passage downstream of the trailing edge and flows in the upstream direction. Pullan et al. (2015) show that rotor incidence is the stall initiating mechanism, as tip clearance spike stall also occurs in rotors without tip clearance. However, the tip clearance flow characteristics reported by Vo et al. (2008) can also trigger spike stall as the associated blockage leads to increased rotor incidence.

In distorted inflow conditions, stall conditions are also of interest as they can limit the operating range of a compression system. Cao et al. (2017) and Peters et al. (2015) investigate the flow pattern within intakes at a high angle-of-attack. In such conditions, the flow tends to separate locally, creating a stagnation pressure distortion that the fan must cope with. The stagnation pressure distortions associated with this flow pattern are investigated by Wartzek (2017). Different distortion generators of different radial and circumferential extent are placed two rotor chord lengths upstream of the rotor leading edge of a transonic compressor. Two distortion generators with a radial extent of 5 and 10 % with respect to the blade height cover a 120° sector in the circumferential direction. In addition, two circumferential distortion screens of 60° and 90° are considered with an extent of 10% in

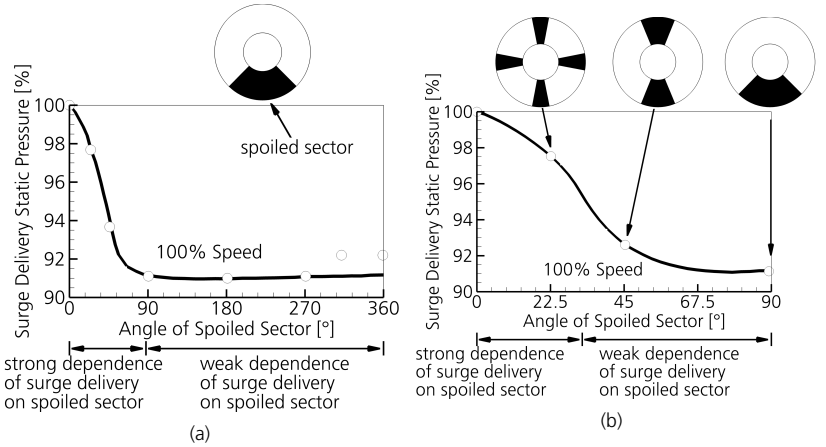

Figure 2.10.: Static pressure delivery at surge for different extents of the spoiled sector (a). Impact of the number of spoiled sectors and their circumferential location around the circumference (b). Figure adapted from Reid (1969).

radial blade height. Wartzek (2017) observes the instantaneous rotor stall of the entire rotor stage instead of the emerging stall cell at a specific circumferential position. The disturbances leading to stall are found at values of 0.5 of the engine order and the stall cells move around the circumference at half the rotor speed. This is consistent with the stall initiation research presented above. In addition, the radial extent of the distortion screen has a more pronounced effect on stall initiation than the circumferential extent. Perovic et al. (2015) investigates the stall inception of a low Mach number fan stage in the case of BLI. Static pressure perturbations associated with stall inception are found at frequencies below the blade passing frequency. Stall cells occur in the tip region where the blade incidence is above the stall inception incidence at clean inflow and the stall cell speed is 56% of the blade speed. As the stall cell propagates in the circumferential direction, it decays in the high momentum inflow regions under stable operating conditions. The fan stalls if the stall cell remains in the flow during circumferential propagation. These conditions are found when the blade incidence is sufficiently high to attenuate the decay process over a large part of the circumference. In the study of Reid (1969) a 6-stage compressor is subjected to several stagnation pressure distortions. The distortion generators are located 0.25% of compressor diameter upstream of the rotor inlet and result in stagnation pressure drops between 3.3% and 13%. Two radial distortions of 25% spanwise are investigated. One is located at the hub and the other at the tip. Irrespective of the spanwise location, the distortions cause only a small reduction of less than 2% in the surge static pressure rise. In contrast, both the circumferential extent and the intensity of the distortion are important in terms of decreasing the surge pressure rise. The static pressure rise decreases as the distortion intensity increases. Figure 2.10 shows the resulting surge pressure rise compared to clean inflow for different distortion patterns. According to the experimental data, Reid (1969) reports a strong dependence of the surge delivery static pressure for the spoiled sector between 0 and 90°. Figure 2.10 (a) shows a steep slope there. Beyond the critical angle the compressor performance remains largely constant 2.10 (a). Figure 2.10 (b)

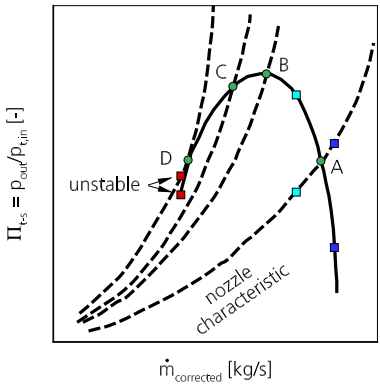

Figure 2.11.: Fan characteristic and specific stability related operating points Cumpsty (2004).

shows the effect of three different distortion patterns on the static pressure rise at surge operating conditions. All the distortion patterns have a 90° segment of low momentum fluid, but the low momentum fluid segments are arranged differently. One pattern blocks four 22.5° segments, one pattern blocks two 45° segments and one pattern blocks one 90° segment contiguously. The static pressure rise at surge decreases as the distorted sector expands in the circumferential direction. For part speed operation, the trends remain, but there is a smaller decrease in the static pressure rise at surge.

Page et al. (2017) investigate the stall behaviour of a transonic rotor. At clean inflow conditions, the aforementioned tip gap flow structures are confirmed. In addition, the rotor response to different inflow distortions is investigated. The distortion types caused by an S-shaped duct are steady and unsteady vortices, static pressure distortion and stagnation pressure distortion. All types of inlet distortion are found to be detrimental to rotor performance, while stagnation pressure distortion is found to be detrimental to rotor stability. The co-swirl part within the distorted sector is most likely to incept stall as backflow in the axial direction and spillage effects of the tip clearance flow are observed there.

There are several approaches in the literature to assess the stability of fans and compressors. A method that is based on fan and compressor maps is published by Cumpsty (2004) and will be discussed further. The solid black line in fig. 2.11 shows a characteristic in terms of stagnation-to-static pressure ratio over corrected mass flow. The dashed lines represent different nozzle characteristics that differ in nozzle area. The intersection of the nozzle with the fan characteristic at point A is a stable operating point and is marked by the green circle. The reason why this operating point is stable is discussed below. Firstly, an increase in mass flow is considered and the corresponding fan and nozzle operating points are marked by the blue squares. At these conditions, the fan pressure ratio decreases while the nozzle pressure ratio increases. Therefore, the higher nozzle pressure ratio compared to the fan pressure ratio results in a decrease in mass flow and the overall operating point shifts to point A. Secondly, a decrease in mass flow is analysed and the fan

and nozzle operating conditions are represented by the cyan squares. At these conditions, the fan pressure ratio increases while the nozzle pressure ratio decreases. Therefore, the fan is able to increase the mass flow through the nozzle until operating point A is reached again. The same explanations apply to the operating points at point B, where the slope of the fan characteristic is equal to zero, and at point C. At these points, small variations in flow conditions do not lead to instability. Contrary to the three operating conditions A to C, point D is unstable as the mass flow decreases. The resulting fan and nozzle operating points are shown by the red squares. In these conditions, the fan pressure ratio is lower than the nozzle pressure ratio. Consequently, the nozzle causes a further decrease in mass flow. The fan pressure ratio then decreases further and the whole system cannot reach stable operating conditions. Assessing stability is a difficult task and requires consideration of accurate representation of realistic flow conditions. For example, the inertia of the entire system (i.e. the storage of compressed air) can significantly alter the stable operating range of the fan. The reader is referred to the comprehensive discussion of this topic by Cumpsty (2004). Nevertheless, a simple approach is to consider the operating range up to point B as stable in order to obtain an estimate of the stability limit.

There are different measures to assess the margin to the stability limit. Throughout this study, the criteria in eq. (2.12) are applied according to Cumpsty (2004).

$$SM = 1 - \frac{\Pi_{t,working}}{\Pi_{t,surge}} \cdot \frac{\dot{m}_{surge}}{\dot{m}_{working}} \tag{2.12}$$

In fan and compressor design, it is also common to use metrics that consider the load on the blades and vanes. One of these is introduced by DeHaller (1955). The corresponding DeHaller number is a measure that quantifies flow deceleration according to eq. (2.13). Typically, values above 0.7 should be aimed for to avoid flow separation.

$$DH = \frac{w_{out}}{w_{in}} \tag{2.13}$$

Another measure of compressor blade loading is introduced by Lieblein et al. (1953). In principle, the blade loading coefficient is derived from subsonic cascade tests and is therefore valid for similar airfoils. The development of the diffusion factor makes use of some simplifications and assumptions. The basic idea is briefly outlined. The isentropic Mach number distribution of the airfoil is approximated as a triangle. On the suction side, a constant deceleration is assumed between the peak velocity and the trailing edge of the rotor. In addition, the boundary layer growth and the velocity distribution on the suction side are assumed to be independent of the blade geometry. This leads to the empirically based diffusion factor in eq. (2.14).

$$DF = 1 - \frac{w_{out}}{w_{in}} + \frac{|\Delta w_\Theta|}{2 \cdot w_{in}} \cdot \frac{s}{c} \tag{2.14}$$

The diffusion factor combines the DeHaller number with a flow turning related quantity in which the inverse pitch to chord ratio incorporates the geometric feature of the blade. Typically, the diffusion factor should be kept below 0.55 to avoid instability.

There are also approaches in the literature to assess the stability of fans and compressors in distorted inflow. Hynes and Greitzer (1987) consider two-dimensional, incompressible flow within their approach. The stability assessment is divided into two steps. First, the

steady-state distortion transfer is calculated. Secondly, a common stability analysis for aerodynamic flows is performed. In such an analysis a perturbation is imposed and the stability can be assessed by considering the growth or decay of the perturbations Hynes and Greitzer (1987). Hynes and Greitzer (1987) find the onset of instability near the point where the derivative of the distorted compressor characteristic is zero. Hynes and Greitzer (1987) use the experimental data from Reid (1969) to validate their approach. The numerical results show the same trends in static pressure rise loss as the experimental data. In addition, the critical angle of the spoiled sector is well predicted by the model. Mazzawy (1977) treats the flow as unstable when any of the individual sectors around the circumference reaches the peak of its individual stagnation-to-static characteristic. Similar treatment is given by Lecht (1987).

Structural and aeroelastic stability

In addition to aerodynamic stability, BLI introduces challenges in terms of structural and aeroelastic stability. Firstly, structural integrity and therefore high cycle fatigue strength is addressed. Demonstrating high cycle fatigue strength requires the calculation of stress levels due to centrifugal and pressure forces. According to Saravanamuttoo et al. (2017), fan blades of modern engines have an almost constant stress distribution. Considering a simplified cylindrical blade leads to eq. (2.15), which provides a formula for the required blade section A_i. The cross-section at a given spanwise position i depends on the specified stress level σ_a, the material density ρ, the square of the rotational speed ω and the hub radius R_{hub}.

$$A_i = A_{hub} \cdot exp\left[\frac{-\rho\omega^2}{\sigma_a} \cdot (R_i^2 - R_{hub}^2)\right] \tag{2.15}$$

Thus, the fan blade thickness increases with increasing shaft speed for a fixed stress level. If the blade geometry is fixed, the formula can also be used to calculate the stress level as a function of shaft speed. The resulting blade stress level must be below the maximum strength of the material with safety margins for additional dynamic stresses. Haigh diagrams are commonly used to specify the specific material limits.

Aeroelasticity related stability limiting effects are flutter and forced response (see Cumpsty (2004)). Self-excited blade vibrations with a frequency close to the natural frequencies of the blade with insufficient damping are called flutter. Forced response refers to vibrations caused by external aerodynamic forces, i.e. rotor-stator interaction Mailach (2010) or in the case of BLI. The induced excitation can lead to blade vibration and adversely affect the aeroelastic stability Hall et al. (2022). If the excitation frequency is equal to one of the natural frequencies of the blade, the forced response of the blade can negatively affect the aeroelastic stability (see Cumpsty (2004)). Critical operating conditions can be identified by the intersection of the engine order characteristics with the blade natural frequencies in the Campbell diagram. Typically, the crossings of low engine orders with the blade frequencies are of most interest, as these contain a higher energy density, and therefore the blade design aims to avoid such crossings. However, both flutter and forced response lead to elastic deformations of the blade which cause dynamic stresses. If the dynamic stress exceeds the tolerable limit at a given mean stress level, high cycle fatigue strength will not be achieved and service life will be reduced or even instantaneous damage may occur.

Besides the usual rotor-stator interaction, the time-dependent inflow variation from the rotor perspective is a challenge in BLI integration scenarios. Bakhle et al. (2012) analyse an

intermediate design iteration of the NASA distortion tolerant fan. The first two harmonics of the distortion show the highest model force amplitudes with a peak in the third mode of the blades. With ADP, the blade tip trailing edge displacement is less than 1.4 mm and the maximum dynamic stress at the fan blade root is less than 5 MPa. In addition, ADP avoids blade flutter. The resulting fan design, introduced by Cousins et al. (2017), features increased blade thickness over a large part of the span and rebalancing to limit blade deformation and stress levels. This fan blade is mechanically assessed by Bakhle et al. (2018) and the intake-fan interaction is addressed by Heinlein et al. (2019). They demonstrate aeromechanical stability in terms of blade stresses, blade displacement and flutter.

Eichner et al. (2019) and Eichner and Belz (2019) consider a boundary layer ingesting counter-rotating fan and investigate the first rotor blade response to boundary layer ingestion during take-off, climb and cruise. The boundary layer patterns are dominated by the first three harmonics. The first bending mode of the first rotor is the major contributor to the stress levels at high shaft speeds, while the second blade mode is dominant at part speed. In addition, they find that the BLI induced vibrations are more severe than the rotor-stator related vibrations, highlighting the importance of aeromechanical blade assessment in the case of BLI.

2.3. Applied methods to assess fan stages in distorted inflow

This subsection provides an overview of different approaches applied to fans and compressors to assess performance and stability at distorted inflow conditions. The level of accuracy of the different methods continuously increases throughout this subsection.

2.3.1. Compressors-in-Parallel

The basic idea of the compressors-in-parallel approach has already been introduced in section 2.2.1. To recapitulate, the existing fan and compressor characteristics obtained under homogeneous flow conditions are used to calculate the fan or compressor performance under distorted inflow conditions. Compressor performance is obtained by analysing two stream tubes coupled by a common static pressure at the outlet. All interactions of the stream tubes throughout the compression system are neglected. There are several approaches in the literature that take advantage of this simple model and extend its capabilities.

Multiple Compressors in Parallel

One of these extensions is the multiple compressors in parallel approach introduced by Mazzawy (1977). In this study, the circumferential extension of a segment is of the order of 20°. In addition, the unsteady behaviour of the flow is implemented, which is explained in detail in section 2.2.2. Another extension is the deflection of the flow within the rotor. The static pressure condition at the compressor outlet remains an input, but can vary around the circumference. Taking these effects into account leads to a good agreement of the performance prediction with experimental data of Sulam et al. (1970).

Radial Compressors in Parallel

Another extension of the model is the consideration of radial compressors in parallel, as suggested by Voigt and Friedrichs (2021). In this approach, the compressor is divided into equally spaced radial segments. Consequently, the compressor map is divided in the same fashion and can be used in BLI calculations. In the study of Voigt and Friedrichs (2021), a fuselage engine designed by Giesecke et al. (2017) operates in a purely radial stagnation pressure profile. In such conditions, the BLI induced variation of the flow coefficient in the radial direction is high and therefore the approach is expected to have advantages over the classical CIP model. In addition, Voigt and Friedrichs (2021) analyse the effect of radial segmentation on performance prediction. The use of five radial segments is the best trade-off between radial resolution and performance prediction accuracy gain.

Compressors in Parallel with unsteady blade aerodynamics

Lecht (1987) studies the response of two transonic compressors to distorted inflow. Comparing the measured data with conventional CIP results, Lecht (1987) observes that the calculated operating points and in particular the stability limit are located at higher mass flows. The reason for this is expected to be of an unsteady nature. Therefore, Lecht (1987) includes operating conditions beyond the stable operating range obtained at homogeneous inflow. The extension is based on the findings of Melick Jr. and Simpkin (1972) that the performance of a single airfoil exhibits unsteady behaviour in the case of instantaneous changes in blade incidence. In particular, the airfoil operates stall free beyond the steady-state stall limit. The extent of the range extension is dependent on the reduced frequency mentioned above. There is also an additional gain in lift due to the increased airfoil incidence. Satyanarayana et al. (1974) found similar results for compressor cascade arrangements. Lecht (1987) incorporates these findings and calculates the effective blade pitch to extend the compressor characteristics. The compressor pressure ratio characteristics are extrapolated by keeping the pressure ratio constant, while the isentropic efficiency is extrapolated linearly. The resulting performance calculation is in good agreement with experimental data.

2.3.2. Two-dimensional approaches

Two-dimensional approaches are widely used in the design of turbomachinery components because they require low numerical effort to calculate the flow field and provide a good assessment of performance.

Axial-radial plane - Throughflow

Streamline curvature (SLC) approaches are throughflow codes. By assuming circumferentially averaged flow in an axial-radial plane, the numerical effort of flow field calculations is low. This leads to the use of streamline curvature approaches in the early design stages of turbomachinery components. Due to the fact that SLC is well known in the turbomachinery industry and research, this approach is considered for the new design and assessment methodology for distorted inflows.

Figure 2.12 illustrates the basic idea of streamline curvature, which according to Denton (1978) is to solve the flow field represented by a number of stream surfaces between the

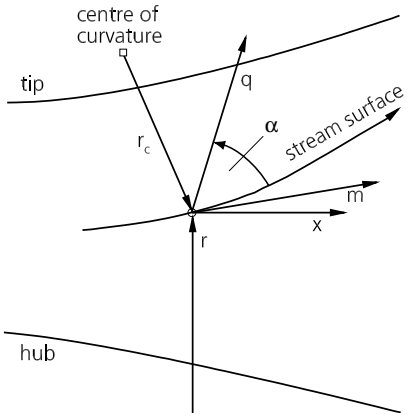

Figure 2.12.: Visualisation of the coordinate system used within streamline curvature according to Denton (1978).

hub and the tip. The corresponding coordinate system is given by a streamwise coordinate m and a quasi-orthogonal coordinate q. Based on the name of the latter, m and q are typically orthogonal in such approaches. A discrete number of stations has to be defined along the flow direction at which the motion of a fluid particle has to be calculated. Equation 2.16 provides the equation of motion for a fluid particle located outside of the bladed sections and expresses the radial equilibrium. The numerical integration of eq. (2.16) from hub to tip gives the meridional velocity field as a function of an integration constant at each station q.

$$\frac{d}{dq}\left(\frac{c_m^2}{2}\right) = \underbrace{\frac{dh_t}{dq}}_{I} - \underbrace{T\frac{ds}{dq}}_{II} - \underbrace{\frac{1}{2r^2}\frac{d(r^2c_\Theta^2)}{dq}}_{III} + \underbrace{\frac{c_m^2}{r_c}sin(\alpha)}_{IV} + \underbrace{c_m\frac{dc_m}{dm}cos(\alpha)}_{V} \tag{2.16}$$

The terms *I*, *II* and *III* refer to the variation of the stagnation enthalpy h_t, entropy s and angular momentum rc_Θ along the quasi-orthogonal plane. Therefore, the values of these variables must be known at each station q. The angular momentum conservation is given in eq. (2.17) and takes into account the term consisting of the radius r_i times the circumferential velocity $c_{\Theta,i}$.

$$r_i \cdot c_{\Theta,i} = r_{i+1} \cdot c_{\Theta,i+1} \tag{2.17}$$

This term is conserved between stations i and i+1. It also follows from the third term that only computational domains with non-zero hub radii can be used. The fourth term considers the centrifugal force to which a fluid particle is subjected. Therefore, the curvature of the stream surface is accounted for by the radius of curvature r_c. The flow angle α is measured between the stream surface and the quasi-orthogonal line q. The term V accounts for the variation of the meridional velocity along the stream surface and is approximated in each iteration by solving the velocity field. The values of the stagnation enthalpy, entropy and angular momentum are still unknown. At the first quasi-orthogonal line of the

flow field these values are processed by evaluating the inlet boundary condition. In blade and vane-less parts of the domain, these values are preserved along a stream surface and depend on the upstream quasi-orthogonal q. Within blade and vane rows, the circumferential velocity c_Θ changes depending on the specific blade or vane performance, which is considered by evaluating (empirically based) correlations. Taking into account the velocity field at the rotor outlet, the Euler work equation gives the stagnation enthalpy increase according to eq. (2.1). In addition, the calculation of the entire flow field allows the evaluation of the angular momentum. The entropy increase is achieved by evaluating the loss correlations, which will be discussed in more detail later in this subsection. As mentioned above, the velocity field can be evaluated as a function of an integration constant. The consideration of the conservation of mass according to eq. (2.18) allows the calculation of the integration constant.

$$\dot{m} = \int_{hub}^{tip} 2\pi\rho c_m sin(\alpha)(1-b)dq \tag{2.18}$$

The density ρ of the fluid is given using the ideal gas equation. The mass flow is calculated by integrating over the entire circumference. In bladed rows the blades block a part of the cross-section and this is taken into account by the variable b in eq. (2.18).

Throughflow solvers provide circumferentially averaged flow fields in an axial-radial plane. Therefore, the circumferential flow redistribution upstream of the fan stage cannot be accounted for within this approach. As long as the flow redistribution is not a driving flow feature such as in axisymmetric, radial stagnation pressure distortions, throughflow can provide a good estimate of fan and compressor performance. Lee et al. (2018) and Abbasi et al. (2018) take advantage of this approach in the aforementioned flow conditions. Mennicken et al. (2019) extends a common throughflow approach by incorporating flow redistribution via a calibration data set. The preliminary design and assessment approach presented in chapter 3 is based on this work.

Blade-to-Blade plane

Another two-dimensional approach to consider distorted inflow is to calculate the flow in a blade-to-blade or axial-circumferential plane (S1). The radial variation of the flow field is neglected and therefore the approach is valid for compression systems with a high hub-to-tip ratio. The treatment of incompressible and inviscid flows can be found in the studies of Dunham (1965), Greitzer and Griswold (1976), Stenning (1980), Hall (2015) and Hall et al. (2022). The interaction of the blade and vane rows, or even the entire compressor/fan, is incorporated by actuator discs. These actuator discs change the swirl and energy level within the compression system.

2.3.3. Three-dimensional approaches

The solution of the Favre and Reynolds-averaged Navier-Stokes (RANS) equations is usually required to calculate density-variable flows in turbomachinery. This set of equations considers the conservation of mass, momentum and energy. Several RANS-based approaches have been used in previous BLI studies. These are presented below.

Steady approaches - single passage and frozen rotor

In turbomachinery applications, steady-state calculations are often used to investigate component performance or to identify specific flow features. The challenging BLI flow features usually require a time-resolved calculation of the flow. However, Schoenweitz and Schnell (2016) consider commonly used turbomachinery setups. The first approach is the single-passage setup, which assumes periodic flow in the circumferential direction. As introduced in section 2.2.1, these assumptions are not valid in BLI cases and flow redistribution effects cannot be resolved due to the simplified modelling. Consequently, the flow kinematics at the rotor inlet differ from the reference data obtained by uRANS. Another setup for steady-state simulations is the frozen rotor approach. In this modelling a full annulus setup is used, but the rotor is fixed in one position. This results in a fixed position of the rotor with the distorted inflow as well as with the downstream stator. As a result, the time-dependent changes in inflow and outflow conditions are neglected. Consequently, the rotor loading and blockage effects within the distorted sector are overpredicted, resulting in a pessimistic performance prediction. It should be noted that the frozen rotor calculation differs from the instantaneous flow field of a time-resolved calculation due to the aforementioned simplifications.

3D Body Forces

Body force approaches incorporate the rotor and stator performance by adding source terms to the Navier-Stokes equations rather than resolving the three-dimensional rotor and stator geometries. Therefore, the specific blade geometry is not required as an input, instead a parametric description of the performance data is included. Body force approaches are therefore similar to the flow calculations introduced above. Typically, the rotor and stator performance is averaged. The simplified consideration of the rotor and stator rows allows the use of coarser meshes compared to conventional meshes which resolve all geometric features of the specific component. The parametric description of the blade performance must be specified as input. Different fidelities of body force approaches are available in the literature. A three-dimensional, inviscid (Euler equations) and steady-state representation of the flow is introduced by Hall et al. (2017) and Peters (2014). Thollet et al. (2016) implements the body force approach within a RANS solver. This includes viscous flow as well as time-dependent variations. Godard et al. (2019) applies this method to conceptual fan design.

Frequency domain based approaches

The main idea of frequency domain methods is to exploit the periodic and deterministic nature of turbomachinery flow. The spatial resolution of blades and vanes is included. Transient flow perturbations are approximated by Fourier series. The accuracy of frequency domain methods depends on the number of harmonics considered. In general, the number of harmonics required increases with the complexity of the flow field. In addition, the numerical complexity of frequency domain methods increases with the number of harmonics considered. However, this method offers the possibility of reducing the numerical effort while resolving the main flow features. Schoenweitz and Schnell (2016), Frey et al. (2017) and Junge (2023) demonstrate the ability of such an approach to resolve BLI flow features. Further information, explanation and discussion of frequency domain methods can be found in Junge (2023).

Unsteady RANS (uRANS)

In general, unsteady RANS calculations take into account the time-dependent changes of the flow. Within this approach, the rotor and stator geometries are resolved and the full interaction of the fan stage with the distortion, which is fully described in section 2.2.1 and section 2.2.2, is taken into account. Therefore, a time accurate calculation of the flow can be obtained by uRANS computations, but the numerical effort and the requirement of an existing detailed three-dimensional design of the fan stage reduces its applicability during preliminary design. Nevertheless, this approach is still necessary during the design process, but is more likely to be advantageous at a later design stage.

2.4. Interim conclusion

This chapter deals with the specific challenges of fan operation within different distortions. In the case of BLI, fan performance is affected predominantly by stagnation pressure distortions. In conjunction with this type of distortion, BLI-specific flow characteristics occur upstream of the fan stage due to the interaction of the fan stage with the distortion. The main changes within the flow can be divided into the specific effects of low momentum fluid within the distortion, flow acceleration due to circumferential flow redistribution and corresponding swirl upstream of the fan. The flow redistribution also changes the fan performance. For example, the occurrence of counter-swirl results in positive incidence combined with increased Mach number levels. These inflow conditions amplify the flow through the rotor tip gap and significantly increase the rotor losses. In a subsequent step, different approaches to calculating fan performance in distorted inflow conditions are presented. These approaches are either too imprecise (i.e. CIP) or the numerical effort is too high (i.e. uRANS), which prevents their application at an early stage of the design process. Consequently, there is a need to develop a new design methodology for fan design and assessment that can be used during the preliminary design phase.

3. Methodology development for fan design and assessment in distorted inflow

This chapter deals with the development of a preliminary fan design and assessment methodology for distorted inflow conditions. Based on the literature review presented in the previous chapter 2, the BLI related flow features are introduced. Furthermore, the need to develop a methodology that can be used during preliminary design is identified. This methodology is required to be applicable to the flow path as well as the rotor blade and stator vane design. In addition, the methodology is required to have the capability to capture BLI flow features such as flow redistribution (i.e. flow kinematics and static pressure distribution upstream of the fan rotor) and BLI related performance changes around the circumference. In this context, capability is understood as a trade-off between low numerical effort and the quality of the results. At an early design stage, few design parameters are fixed and thus, the degree of freedom is high. Therefore, a low numerical effort allows the exploration of large parameter spaces, which is advantageous at this design stage. Furthermore, the methodology must be applicable to different integration scenarios (i.e. the scenarios presented in chapter 1).

Firstly, the different methods used in this thesis are discussed. The preliminary design and assessment methodology combines a streamline curvature code, as introduced in section 2.3.2, and a steady RANS approach. A time-accurate approach used for data verification is also presented. In a subsequent step, the challenges of post-processing BLI flow fields are addressed. Secondly, the newly developed methodology is comprehensively presented and discussed. This includes the coupling of the different methods, the identification of relevant circumferential positions for the flow field calculation and the incorporation of BLI specific flow features in streamline curvature. The preliminary newly developed design methodology is applied to a fan stage exposed to boundary layer ingestion in the embedded turbofan scenario. Thirdly, the limitations of the approach are discussed.

3.1. Baseline methods and theory

3.1.1. Streamline curvature code ACDC

The *DLR* in-house streamline curvature code *ACDC* is based on the developments of Schmitz et al. (2012). Within the code, a number of different loss correlations are included to account for loss mechanisms of three-dimensional flows that cannot be resolved directly. Losses due to secondary flow are predicted by the model introduced by Grieb et al. (1975). The spanwise distribution of deviation and losses are calculated by the model of Roberts et al. (1986). Radial mixing is included by the model of Gallimore and Cumpsty (1986). The prediction of tip gap related losses is included by considering a correlation

Table 3.1.: Design space of the airfoil database according to Schnös (2020).

	Ma_{in} [-]	Re [-]	DF^{ADP} [-]	$MVDR$ [-]	$\frac{s}{c}$ [-]	γ [°]	$\frac{a}{c^2}$ [%]
Minimum	0.35	$5 \cdot 10^5$	0.35	1.0	0.5	110.0°	1.5
Maximum	1.20	$5 \cdot 10^6$	0.55	1.2	1.2	147.5°	8.5

based on the work of Denton (1993) and Banjac et al. (2014). The influence of the tip gap flow on the flow angle at the blade or vane outlet is considered using the model of Lakshminarayana (1970). In addition to the modelling mentioned above, *ACDC* consists of a database of optimised airfoils, which is discussed in detail in Schnös (2020). The main idea is to have a database of optimised airfoils that can be applied to specific new fan and compressor designs. The database contains the parametric description of the airfoil performance for SLC calculations. Table 3.1 shows the design parameters and their lower and upper limits. The parameter set can be divided into three main groups. The first group contains flow field related parameters such as inflow Mach number and Reynolds number. The second group is related to the aerodynamic performance of the airfoils. These include the diffusion factor at the ADP and the meridional velocity density ratio (MVDR). The third group of parameters is related to the geometric features of the airfoils. Here the pitch-to-chord ratio (solidity; s/c), the stagger angle γ and the non-dimensional airfoil cross-sectional area a/c^2 are considered. As mentioned above, within the blade rows there is both flow turning and loss generation. Schnös (2020) accounts for these effects by individually calibrated correlations for each airfoil in the database. The airfoil performance calibration uses 40 loss polars representing eight different inflow Mach numbers, three different levels of Reynolds number and three levels of MVDR. To obtain the airfoil performance, the *Mises* solver is used to calculate the flow field in a blade-to-blade plane. A detailed description of the specific correlations, the calibration parameters and the calibration procedure is given in Schnös (2020).

The calibrated airfoil performance consists of the reference flow angle at ADP and the operating range of the specific airfoil (i.e. including the flow angle at choke), the deviation, the stagnation pressure loss at ADP and the loss levels at off-design performance. Figure 3.1 shows the loss polar of an airfoil at two different Mach number levels. The squares represent the *Mises* results and the solid lines show the correlation based airfoil losses. Minimum losses are found at low incidence inflow conditions. The operating range of the airfoil covers incidence angles at which the airfoil losses are less than two times of the loss minimum. Beyond the *Mises* based operating range, the airfoil performance is obtained by extrapolation. Thus, the losses of the black line increase as the angle of incidence increases. At higher Mach numbers, choking conditions can occur and limit the operating range at negative incidence. The kink in the blue line in fig. 3.1 shows the increase in airfoil losses at a given negative incidence associated with that flow feature. Beyond the last *Mises* predicted operating points at positive incidence, the losses increase as the angle of incidence increases.

The individual airfoil performance is incorporated into the streamline curvature approach. A number of individual airfoils are stacked to define a rotor blade or stator vane. Depending on the operating point and specific fan performance, this results in varying radial blade

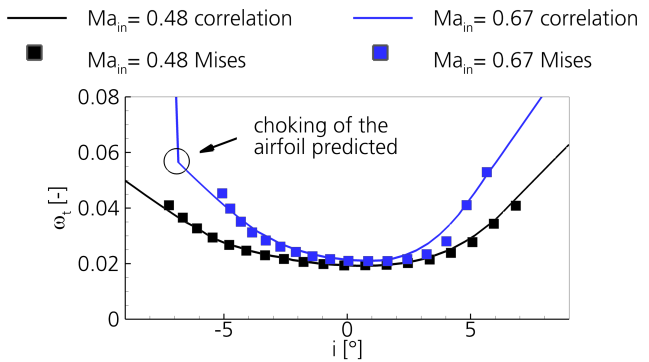

Figure 3.1.: Working range of an individual airfoil at different inflow Mach numbers.

or vane performance along a speed line. Individual sections of blades and vanes can exceed their operating range (derived from S1 calculations) without affecting the aerodynamic stability of the entire stage. If an airfoil operates beyond its individual working range, the airfoil performance can be extrapolated.

For undistorted inflow conditions (i.e. fan map calculations), incidence and loss extrapolation is considered. The operating range is determined with respect to three limiting factors. The operating limits of a fan are reached when the meridional Mach number exceeds the limits of 0.9 or 0.01. These are therefore numerically related operating limits. When a converged operating point is reached, the stability limit of the fan is considered to be reached when the stagnation-to-static fan characteristic peaks. This is consistent with the explanations given in section 2.2.4.

Distorted inflow conditions can be accounted for by applying individual spanwise stagnation pressure and swirl distributions as well as an individual mass flow in each local operating condition. The conventional SLC approach is extended by a stream tube contraction model, which allows the flow redistribution effects to be taken into account. The working area extrapolation takes into account the incidence range extrapolation, but the loss level is kept constant from the last stable operating point of the individual airfoil. The calculation of local flow fields is discussed in greater detail in this section.

In addition to the parametric performance description, the optimal airfoil database contains the specific airfoil geometry. This enables three-dimensional blade and vane generation by stacking a number of airfoils along the span. This provides an end-to-end coupling between preliminary and detailed design, and allows the subsequent analysis of the preliminary design geometry using three-dimensional CFD or experimental approaches.

3.1.2. Three dimensional Favre- and Reynolds-averaged Navier-Stokes code TRACE

The three-dimensional Favre and Reynolds-averaged Navier-Stokes code *TRACE* is a parallelized flow solver that calculates the flow field on a mesh of finite volumes (cf. Becker

et al. (2010)). The density based code is specifically developed for turbomachinery applications considering compressible flow and is widely used in industry and research.

Structured meshes are used in this study. Blades are meshed using OCH topologies, while bladeless rows are meshed using H topologies. The spatial discretisation is of second order accuracy. The flow near solid surfaces is modelled by wall functions. Therefore, the cell size near surfaces is chosen such that the dimensionless wall distance (y^+) is between 30 and 70.

Inflow boundary conditions consist of stagnation pressure and stagnation temperature, radial and circumferential flow angles. For homogeneous inflow conditions, each quantity is defined by a specific value. In BLI integration scenarios, the inflow conditions vary in both the spanwise and circumferential directions. Therefore, two-dimensional distributions of stagnation pressure and swirl angle are applied at the domain inlet. Unlike the stagnation pressure and swirl, the stagnation temperature is constant. A static pressure boundary condition is applied at the outlet. Throughout this study, the static pressure at the domain outlet remains at the value of the ADP conditions.

Fully turbulent flow is considered and the k-ω turbulence model of Wilcox (1988) is applied. In addition, streamline curvature effects are taken into account by the model of Bardina et al. (1985). At stagnation points the turbulent kinetic energy is usually overpredicted by RANS. The model of Kato and Launder (1993) is used to correct the increase of this quantity. Turbulence modelling requires the additional prescription of two quantities. Typically, the turbulence intensity and the turbulent length scale must be specified.

Three-dimensional CFD is used in this study for several purposes. Firstly, the fan performance is calculated with steady, single passage setups when homogeneous inflow or radial stagnation pressure distortions are considered. Within such setups, mixing planes, which perform a circumferential averaging of the flow, are used to couple adjacent blade rows. Secondly, the newly developed methodology takes advantage of RANS setups to account for flow redistribution within the intake. This is further discussed in section 3.3. Thirdly, the calculation of the flow field in BLI integration scenarios is performed by time-accurate RANS approaches. For this, full-annulus setups are required. For the coupling of adjacent blade rows, sliding non-one-to-one interfaces (also known as zonal interfaces) are used according to Yang et al. (2002). For the time discretisation, a second order implicit Euler backward scheme is used.

3.2. Post-processing of uniform and non-uniform inflow

For uniform inflow conditions, two main assumptions are made to simplify the analysis. Firstly, the flow is assumed to be periodic in the circumferential direction. Secondly, the radial performance calculation assumes that the fraction of the flow (in terms of mass, area or flux) remains at the same relative spanwise position at all streamwise positions within the numerical domain. This in turn neglects radial crossflow. An example of such a flow feature is a corner separation with transverse mixing that redistributes a portion of the flow. Conventional analysis techniques are used to

- operating conditions with homogeneous inflow stemming from 3D CFD and SLC.
- operating points with purely radial distortions stemming from 3D CFD and SLC.

- all local operating points of the new design and assessment methodology as those operating points also fulfil the assumption of no interaction in the circumferential direction.

BLI is associated with non-homogeneous inflow. In chapter 2, the effect of flow redistribution on the upstream flow field of the fan stage is introduced. This flow feature violates the assumption of periodic flow in the circumferential direction. Therefore, a more complex approach is required to follow the particles as they pass through the fan stage. In time-resolved flows this is a complex task to accomplish and Fidalgo et al. (2012) as well as Gunn and Hall (2014) showed that the complexity of tracking the time-resolved particle path can be reduced by first time-averaging the flow field and then taking advantage of conventional streamline tracking in the time-averaged flow field. A similar approach is used in this study, which is based on the development of Schoenweitz and Schnell (2016).

The post-processing procedure consists of three main steps, which are shown in fig. 3.2 and fig. 3.3. Figure 3.2(a) shows the instantaneous axial velocity field in the fan stage. In the lower part, the boundary layer fluid and therefore lower axial velocities are present. In the first step, the blades and vanes are removed from the flow and the flow field is transferred to the absolute reference frame. According to Adamczyk (1984), a "gate function" is applied to ensure that parts of the volume where a blade or vane is located do not contribute to the mean value in that particular volume. The resulting instantaneous flow field is shown in fig. 3.2 (b).

In this study, a number of 16 instantaneous snapshots per rotor pitch are then used for the time average. Depending on the number of blades, this leads to a minimum of 240 and up to 272 distortion to rotor to stator positions. This is in the same order of magnitude as presented in Castillo Pardo and Hall (2022). The time-averaged flow field is shown in fig. 3.2 (c). Streamlines are tracked within the time-averaged data. The black lines in fig. 3.3 (a) represent a stream tube consisting of a number of streamlines. Along a stream tube the conservation of mass and rothalpy is evaluated to verify the results within

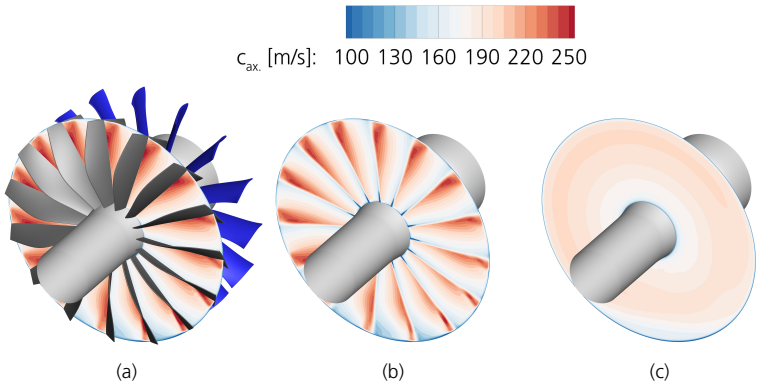

Figure 3.2.: Instantaneous flow field in (a), removed blades from the instantaneous flow field (b) and time-averaged flow field in (c).

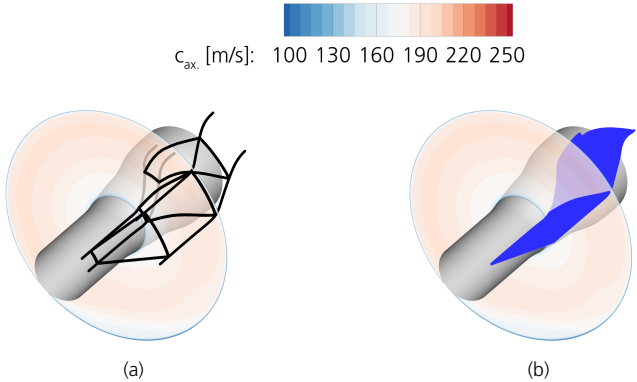

Figure 3.3.: time-averaged BLI flow field. Stream tube tracking in (a) and stream line tracking in (b).

the post-processing. Based on the streamlines, radial performance data is then obtained by circumferentially averaging the data. In addition, radial and circumferential averaging results in zero-dimensional performance data.

Within the newly developed design methodology, explained in detail in the next section, the fan flow field is resolved in an axial-radial plane. Consequently, the fan performance data represent a specific circumferential position which has an infinitesimal extent in the circumferential direction. The analysis of the flow redistribution upstream of the fan stage is therefore achieved by tracking streamlines as shown in fig. 3.3 (b) within the intake. For the sake of comparability, the spanwise rotor performance of the time-resolved calculation is determined with stream tubes that have an infinitesimal circumferential expansion. This reduces the stream tubes to a spanwise array of streamlines introduced into the flow field at a given circumferential position at the inlet.

In contrast, stator performance requires the analysis of stream tube data which has a circumferential extent. The reason for this is that the vane wakes remain in the time-averaged flow field. Therefore, the stream tube averaged data is the appropriate data to assess the vane performance itself. It is also the appropriate data to compare with the data from the preliminary fan assessment.

Stream tube post-processing is restricted to flows where the time-averaged particle path coincides with the time-accurate particle path. This assumption is violated in flow fields with short length scale disturbances or when secondary flow dominates the flow field. Short length scale disturbances occur in VTP wakes and are discussed further in chapter 5. An example of secondary flow is a corner separation. This flow feature leads to crossflow associated with flow redistribution from the hub to the midspan and vice versa. The time-accurate and time-averaged particle paths can then diverge, making performance data questionable.

3.3. Methodology for fan design and assessment

As introduced in chapter 1 and section 3.1.2, the assessment using unsteady CFD methods is very time consuming, making it unsuitable for the exploration of large design spaces. Therefore, the new methodology focuses on methods that are numerically more efficient and the selection of methods supports the main objective of achieving an efficient preliminary design and assessment of boundary layer ingesting fans allowing the exploration of wide design spaces.

A predecessor of this methodology is presented in the study of Mennicken et al. (2019) and relies on calibration. The data set used to calibrate the upstream flow redistribution includes BLI flow fields of twelve individual fans from a design study conducted by Lengyel-Kampmann (2016). The fans have a high and comparable level of maturity in terms of fan aerodynamics. The need for a calibration data set might introduce non-physical effects. This would lead to an incorrect assessment of new BLI configurations. For this reason, the following subsection presents the extended calibration-free design and assessment methodology, which only requires information on the fan stage and the fan integration scenario.

3.3.1. Concept and method coupling

Figure 3.4 (a) shows the fan and bypass section of a turbofan engine. For simplicity, the core engine and core-related geometric features are neglected. This is reasonable for engines with high bypass ratios, as the fraction of core mass flow is of little interest for fan performance. Typically, only the internal flow is considered in fan design, which is shown in green in fig. 3.4 (a). The BLI related flow redistribution takes place at the inlet. As explained in chapter 2, this is a three-dimensional flow phenomenon. Consequently, a steady state RANS approach is suitable to capture this redistribution process if the static pressure field upstream of the fan stage at the aerodynamic interface plane (AIP) is known.

Figure 3.4 (b) shows the section of the bypass that is commonly considered during fan design. The preliminary fan design takes advantage of a streamline curvature approach and is shown in orange. As can be seen in fig. 3.4 (b), the inlet flow field is also covered by SLC. A common SLC approach is not able to cover the circumferential flow redistribution. Therefore, an enhanced SLC approach is required to account for these flow features. Furthermore, the overlap between SLC and RANS requires a coupling of both approaches, which is achieved at the AIP. The entire process of designing and assessing a fan stage is explained in detail afterwards.

The flowchart in fig. 3.4 (c) shows the general idea of the newly developed methodology. Essentially, the methodology can be divided into three parts, namely *Specification and design*, *Flow redistribution within the intake* and *Local fan operating points*.

Specification and design

The first part requires decisions on global design choices. Depending on the fan integration scenario, the stagnation pressure distortion may differ significantly. The embedded turbofan distortion pattern addressed in chapter 4 is different from the aft-propulsor integration distortion pattern addressed in chapter 5. Both patterns are already shown in

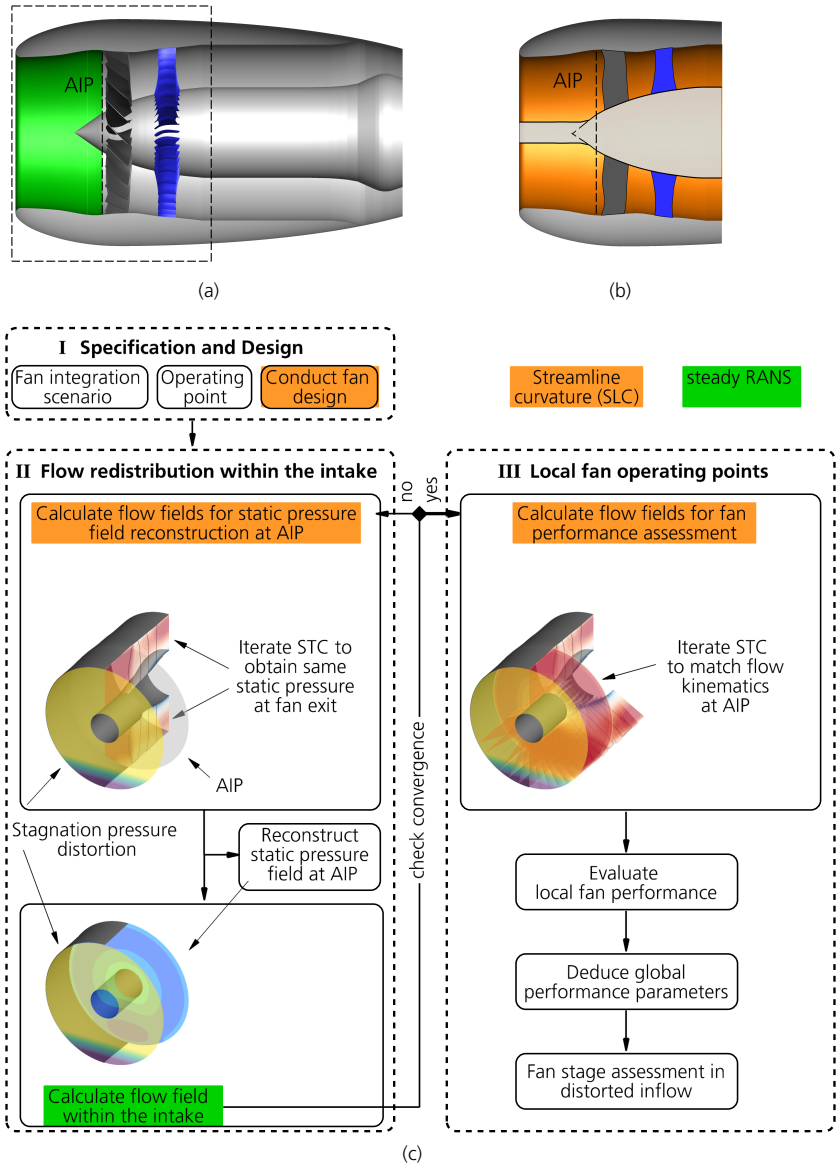

Figure 3.4.: Sectional drawing of the bypass section of a turbofan engine (a) and the corresponding design space for fan design (b). The lower part shows the flow chart of the fan design and BLI assessment methodology.

fig. 1.2. In addition, the operating points of BLI propulsors are likely to differ from the design conditions of fans installed in underwing engines. These changes can be due to BLI induced changes in inflow conditions or due to the application of the fan stage. The latter can be divided into fan stages that are required to provide a large portion of the overall thrust, such as the fans of embedded turbofan engines, and fan stages that are an additional thrust generator, such as aft-propulsors in the rear of the fuselage. The integration scenario must therefore be carefully considered when specifying the operating point. The design is then carried out using the streamline curvature approach. When designing the fan, clean inflow conditions, an averaged stagnation pressure resulting from the two-dimensional distortion pattern or a purely radial stagnation pressure distribution can be considered. The choice of which inflow condition is advantageous for the design depends on the integration scenario. With a fan design that meets the specification, it is possible to move on to the second part of the fan design and assessment.

Flow redistribution within the intake

The second part of the methodology aims to calculate the flow redistribution within the intake. In general, it is necessary to include a number of different local operating conditions around the circumference sufficient to reconstruct the static pressure field at the AIP. Within the example in fig. 3.4 (c) two local operating points are sufficient. One is in the centre of the distortion and the other is outside the boundary layer. Each individual circumferential position has an individual mass flow and an individual stagnation pressure distribution. The latter changes the fan characteristic as explained in section 2.1. Overall, the operating conditions of the entire fan stage are characterised by a prescribed static pressure at the fan stage outlet, which remains fixed during the calculation of the flow redistribution. The stream tube contraction is then iterated in each individual local operating condition to match the static pressure at the fan stage outlet. The enhancement of the SLC code with stream tube contraction captures the acceleration and deceleration effects associated with flow redistribution.

The flow field of the different passages is then evaluated to reconstruct the static pressure field at the AIP, which is used as the outlet boundary condition for the RANS-based intake calculation. The resulting flow field within the intake provides information about the flow field and flow redistribution. The flow field analysis is fed back into the loop. This includes an update of the mass flow in the specific passage and the evaluation of the swirl at the AIP. With regard to the conservation of the swirl within the SLC, the swirl is converted according to eq. (2.17) into a swirl angle distribution at the inlet, which is considered within the inlet boundary condition. The local flow fields are then calculated with the updated inflow conditions. Again, the stream tube contraction is iterated until the static pressure at the outlet of the fan stage is reached.

The procedure is repeated until the intake flow converges. Convergence is achieved when the mass flow variation (RANS calculation) of two consecutive loops is less than 0.5%. This is typically achieved after two to five loops, while one loop takes approximately 15 minutes on a conventional workstation.

Local fan operating points

The third part of the methodology then begins, which involves calculating the local operating point around the circumference. Similar to the second part, it is necessary to define a number of passages that are important for the calculation of the fan performance at the circumference. The analysis of the intake flow field gives the passages specific inlet boundary conditions in terms of radial stagnation pressure, swirl angle distribution (calculated as explained above) and mass flow. The fan assessment is based on the converged flow redistribution calculation and therefore the coupling of both methods is achieved at AIP. In this step, the stream tube contraction is iterated until the meridional velocity at AIP matches between the two approaches. Consequently, the fan back pressure is a result of the local operating point calculations and may vary. However, as the flow kinematics are the main driver within the fan performance prediction, these changes are expected to be small. The resulting circumferential flow fields allow the performance of any circumferential position to be assessed and therefore the assessment of a fan stage at distorted inlet.

The third step of the fan stage assessment takes approximately five to ten minutes, depending on the number of local operating points. All in all, the entire fan stage assessment requires approximately 35 to 85 minutes without the need for high performance computers.

In the following subsections, the newly developed design and assessment methodology for BLI fans is applied to an embedded turbofan engine and the results are verified by performance data derived from time-resolved calculations.

3.3.2. Specification and design

This subsection is dedicated to the verification of the first part of the new methodology and deals with the specification and design as presented in fig. 3.4. First of all, the integration scenario is selected. This is followed by the specification of the design point and then the fan design is introduced.

The integration scenario envisions a turbofan engine embedded in the rear fuselage of a short-to-medium range aircraft. A typical fuselage length of 36m for such an aircraft is considered. The aircraft boundary layer is assumed to behave as a fully turbulent flat plate. The equations are given in appendix A.3. Figure 3.5 shows the resulting stagnation pressure distortion, which has a stagnation pressure deficit of 12% compared to the freestream stagnation pressure. Due to the large fan diameter, the entire stagnation pressure profile is scaled to cover the upper 50% of the blade from midspan to tip. The distortion intensity of a 60° segment ($DI_{60°}$) is 0.0301.

Table 3.2.: Global fan design parameters.

Ma [-]	$\Pi_{t,ADP}$ [-]	$u_{tip,corrected}$ [m/s]
0.65	1.30	299.5

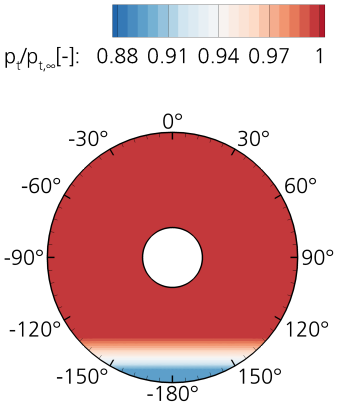

Figure 3.5.: Non-dimensional stagnation pressure distribution. The distribution is based on the assumption that the fuselage body behaves like a fully turbulent flat plate.

A typical design point for fan stages that power short-to-medium range aircraft is summarized in table 3.2. The global design point is defined by a fan pressure ratio of 1.3 at a fan-face meridional Mach number of 0.65 and an ISA corrected blade tip speed of 299.5 m/s.

This baseline fan is derived from the design study of Lengyel-Kampmann (2016) and the aerodynamic design of the fan stage is at a high level of maturity. The SLC representation of the fan stage aims to match the key design features of that fan stage. In the thesis of Schnös (2020), compressor designs obtained by *ACDC* are comprehensively verified by RANS simulations. In this subsection, *ACDC* is applied to fan stages and a dedicated verification is performed. Similar comparisons are already presented in Mennicken et al. (2019) Within this study, the focus is on the fan bypass flow and the corresponding flow path is shown in fig. 3.6.

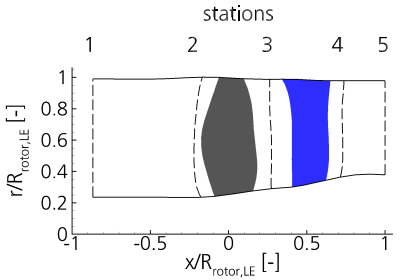

Figure 3.6.: Fan stage flow path stemming from the study of Lengyel-Kampmann (2016).

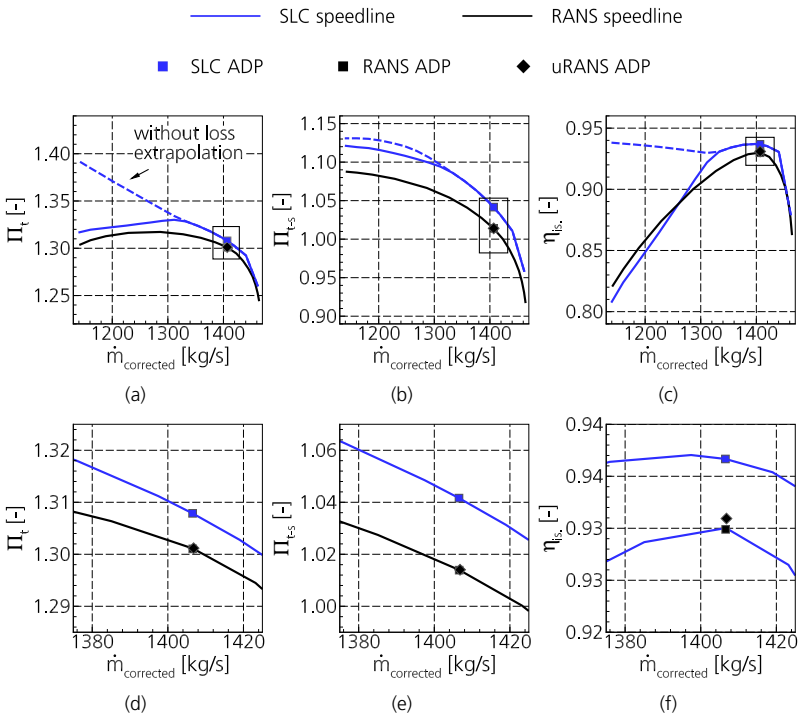

Figure 3.7.: Fan map of the fan stage stemming from SLC and RANS.

Figure 3.7 shows the fan map of the fan stage in terms of fan pressure ratio, stagnation-to-static pressure ratio and isentropic efficiency derived from SLC and RANS. The top row of the figure shows the full range of the fan map, while the bottom row shows a zoom into the region of the ADP. In terms of FPR, the agreement between SLC and RANS is good. The FPR characteristic shows a similar slope over the whole working range, while the FPR level is slightly higher for SLC than for RANS. As mentioned above, the working range of the fan stage in SLC is limited either when the peak of the stagnation-to-static pressure ratio is reached or when no convergence of the flow field can be achieved (i.e. low meridional Mach numbers). Figure 3.7 (b) shows a slightly increasing characteristic (solid blue line). In terms of the stagnation-to-static characteristic, the stability limit of the fan is not reached. The operating range of the fan stage is limited due to the low Mach number levels occurring downstream of the vane hub. In line with the FPR trend, SLC predicts a slightly higher static pressure rise than can be verified with RANS. This is associated with higher fan efficiencies as shown in fig. 3.7 (c) and (f). In addition, the agreement between the RANS and uRANS-based operating point is very good and changes are only visible in the isentropic efficiency shown in fig. 3.7 (f).

In section 3.1.1 the extrapolation of the airfoil working range is discussed. The solid blue

Table 3.3.: Operating point at ADP.

	$\dot{m}$ [kg/s]	$\dot{m}_{corrected}$ [kg/s]	Π_t [-]	$\eta_{is.}$ [-]
RANS	527.2	1406.6	1.3010	0.9299
SLC	527.1	1406.5	1.3079	0.9367

line is from a calculation where both the incidence and the losses are extrapolated beyond the stored airfoil working range. If the incidence working range is extrapolated but the losses of the individual blade sections are kept constant at the value of the last stable operating point, the fan off-design performance of the fan stage changes. The dashed blue line in fig. 3.7 shows the fan off-design performance with this working range extension. There are no changes within the working range. In other words, above 1320 kg/s ISA corrected mass flow, the characteristics are identical. Below this ISA corrected mass flow, the fan performance differs. In addition, the fan efficiency actually increases slightly under these conditions. The fan pressure ratio characteristic is much steeper than the one with additional losses. This results in a higher static pressure rise of the fan stage at off-design (see fig. 3.7 (b)). Table 3.3 summarises the fan performance metrics of both approaches at ADP.

A deeper insight into the flow field is taken to compare the fan performance resulting from both approaches. Figure 3.8 shows the flow kinematics through the fan stage at the rotor inlet (station 2), between the rotor and stator (station 3) and at the stator outlet

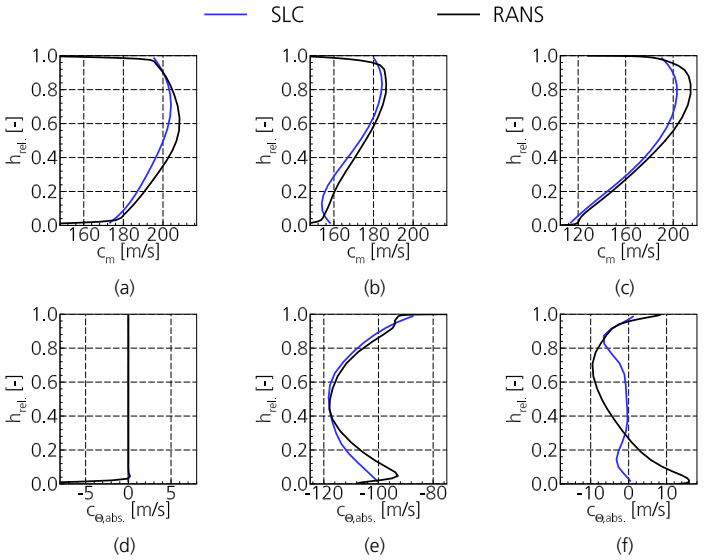

Figure 3.8.: Radial distribution of flow kinematics at station 2 (a) & (d), station 3 (b) & (e) and station 4 (c) & (f).

(station 4). In general, the hub and tip boundary layers are not included in the streamline curvature. Consequently, the radial distributions of the flow kinematics are different. In addition, the hub and tip boundary layers cause the flow to be redistributed towards the midspan. This is one reason for the differences in meridional velocity at the rotor inlet (station 2) fig. 3.8 (a). In addition, the fan rotor has a leading edge sweep, which also leads to flow acceleration at the midspan. Nevertheless, the meridional velocity matching at the rotor inlet is good, with less than 3% variation at midspan. At ADP, the rotor receives an axial inflow and the circumferential velocity is zero at station 2 in fig. 3.8 (d). Only a small part of the hub flow (below 5% span) has to deal with a small amount of swirl at the rotor inlet. Between the rotor and the stator (station 3) the meridional velocity distributions match very well. According to Euler's work equation, the work input is associated with the circumferential velocity in the absolute reference frame at the rotor outlet. Figure 3.8 (e) shows this velocity component along the span. For the SLC, the velocity component is slightly higher in the hub region. There the isentropic efficiency is lower in SLC than in RANS, requiring more work to achieve the specified fan pressure ratio.

At the fan exit (station 4) the meridional velocity matching is well achieved. Both spanwise velocity distributions show a large velocity gradient from hub to tip. Above midspan the meridional velocities are slightly lower than in RANS. The reason for this is twofold. Firstly, the aforementioned flow features near the end walls, which are not covered by SLC, lead to a contraction of the flow beyond the end walls in RANS. Secondly, the fan stage representation shows a slightly higher static pressure rise, resulting in lower meridional velocities. In addition, the swirl remains at the outlet of the fan stage. Figure 3.8 (f) shows swirl velocities between -10 and 15 m/s within the RANS-based assessment, while the SLC-based stator assessment shows less swirl.

Figure 3.9 shows the spanwise fan performance. The rotor has a radially increasing fan pressure ratio (see 3.9 (a)). Figure 3.9 (b) shows the blade loading in terms of 1-DH and the diffusion factor. Over the full span, the blade loading and flow deceleration are in a reasonable range, resulting in DF < 0.55 and 1-DH < 0.3. Near the hub, the rotor design features are unconventional compared to state-of-the-art engines that deliver compressed air to the compressor. Typically, higher fan pressure ratios are targeted (around 1.20 or even higher). As the work input near the hub is challenging due to low circumferential

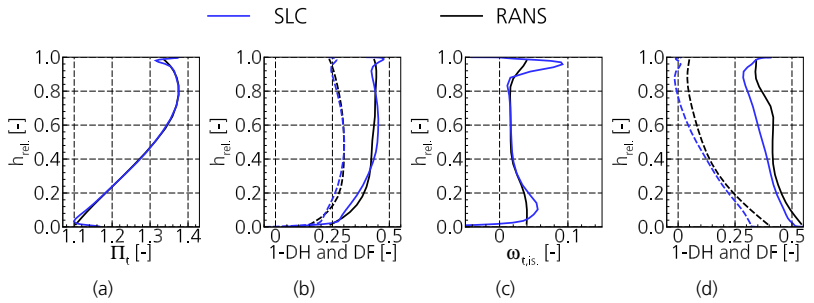

Figure 3.9.: Radial distribution of rotor pressure ratio (a), rotor blade loading (b), vane losses (c) and vane loading (d).

blade velocities, it is necessary to increase the flow turning. Conventional fan rotor hub sections achieve the high fan pressure ratio at the expense of reduced flow deceleration or even local flow acceleration. In contrast, this fan provides significant flow deceleration over the entire span, which is unusual for rotor hub sections. The stator performance is assessed by the stagnation pressure loss coefficient in 3.9 (c) and the vane loading in 3.9 (d). The loss prediction in the SLC agrees well with the higher fidelity results at midspan. Near the end walls the loss generation is underestimated in SLC. In ADP, the blade hub section significantly slows down the flow while the blade loading is reasonable in terms of the diffusion factor. Thus, the maximum DF is below 0.55 and the maximum 1-DH is 0.4 near the hub, reflecting the design philosophy reported by Schönweitz et al. (2017). As mentioned above, the flow path downstream of the rotor is simplified. Therefore, the low stagnation pressure fluid and the high stagnation pressure fluid are coupled at the fan stage outlet. On the one hand, this leads to the challenge of decelerating the hub flow to achieve a high static pressure. On the other hand, the flow between the midspan and the tip is only slightly decelerated, resulting in the velocity gradient observed in fig. 3.8. In addition to the information presented in the previous figures, the low velocities near the vane hub limit the operating range at low mass flows.

In this subsection, the integration scenario (embedded turbofan engines), the global design parameters, as well as the baseline fan are chosen. So, all results of the first step within the design methodology, which is visualized in fig. 3.4 (c), are achieved and the fan stage assessment in distorted inflow can be conducted.

3.3.3. Flow redistribution within the intake

This subsection deals with the calculation of the flow redistribution upstream of the fan stage. According to fig. 3.4 (c), this task includes the selection of local operating points and the corresponding stream tube contraction in the specific passages, as well as the reconstruction of the static pressure field at the AIP. The latter serves as the outlet boundary condition of the RANS-based flow redistribution calculation.

Firstly, the choice of local fan operating points is introduced. Figure 3.10 (a) shows a generic circumferential stagnation pressure distribution at a specific radius. As introduced in chapter 2, the flow redistribution upstream of the fan stage is related to the stagnation pressure pattern. The static pressure is expected to be at its minimum where the minimum stagnation pressure is located. In addition, it is helpful to place local operating points in positions where the swirl distortion is expected to be low. Therefore, the position in the middle of the distortion at $\pm 180°$ is considered in the flow redistribution calculation. The stagnation pressure distribution is characterised by a constant stagnation pressure over a large part of the circumference. The opposite position to the distortion is expected to have no pre-swirl, so the 0° position is also included as an operating point to predict the flow redistribution.

If the stagnation pressure distribution also has a maximum, this position must be considered because of the expected static pressure peak (see Reutter et al. (2020)). In case of a more complex stagnation pressure distribution, all maxima and minima have to be considered. This is addressed in chapter 5.

Secondly, the stream tube contraction must be determined within the different pas-

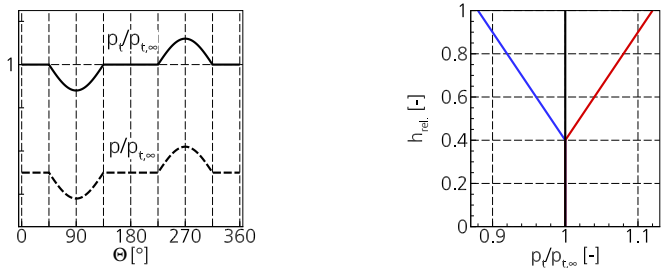

Figure 3.10.: Circumferential distribution of dimensionless stagnation and static pressure in (a) and radial stagnation pressure distribution within the stagnation pressure sink (blue) the stagnation pressure maximum (red) and in regions of constant stagnation pressure (black) in (b).

sages. According to eq. (3.1), the stream tube contraction stc_j accounts for the difference between the reference stagnation pressure and the individual stagnation pressure at a given spanwise position j. As already introduced in section 2.3.2 eq. (2.18), streamline curvature codes account for the conservation of mass. Usually the blockage parameter b, that is considered there, is used to account for smaller cross-section areas in blade rows as blades and vanes partly cover the volume of the flow path. Consequently, the blockage parameter is equal to zero in bladeless sections. Here the stc array is used to modify the blockage parameter locally even in bladeless parts of the flow path. This artificial modification of the cross-section area is a simple way to introduce the effects of flow redistribution.

$$\vec{stc} = \begin{pmatrix} stc_1 \\ \vdots \\ stc_L \end{pmatrix} = \frac{1}{\max\limits_j |stc_j|} \begin{pmatrix} p_{t,ref,1} - p_{t,i,1} \\ \vdots \\ p_{t,ref,L} - p_{t,i,L} \end{pmatrix}. \tag{3.1}$$

Furthermore, a radial resolution for the array needs to be chosen with respect to the specific distortion pattern. Throughout this study it is sufficient to resolve the radial height by scan points at 0.2, 0.4, 0.5, 0.6 and 0.8 relative span. Between 0.2 and 0.8 relative span the stream tube contraction values are interpolated, while below 0.2 and above 0.8 relative span the contraction is kept constant.

So far, the relative contraction of the stream tubes is defined at the AIP. In section 2.2.1 the behaviour of the flow redistribution in the axial direction is addressed. Upstream of the fan the static pressure distortion decays. Downstream the static pressure distortion is attenuated by the fan stage (see fig. 2.4 (b)). Therefore, the radial distribution must be converted to a two-dimensional distribution in the axial-radial plane. Figure 3.11 (a) shows the stc distribution at the centre of the distortion at $\pm 180°$. In accordance with the behaviour of the static pressure distortion described above, the stc distribution increases in the flow direction upstream of the fan stage and reaches its maximum at the leading edge of the rotor. Since the intake flow field is calculated using a steady-state RANS approach, modelling the stc distribution upstream of the AIP is of little interest in SLC. However, the stc effect downstream of the AIP is important for the SLC-based performance assessment. In accordance with the findings of Stenning (1980), a linear decay of the stc values is im-

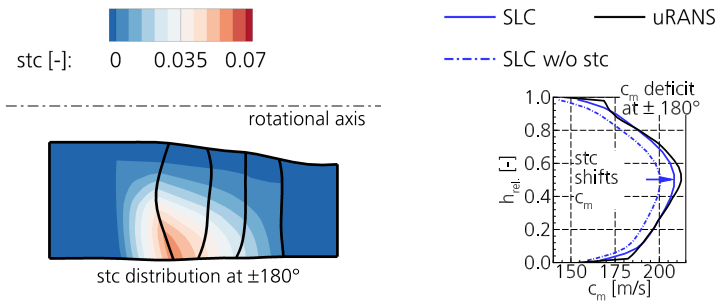

Figure 3.11.: Stream tube contraction within axial-radial plane (a) and impact on meridional velocity at AIP (b).

plemented between the rotor leading edge and the stator trailing edge (see fig. 2.4). As the static pressure distortion vanishes downstream of the stator, $\vec{stc}$ is equal to $\vec{0}$ at the stator trailing edge.

The stc array has a direct impact on the meridional velocity distribution because the stc array locally affects the cross-sectional area. Figure 3.11(b) shows the meridional velocity distribution of the ±180° position. Above 50% span, the boundary layer leads to a reduced meridional velocity. The dashed-dotted line shows the meridional velocity along the span when stream tube contraction is not considered. The consideration of the stream tube contraction leads to an increase of the meridional velocity and the spanwise distributions of the time-resolved calculation and the SLC become narrower.

After determining the local stream tube contraction arrays, the local operating point is calculated with respect to a common static back pressure in both passages at 0° and ±180°, which couples both flow fields. At AIP, the static pressure field is derived from the static pressure distributions of the flow fields obtained by SLC. Due to the axisymmetric stagnation pressure distribution shown in fig. 3.10, an axisymmetric static pressure field is assumed for the reconstruction of the static pressure field at AIP. As discussed in chapter 2, the static pressure starts to decrease at the circumferential position where the stagnation pressure decreases. In the case of the stagnation pressure pattern in fig. 3.5, these conditions are found at ±128°. Therefore, the static pressure of the 0° calculation is assumed to be constant between -128° and 128°. Between -128° and 180°, and 128° and 180°, the static pressure field is expected to have a smooth distribution without discontinuities [1] and a minimum static pressure at ±180°.

The approximation of the static pressure field is achieved by a continuously differentiable function combining second and third order polynomials. The circumferential pressure

$$p(\Theta) = \begin{cases} a\Theta^3 + b\Theta^2 + c\Theta + d, & \text{if } \Theta_{mean} <= \Theta <= \Theta_{mid} \\ e\Theta^2 + f\Theta + g, & \text{if } \Theta_{mid} < \Theta <= \Theta_{extrema} \end{cases} \tag{3.2}$$

[1] Discontinuities occur at shocks or can occur when shear layers are present, i.e. downstream of a shock-boundary layer interaction.

Table 3.4.: Restrictions for static pressure field reconstruction.

outer part third order	coupling coupling	inner part second order
$p(\Theta_{mean}) = p_{mean}$	$p_{mid,2^{nd}} = p_{mid,3^{rd}}$	$p(\Theta_{extrema}) = p_{extrema}$
$p'(\Theta_{mean}) = 0$	$p'_{mid,2^{nd}} = p'_{mid,3^{rd}}$	$p'(\Theta_{extrema}) = 0$
$p''(\Theta_{mean}) = 0$		

is approximated by a third order polynomial in the outer part and a second order polynomial in the middle of the static pressure pattern. Both polynomials are coupled and the coefficients a to g are calculated individually for each spanwise position. Table 3.4 shows the constraints of the static pressure reconstruction. The second order polynomial approximates the inner part of the static pressure field around an extremum (in this case a minimum). So at $\Theta_{extrema}$=±180° the static pressure is known and the derivative of the static pressure field is zero. At the edge of the stagnation pressure distortion (±128°) the static pressure is assumed to be equal to the static pressure of the 0° position. In addition, the static pressure distribution is required to have a smooth transition to constant static pressure. This leads to the requirement that the first and second derivatives of the third order polynomial are equal to zero at the edge of the distortion pattern. Finally, the two polynomials are coupled. In this study, the spatial position of the coupling is halfway between the edge and the middle of the distortion. At this position the static pressure of the second and third order polynomials are equal. In addition, the derivatives of both functions are equal to ensure a smooth transition from one part of the static pressure field to the other. Having defined the simplified description of the static pressure field, it can be calculated at AIP.

Figure 3.12 shows the dimensionless static pressure distribution obtained from the preliminary design methodology (a) and from the time-resolved RANS calculations (b). As explained above, the static pressure distribution is updated during the different loops un-

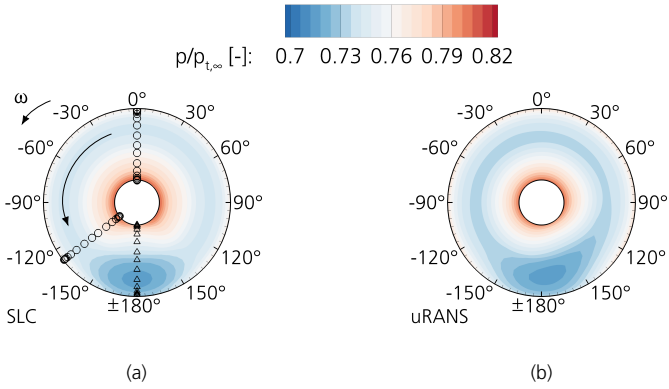

Figure 3.12.: Non-dimensional static pressure distribution at AIP (station 2).

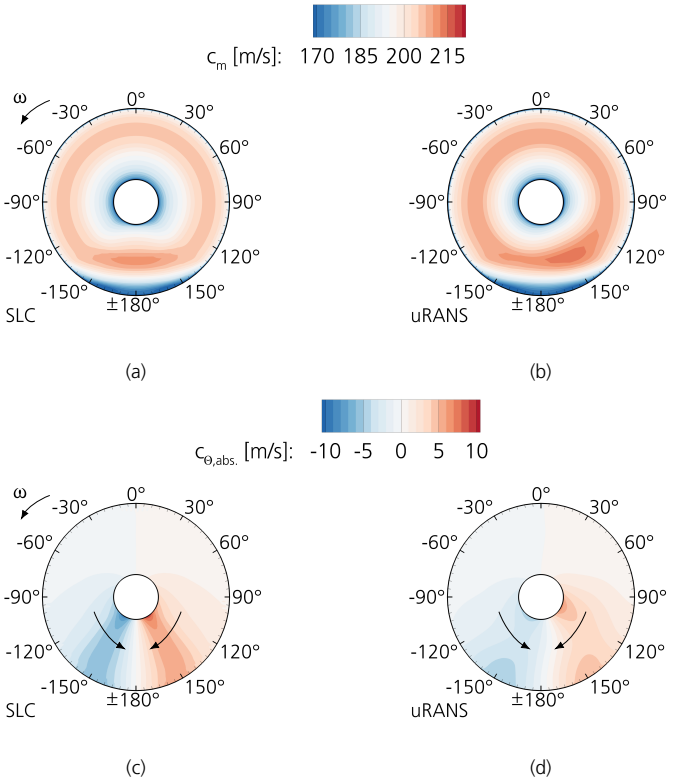

Figure 3.13.: Meridional and circumferential velocity distribution stemming from SLC (a) and (c) and uRANS (b) and (d) at AIP (station 2).

til convergence of the intake flow field is achieved. Contrary to the axisymmetric pressure field in fig. 3.12 (a), the static pressure field of the time-resolved calculation is non-axisymmetric as shown in fig. 3.12. The underlying flow feature that causes lower static pressure levels in the counter-swirl region between 120° and 180° is the amplified tip gap flow, which leads to flow acceleration in the midspan section of the blade. Apart from this difference, the general static pressure pattern as well as the (non-dimensional) static pressure level is similar between fig. 3.12 (a) and (b). Between -128° and 128° the static pressure field is constant around the circumference and shows the same spanwise variation with high static pressures near the hub and lower static pressures at midspan. As discussed in the previous section, the RANS-based assessment of the fan stage shows higher meridional velocities than in SLC. Therefore the static pressure is lower in the midspan region in fig. 3.12 (b). By definition, the minimum static pressure is in the middle of the distortion within the preliminary assessment (cf. fig. 3.12 (a)). The time-resolved result also shows the minimum static pressure near ±180°. Since the static pressure field is derived from individual SLC flow fields, only an indirect coupling of the static pressure is achieved at AIP.

In particular, the static pressure near the hub is slightly lower in SLC than it would be in a fully coupled flow field visualised in (cf. fig. 3.12 (b). Nevertheless, the general matching of the static pressure fields is very good and, at the same time, the numerical effort to obtain this flow field is significantly lower. The static pressure distribution directly translates into the flow kinematics at AIP. Figure 3.13 shows the meridional and circumferential velocity distributions at AIP. The results of the preliminary fan assessment are shown on the left and the detailed design assessment is shown on the right. Consistent with the static pressure field, the uRANS-based meridional velocity distribution shows slightly higher velocity levels outside of the distortion at midspan. In addition, the meridional velocity distribution is non-axisymmetric whereas the preliminary assessment velocity distribution is axisymmetric. However, the main variation in meridional velocity is due to BLI. The meridional velocity decreases within the boundary layer due to the low stagnation pressure. This variation is well captured by the preliminary fan assessment. In addition, swirl is another important BLI flow characteristic resulting from flow redistribution. The symmetric static pressure field directly translates into symmetric velocity fields in the SLC. Contrary to this symmetry, the velocity fields obtained by time-resolved calculations are slightly non-axisymmetric. The preliminary evaluation gives slightly higher swirl velocity levels than the result from the time-resolved calculation (see fig. 3.13 (c) and (d)). However, the circumferential velocity levels are well captured in fig. 3.13 (c) and (d). In addition, the circumferential velocity levels obtained by SLC are slightly higher near the hub. This is consistent with the slightly lower static pressure levels there and results from the indirect coupling of the static pressure field at AIP.

In summary, this subsection presents the selection of the necessary locations around the circumference to calculate the flow redistribution, the definition and effect of the stream tube contraction, and the consistency of the intake flow fields. These results are used in the third stage of the fan assessment.

3.3.4. Local fan operating points

This subsection deals with fan performance at distorted inflow conditions, corresponding to the third stage of the design methodology. Firstly, the focus is on the global fan performance. Secondly, a more detailed assessment of local operating points and flow conditions around the circumference is presented.

Fan stage performance

Figure 3.14 (a) shows the fan pressure ratio of the entire fan stage projected onto the inlet plane. On the one hand, the fan design intent of an increasing fan pressure ratio in the spanwise direction is visible around the entire circumference. On the other hand, the fan pressure ratio increases within the distorted sector compared to undistorted inflow conditions. Figures 3.14(b) and (c) show fan maps in terms of fan pressure ratio and isentropic fan efficiency over ISA corrected mass flow. Both maps include the steady-state characteristics (solid lines) as well as the connecting line of local operating points (orbit) obtained by uRANS. The uRANS performance data is used to verify the results from the preliminary fan assessment. The SLC orbit is obtained by an operating point at 0°, which represents homogeneous inflow conditions. In addition, a local operating point is calculated every 10° between $\pm 120°$ and $\pm 180°$ to cover the distorted sector. A compressors-in-parallel (CIP) approach is also considered. The steady-state operating points are visualised by squares

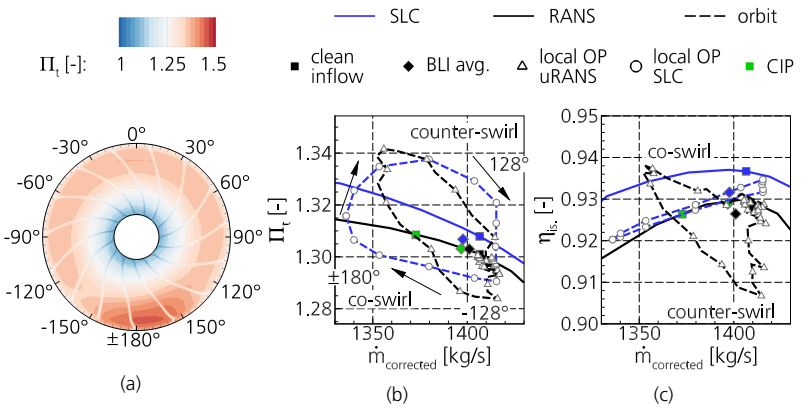

Figure 3.14.: Fan map including speed lines at undistorted inflow, the aerodynamic design point, the local operating points (orbits) around the circumference as well as the averaged BLI operating point in terms of fan pressure ratio (a) and isentropic efficiency (b).

while diamonds represent averaged BLI operating points.

The CIP operating point is obtained by area averaging the stagnation pressure within the distorted area. With respect to a common static pressure at the fan stage outlet, the total-to-static characteristic gives the ISA corrected mass flow with distorted inflow. The fan pressure ratio and isentropic efficiency are then obtained. The averaged operating point is calculated by averaging the distorted and undistorted operating points.

Figure 3.14 (b) shows that the local operating points outside the distortion (at 0°) have a slightly higher corrected mass flow than the aerodynamic design point. This variation is not captured by the CIP approach as ADP conditions are used for the operating conditions outside the distortion. As the fan rotates around the circumference, it enters the distorted sector at -128°. Both methods take into account the decreasing corrected mass flow as well as the decreasing fan pressure ratios at co-swirl conditions. Figure 3.14 (b) shows that the fan pressure ratio is underestimated in SLC compared to uRANS. In the middle of the distortion (at ±180°) the minimum corrected mass flow is reached. As introduced in section 3.2, the local operating points of the time-resolved calculations are obtained by averaging over a sector. In contrast, the SLC approach considers the operating conditions at a specific circumferential position with an infinitesimal circumferential extent. Therefore, the minimum corrected mass flow is slightly lower for SLC. In CIP, the operating point of the low momentum stream tube has a significantly higher corrected mass flow due to the fact that the entire distorted sector is averaged. Therefore, the CIP based operating point does not give a good indication of the operating conditions in the distorted sector and the preliminary design methodology is superior.

The SLC and uRANS orbits show their maximum fan pressure ratios near the middle of the distortion in the counter-swirl region. As the fan rotates through the counter-swirl

Table 3.5.: Operating points in case of BLI.

	$\dot{m}$ [kg/s]	$\dot{m}_{corrected}$ [kg/s]	Π_t [-]	$\eta_{is.}$ [-]
uRANS	521.8	1401.0	1.3030	0.9274
SLC	520.7	1398.0	1.3068	0.9316
CIP	521.0	1396.8	1.3032	0.9289

region of the distortion, the fan pressure ratio decreases until undistorted inflow conditions are reached. Both methods capture this effect, but SLC slightly overpredicts the fan pressure ratios at high mass flows between 128° and 0°.

The averaged operating points from the orbit calculations are given by the diamonds in fig. 3.14 (b) and are listed in table 3.5. The decrease in corrected mass flow is slightly overpredicted by SLC and even the CIP based operating point shows a good agreement with the uRANS-based data. The fan pressure ratio of the CIP and uRANS-based operating points is slightly higher than that of the steady state operating point. As the fan pressure ratios within the co-swirl area are lower in SLC and the fan pressure ratio peak is slightly lower than in uRANS, the resulting averaged operating point is also slightly lower than the steady-state reference operating point.

Figure 3.14 (c) shows the isentropic efficiency variation around the circumference. Outside the boundary layer, the fan efficiency is similar to the ADP efficiency for both approaches. As the fan enters the distortion, the uRANS-based fan efficiency increases slightly and reaches its maximum near the middle of the distortion. Within the counter-swirl region, the fan efficiency decreases and is about 2% lower than for ADP. The averaged fan efficiency is 0.26% lower than the reference efficiency. This decrease is relatively small compared to the efficiency degradation reported in the literature (see chapter 2). The efficiency orbit obtained by the SLC shows a different behaviour. The orbit is narrow in terms of efficiency variations. In addition, the counter-swirl part of the orbit is slightly above the co-swirl part. This results in an under-prediction of the fan efficiency in the co-swirl and an overprediction of the fan efficiency in the counter-swirl. The trend of the fan efficiency orbit is therefore not captured by the preliminary assessment. The resulting efficiency degradation is 0.5%, which is slightly higher than the uRANS-based efficiency degradation. As the trend of the isentropic efficiency orbit is not captured by the SLC methodology, the matching of the averaged degradation of isentropic efficiency is arbitrary. A detailed analysis of this specific issue is given later in this thesis. Coincidentally, both values are in the same order of magnitude and this quantity must be treated with caution.

As mentioned above, the fan orbit is obtained by calculating an operating point every 10° within the distorted sector, complemented by an operating point at the 0° position. To verify the chosen orbit resolution, fig. 3.15 contains three different local operating point spacings, visualised by the orange orbits. The orbit in fig. 3.15 (a) uses local operating points every 10° around the circumference. Therefore the orbit is similar over a large part of the circumference. The additional operating points outside the distortion, between -120° and +120°, are visible by the accumulation of operating points near ADP. The effect

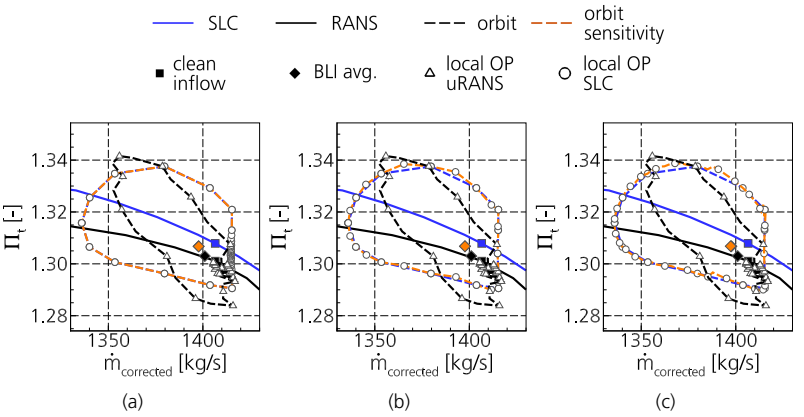

Figure 3.15.: Orbit sensitivity with respect to local operating point resolution. Operating points every 10° (a) over the circumference, every 5° (b) or 1°(c) respectively within the boundary layer.

of these additional operating points on the averaged operating point is negligible. It is therefore sufficient to consider a homogeneous inflow with only one operating point at 0°. Figures fig. 3.15 (b) and (c) show refined orbit resolutions within the boundary layer of 5° and 1° respectively. For the most part, the orbits are similar to the baseline orbit resolution. Small variations are visible within the counter-swirl part. As the local operating point variations are small, the averaged operating points show only small variations. Therefore, the baseline orbit resolution is sufficient to capture the main BLI related changes in fan performance.

In this subsection the BLI related operating point variations within the fan map are presented. The fan pressure ratio orbit as well as the averaged operating points are well predicted by the SLC compared to the results of the time-resolved calculations. In contrast, the local fan efficiency prediction shows differences compared to the verification data set. Therefore, a more detailed analysis of the local flow conditions, work input and loss generation is addressed in the following subsection.

Rotor flow

This subsection deals with the detailed assessment of the fan performance around the circumference. The flow redistribution calculation provides the flow kinematics at the AIP and are already presented in fig. 3.13. These conditions translate directly into the relative Mach number and incidence patterns shown in 3.16. The Mach number levels and Mach number variation are well captured by the preliminary design methodology in fig. 3.16 (a) compared to the high fidelity result in fig. 3.16 (b). The same is true for the incidence variation shown in fig. 3.16 (c) and (d). Within the boundary layer the decrease in axial velocity causes the main variations in both quantities. The relative Mach number values decreases due to lower axial velocities within the distortion. However, the swirl velocities also affect these distributions in the tip region. In the co-swirl region, the swirl causes an

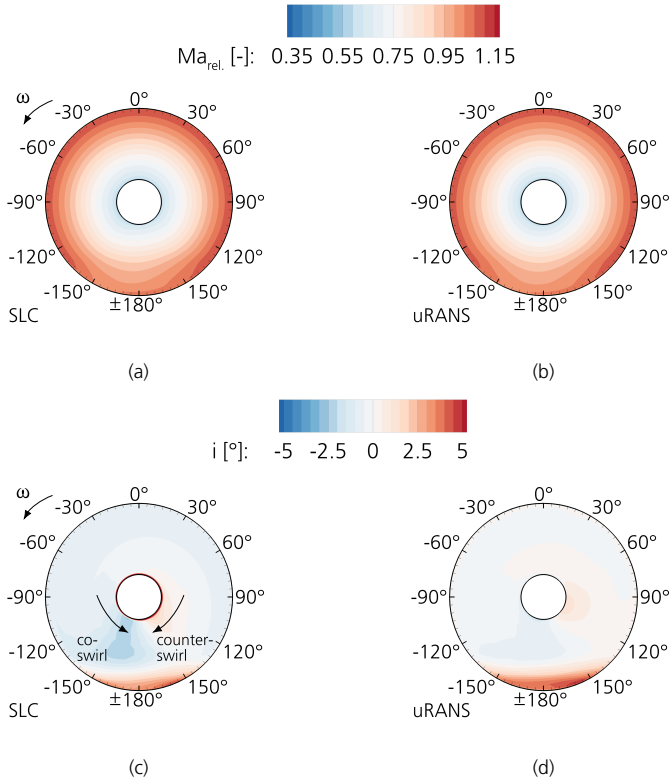

Figure 3.16.: Relative Mach number and incidence at AIP.

additional decrease in the relative Mach number levels and the positive incidence is slightly lower. In contrast, both quantities are slightly higher in the counter-swirl region.

From hub to midspan, the circumferential variations in relative Mach number are negligible. In contrast, the blade incidence varies in the co- and counter-swirl regions. While the co-swirl leads to negative incidence at -160°, the counter-swirl region has positive incidence. Furthermore, fig. 3.16 (c) shows slightly higher negative incidences at -160° than the uRANS-based results in fig. 3.16 (d).

Based on the observations of varying inflow conditions, specific local operating conditions are now considered for further investigation. At 0° the local fan performance is hardly affected by the fuselage boundary layer. In the co-swirl region, the maximum negative incidence is observed at -160°. In the middle of the distortion (±180°) the lowest meridional velocity levels are observed, mainly no swirl is expected. At 170° the positive incidence almost reaches its maximum and the maximum fan pressure ratio is obtained. The relative Mach number peaks at 140° and counter-swirl is still present in this position.

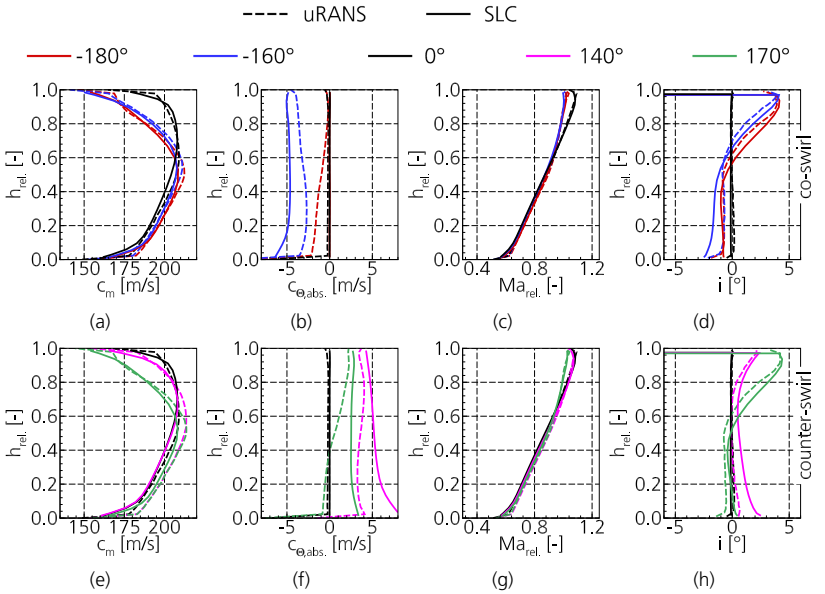

Figure 3.17.: Spanwise distributions at rotor inlet. Upper row: co-swirl. Lower row: counter-swirl.

Thus, amplified tip gap flow is expected.

The layout of the following figures showing the spanwise distributions is similar. The solid lines show the SLC results while the dashed lines show the uRANS-based results. The co-swirl operating point is at -160° shown by the blue line, the middle of the distortion (±180°) is shown by the red lines and the operating conditions outside the distortion (0°) are shown by the black lines. Counter-swirl operation is shown by the green lines (at 170°) and by the purple lines (at 140°).

Figure 3.17 shows the spanwise distributions of the meridional and circumferential velocities as well as the relative Mach number and incidence at the abovementioned circumferential positions. As already seen at AIP, the BLI related flow features are well captured by the preliminary design methodology and the variations between different local operating conditions are greater than the differences between uRANS and SLC-based results. Furthermore, the main trends between the circumferential positions are covered by the preliminary fan assessment compared to the uRANS-based results. Only in the counter-swirl region minor differences are visible. The time-resolved calculation shows a non-axisymmetric static pressure distribution and lower pressure levels are present in the counter-swirl region. Therefore, the uRANS-based meridional velocity c_m also differs there as shown in fig. 3.17 (e). Consequently, both the circumferential velocity and the blade incidence are affected. Near the hub, the uRANS-based meridional velocities are essentially the same when compared between 140° and 170°, while the SLC shows slightly lower

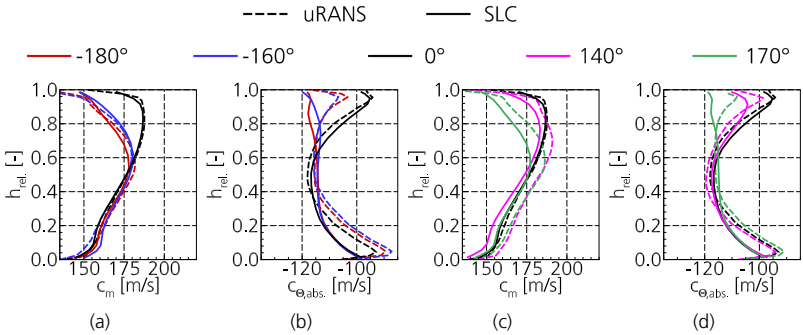

Figure 3.18.: Meridional velocity at rotor outlet within co-swirl (a) and counter-swirl (c) as well as circumferential velocity in the co- (b) and counter-swirl area (d).

velocities at 140°. Nevertheless, SLC captures the correct trend in the upper part of the blade where the boundary layer fluid is located.

Figure 3.18 shows the flow conditions downstream of the rotor. In terms of meridional velocity, the SLC-based preliminary assessment covers the main trends between the passages and a very good match is achieved within the co-swirl and the middle of the distortion. Especially above midspan the meridional velocity remains low in the -160° and ±180° position compared to the undistorted inflow (see fig. 3.18 (a)). In the counter-swirl region, the main BLI related variations are also captured by SLC. However, the meridional velocity remains lower in the counter-swirl, as already seen at the rotor inlet. In addition, the slightly lower velocities near the hub at 140° compared to the 170° position persist. In the counter-swirl positions the meridional velocities near the tip are higher in the time-resolved results than in the SLC. This is an indication that the tip gap modelling is not able to fully capture the complex flow within the tip gap region. The amplified flow through the tip gap leads to blockage in the upper part of the blade and to higher meridional velocities towards the midspan due to contraction.

According to Euler's equation 2.1, the circumferential velocity in the absolute frame of reference is directly related to the work input. Therefore fig. 3.18 (b) and (d) show this velocity component along the span at different circumferential positions. As explained in the previous section, the fan shows a more efficient hub section within the RANS-based assessment and therefore work input related variations in the circumferential velocity. This trend is maintained below 20% span and therefore SLC shows higher velocity levels. Between 20% and 70% span, both approaches show that the circumferential velocities within the distorted sector are slightly lower compared to the undistorted inflow (0°), except for the 140° position. Therefore, the work input is expected to be slightly lower for the distorted sector than for the undistorted flow, except for the 140° position. Above 70% the distorted sectors show higher circumferential velocities than the undistorted inflow condition at 0° in both approaches. Therefore, a higher work input is expected within the distortion. In addition, there are discrepancies above 70% of the span between SLC and uRANS. The lower circumferential velocities within the uRANS results are due to the deviation. Within the SLC assessment, the deviation model is not able to resolve all BLI related flow features.

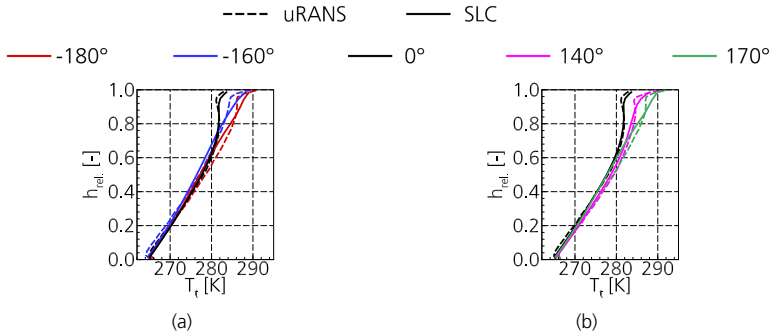

Figure 3.19.: Stagnation temperature variation at rotor outlet.

In general, the spanwise variations around the circumference calculated by SLC are verified by the uRANS results. As explained earlier, the varying inflow conditions around the circumference lead to variations in work input and therefore fig. 3.19 shows the spanwise stagnation temperature distribution at the rotor outlet. SLC showed lower circumferential velocities within the distorted sector at midspan, except for the counter-swirl position (140°). As expected, the stagnation temperature level is slightly lower at -160°, ±180° and 170° compared to 0°. In addition, the slightly higher level at 140° compared to 0° is expected: the tip section shows higher circumferential velocities throughout the distorted sector and consequently the stagnation temperature distribution shows higher levels than at 0°. In contrast, the uRANS results show a different behaviour at the midspan. The same trend as for SLC is expected, but the stagnation temperature levels of the BLI related flow are higher than at 0°.

In the tip section, the uRANS-based data shows deviation that limit the circumferential velocity level. This tip flow related flow feature is not captured within SLC and higher circumferential velocity levels are present. Consequently, the work input and stagnation temperature levels of the SLC data exceed the uRANS levels near the casing. The additional work input is therefore associated with unsteady effects. Due to the steady-state modelling, this trend is not considered in SLC. Contrary to the expectation that unsteady effects can be neglected, the unsteady work input addressed by Mazzawy (1977) is relevant in such conditions.

Previously the increased isentropic efficiency in the co-swirl section up to the middle of the distortion was discussed. As seen above, the increase is partly due to increased stagnation temperatures caused by unsteadiness. The other important quantity related to isentropic efficiency is entropy generation. Therefore, a detailed analysis of this quantity is presented. During this study the reference state for entropy calculation is set to T_{ref} = 250 K and p_{ref} = 35000 Pa. Figure 3.20 shows the instantaneous entropy distribution at different streamwise positions. At the rotor inlet in fig. 3.20 (a) high entropy levels can be observed within the distorted sector. The entropy is transported convectively through the fan stage. As the high entropy fluid enters the rotor, it is shifted in the direction of fan rotation. Figure 3.20 (b) shows the entropy distribution at rotor mid-chord. Within the blade boundary layers the entropy increases at each circumferential position. In addi-

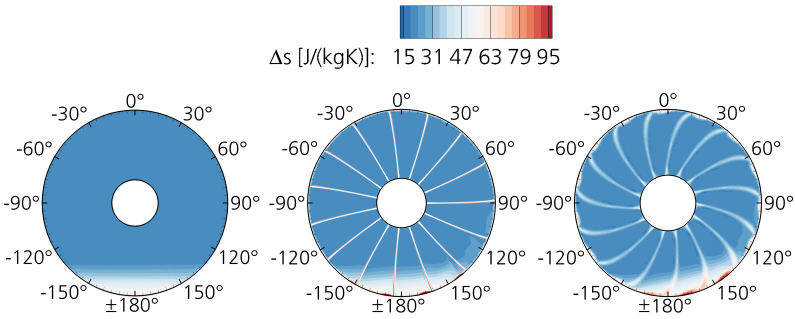

Figure 3.20.: Entropy at rotor inlet (a), mid-chord of the rotor (b) and downstream of the rotor (c).

tion, the flow related losses in the tip gap lead to an increase in entropy in the tip region around the entire circumference. As expected, the area of high entropy fluid is larger in the counter-swirl region and is associated with the amplified tip gap flow. Figure 3.20 (c) shows the entropy distribution downstream of the rotor. Here the rotor wakes can be seen by the increased entropy values in the spanwise direction. In addition, the tip gap fluid mixes with the fluid passing through the passage. Therefore the entropy distribution in the tip region is smeared. However, the counter-swirl region shows the highest entropy level, partly due to convection of the high entropy fluid and partly due to increased loss generation within the fan stage. Figure 3.21 shows the instantaneous time derivative of the entropy downstream of the rotor (a) and the associated standard deviation (b). The formula for both quantities is given in appendix A.5. In general, the time derivative of the entropy is closely related to the instantaneous loss generation within the flow. This is complemented by the evaluation of the standard deviation at fixed position. The time-average

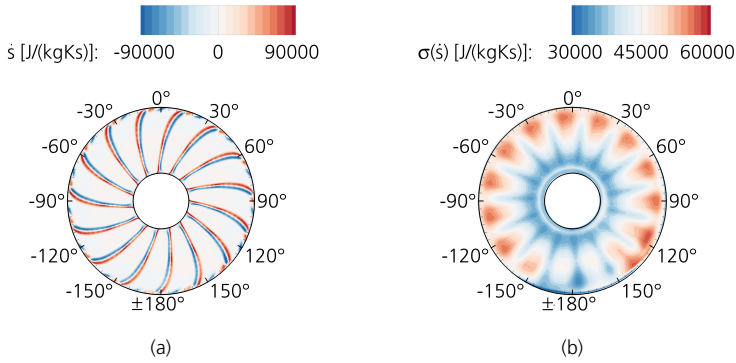

Figure 3.21.: Entropy rate and standard deviation at rotor outlet.

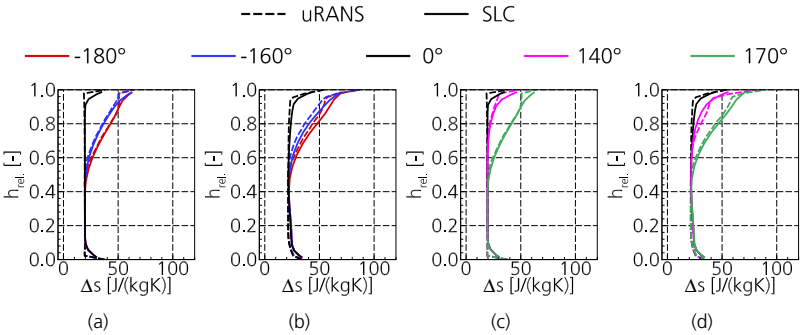

Figure 3.22.: Entropy increase (Δs) compared to reference conditions at rotor inlet (a) and (c) as well as at rotor outlet (b) and (d).

of the entropy derivative is zero. The level of the standard deviation is therefore related to the entropy generation at a specific position.

In fig. 3.21 (a) the rotor wakes are visible by the high values of the entropy rate. The wakes move counter-clockwise around the circumference. Positive values indicate that a wake was not present at a specific circumferential location in the previous time step and vice versa. Between -150° and $\pm$180° the entropy derivation is smaller over a large part of the span than in the undistorted inflow conditions. In addition, the tip gap fluid causes higher entropy derivatives in the counter-swirl region between 120° and 150°. Figure 3.21 (b) shows that the flow from the counter-swirl region up to the middle of the distortion undergoes a smaller entropy variation over a large part of the span than the fluid in the undistorted passages. In addition, entropy generation increases in the tip region of the counter-swirl fluid. Thus, based on the rotor flow field, the high efficiencies in the co-swirl region are associated with the higher stagnation temperature rise and lower loss generation. In contrast, the additional losses in the counter-swirl region outweigh the additional work input.

In line with the analysis of the uRANS data, the spanwise data from both approaches are analysed. Figure 3.22 shows the change in entropy between the rotor inlet and outlet. As can be seen, the entropy is higher within the boundary layer as expected (see 3.22 (a) and (c)). There the distributions are in good agreement between the low-fidelity and high-fidelity approaches. At the rotor outlet the entropy is increased due to losses within the rotor. SLC is able to predict the trends between the circumferential positions compared to the uRANS results. Nevertheless, the entropy increase is higher in SLC in all passages except the 140° position. It is worth mentioning that no further loss extrapolation is taken into account for the local operating point calculation. These results underline that a further increase of losses due to local loss extrapolation is not reasonable.

Rotor performance

Figure 3.23 (a) and (e) shows the rotor performance in the specific passages. The trends in the fan pressure ratio are well captured by the SLC-based approach. Within the boun-

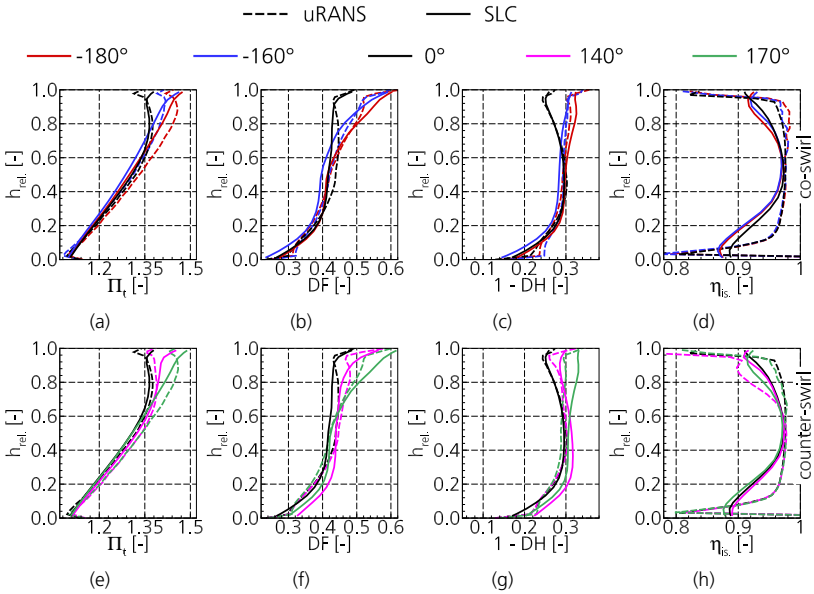

Figure 3.23.: Spanwise rotor performance in terms of fan pressure ratio, diffusion factor, DeHaller number and isentropic efficiency.

dary layer fluid, the fan pressure ratio increases and peaks at 170°. The slightly lower fan pressure ratios in the spanwise direction are reasonable as the stagnation temperature rise is slightly lower in the SLC and the loss generation is slightly overpredicted. Within the distorted sector the blade loading increases compared to the homogeneous inflow conditions. These trends are also well captured by the preliminary design methodology. The

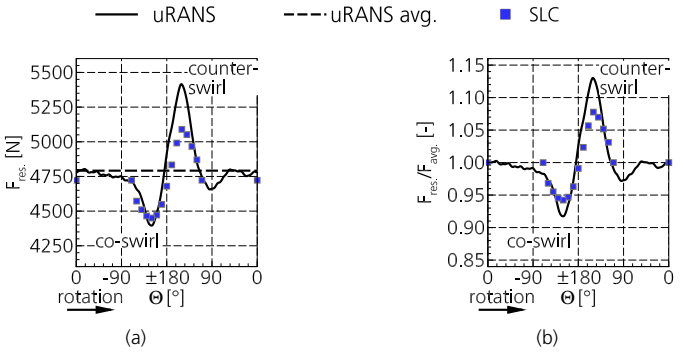

Figure 3.24.: Absolute rotor blade forces (a) and non-dimensional blade forces in (b).

aforementioned differences in the velocity distributions lead to differences in the blade loading metrics, which are mainly located in the tip region. The blade loading is overpredicted and the largest difference is seen at the 170° position. Another important metric is the rotor blade force variation around the circumference. Figure 3.24 shows the resulting and relative blade forces around the circumference. The black solid line shows the instantaneous blade force around the circumference, the black dashed line shows the time-averaged blade force and the blue squares show the blade forces resulting from the SLC approach. The blade forces are therefore calculated differently. While the blade forces of the time-resolved calculations take into account the pressure and friction forces acting on the blade surface, the SLC-based forces are obtained by solving the momentum balance within the rotor. Friction is therefore neglected. In appendix A.4 the equations for blade force calculation are given.

In general, the instantaneous blade force outside the distortion is close to the time-averaged value of the blade force. There the absolute value of the blade force obtained by SLC is slightly lower than the instantaneous value obtained by uRANS. As the rotor enters the co-swirl region, the blade force decreases and reaches its minimum approximately half way through the distortion. The blade force then increases and reaches its maximum in the middle of the counter-swirl region. The blade force then decreases and enters a largely constant distribution. As can be seen from the fan map and the radial distributions, the fan blade force variation is well predicted within the preliminary fan assessment. The maximum fan blade force in the counter-swirl region is approximately 5% lower than the instantaneous blade force variation. This trend is well captured by the approach and can be used in early design stages for a distortion tolerant fan design.

Stator flow and performance

Figure 3.25 shows the spanwise distribution of the flow field at the stator outlet. As can be seen in fig. 3.25 (b) and (e), the OGV reduce the swirl as intended. The remaining swirl is less with SLC than with the higher fidelity approach, which is consistent with the comparison of fan performance at ADP (see section 3.3.4). In addition, fig. 3.25 (a) and (d) show a good match of the meridional velocity between the two approaches at the stator outlet, except for the 170° position. There the meridional velocity is significantly lower. As already introduced in section 3.3.1 during the calculation of the local operating points, the velocity triangles are matched at AIP and the static pressure at the fan stage exit is a result of the fan performance assessment. Therefore, the spanwise static pressure varies around the circumference within the SLC while the uRANS distributions are essentially the same. Within the 170° position, the stagnation pressure at the fan stage outlet is lower due to the incoming momentum deficit at the rotor inlet. In addition, the static pressure is at its maximum there, resulting in the low meridional velocity. Thus, the three-dimensional flow and the coupled static pressure field within the time-resolved calculation leads to a more complex flow than the SLC approach can capture at this position. Figure 3.26 shows the stator loading at specific circumferential positions. The main trends of increasing diffusion factor or DeHaller number related loading coefficient are captured by the SLC-based results. As seen in the velocity distributions, the 170° passage shows the biggest difference between the two approaches. The stator hub section is also highly loaded at the ADP as introduced in section 3.3.4. In contrast to the uRANS-based results, the vane loading within this region increases further in the SLC. In particular, the flow fields in the blade hub regions are very complex and highly three-dimensional. These flow characteristics are

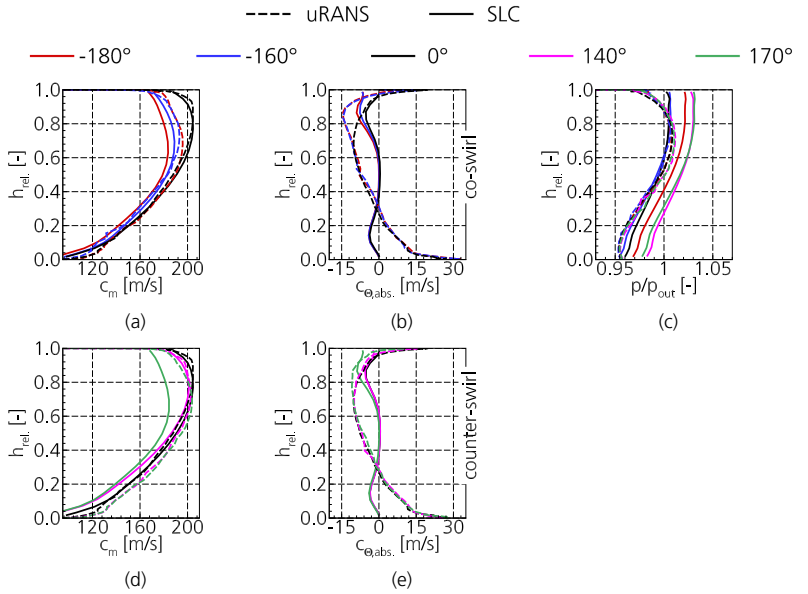

Figure 3.25.: Flow kinematics at stator outlet in terms of meridional velocity (a) and (d) and circumferential velocity (b) and (e). Spanwise static pressure distribution in (c).

not taken into account in SLC and therefore differences between the two approaches are to be expected.

The uRANS-based flow field is also evaluated in terms of distortion intensity downstream of the stator. The fan significantly attenuates the distortion and the distortion intensity of

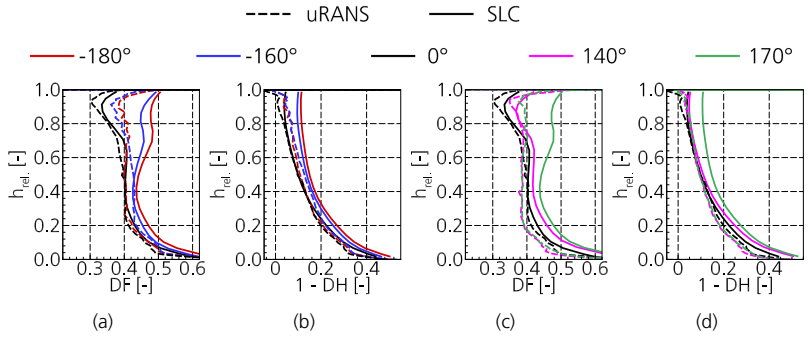

Figure 3.26.: Stator loading. Co-swirl in (a) and (b), counter-swirl in (c) and (d).

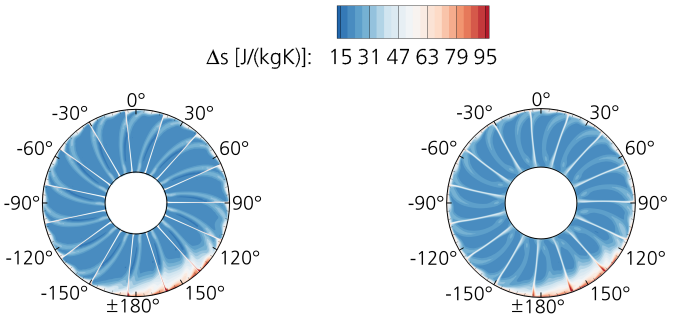

Figure 3.27.: Distribution of the entropy increase at stator mid-chord (a) and downstream of the stator (b).

a 60° segment is 0.0213. This is a reduction of 29.27% compared to the inflow distortion. The loss analysis carried out for the rotor is also applied to the stator. As the fluid enters the stator, the rotor wakes are shredded. This can be seen in fig. 3.27 (a), which shows the entropy variation at mid-chord of the stator. The bowed rotor wake passes through two stator passages. In addition, the vane boundary layers are visible due to the increased entropy levels. In particular, the flow within the tip corner between ±180° and 150° shows high levels of entropy. Downstream of the vane the complex distribution of rotor and stator wakes persists and the high and low entropy fluids mix. Therefore the distribution in 3.27 (b) is more smeared than at the vane mid-chord.

In addition, the time derivative of the entropy with the standard deviation downstream of the stator is shown in fig. 3.28. Essentially the same trends as those observed for the rotor are present downstream of the stator. The time derivative of the entropy shows the

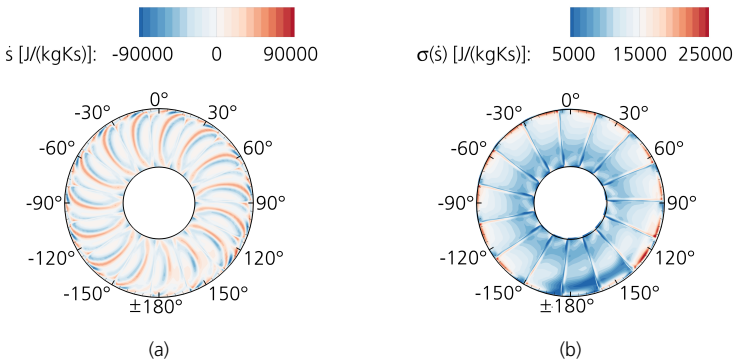

Figure 3.28.: Entropy generation rate and standard deviation at stator outlet.

rotor and stator wakes. The latter are the straight lines, while the rotor wakes remain bowed but are attenuated compared to the upstream position. The two-dimensional pattern of the entropy time rate in fig. 3.28 (a) is much more complex than in fig. 3.21 (a). Similar to the findings at the rotor outlet, higher values are obtained within the counter-swirl region at the stator outlet. The standard deviation shows significantly lower values downstream of the stator than in the upstream position. Figure 3.28 (b) shows small variations in the co-swirl related part and higher values in the counter-swirl region. The vane flow field confirms the observations of rotor related loss generation.

All in all, the reason for the unexpectedly high efficiency region in the efficiency orbit is twofold. As explained in this subsection, there is a higher work input due to unsteadiness. In addition, the entropy rise within the fan stage also varies within the different regions of the boundary layer. Smaller variations in the entropy rise in the co-swirl region up to the middle of the distortion, combined with unsteady work input, lead to increased fan efficiency. In contrast, the entropy rise associated with the tip gap flow outweighs the additional stagnation temperature rise and leads to a decrease in fan efficiency in the counter-swirl region, which is consistent with the findings presented in chapter 2.

Considering that the preliminary fan evaluation requires about 3 CPUh compared to about 10000 CPUh in the uRANS case, the results are encouraging for wide design space explorations.

3.4. Limitations of the methodology

The newly developed fan design and fan assessment methodology has mainly three limitations, which have already been discussed in the previous section. Nevertheless, it is helpful to summarise these limitations again in this subsection.

3.4.1. Steady-state modelling

Mazzawy (1977) finds that the unsteady work input has an impact on the performance calculation within the enhanced multiple compressors in parallel approach. This approach is described in chapter 2. The newly developed design and assessment methodology takes advantage of steady-state approaches and therefore does not resolve time-dependent flow features. Consequently, the unsteady work input is not considered and the stagnation temperature at the rotor outlet misses the additional stagnation temperature rise due to unsteadiness as shown in fig. 3.18 (c) and (f).

3.4.2. Loss generation

The calculation of viscous losses is dependent on the inlet Mach number, the blade incidence and the contraction of the specific stream tube. The loss generation within the streamline curvature approach overestimates the loss generation compared to the time-resolved data. This is shown in fig. 3.18 (b) and (e). The unsteady variation of inflow conditions present in the time-resolved calculation changes the loss generation, which is not accounted for in the preliminary design methodology.

Shock prediction

The presence of transonic flow is likely to lead to flow deceleration due to shocks. As introduced in 3.3, a model that accounts for shock losses is used. This model is calibrated using MISES calculations, which resolve the flow field in a blade-to-blade plane. The flow is treated as two-dimensional in MISES. According to Cumpsty (2010), the nature of transonic flow, including shocks, is three-dimensional. Furthermore, in three dimensions the flow is able to radially redistribute within the blade passage (see Taylor and Miller (2016)) or maintain radial velocity components (see Gunn and Hall (2014)). This three-dimensional flow feature affects the flow conditions within the passage and consequently the shock. However, both the calibration data and the flow fields derived from the streamline curvature approach are two-dimensional. Therefore, discrepancies in the predicted shock position and curvature of the shock compared to the three-dimensional shock are likely.

Tip gap modelling

The tip gap model is a simplified model that takes into account the static pressure difference in the specific blade section. The static pressure difference is used to predict the flow through the tip gap and the associated losses. Due to the two-dimensional treatment of the flow, the specific flow conditions in the co- and counter-swirl regime are not taken into account. In the counter-swirl regime, the static pressure gradient resulting from the flow redistribution is aligned with the static pressure difference across the blade. As a result, the tip gap flow is amplified. In the co-swirl region, the static pressure gradient of the flow redistribution and the static pressure difference feeding the tip gap flow are in the opposite direction, resulting in less attenuation of the tip gap flow and lower losses. As a result, loss prediction misses relevant flow features.

3.5. Interim conclusion of the methodology development

This subsection presented the detailed comparison of the flows from the newly developed preliminary design and assessment methodology with the results from a time-resolved calculation. The preliminary design methodology is able to capture the BLI related flow redistribution within the inlet very well. The quantitative and qualitative prediction of the relative Mach number distribution, as well as the incidence distribution, is in very good agreement with the uRANS-based results. The corresponding fan performance analysis captures the main trends in orbit width and height, and the averaged fan operating point is also in good agreement with the verification data. The spanwise distributions are especially well predicted within the fan rotor. The flow kinematics, resulting fan pressure ratio and blade loading are also well predicted. The stator performance is reasonably well predicted. However, the decoupling of the different passages within the SLC is an inherent difference in the approach compared to the calculation of three-dimensional flow. Considering that the preliminary fan design and assessment methodology allows a reduction in computational time of four orders of magnitude compared to uRANS calculations, the accuracy of the results is encouraging for large design space explorations.

4. Fuselage embedded fans

This subsection deals with turbofan engines embedded in the aft section of an aircraft fuselage. Therefore, the boundary layer fluid entering the fan stage is from the midspan to the tip region of the blade. Throughout this section, a similar boundary layer pattern is applied to the fan stages as introduced in chapter 3.

In contrast to the previous chapter, the fan stage dimensions are better matched to the boundary layer thickness at the assumed integration location and therefore no scaling of the distortion is required. Firstly, conceptual design considerations are presented in terms of top-level design parameters that include boundary layer properties as well as fan performance parameters. Secondly, three fan stages with different radial fan pressure ratios are investigated for their ability to operate within the boundary layer fluid. Thirdly, the effect of circumferential blade tip speed on distortion tolerant fan design is presented. Based on the findings in this section, design suggestions for a distortion tolerant fan are given.

4.1. Conceptual design considerations

At the conceptual design stage, aircraft requirements result in a top-level specification of fan design parameters. In general, the aircraft drag gives the engine thrust, which is translated into a mass flow and fan pressure ratio requirement. Figure 4.1 shows a velocity distribution representing the middle of the distortion. In addition, fig. 4.1 shows a cut through the fan stage. The core engine is neglected in the following considerations. The sizing of the fan diameter requires the consideration of flight conditions (altitude and Mach number) as well as the specification of the hub-to-tip ratio and a target flow capacity. The latter is closely related to the meridional Mach number at the rotor inlet. The nozzle area is obtained by considering the flow state at the nozzle exit, the ambient conditions and the specified mass flow. As already introduced in chapter 1, a distortion tolerant fan design

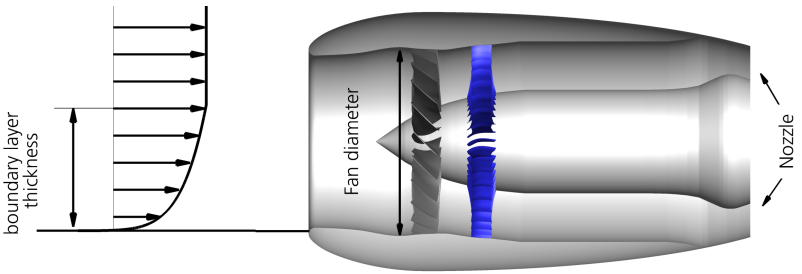

Figure 4.1.: Velocity distribution in the midsection of a generic boundary layer (left) and cross-sectional view an a fan stage (right).

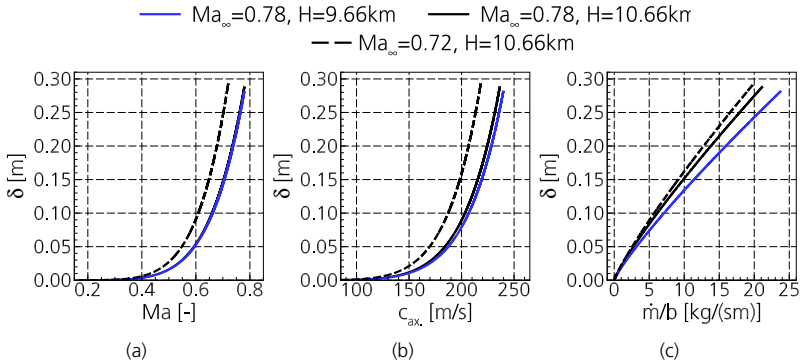

Figure 4.2.: Distributions of Mach number (a), axial velocity (b) and mass flow per meter boundary layer width (c) for two flight Mach number levels and flight altitudes, respectively.

is an interdisciplinary task between aircraft and propulsion unit design. Especially in the conceptual design phase, it is necessary to be aware of the sensitivity to different design considerations.

The fuselage's boundary layer is assumed to be similar to that of a fully turbulent, flat plate, with the velocity field of the boundary layer following the one-seventh power law. A.3 provides a set of equations to calculate the boundary layer properties, which depend directly on the Reynolds number. The latter is influenced by ambient conditions and flight Mach number, and as a result, the analysis examines three sets of altitude and flight Mach number. The properties of the boundary layer are defined by the flight conditions, specifically the flight Mach number and altitude. Two different Mach number levels, 0.78 and 0.72, have been examined. The Mach number of 0.78 represents the cruise conditions of a state-of-the-art aircraft, for short to medium range flights. The MIT D8 double bubble aircraft, which utilizes BLI propulsion, cruises at Mach 0.72 (see Hall's analysis, 2015). Additionally, two distinct altitudes, namely 9.66km and 10.66km, are presented as they are representative for cruise (see Silberhorn et al. (2019)). Figure 4.2 shows the distribution of Mach number (a), axial velocity (b) and mass flow per metre of boundary layer width (c) within the boundary layer. Generally, the boundary layer thickness increases as Reynolds number decreases. The Reynolds number varies from $1.9 \cdot 10^8$ (Ma=0.72, H=10.66km), through $2.1 \cdot 10^8$ (Ma=0.78, H=10.66km), to $2.3 \cdot 10^8$ (Ma=0.78, H=9.66km). Therefore, the thickness of the boundary layer shows a slight increase at a fixed flight Mach number and higher altitude. Correspondingly, the density and static temperature decrease as altitude increases. The latter results in the spread of the axial velocity distribution for the Mach number 0.78 cases. Additionally, in the lower Mach number case, the boundary layer thickness increases slightly at a fixed altitude.

When considering the velocity and density changes, there is a variation in the distributions of mass flow per meter boundary layer thickness as visualised in fig. 4.2(c). Within the boundary layer, there is a mass flow of 20 to 24 kg/s per meter boundary layer width. For the flight Mach number of 0.78, the mass averaged Mach number is 0.687. While

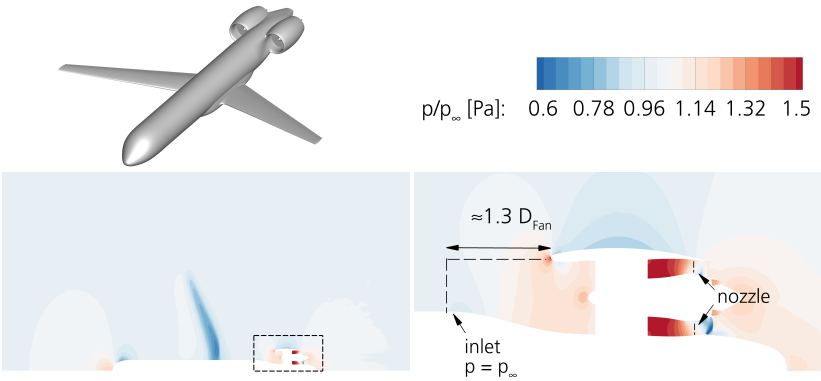

Figure 4.3.: Pressure field around an aircraft with BLI engines. Adapted from Vinz and Raichle (2022). Courtesy *DLR Institute of Aerodynamics and Flow Technology*.

the flight Mach number of 0.72 has an averaged Mach number of 0.635. Especially, the averaged Mach number of the flow entering the engine is a crucial metric for the top-level BLI fan specification.

As highlighted in chapter 1, calculating the drag and thrust becomes more challenging for aircraft utilizing boundary layer ingesting propulsion units. Specifically, the non-uniform static pressure field occurring upstream of the intake should be taken into account when employing the classical thrust equation, as discussed by Plas (2006). Normally, the control volume extends well upstream of the engine, with ambient conditions present at the control volume inlet. This study investigates the static pressure field around an aircraft powered by BLI engines, as shown in fig. 4.3. As shown in fig. 4.3, the static pressure field is predominantly uniform at a distance of 1.3 fan diameters upstream of the fan stage. Consequently, the 1.3 fan diameter upstream is selected as the control volume inlet for the fan thrust calculation and the outlet is positioned at the bypass nozzle exit. The conventional thrust accounting method is utilized in the sensitivity analysis going forward. The net thrust equation is given by eq. (4.1). The thrust comprises a term that calculates the velocity difference between the inlet and nozzle multiplied by the mass flow. As this analysis considers only the bypass flow, the mass flow remains constant. Additionally, if the nozzle is choked, the static pressure difference between the nozzle and ambient conditions contributes to the thrust. However, this term vanishes in the case of unchoked nozzle operating conditions.

$$F_{net} = \dot{m} \cdot (c_{nozzle} - c_{avg,in}) + A_{nozzle} \cdot (p_{nozzle} - p_\infty) \tag{4.1}$$

Equation 4.2 calculates the power added to the flow by the fan blade. The power depends on the mass flow through the fan stage, the isobaric heat capacity, and the stagnation temperature rise between the fan inlet and outlet.

$$P = \dot{m} \cdot c_p \cdot (T_{t,nozzle} - T_{t,in}) \tag{4.2}$$

Additionally, the efficiency of the thrust power compared to the shaft power is accounted

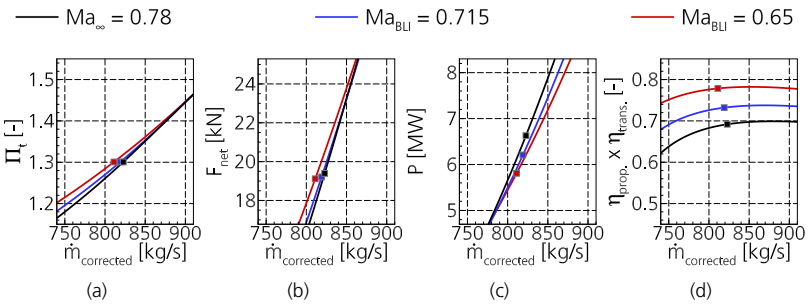

Figure 4.4.: Working lines with constant bypass nozzle cross-section area. Design parameters: Π_t=1.3, $\eta_{is,Fan}$=0.93 and ω_t=0.05.

for to evaluate the efficiency of the thrust power generation.

$$\eta_{trans.} \cdot \eta_{prop.} = \frac{E_{kin.,jet}}{P} \cdot \frac{E_{thrust}}{E_{kin.,jet}} = \frac{F_{net} \cdot c_\infty}{P} \tag{4.3}$$

A simple working line calculation is performed as part of the sensitivity study. The nozzle performance only takes into account the gas dynamic properties. Therefore, the working line is determined by the specification of the ambient conditions, an assumption of the fan efficiency and the losses upstream and downstream of the fan stage, and an initial size of the bypass nozzle. Throughout the sensitivity study, the fan efficiency and losses are kept constant. Operating points with the same net thrust are investigated as those operating points comparable to powering an aircraft with a fixed thrust requirement. These assumptions would need to be verified in more detailed and multidisciplinary designs. The purpose of the conceptual design considerations is rather to give general directions for a distortion tolerant fan design.

In the following, a sensitivity study is depicted which accounts for the impact of BLI on performance metrics. The baseline case considers an aircraft that operates at a flight Mach number of 0.78. No boundary layer ingestion is foreseen and the stream tube enters the engine with the free stream momentum of the flight Mach number Ma_∞. The other two cases take advantage of BLI. The aircraft still operates at a flight Mach number of 0.78, but due to the fuselage boundary layer, the momentum of the stream tube entering the engine is lower. In one case the stream tube entering the engine has an averaged Mach number due to BLI (Ma_{BLI}) of 0.715. In the other case, Ma_{BLI} is set to 0.65. In all cases the fan operates at a meridional Mach number at fan inlet of 0.62 and a fan pressure ratio of 1.30.

Figure 4.4 shows the data obtained for a scenario where the engine is designed for clean inflow and then exposed to BLI. Due to the nozzle sizing for clean inflow conditions, the working lines for the BLI cases are shifted to the left as revealed in fig. 4.4 (a). However, the net thrust remains almost unchanged as shown in fig. 4.4 (b). The slight decrease in net thrust would require an increase in the corrected fan shaft speed. A small increase in the corrected mass flow and fan pressure ratio will then give the same net thrust. Figure 4.4 (c) illustrates the beneficial effect of BLI in terms of reducing the power input to the

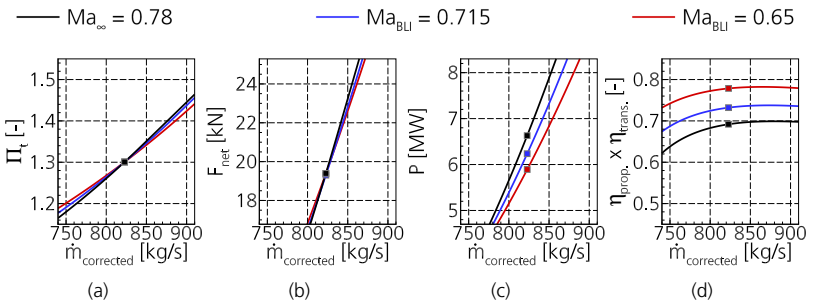

Figure 4.5.: Working lines with adjusted bypass nozzle cross-section area. Design parameters: Π_t=1.3, $\eta_{is,Fan}$=0.93 and ω_t=0.05.

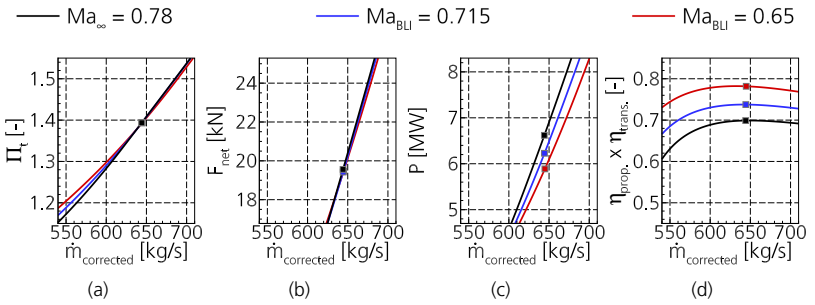

Figure 4.6.: Working lines with adjusted bypass nozzle cross-section area. Design parameters: Π_t=1.39, $\eta_{is,Fan}$=0.93 and ω_t=0.05.

flow for a comparable thrust level. Reducing the inlet Mach number from 0.78 to 0.715 results in a 6.36% reduction in power input. Further reducing the Mach number level to 0.65 results in a 12.4% reduction in power input compared to the baseline case. Correspondingly, the product of the transfer and propulsive efficiencies in the BLI cases increases by 4% and 8.67% respectively.

In a further step, the BLI conditions are considered in the nozzle sizing, while the fan specification remains fixed. This means that as the inlet momentum decreases due to BLI, the nozzle area increases. This allows the specified mass flow to pass through the nozzle. Figure 4.5 (a) shows the working lines for this particular redesign. As the nozzle area is slightly increased by 0.46% and 1.45% respectively, the working lines of the lower Mach number cases are shifted to the right within the map. Consequently, the thrust level is achieved at the same corrected mass flow and fan pressure ratio as in the reference case. The trends in power requirement and thrust generation efficiency remain similar to the fixed nozzle case. Therefore, for the sake of comparability, the dedicated nozzle design is applied for the cases with increasing fan pressure ratios.

Figure 4.6 shows the results for a fan stage pressure ratio of 1.39. As the fan pressure ratio increases, less mass flow is required to generate thrust. Consequently, the fan diameter decreases by about 11.8% compared to the baseline fan. In addition, the bypass nozzle area is approximately 26% smaller than the baseline nozzle. Both effects are expected to result in a lower engine weight, which will be beneficial in facilitating engine integration and associated fuselage redesign. Due to the increased FPR, the operating points are at lower corrected mass flows. The trend in terms of lower power consumption due to BLI remains identical (see fig. 4.6 (c)). In addition, the slope of the efficiency curves changes and the operating points are close to the peak efficiency as shown in fig. 4.6 (d).

Lastly, a fan pressure ratio of 1.52 is analysed and the results are shown in fig. 4.7. The corrected mass flow decreases further for the given thrust requirement. This reduces the fan diameter by approximately 21.5% compared to the base case. The bypass nozzle is also about 45% smaller. The trend of decreasing power consumption with decreasing inlet Mach number remains. Taking into account the efficiency of thrust generation, fig. 4.7 shows that the operating points are beyond the efficiency maximum.

Within fig. 4.8 the results for the different fan pressure ratios and Mach numbers of 0.78 and 0.715 are presented. The minimum power input is obtained for the fan pressure ratio of 1.39 (see fig. 4.8) and the operating point is close to the maximum of the efficiency characteristic. Considering that the mass flow within the boundary layer is relatively small (see 4.2 (c)), the inlet geometry is expected to be non-axisymmetric and more elliptical than conventional inlets. This results in a highly three-dimensional intake geometry, as the elliptical cross-section is required to smoothly transition to a rotationally symmetric cross-section within the fan stage. Comparable geometries are presented in the literature and related studies are discussed in chapter 2.

These results are consistent with the literature and similar results are presented by Plas (2006), Sato (2012) or Hall (2015). However, the results presented in this study are more focused on typical fan design metrics. In addition, the study of working lines and the effect of nozzle size complement the above studies.

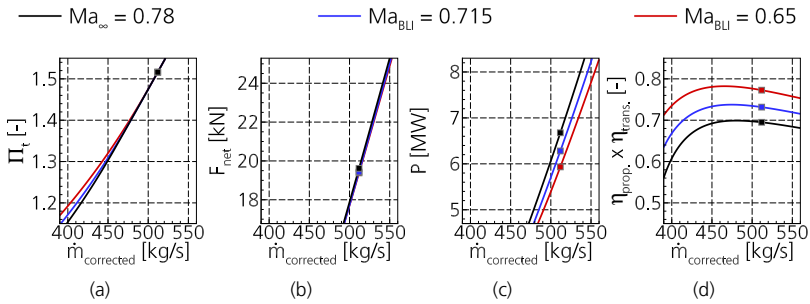

Figure 4.7.: Working lines with adjusted bypass nozzle cross-section area. Design parameters: Π_t=1.52, $\eta_{is,Fan}$=0.93 and ω_t=0.05.

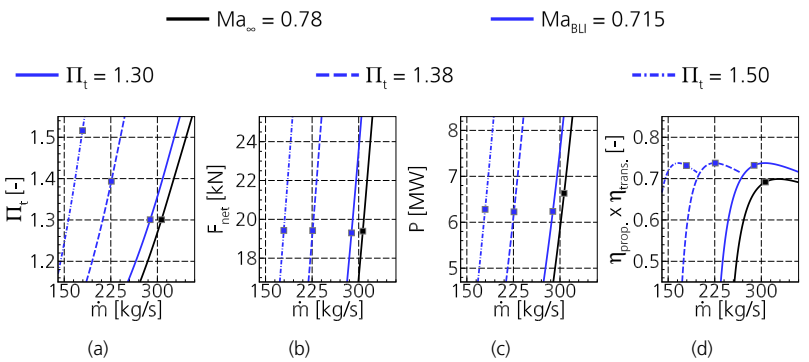

Figure 4.8.: Synthesis of the sensitivity study considering different fan pressure ratio levels.

4.2. Impact of the spanwise fan pressure ratio distribution on distortion tolerance

4.2.1. Fan design philosophy and performance at homogeneous inflow

The following subsection investigates the impact of different spanwise fan pressure ratio distributions on distortion tolerance. Since the stagnation pressure distortion is located in the tip region of the fan blade, it is expected that the variation of the radial fan pressure ratio will affect the flow redistribution and distortion attenuation. Figure 4.9 shows the distinguishing design feature of the three fans, which is an ascending, a constant and a descending spanwise fan pressure ratio distribution. These fans are designed and reported by Schönweitz et al. (2017). In addition, the fan stages are investigated as a verification data set for the intermediate design methodology presented by Mennicken et al. (2019).

Table 4.1 summarises the design objectives for the fan stages. The specification includes a fan pressure ratio of 1.32, a meridional Mach number of approximately 0.63 and a corrected fan blade tip speed of 292 m/s. For the sake of completeness, fig. A.3 visualises the flow paths of the specific fan stage designs. All flow paths cover a simplified spinner

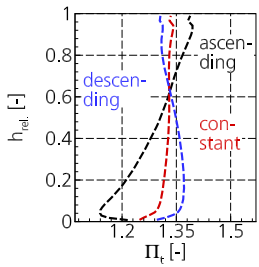

Figure 4.9.: Spanwise fan pressure ratios for the ascending, constant and descending fan.

Table 4.1.: Fan stage specification for verification.

Π_t [-]	Ma_m [-]	$u_{tip,corrected}$ [m/s]
1.32	~ 0.63	292

geometry upstream of the rotor. In particular, the constant and descending fan stages show a concave hub line close to the rotor leading edge in fig. A.3 (b) and (c). In addition, the higher work input in the fan blade hub section requires more contraction in the fan hub section. The stator flow path shows a slight increase in the hub line for the ascending fan in fig. A.3 (a), while the cross-sectional area is mainly preserved throughout the stators of the other fan stages in fig. A.3 (b) and (c).

The SLC models of the fan stages are adjusted to match the fan stage performance of the high fidelity results. The SLC results are shown by the solid lines, while the RANS results are shown by the dashed lines. Figure 4.10 shows the Mach number distributions at different flow positions. At the rotor inlet the relative Mach number is similar for all fans because the meridional Mach number and the fan blade speed are similar (see fig. 4.10 (a)). The absolute Mach number is shown between the rotor and stator and at the fan stage outlet. As mentioned above, the increased fan pressure ratio near the hub requires an increased work input there. As the circumferential speed at the trailing edge of the rotor is limited by the hub radius, the rotation of the flow and hence the circumferential speed in the absolute frame of reference increases. Consequently, the Mach number level increases for the constant and descending fan stages. Downstream of the fan stage, the Mach number distribution reflects the radial fan pressure ratio profile. As expected, the ascending fan stage has low Mach number levels near the hub and higher Mach numbers near the tip. In contrast, the constant fan stage has an almost constant Mach number distribution downstream of the fan stage, while the descending fan stage even has the highest Mach numbers near the hub. Figure 4.11 (a) illustrates the specific design intent of the three fan stages. The design of the ascending fan stage shows a similar design

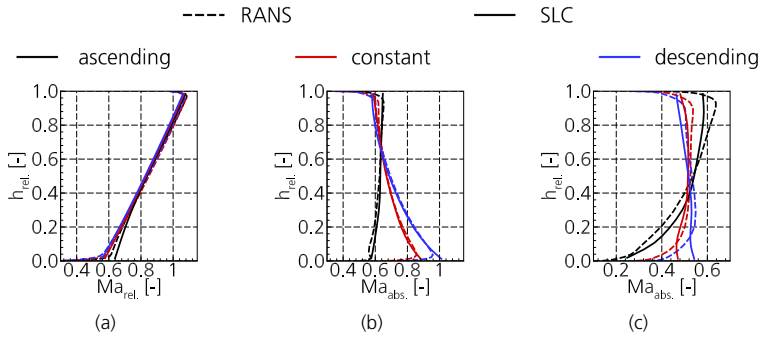

Figure 4.10.: Spanwise relative Mach number at rotor inlet (a) and absolute Mach number distributions at stator inlet (b) and stator outlet (c) at ADP.

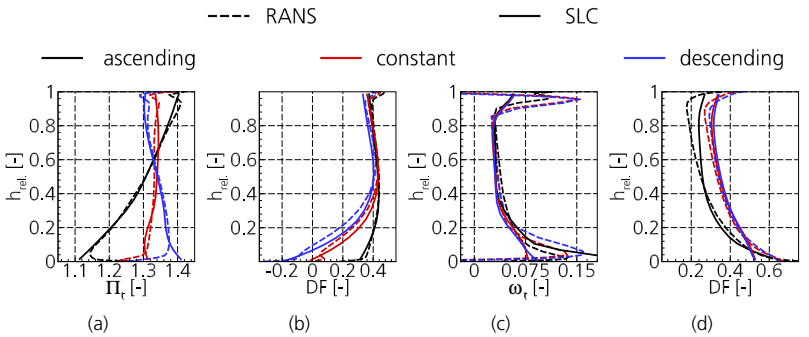

Figure 4.11.: Rotor performance in (a) & (b) and stator performance in (c) & (d) at design conditions.

intent to the fan stage introduced in chapter 3. So the same comments about the low fan pressure ratio near the hub apply to this fan. The constant and decreasing spanwise fan pressure ratio fans show a higher fan pressure ratio near the hub. In general, a higher fan pressure ratio requires a higher flow turning. As a result, the spanwise stagger angle distribution of the fan blade designs differs. Near the hub, the stagger angle of the ascending fan is bigger than in the descending case. Close to 60% of the span the trend changes and the stagger angle of the ascending fan is smaller than that of the descending fan. Over the entire span, the stagger angle distribution of the fan with constant fan pressure ratio is between the others.

The fan blade loading differs significantly near the hub. A high FPR requirement leads to flow acceleration in the rotor hub section and thus the DeHaller number is above unity and the diffusion factor is below zero as it is DeHaller number driven (see fig. 4.11 (b)). Furthermore, fig. 4.11 (b) shows that the upper part of the fan blades have almost the same blade loading. The stator performance is shown in fig. 4.11 (c) and (d). The stator losses are mainly related to the flow near the hub and tip end walls. Near the hub, the SLC does not capture the trends of the RANS results. The stator of the ascending fan shows higher losses in SLC than in RANS, while the constant and descending fan stages show lower losses in this region. Near the tip, the SLC-based assessment shows lower losses than RANS. However, over a wide range of the span, the loss prediction is in good agreement for all designs.

The vane loading is shown in fig. 4.11 (d) and is in good agreement for the three fan stages over a wide portion of the span. Variations between the two approaches appear near the end walls. In particular, the blade hub sections are highly loaded. In order to achieve better vane hub performance, the flow path could be improved by adding contraction in this specific region. However, this analysis analyses the effect of a rotor design feature on distortion sensitivity and therefore accepts the lower level of maturity within the vane section. Based on this comparison, the redesign of the three fan stages compares very well with the baseline designs at ADP.

Figure 4.12 shows the corresponding fan map performance in terms of fan pressure

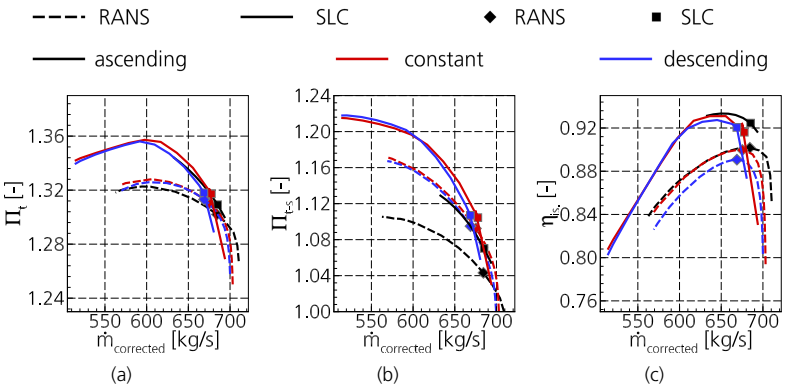

Figure 4.12.: Fan map in terms of total-to-total fan pressure ratio (a), total-to-static fan pressure ratio (b) and isentropic efficiency (c) stemming from SLC and RANS.

ratio (a), stagnation-to-static fan pressure ratio (b) and isentropic efficiency (c). As can be seen in fig. 4.12, the fan pressure ratio at off-design is steeper for all fan stages. In addition, the static pressure rise is higher in SLC than in RANS due to the lower loss generation within the SLC representation. Consequently, the isentropic efficiencies are higher in SLC than in RANS. In addition, a higher static pressure rise is achieved for the constant and descending fan, which is maintained between the different approaches. As the ascending fan hub has a very low fan pressure ratio, the static pressure downstream of the fan shows a radial profile in the hub region even at ADP. In the off-design, the increase in static pressure leads to a further reduction in Mach number levels. Thus, in SLC, the stator hub area limits the operating range to lower corrected mass flows. In RANS, the complex three-dimensional flow pattern allows the fan stage to operate at lower mass flows, which cannot be reproduced in SLC. This is the reason for the significant reduction in operating range. In contrast to the ascending fan, the operating limit of the other two fan stages is reached when the stagnation-to-static characteristic peaks.

Overall, the redesigned fan stages match the baseline design characteristics at the aerodynamic design point. The off-design performance differs as the fans approach the specific aerodynamic stability limits. In the next subsection, the performance at distorted inflow conditions is investigated.

4.2.2. BLI fan performance assessment

All three fan stages from the previous subsection are subjected to a generic boundary layer profile as described in chapter 3. In contrast to the previous section, no scaling of the boundary layer profile is required as the fan stage dimensions and the boundary layer profile are in a reasonable proportion. The minimum stagnation pressure of the two-dimensional boundary layer profile is limited to 89.3% of the freestream stagnation pressure to avoid numerical challenges during the calculations. This results in a distortion intensity of 0.0368. As mentioned in chapter 3, the fan stages are exposed to the BLI flow while the static pressure at the fan stage outlet remains at the level of the ADP conditions.

Table 4.2.: BLI related shift of the operating points with respect to ADP.

		$\frac{\dot{m}_{BLI}-\dot{m}_{ADP}}{\dot{m}_{ADP}}$ [%]	$\frac{\dot{m}_{corrected,BLI}-\dot{m}_{corrected,ADP}}{\dot{m}_{corrected,ADP}}$ [%]	$\frac{\Pi_{t,BLI}-\Pi_{t,ADP}}{\Pi_{t,ADP}}$ [%]
ascending	BLI SLC	-1.35	-0.20	-0.15
	BLI uRANS	-1.41	-0.54	0.01
constant	BLI SLC	-1.20	-0.52	0.30
	BLI uRANS	-1.79	-0.94	0.27
descending	BLI SLC	-1.01	0.00	-0.55
	BLI uRANS	-1.88	-1.03	0.43

Averaged fan performance

Table 4.2 summarises the operating point variations due to BLI relative to ADP from the preliminary fan assessment and high-fidelity verification. The time-resolved calculations show that the reduction in mass flow due to BLI compared to ADP is between -1.41% for the ascending and -1.88% for the descending fan stage. In terms of corrected mass flow, the variation is slightly smaller, ranging from -0.54% to -1.03%. On the other hand, the fan pressure ratio remains mainly at the ADP level and the descending fan shows the highest increase of 0.43%. The most sensitive parameter is the isentropic fan efficiency. The ascending fan loses 2.5% due to the distorted inflow compared to ADP, while the variation of the constant and descending fans is less severe. The efficiency of the constant fan decreases by about -0.65% and the efficiency of the descending fan decreases by -0.82% compared to ADP.

In terms of averaged operating points, the preliminary fan assessment is able to predict

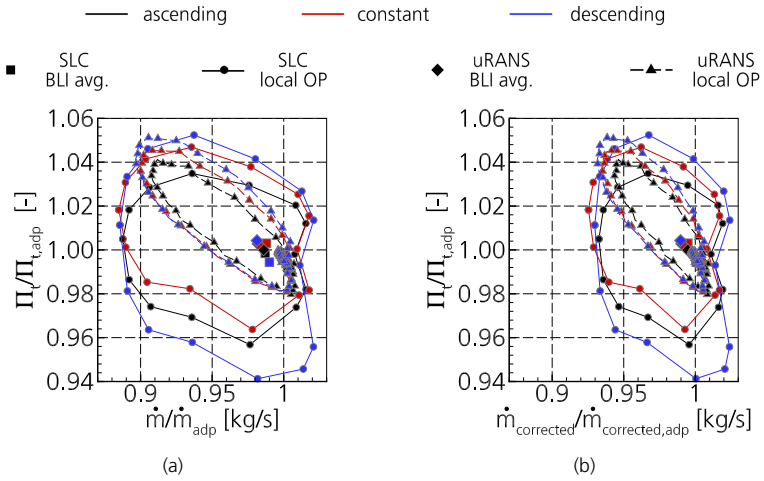

Figure 4.13.: Relative operating point variation with respect to ADP.

the correct magnitude of operating point variation. The ascending fan shows a mass flow reduction of -1.35%, while the other fans show smaller BLI related mass flow reductions of -1.2% and -1.01% respectively. As already seen for the uRANS data, the corrected mass flow variation is smaller compared to the mass flow variation and the descending fan stage shows no change in corrected mass flow. For this fan, the stagnation pressure term coincidentally offsets the mass flow decrease within the correction formula. However, it is worth noting that the mass flow variation is close to the convergence criterion for the flow redistribution calculation. Therefore, variations in this order of magnitude can be expected from the approach. Furthermore, the SLC-based fan pressure ratio variation is small. The largest increase of 0.3% shows the constant fan, while the descending fan shows the largest decrease of -0.55%. The trends between the fans and the direction of the fan pressure ratio changes are not fully captured by SLC. For example, the fan pressure ratio increases at BLI, but the ascending and descending fans have slightly lower FPRs than at ADP.

Figure 4.13 shows the local operating point excursion as well as the averaged operating point in relation to ADP. The preliminary design methodology is capable of covering the orbit width in terms of (corrected) mass flow. This includes the increase in (corrected) mass flow outside the boundary layer as well as the decrease in (corrected) mass flow inside the

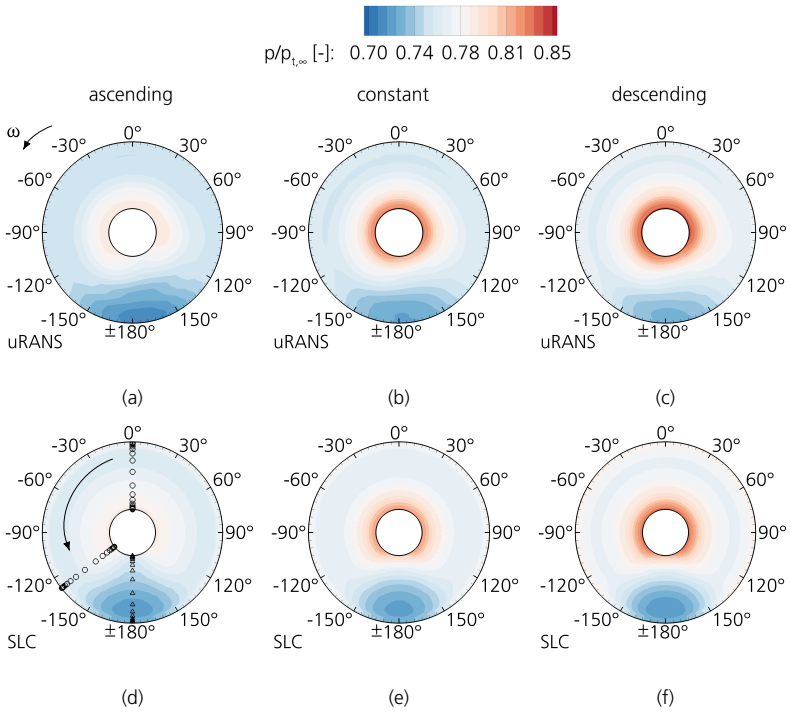

Figure 4.14.: Relative static pressure at the aerodynamic interface plane.

boundary layer. As already introduced in chapter 3, the stagnation pressure rise within the co-swirl region is underestimated in the preliminary assessment. The uRANS results of the three fans show only minor differences within the co-swirl, while SLC shows a more pronounced tendency there. Within SLC, the descending fan operates under choking conditions in the co-swirl region, so the fan pressure ratio decreases. In good agreement with fig. 4.13, the choking is less pronounced for the fan rotor with constant fan pressure ratio. The instantaneous flow fields of the time-resolved calculations do not show severe choking in the co-swirl region. As mentioned in section 3.4, the prediction of choking is one of the limitations of the SLC approach. The variations and trends within the counter-swirl region are well covered by SLC, and the variation of the fan pressure ratio of the orbit is well captured by the approach. Even the BLI-related operating point variations show differences between the three fans. A more detailed analysis of the flow field and local fan performance is therefore carried out.

Rotor performance

Flow redistribution is a key feature of the BLI flow and therefore, it is present in the results of the three fans. Figure 4.14 shows the non-dimensional static pressure distribution

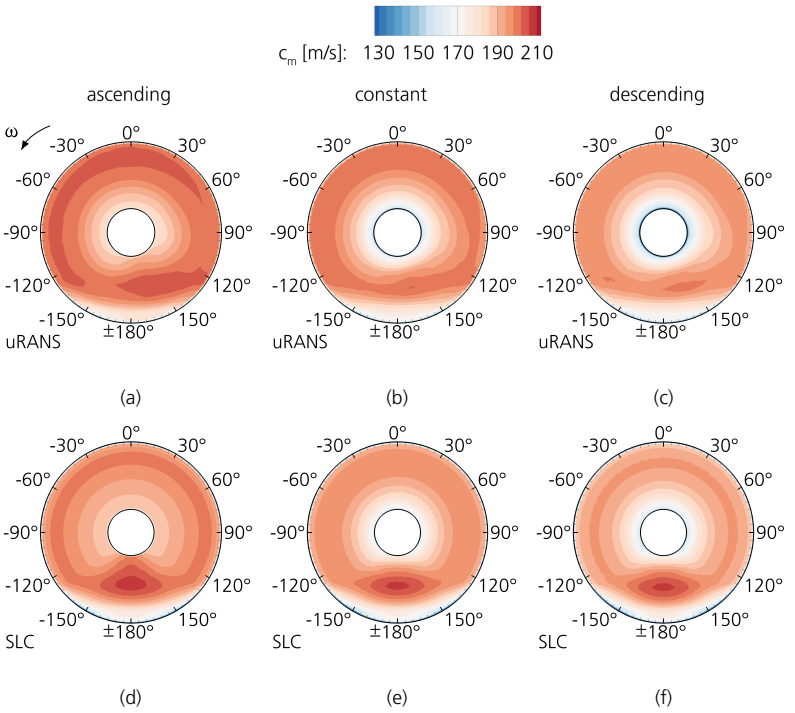

Figure 4.15.: Meridional velocity at the aerodynamic interface plane.

related to the free stream stagnation pressure. In chapter 3 the indirect coupling of the upstream flow for the static pressure reconstruction as well as the assumed axial symmetry is discussed. Figure 4.14 (d) shows the effect on the static pressure distribution. Since the spinner geometry leads to an acceleration of the hub section and the stream tube contraction of the tip region of the blade affects the static pressure level through the static pressure equilibrium, the static pressure within the hub section at ±180° decreases in 4.14 (d). The time-resolved static pressure field shows higher values at this position, as the static pressures of the other circumferential positions interact in a fully coupled flow field, as shown in fig. 4.14 (a). The prediction of the relative static pressure field of the constant and descending fans shows a better match within the hub section at ±180°. This is due to the concave hub line mentioned at the beginning of this subsection. The flow deceleration caused by this geometric feature leads to good matching there. With the exception of the hub section of the ascending fan stage and the slightly more smeared relative static pressure pattern of the high-fidelity results, the preliminary fan assessment covers the BLI related variations both qualitatively and quantitatively, the static pressure minimum is well matched as is the spanwise distribution around the circumference. In addition, the varying static pressure levels between the different fan stages are also captured. Accordingly, the velocity distributions upstream of the rotors are similar for both approaches. The afore-

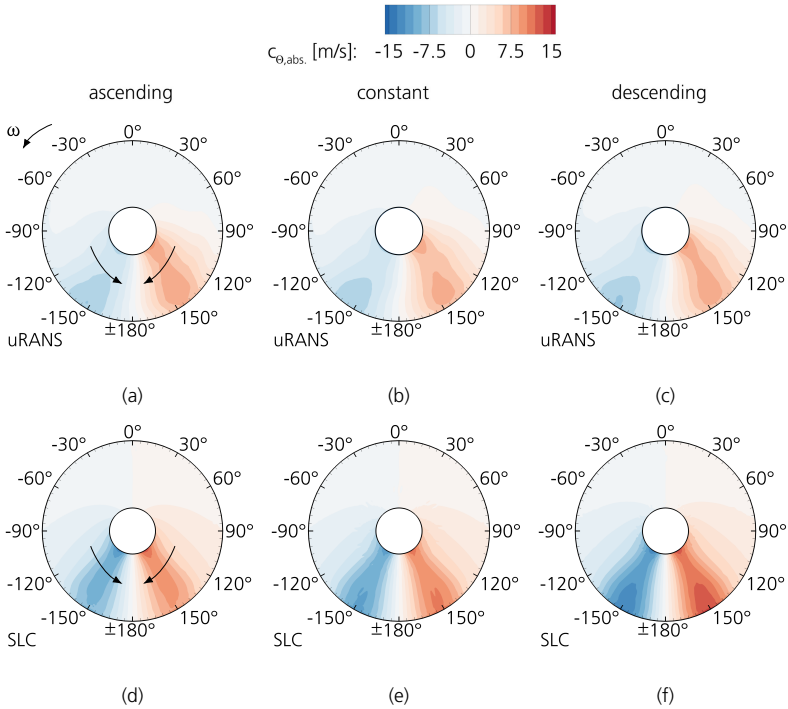

Figure 4.16.: Circumferential velocity in the absolute frame of reference at the aerodynamic interface plane.

mentioned trends around the circumference as well as the differences between the fan stages persist. Figure 4.15 shows the meridional velocity distribution while fig. 4.16 depicts the circumferential velocity in the absolute reference frame. The hub section of the ascending fan stage shows the greatest differences at ±180°, as expected from the relative pressure distribution. According to the more smeared static pressure distribution of the time-resolved calculation, the circumferential velocity levels are slightly smaller than those calculated by SLC (see fig. 4.16). Nevertheless, both the velocity pattern and the magnitude of this quantity are well predicted. The velocity components presented above translate directly into the rotor incidence, which is visualised in 4.17. As introduced in chapter 3, the decrease in axial velocity within the boundary layer leads to positive incidence in the tip region of the fan stage and can be found in the results of both approaches. From hub to midspan, the incidence is dominated by the circumferential velocity in the co- and counter-swirl regions. Furthermore, the negative incidence (at -130°) is more pronounced than the positive incidence (at 130°) which is captured by SLC and uRANS. The velocity distribution also affects the Mach number pattern at the AIP. However the differences between the different fans are small. For the sake of completeness, the relative Mach number distributions are shown in fig. A.4. The characteristic Mach number distribution with lower Mach number levels in the co-swirl area than in the counter-swirl region is well predicted by the SLC. As explained in chapter 2 and chapter 4, high Mach numbers

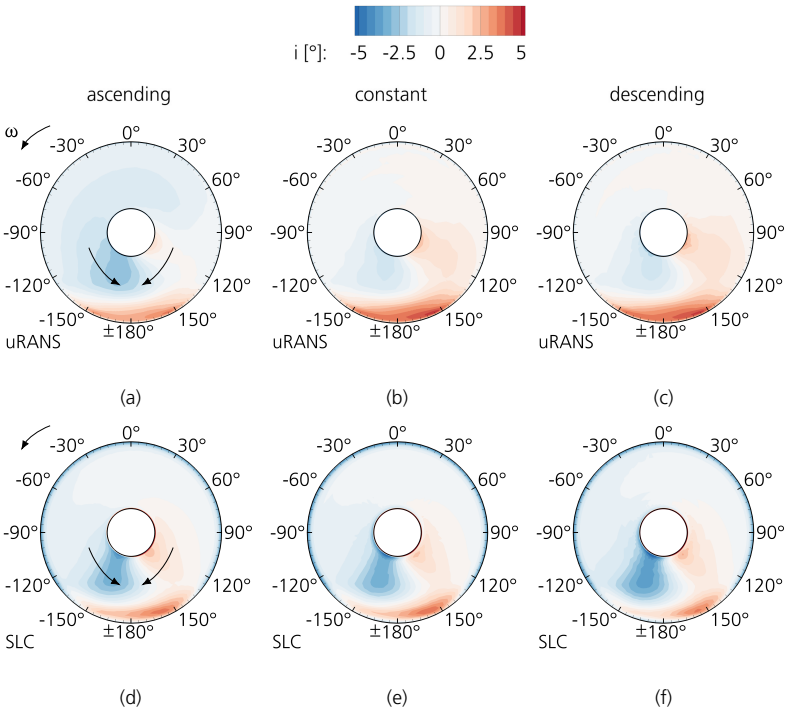

Figure 4.17.: Rotor incidence at the aerodynamic interface plane.

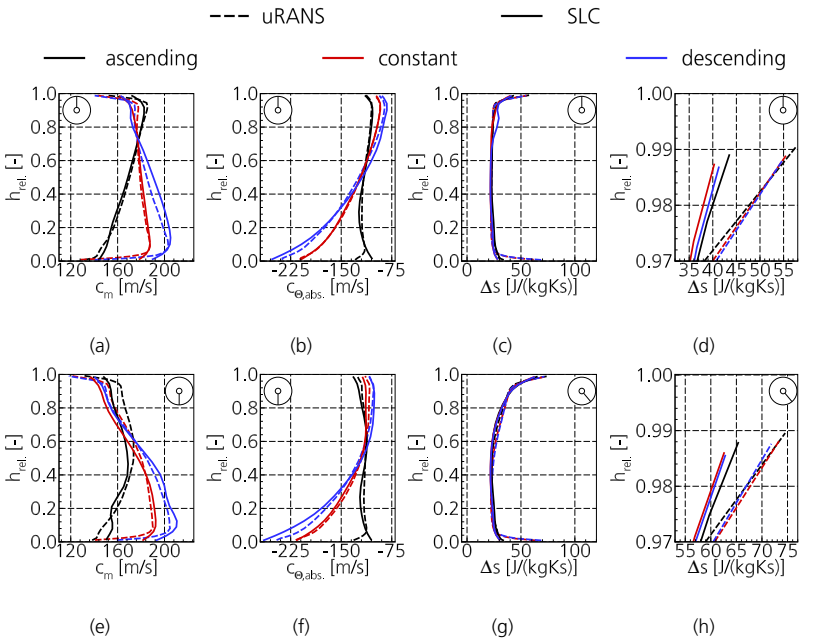

Figure 4.18.: Velocity triangles at rotor outlet at 0° in (a) and (b) as well as at ±180° (e) and (f). Entropy distribution at rotor outlet at 0° in (c) and (d) as well as at 140° (g) and (h).

combined with positive incidence lead to an increasing static pressure difference between the pressure and suction sides of a blade. In addition, with the static pressure gradient due to flow redistribution, the tip gap flow is amplified and the associated losses increase.

For the sake of simplicity, only a few specific operating conditions around the circumference are considered. Figure 4.18 shows the spanwise velocity distributions downstream of the rotor at 0° (a) and ±180° (e). The low momentum boundary layer fluid is re-energised by the fan stage. Nevertheless, a meridional velocity deficit remains in the flow. Above 50% span, the undistorted inflow at 0° has significantly higher meridional velocities than at ±180°, as shown in fig. 4.18 (a) and (e). This trend is well captured by the preliminary fan evaluation. The BLI fluid also changes the circumferential velocity distributions above 50% span compared to the undistorted flow (see fig. 4.18 (b) and (f)). So both the slope and the velocity levels of the circumferential velocity distribution change. These variations are also well captured by the preliminary design methodology. As mentioned in chapter 3, the tip gap flow related deviation that is present in the time-resolved calculations is not found in the SLC results. There, the tip gap modelling is not able to reproduce the complex flow.

As discussed in chapter 2 and chapter 3, BLI is associated with convective transport of an

entropy distortion. The BLI related loss generation is analysed by comparing the spanwise entropy distribution at 0° (homogeneous inflow) in fig. 4.18 (c) and 140° (counter-swirl) in (g) at the rotor outlet. Tip gap flow has already been identified as one of the main drivers of loss generation in BLI flows. Therefore fig. 4.18 (d) and (h) provide a zoom into the tip region of the spanwise distributions shown in (c) and (g). As explained in chapter 3, the tip gap flow is amplified within the counter-swirl region. In general, the entropy level within the counter-swirl region is higher than for undistorted inflow conditions above 50% span. This trend is more pronounced in the tip region, as shown by zooming into the specific spanwise distributions, and is captured by both approaches. Related to the convective transport of entropy, the additional entropy rise within the fan stage is of interest and is evaluated for uRANS data. At 0°, the ascending fan has an entropy rise between the rotor inlet and outlet of 22.38 J/(kgKs), while the entropy rise of the constant and descending fans is 20.67 and 20.79, respectively (cf. fig. 4.18 (d)). The higher entropy increase is expected within the rotor of the ascending fan due to the addition of more work in the tip region of the blade. The increase in entropy is almost the same for the constant and descending fans compared to the ascending fan design ((cf. fig. 4.18 (d)). A lower entropy increase for the descending fan would have been expected as the work input for this fan is the lowest compared to the others. Within the counter-swirl region, the entropy rise of all the fan rotors increases and the ascending fan shows an entropy rise of 26.44 J/(kgKs), the constant and descending fans have an entropy rise of 25.25 and 24.84 J/(kgKs), respectively (cf. fig. 4.18 (h)). As expected, the ascending fan has the highest entropy increase at

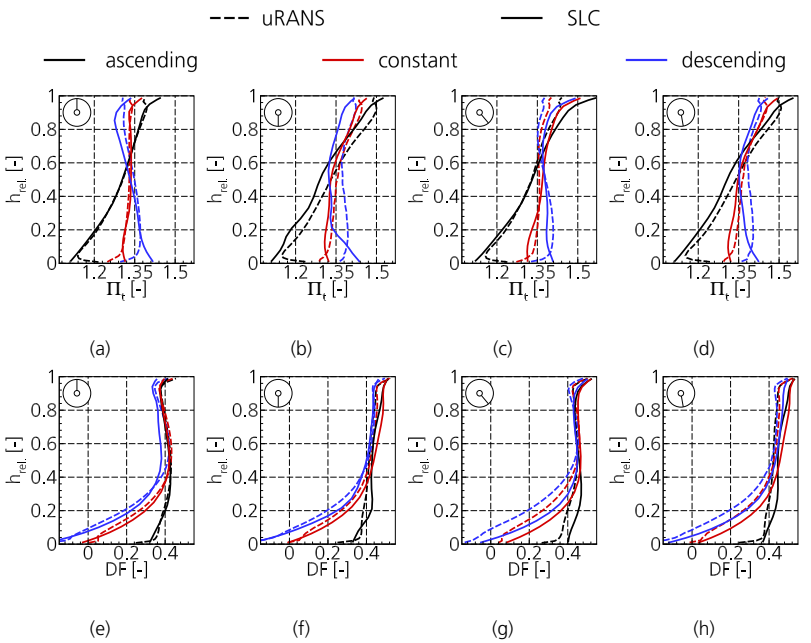

Figure 4.19.: Fan pressure ratio and fan blade loading at 0° (a) and (e), at ±180° (b) and (f), at 140° (c) and (g) as well as at 170° (d) and (h).

both circumferential positions due to its design philosophy. This trend is captured by the SLC. Contrary to the ascending fan, the SLC-based results do not capture the trend between the constant and descending fans. The SLC-based fan assessment results in a lower isentropic efficiency for the constant spanwise fan stage compared to the descending one, while the RANS-based assessment shows the opposite. This trend is maintained in the BLI assessment and leads directly to the differences in entropy at the rotor outlet.

The entropy increase is one important part to account for the isentropic efficiency. The other is the stagnation temperature, which is closely related to the work input. Higher work input leads to higher stagnation temperature. Therefore, the entropy increase of the ascending fan occurs at the same time as the stagnation temperature increases. This affects the isentropic efficiency, and in contrast to the fan stage performance variations, the rotor isentropic efficiency decrease of the ascending fan is 0.62%, while the decrease of the constant fan stage is 0.72%. The highest rotor efficiency decrease occurs for the descending fan rotor and is 1.43%.

The varying inflow conditions caused by BLI result in varying fan performance around the circumference. Therefore, the fan pressure ratio and diffusion factor are evaluated at 0°, ±180°, 140° and 170°. These results are presented in fig. 4.19. In general, the

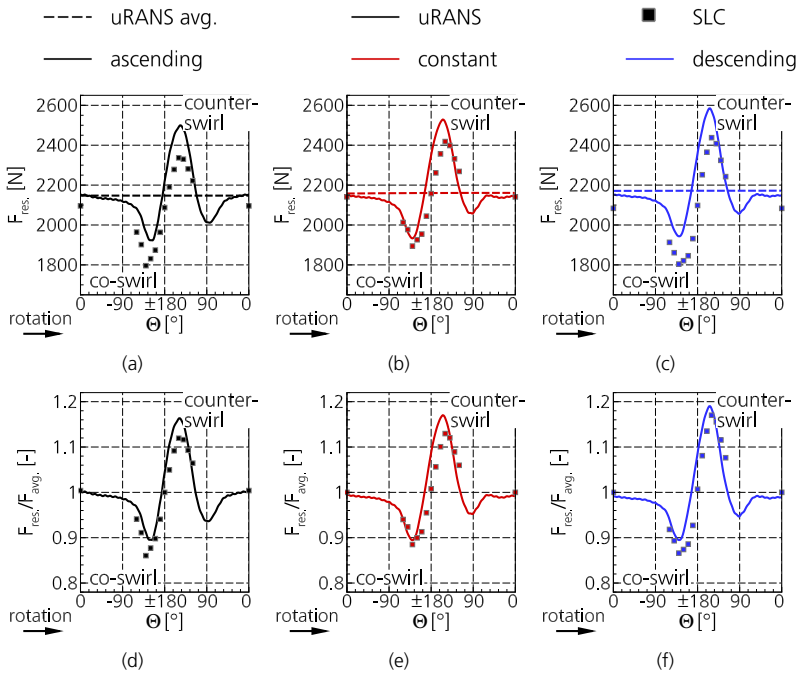

Figure 4.20.: Absolute (upper row) and relative (lower row) blade forces. From left to right: ascending, constant, descending.

performance variations due to BLI are well covered by the SLC-based methodology. For undistorted inflow, only the descending fan shows small differences in fan pressure ratio and blade loading. At 180°, the fan pressure ratio distributions of the SLC assessment are slightly lower than the uRANS results. The reasons for the lower fan pressure ratios are the neglected unsteady work input, already addressed in chapter 3, and the prediction of choking conditions. As mentioned in the discussion of orbits, the descending fan suffers most from the deficit in choke prediction over a wide part of the blade. Therefore, the fan pressure distribution differs the most in fig. 4.19 (b). As the choking and associated shock systems are highly three-dimensional, this feature is not perfectly captured by SLC (see also chapter 3). The spanwise distributions of the two approaches are close for the constant and ascending fan. Nevertheless, the variation in FPR and DF levels and the changed slopes of both quantities are well captured by the SLC approach. The same is true for the other circumferential positions at 140° shown in fig. 4.19 (c) & (g) and at 170° shown in fig. 4.19 (d) & (h).

Figure 4.20 shows the evaluation of the fan blade force variation due to boundary layer ingestion. The main trend around the circumference is similar to that presented in chapter 3. Within the preliminary fan assessment, the quantitative and qualitative prediction of fan blade forces is in good agreement with the uRANS-based data. The slightly increasing fan blade forces from ascending over constant to descending are reasonable due to the corresponding increase in orbit height. This trend is also well captured by SLC.

Stator performance

The question of the slightly greater decrease in mass flow of the descending fan remains unanswered. Figure 4.21 shows the diffusion factor of the stator vanes at 0° (a) and ±180° (b). It is clear that the vane loading is different between the two positions. In particular, the load increases at the mid and tip sections of the vane. Consequently, the slopes of all three fan stages are different. However, the increase in the diffusion factor is greater for the constant and descending fans. It can be seen that both the change in slope and the increase in the spanwise diffusion factor are captured by the methodology. However, the

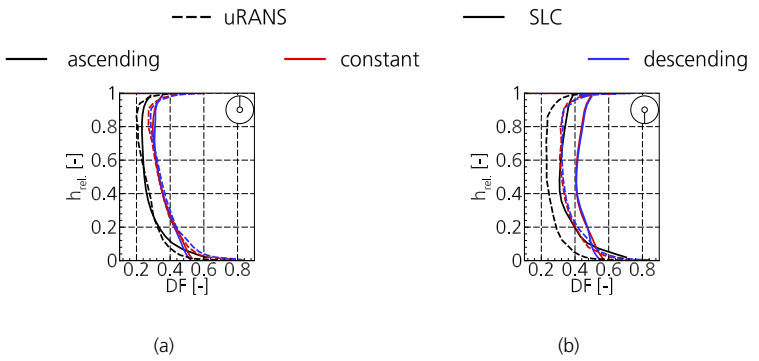

Figure 4.21.: Stator blade loading at position 0° (a) and ±180° (b).

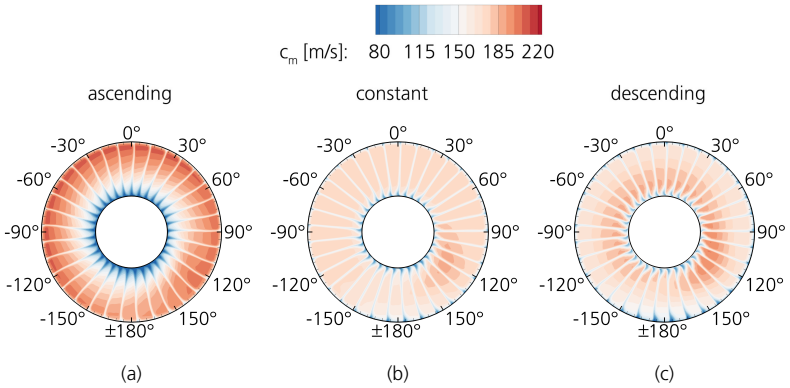

Figure 4.22.: Meridional velocity distribution at fan stage exit of the ascending (a), constant (b) and descending (c) fan..

vane loading is overestimated and the three-dimensional flow characteristics lead to lower values of the diffusion factor. The fan stages re-energize the boundary layer fluid in the tip region of the fan. As a result, low momentum fluid passes through the vane around the $\pm 180°$ position. As the rotor rotates, the BLI fluid is shifted slightly to the right. Figure 4.22 shows the meridional velocity downstream of the stator. As expected, the ascending fan shows the greatest spanwise variation in meridional velocity due to its design intent of radially increasing fan pressure ratio (see fig. 4.22 (a)). However, the circumferential variation downstream of the stator is less than the inlet velocity distribution. In contrast, the constant fan shows a more homogeneous velocity distribution in both the spanwise and circumferential directions, as shown in fig. 4.22 (b). As intended by the design, the increase in the fan pressure ratio in the tip region is lowest in the case of the descending fan stage. Therefore, the attenuation of the boundary layer distortion is less in this fan stage. This results in lower meridional velocities and higher blockage of the tip region at 180°. These conditions are shown in fig. 4.22 (c). In turn, these conditions lead to a greater reduction in the mass flow of the descending fan. The relative stagnation pressure ratio to the averaged stagnation pressure at the stator outlet is shown in fig. 4.23. As explained above, the design intent defines the relative stagnation pressure pattern downstream of the fan stage. As the descending fan stage adds less power to the boundary layer fluid, the circumferential variation of the stagnation pressure ratio is higher than for the other cases.

The distortion intensity $DI_{60°}$ downstream of the fans is 0.0199 (ascending) and 0.0192 (constant and descending) respectively. All fans are therefore capable of reducing the distortion. In terms of axial velocity non-uniformity, the constant fan appears advantageous compared to the ascending and descending fans. In addition, a greater variation in stagnation pressure is likely to lead to variations within the nozzle velocity distribution. Based on the findings of Kožulović (2010), these variations are likely to affect the propulsive efficiency and need to be carefully considered within the nozzle design.

Based on this section, the interim conclusion is that all fan stages are able to cope

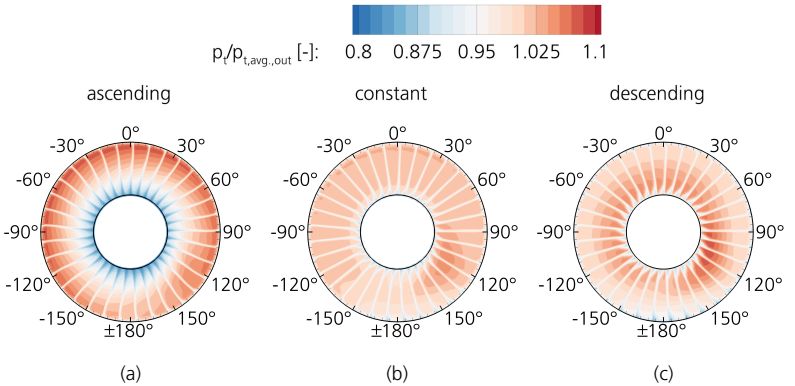

Figure 4.23.: Non-dimensional stagnation pressure at fan stage exit of the ascending (a), constant (b) and descending (c) fan.

with the distortion. Based on the reduction in rotor efficiency and the smaller shift of the averaged operating point compared to ADP, the ascending and constant fans appear to be advantageous for a distortion tolerant fan design. In contrast, the low momentum fluid entering the vane tip section within the descending fan stage leads to a greater reduction in mass flow and should be avoided. Furthermore, even if only rotor design features are of interest, the vane design should not be neglected as it can have a detrimental effect on the overall fan stage performance.

4.3. Exploration study - impact of meridional Mach number and tip speed on BLI performance

In this section a design space exploration in the design space of the meridional Mach number and the blade tip speed is addressed. The purpose of this design study is twofold: firstly, the design space exploration is performed to identify a beneficial parameter range within the aforementioned design space for a distortion tolerant fan design. Secondly, to demonstrate the efficient application of the design methodology over a large design space.

Subsection 4.1 shows that the amount of boundary layer fluid ingested affects the thrust related performance metrics. Increasing the amount of boundary layer fluid leads to a lower inlet momentum and therefore a lower thrust specific power consumption. Closely related to the lower inlet momentum is a reduction in the inflow Mach number. Therefore, it seems beneficial to reduce the meridional Mach number at the rotor inlet. The fan performance is expected to decrease as the meridional Mach number increases due to higher viscous losses. In addition, the meridional Mach number is expected to influence the flow redistribution. The other design parameter is the ISA corrected tip speed of the fan blade. For a given fan pressure ratio and thus work input, this parameter determines the required flow turning according to Euler's work equation eq. (2.1). Consequently, the blade geometry, i.e. the blade stagger angle, is driven by the selection of the blade tip speed.

4.3.1. Exploration study conception

The flow path of the fan stage is derived from the DLR UHBR fan stage. This fan stage is representative of a high bypass ratio turbofan engine and is extensively covered in the publications of Kaplan et al. (2006) and Schnell et al. (2009). Minor variations in the vane hub line are incorporated to improve vane loading. In this study, the fan pressure ratio is set to 1.3 at the ADP and the fan stage geometry is kept constant downstream of the AIP. Thus, the variation of the fan face meridional Mach number is achieved by varying the mass flow. In addition, the fan stage has 18 blades and 38 vanes. An axisymmetric inlet geometry is incorporated upstream of the fan stage. This geometry is adapted from Bräunling (2009) and varies as a function of the meridional Mach number. The reason for the variation is the similarity of the flow conditions upstream of the fan stage. According to the isentropic relation in eq. (4.4), the static pressure depends on the stagnation pressure and the Mach number.

$$p = p_t \cdot (1 + \frac{\kappa - 1}{2} Ma^2)^{(\kappa-1)/\kappa} \tag{4.4}$$

The Mach number is also correlated with the cross-sectional area and mass flow. As all fan stages are exposed to a similar stagnation pressure distortion pattern, the static pressure level determines the mass flow fraction of the distorted and undistorted part of the flow. As a comparable fraction between the distorted and undistorted flow is desired, Mach number similarity is required far upstream. Consequently, it is necessary to change the intake flow path upstream of the fan. However, this directly translates into differences in flow deceleration in this specific component. Figure 4.24 (a) shows the flow path of the fan stage with a meridional Mach number at the rotor inlet of 0.56 and a corrected blade tip speed of 280 m/s. The flow path upstream of the fan stage is divided into two sections: in the first section there is a straight duct followed by a flow decelerating inlet geometry with an axial length of approximately 0.6 fan diameters. The purpose of the straight duct is to decouple the inflow from the convex curvature of the casing. The design fan pressure ratio in the spanwise direction is shown in fig. 4.24 (b). As a consequence of the findings in the previous sections, the fan pressure ratio near the hub is increased to avoid challenging flow conditions due to low momentum fluid at the fan stage outlet. Between 10% and 70% span, the fan pressure ratio increases. This allows the work input to take advantage of higher blade speeds at higher spanwise blade sections. Above 70% span, the fan pressure ratio decreases slightly to attenuate the tip gap flow and associated losses. As mentioned above, the blade speed is directly related to the required flow turning and therefore to the blade geometry. Figure 4.25 illustrates the effect of tip speed on specific

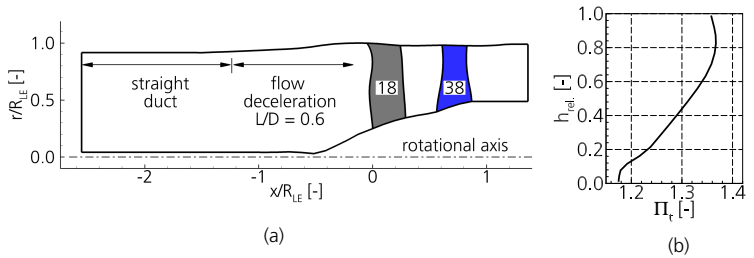

Figure 4.24.: Flow path adapted from the DLR UHBR fan stage.

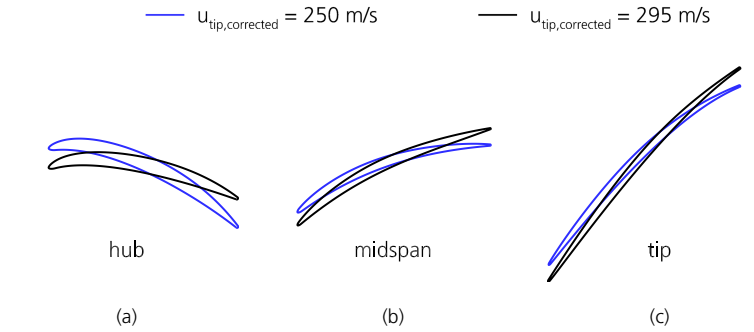

Figure 4.25.: Airfoils dependent on tip speed near the hub (a), at midspan (b) and in the tip section (c).

airfoils at different radial blade sections. The black airfoils are from a fan stage design with a higher blade speed than the blue airfoils. Therefore, the stagger angle is greater at all radial blade sections. In chapter 2 the effect of the blade geometry on the stage characteristic is introduced. The fan stage characteristic becomes steeper with increasing blade speed and increasing trailing edge metal angle. This translates into higher stagger angles and according to chapter 2 the slope of the characteristic is different. At ADP, the characteristics intersect while the off-design performance differs. Steeper characteristics result in lower fan pressure ratios near the choke and higher fan pressure ratios near the stability limit. Figure 4.26 shows the varying design parameters of the fan stages. As the fan pressure ratio is fixed, the work input is similar in all cases. Due to the changes in blade speed, the work coefficient decreases as the tip speed increases. The flow coefficient

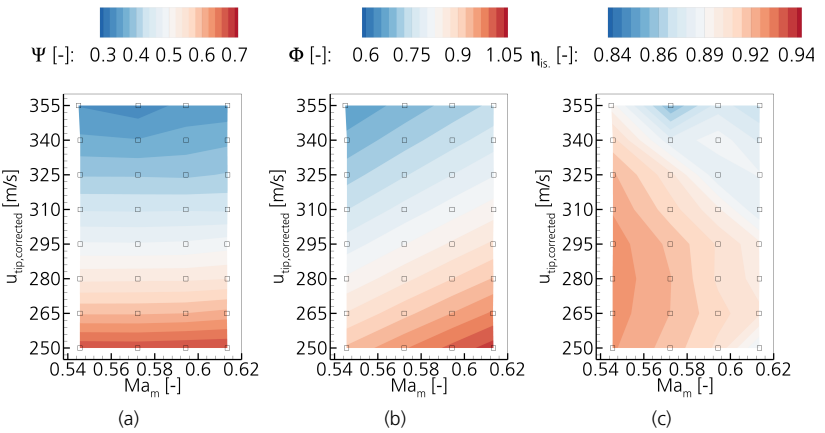

Figure 4.26.: Work coefficient (a), flow coefficient (b) and stage efficiency (c) of the specific fan stages at ADP.

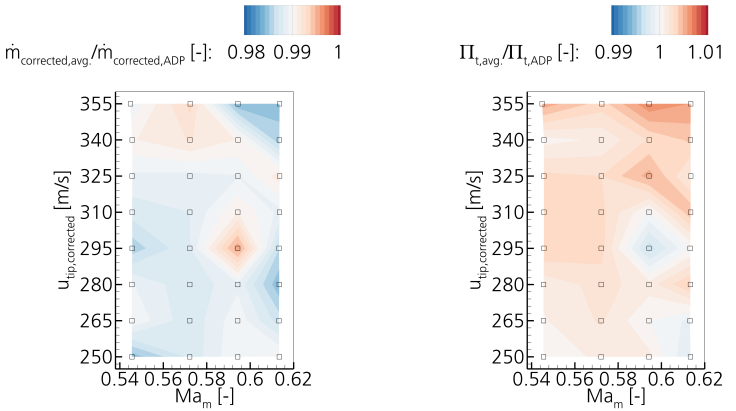

Figure 4.27.: Averaged operating point with respect to ADP conditions.

depends on the axial velocity and the blade speed. Therefore the flow coefficient decreases with increasing tip speed and decreasing meridional Mach number. Consequently, the flow coefficient increases from the upper left to the lower right of the parameter space. The fan stage efficiency shows the highest levels of efficiency at low meridional Mach numbers and moderate blade speeds. This metric decreases with increasing meridional Mach number due to increasing viscous losses within the fan stage. These losses are closely related to the fluid velocity and therefore to the meridional Mach number. The decrease in efficiency with increasing blade speed is related to increasing shock losses. As the blade speed increases, the relative Mach number and therefore the pre-shock Mach number increases, which is the main driver of shock losses.

4.3.2. Distortion tolerance of the specific designs

In this exploration study, all fan stages are exposed to the same stagnation pressure pattern, which is similar to the distortion applied in the previous section. Furthermore, the intake geometry is designed to maintain the same meridional Mach number far upstream of the fan stage at ADP. Therefore, the fraction of distorted and undistorted inflow remains the same over the parameter space. Consequently, the averaged corrected mass flow, normalised by the corrected mass flow at ADP, remains constant. Most of the fan stages show a decrease in corrected mass flow of about 1.2%. This is shown in the distribution in fig. 4.27 (a) and there is little variation between the designs. One outlier is the small decrease in the corrected mass flow of the design with a meridional Mach number of 0.59 and a corrected blade tip speed of 295 m/s. This design shows a tendency to operate close to choking conditions at high momentum inflow (0° position). Therefore, the mass flow increases slightly over a large part of the circumference, as does the averaged mass flow. Figure 4.27 (b) shows the relative increase in the stagnation pressure ratio of the averaged operating point with respect to ADP. There is a slight increase in the fan pressure ratio with increasing blade tip speed. As seen before, the change in the averaged operating point in terms of fan pressure ratio is small. So the undistorted part of the annulus mainly in-

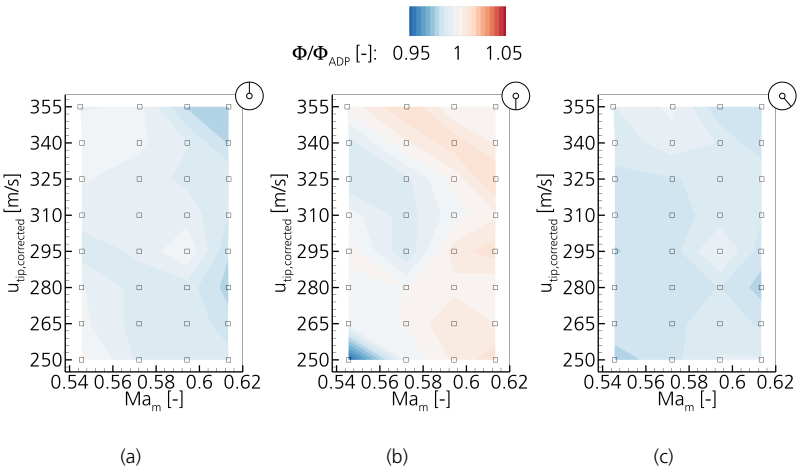

Figure 4.28.: Flow coefficient normalized by the ADP flow coefficient at 0° (a), ±180° (b) and 140° (c).

fluences the averaged operating point. This is consistent with the findings of the previous sections.

Flow redistribution and local operating points

Figure 4.28 shows the flow coefficient normalised to the ADP flow coefficient at 0° (undistorted inflow) (a), ±180° (middle of the distortion) (b) and 140° (counter-swirl) (c). The position outside and in the counter-swirl position show only small variations compared to the ADP conditions. In contrast, a dependence on the meridional Mach number can be seen in the middle of the distortion. The intake decelerates the flow while the flow redistribution tends to accelerate the flow. Furthermore, the intake geometry of the low meridional Mach number designs is required to decelerate the flow more. As the meridional Mach number increases, and with it the flow deceleration, the spanwise averaged axial velocity at the rotor inlet increases. The shape of the intake geometry and the intended flow deceleration thus affect the flow redistribution. This needs to be carefully considered during detailed design, but is beyond the scope of this preliminary design study. Figures 4.29 and 4.30 show flow conditions at 80% span at the rotor inlet. The relative Mach number distribution in 4.29 increases as intended from the lower left to the upper right of the design space. At the 0° position shown in (a) the Mach number level is similar to the ADP conditions. In the middle of the distortion, shown in fig. 4.29 (b), the Mach number level decreases due to the momentum deficit. Conversely, the Mach number level increases in the counter-swirl region as shown in fig. 4.29 (c). The corresponding incidence distribution in fig. 4.30 shows a dependence on both design parameters. While the 0° position in (a) is mainly unaffected by the distortion, the incidence is close to zero. In the middle of the distortion there is a positive incidence. The level of incidence decreases with increasing Mach number and increasing blade speed (see fig. 4.30 (b)). In the counter-swirl the positive incidence is slightly lower than in the middle of the distortion and decreases

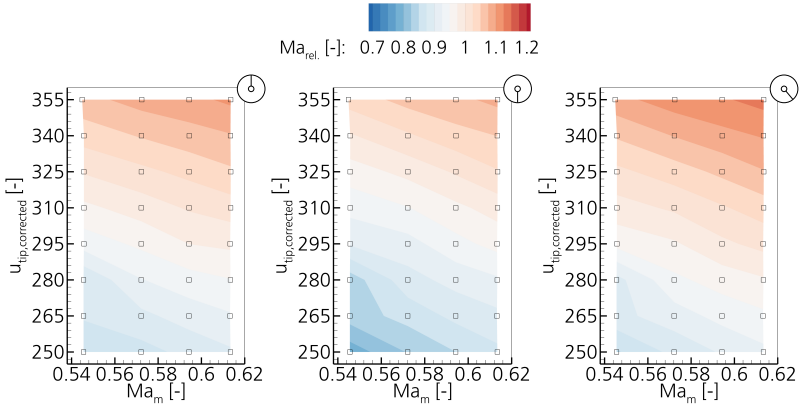

(a) (b) (c)

Figure 4.29.: Relative rotor inflow Mach number at 0° (a), ±180° (b) and 140° (c) at 80% span.

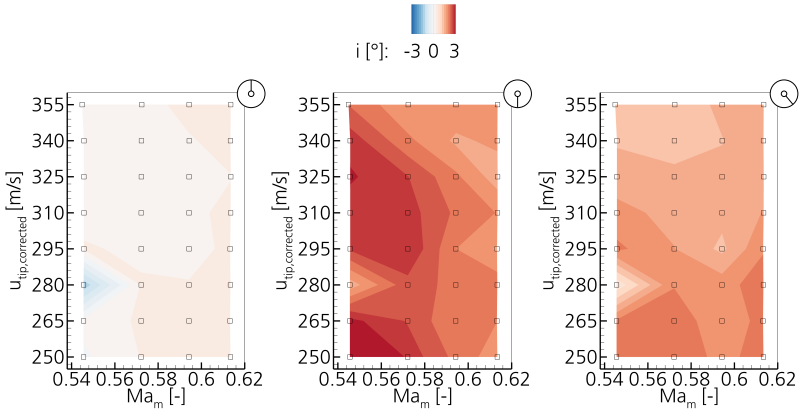

(a) (b) (c)

Figure 4.30.: Rotor incidence at 0° (a), ±180° (b) and 140° (c) at 80% span.

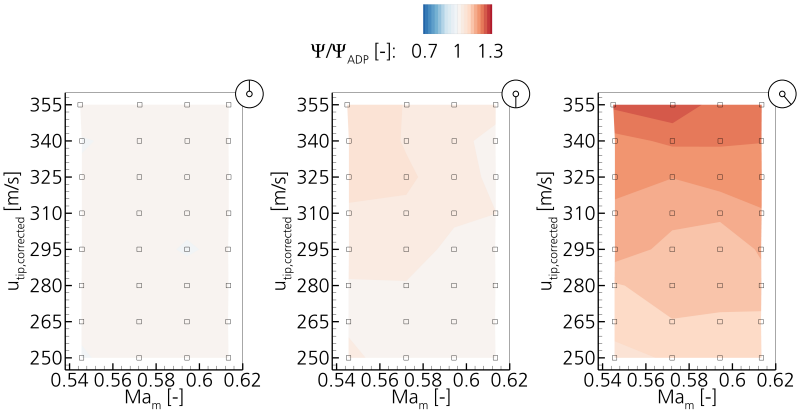

Figure 4.31.: Non-dimensional work coefficient at 0° (a), ±180° (b) and 140° (c).

slightly with increasing blade speed. These conditions are shown in fig. 4.30 (c).

At the rotor inlet, increasing Mach number levels combined with positive incidence are expected to amplify the tip gap flow and associated losses. Thus, as blade speed increases, the lower incidence level needs to be carefully traded against the increasing Mach number level. In addition to this trade-off, other aspects need to be considered: the operating range of a blade is expected to narrow as the tip speed increases. In addition, the variation of the blade pressure distribution along the blade operating range, which feeds the tip gap flow, has to be considered in the detailed design. Another important aspect of fan performance is the interaction of the tip gap flow with the transonic flow, which needs to be considered. It is likely to present more design challenges as the Mach number level increases and the tip gap flow interacts with the transonic flow in the upper part of the blade. As the circumferentially averaged approach is used for performance calculations, this is beyond the scope of the preliminary fan assessment. Nevertheless, the above topics need to be addressed during the detailed design of a distortion tolerant fan.

The impact of local inflow conditions on work input is shown in fig. 4.31. Figure 4.31 (a) shows that the work input at 0° is close to the ADP conditions throughout the parameter space. In contrast, the higher positive incidences at higher blade speeds, combined with the steeper characteristics, lead to higher work input in the middle of the distortion and in the counter-swirl region, as shown in fig. 4.31 (b) and (c). Consequently, the fan stages with higher blade speeds are expected to attenuate the distortion pattern further than the low blade speed fans. In terms of aeromechanical design, the blade force variation due to BLI is of interest. Figure 4.32 shows this variation at 0°, 180° and 140°. At the undistorted inflow shown in (a), the resulting fan blade force is similar to the ADP conditions. In the middle of the distortion, the fan blade forces show slightly increasing blade force levels at low meridional Mach numbers and increasing blade speed. The same

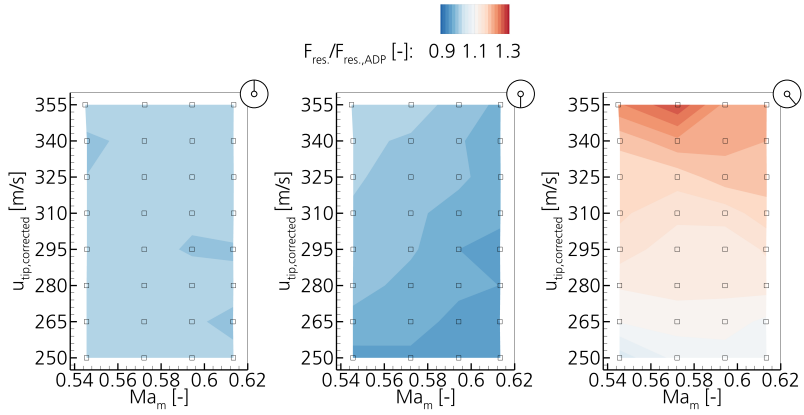

Figure 4.32.: Non-dimensional blade forces at 0° (a), ±180° (b) and 140° (c).

is true for the counter-swirl region shown in fig. 4.32 (c). There is a stronger dependence on blade speed. The relative blade force varies from 8% at the low blade speeds to 25% at the highest blade speeds. Note that the relative blade force minimum is in the same order of magnitude as the relative blade force peak. So the amplitude of the blade force is twice the values shown in fig. 4.32 (c). This is consistent with the circumferential blade force distribution shown in the previous section. According to the simplified consideration of blade stresses due to centrifugal forces presented in eq. (2.15), increasing blade speed would either require thicker blades or increase the stress level for a given fan blade.

An interim conclusion of this subsection is that the preliminary design parameters of meridional Mach number and tip speed have an impact on the design of a distortion tolerant fan. At lower meridional Mach numbers, the efficiency of the fan stage improves due to lower viscous losses at the ADP. In the middle of the distortion, there is a slightly higher work input at lower meridional Mach numbers. This is related to the flow redistribution in the upstream inlet. As the tip speed increases, the work input increases. Consequently, distortion attenuation is expected to improve at the expense of increasing blade forces, which are likely to increase dynamic stresses. These need to be traded against blade stresses due to centrifugal forces. The latter will result in increased mean blade stresses according to eq. (2.15) for a fixed blade cross-section.

4.4. Summary and design recommendations for embedded fan stages

This chapter examines the integration of embedded turbofan engines in the rear part of the fuselage. This integration scenario requires adjustments to the fan design and integration compared to conventional underwing mounted engines. Firstly, the intake design is expected to be highly three-dimensional to increase the amount of boundary layer fluid

ingested, as concluded in section 4.1. As the amount of boundary layer fluid ingested increases, the average Mach number at the engine inlet decreases, which is associated with higher efficiencies at undistorted inflow. Compared to future underwing fans, which are expected to have a fan pressure ratio of 1.3, the fan pressure ratio of distortion tolerant fans should be increased to 1.35 to 1.4. According to Lengyel-Kampmann (2016), the efficiency of the fan stage is expected to decrease slightly due to the increased fan pressure ratio at homogeneous inflow. The same applies to the efficiency of the thrust generation at homogeneous inflow, as the propulsive efficiency decreases. Contrary to the homogeneous inflow conditions, the thrust generation efficiency in the BLI flow may remain at a high level or even increase due to the low momentum inflow as discussed in section 4.1. Increasing the fan pressure ratio results in smaller engine dimensions and lower mass flow requirements. The latter limits the dimensions of the non-axisymmetric intake geometry and potentially simplifies engine integration. Smaller fan diameters are expected to result in less wetted area of the nacelle and a lighter engine in the rear of the fuselage. Both should improve engine integration. Another important aspect related to the fan pressure ratio is the thrust specific power consumption of the fan. As the inlet momentum decreases, so does this metric. In other words, lower jet velocities can be achieved even at higher fan pressure ratios due to the ingestion of low momentum fluid. Furthermore, for fan stages within the above pressure ratio range, the bypass nozzle area can be increased. This shifts the fan operating line and allows the operating point to be precisely located within the fan map.

Based on the studies of the spanwise fan pressure ratio, an ascending or constant distribution is recommended. The fan stage then attenuates the stagnation pressure distortion and increases the momentum of the boundary layer fluid. This results in less OGV tip corner separation, which is observed with the descending design. Nevertheless, the tip section of the blade should be unloaded in terms of work input and fan pressure ratio. The ascending fan pressure ratio showed a more pronounced loss generation in the counter-swirl region than the constant and descending designs. The associated loss generation in the tip region causes the majority of the BLI related losses (at least for a well performing vane row). This is consistent with the research presented in the literature review in chapter 2. Therefore, passive flow control devices, i.e. casing treatments or brush seals, which suppress the tip gap flow and the associated loss generation may be beneficial in the specific part of the annulus. The meridional Mach number and blade tip speed also have an impact on the distortion tolerance of a fan stage. At lower meridional Mach numbers, the efficiency of the fan stage improves due to lower viscous losses at the ADP. In the middle of the distortion there is a slightly higher work input at lower meridional Mach numbers. This is related to the flow redistribution in the upstream intake. As the tip speed increases, the work input increases. Consequently, the attenuation of the distortion is expected to improve at the expense of increasing blade forces. According to eq. (2.15), the mean blade stresses increase due to centrifugal forces for fixed blade thicknesses. The increasing blade forces and mean blade stresses are expected to have a detrimental effect on aeromechanical stability and need to be considered in the detailed design of a distortion tolerant fan. Table 4.3 summarises the design suggestions.

Table 4.3.: Design suggestion for embedded turbofan engines compared to under-the-wing-mounted engines.

parameter	suggestion	advantage	disadvantage
fan pressure ratio	increase fpr to ca. 1.35 to 1.40	decrease of: • fan diameter, engine mass and wetted area • thrust requirement potentially • mass flow increase of: • boundary layer fluid ingested • efficiency of thrust generation	at homogeneous inflow decreases: • fan efficiency • propulsive efficiency
bypass nozzle area	raise slightly	• shifts working lines within the fan map • increase mass flow at fixed fpr	at high fan pressure ratios the effect vanishes due to non-linear compressibility effects
spanwise fan pressure ratio	constant or ascending distribution	• distortion intensity decreases downstream of the fan • re-energizing BLI fluid improves OGV flow	• tip gap flow can be amplified • non-uniform velocity distribution in the nozzle could penalise propulsive efficiency
work input near the casing	unload the very tip section	tip gap flow and associated losses decrease	higher loading of the blade mid section
blade tip speed	raise slightly	• work input increases which is beneficial to attenuate the distortion • mean stresses expected to increase	increase of: • relative Mach number • blade forces

5. Aft-propulsor

This chapter deals with the design and assessment of a rear-integrated, electrically driven propulsor, which ingests the boundary layer of a fuselage around its entire circumference. The fan design study comprises conceptual design studies, preliminary design and detailed analysis of the fan stage to verify the preliminary design.

This chapter is structured as follows: firstly, the aircraft concept, the design objectives and the boundary conditions are presented. Secondly, favourable global design parameters as well as the design philosophy are identified during the conceptual design. Based on these results, the design of the aft fan is presented by considering a purely radial distortion. The aft fan is then subjected to a two-dimensional stagnation pressure distortion representative of the specific fan integration. Within this performance assessment, the preliminary fan assessment methodology is used and the results are verified with time-resolved, high-fidelity data. In a further step, the performance variation due to combined stagnation pressure and swirl distortion is assessed and compared to the performance with isolated stagnation pressure distortion. The newly developed methodology is then used to evaluate the fan stage at off-design conditions along the cruise speed line. Finally, the design objectives and results are discussed and design recommendations are given.

5.1. Aircraft and propulsion concept, design targets and inflow conditions

This subsection describes the aircraft and propulsion concept as well as the design objectives of the aft-propulsor. Figure 5.1 shows the aircraft and the hybrid-electric propulsion concept, consisting of under-wing engines and the electrically driven aft-propulsor. The aircraft is designed to provide an alternative for future short to medium range commercial passenger aircraft. A detailed analysis of the overall aircraft design is given in Silberhorn et al. (2020). The focus of this study is on the aft integrated propulsor as it is exposed to the boundary layer fluid.

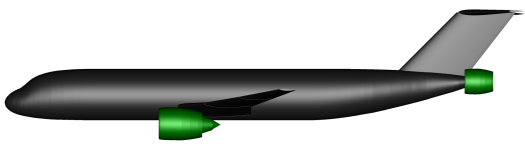

Figure 5.1.: Aircraft and propulsion unit concept taking advantage of hybridization and boundary layer ingestion. Adapted from Silberhorn et al. (2020).

Table 5.1.: Aft-fan requirements.

Altitude [m]	F_{net} [N]	$\dot{m}$ $\left[\frac{kg}{s}\right]$	$\dot{m}_{corrected}$ $\left[\frac{kg}{s}\right]$	Π_t [-]	$\eta_{is.}$ [-]
10363.2	8000	99.5	294.0	1.27	0.90

Table 5.1 summarises the specification for the aft-propulsor design. At cruise, the total aircraft drag is 40 kN and the fuselage drag is 20%. Therefore, the net thrust of the aft-propulsor is set at 8 kN. The thrust requirement translates into a mass flow of 99.5 kg/s and a fan pressure ratio of 1.27. At the given altitude of 10363.2 m the mass flow can be converted to a corrected mass flow of 294 kg/s. In addition, the isentropic efficiency of the fan stage is assumed to be greater than 90% within the aft fan specification.

A circumferentially averaged stagnation pressure distribution is used in the preliminary design of the rear propulsor. The dashed line in fig. 5.2 (a) represents a circumferentially averaged radial distortion derived from a flat plate boundary layer analysis provided by Silberhorn et al. (2020). The stagnation pressure distribution is characterised by a low momentum fluid near the hub and a stagnation pressure increase in the spanwise direction. The fluid entering the tip section is still at a lower stagnation pressure than the free flow, so the fan operates entirely within the circumferentially averaged boundary layer.

The realistic flow field entering the aft-propulsor has circumferential variations in stagnation pressure and swirl as visualised in fig. 5.2 (b) and (c). A distortion generator developed by Cinquegrana and Vitagliano (2021) provides these distortion patterns. Table 5.2 shows the parameters and corresponding parameter ranges of the distortion generator. The ge-

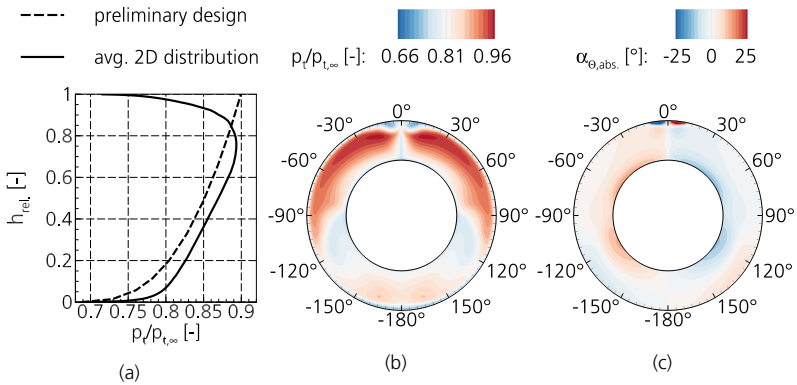

Figure 5.2.: Circumferentially averaged fuselage boundary layer (a), two-dimensional stagnation pressure distortion pattern (b) and corresponding swirl distortion in (c). Boundary layer profiles stemming form Silberhorn et al. (2020) and Cinquegrana and Vitagliano (2021), respectively.

Table 5.2.: Design space of the distortion generator according to Cinquegrana and Vitagliano (2021).

	x [m]	A [m²]	r_{hub} [m]	l_{intake} [m]	$\frac{\dot{m}}{A}$ [kg/s]	Ma_∞ [-]	Re_∞ $\cdot 10^7$[-]	AoA [°]
Minimum	35.8	1.31	0.425	0.50	55.19	0.74	2.32	0.0
Baseline	36.0	1.54	0.500	0.60	64.93	0.78	2.44	0.0
Maximum	37.2	1.77	0.575	0.85	68.00	0.82	2.56	2.0

ometry related parameters are the axial integration position of the propulsor x, the fan hub radius at the fan inlet r_{hub}, the fan face area A (can be converted to tip radius) and the intake length l_{intake}. Based on these parameters, the hub-to-tip-ratio varies between 0.492 and 0.665. In addition, the mass flux at the fan face $\dot{m}/A$, the flight Mach number Ma_∞, the Reynolds number Re_∞ and the angle of attack (AoA) represent the operating conditions of the fan and the aircraft.

The distortion generator is a Proper Orthogonal Decomposition based dataset derived from aircraft CFD calculations. The aircraft geometry includes a nacelle at the rear of the fuselage intersecting the vertical tail plane (VTP). NACA 1 profile series are used to derive the nacelle geometries. The fan stage modelling uses an actuator disc approach, where the fan behaviour is represented by stagnation pressure and stagnation temperature increases. The results from 80 individual aircraft and aft-fan configurations form the training database to calibrate the distortion generator.

Figure 5.2 (b) and (c) show a typical distortion pattern in this integration scenario. The distortion pattern shows flow features resulting from the fuselage and nacelle geometry. At 0° the VTP wake is present and leads to a decrease in the stagnation pressure. In addition, the intersection of the VTP and the nacelle causes separations that further reduce the stagnation pressure. There is also a high degree of co- and counter-swirl. The upper part of the fuselage shows only minor geometric variations upstream of the aft-propulsor integration. Therefore, the upper half of the annulus shows a boundary layer profile characterised by low momentum fluid close to the fuselage and increasing stagnation pressure in the spanwise direction. The dimensionless stagnation pressure reaches 96% of the free flow stagnation pressure. The lower part of the fuselage geometry is characterised by the upsweep of the fuselage leading to lower stagnation pressure values in the lower part of the stagnation pressure distribution in 5.2 (b). The minimum stagnation pressure is located at $\pm$116°. In addition, the upsweep of the fuselage induces a swirl that moves from $\pm$180° to 0° along the fuselage, except for the tip region at $\pm$116°. There the swirl is in the opposite direction, which is also associated with the upsweep of the fuselage. The inner surface of the nacelle causes a decrease in the stagnation pressure due to the tip wall boundary layer. The distortion intensity DI_{60} of the stagnation pressure pattern is 0.048.

5.2. Conceptual design considerations

This section deals with the conceptual design of the aft-propulsor, which is in line with the publication of Mennicken et al. (2020). As explained in chapter 1, the beneficial effect of BLI is due to the lower power required to re-energize the low momentum fluid

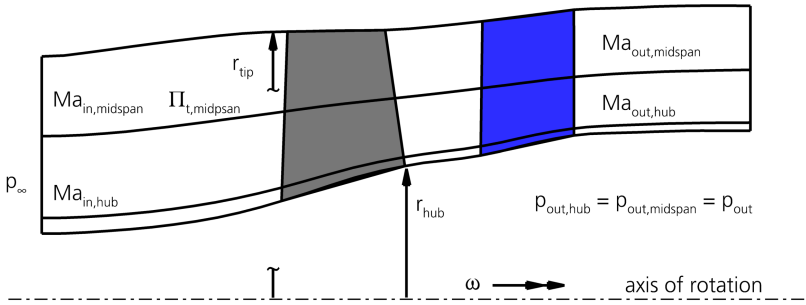

Figure 5.3.: Simplified flow path of the aft-propulsor. Two streamlines are visualized representing flow conditions near the hub and at midspan.

compared to high momentum fluid thrust generation. In this integration scenario, the low momentum fluid is concentrated near the hub of the aft propulsor (see 5.2 (a) and (b)). Consequently, the hub section of the aft fan is required to add more power to the fluid than the upper sections when aiming to homogenise the stagnation pressure profile. A fan stage that accomplishes this task will have a radially descending fan pressure ratio profile in the spanwise direction. In addition, distortion attenuation is expected to reduce velocity gradients downstream of the fan stage. According to Denton (1993), shear flow characterised by velocity gradients leads to entropy generation and adds losses to the flow. In addition, a more uniform velocity distribution in the nozzle is expected and beneficial to achieve high levels of propulsive efficiency (see Kožulović (2010)).

As the design philosophy of a descending radial fan pressure ratio is identified for this specific fan integration, three questions need to be answered during the conceptual design:

1. Which fan pressure ratio is required near the hub to obtain more homogeneous outflow?
2. Which design parameters influence the fan pressure ratio near the hub and how must they be chosen?
3. How do these design parameters influence the blade tip section?

These questions are individually discussed in the following subsections.

5.2.1. Fan pressure ratio near the hub for homogeneous outflow

This subsection answers the first question about the fan pressure ratio near the hub to obtain a more homogeneous outflow. The spanwise fan pressure ratio can be selected in the preliminary design and the decision on its radial distribution affects the flow conditions downstream of the fan. Figure 5.3 shows the simplified flow path of the aft-propulsor and two individual streamlines at midspan and near the hub. The inflow conditions are defined by the fuselage boundary layer. In addition, the midspan fan pressure ratio is set and directly translates into a stagnation pressure at the fan stage exit. Assuming a meridional Mach number level at the fan stage exit translates to a static pressure level. At the fan

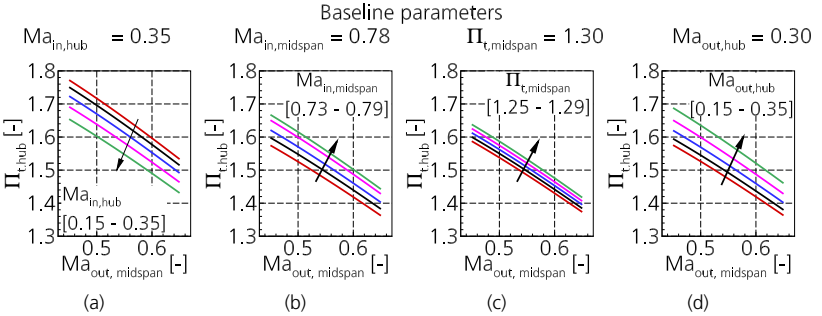

Figure 5.4.: Fan pressure ratio near the hub over Mach number levels at midspan downstream of the fan stage dependent on hub inflow Mach number (a), fan pressure ratio at midspan (b), inflow Mach number at midspan (c) and outlet Mach number near the hub (d).

stage exit, this static pressure is assumed to be constant in the radial direction, which in turn couples the hub and midspan streamlines. Then the fan pressure ratio near the hub that satisfies the above assumptions can be expressed by eq. (5.1). The hub fan pressure ratio

$$\Pi_{t,hub} = \frac{(1+\frac{\kappa-1}{2}\cdot Ma^2_{midspan,in})^{\kappa/(\kappa-1)}\cdot\Pi_{t,midspan}}{(1+\frac{\kappa-1}{2}\cdot Ma^2_{midspan,out})^{\kappa/(\kappa-1)}}\cdot\frac{(1+\frac{\kappa-1}{2}\cdot Ma^2_{hub,out})^{\kappa/(\kappa-1)}}{(1+\frac{\kappa-1}{2}\cdot Ma^2_{hub,in})^{\kappa/(\kappa-1)}} \tag{5.1}$$

is dependent on the Mach number levels near the hub and at midspan at the inlet and outlet, and the fan pressure ratio at midspan. Figure 5.4 shows the baseline values of each design parameter and the effect of these parameters on the pressure ratio of the hub fan as a function of the Mach number at the fan outlet. In general, the increase in the midspan Mach number level at the fan stage outlet results in a decrease in the required fan pressure ratio near the hub. The increase in the hub inlet Mach number associated with the higher momentum fluid in the boundary layer leads to a decrease in the fan pressure ratio near the hub (see fig. 5.4 (a)). However, increasing the momentum of the fluid at midspan, while having low momentum fluid near the hub, results in a higher fan pressure ratio requirement near the hub, as shown in fig. 5.4 (b). This is due to the increased static pressure downstream of the fan stage imposed by the midspan stream tube. The same explanation applies to the increase of fan pressure ratio at midspan. Consequently, the fan pressure ratio near the hub increases when the fluid receives a higher work input at midspan. Figure 5.4 (d) shows that aiming for higher Mach numbers near the hub leads to an increase in the hub fan pressure ratio. However, it is clear that the effect of the incoming boundary layer and the hub Mach number downstream of the stator have a greater influence on the hub fan pressure ratio than the midspan flow related parameters.

All in all, this sensitivity study clearly shows that the hub fan pressure ratio needs to be higher compared to the hub sections of conventional fan stages. Furthermore, the fan pressure ratio of the hub section can be intentionally reduced by specific design choices.

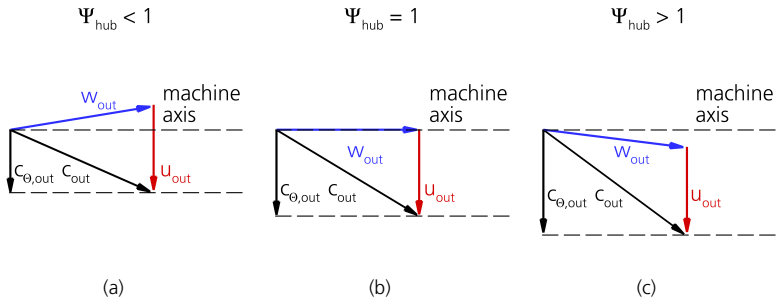

Figure 5.5.: Velocity triangles for Ψ_{hub}<1 (a), Ψ_{hub}=1 (b) and Ψ_{hub}>1 (c).

5.2.2. How to control the hub fan pressure ratio and the impact on the tip radius

In the previous subsection, the sensitivity study revealed challenging performance requirements for the fan hub. Therefore, an analysis is given to quantify the realistically achievable hub fan pressure ratio. This analysis is complemented by an estimate of the tip radius. As before, a simple model is set up for the sensitivity study, based on the definition of isentropic efficiency and the Euler work equation. The isentropic efficiency in eq. (5.2) relates the stagnation pressure ratio Π_t and the stagnation temperature ratio τ_t.

$$\eta_{is} = \frac{\Pi_t^{(\kappa-1)/\kappa} - 1}{\tau_t - 1} \tag{5.2}$$

Considering the work input for non-swirling inflow, given in eq. (2.1), and assuming adiabatic flow, leads to the similarity of work input and stagnation enthalpy rise presented in eq. (5.3).

$$a = u_{out} \cdot c_{\theta,abs.,out} = c_p \cdot (T_{t,out} - T_{t,in}) \tag{5.3}$$

In eq. (2.1) the work input depends on the circumferential velocity of the blade and the circumferential velocity $c_{\theta,abs.,out}$. Taking into account the axial inflow, the work coefficient given in eq. (2.3) can be expressed by the ratio of the aforementioned velocities and is given in eq. (5.4).

$$\Psi_{hub} = \frac{c_{\theta,abs.,out}}{u_{out}} \tag{5.4}$$

Figure 5.5 visualises the influence of Ψ_{hub} on the velocity triangles at the rotor outlet. The velocity triangle in fig. 5.5 (a) has a Ψ_{hub}<1 and the circumferential velocity $w_{\theta,out}$ is in the opposite direction to the blade rotation. This results in the lowest flow turning and therefore the lowest work input of the three cases. The case of Ψ_{hub} equal to one leads to a vanishing circumferential velocity $w_{\theta,out}$ as can be seen in fig. 5.5 (b), the flow turning increases and so does the fan pressure ratio. The velocity triangle in fig. 5.5 (c) shows the highest flow turning. All the circumferential velocity components are oriented in the same direction, which is associated with a Ψ_{hub} value greater than one, and the fan pressure ratio increases.

The combination of eq. (5.2) and eq. (5.3), taking into account eq. (5.4), gives the formula for the fan pressure ratio near the hub. A comprehensive derivation of eq. (5.5) is

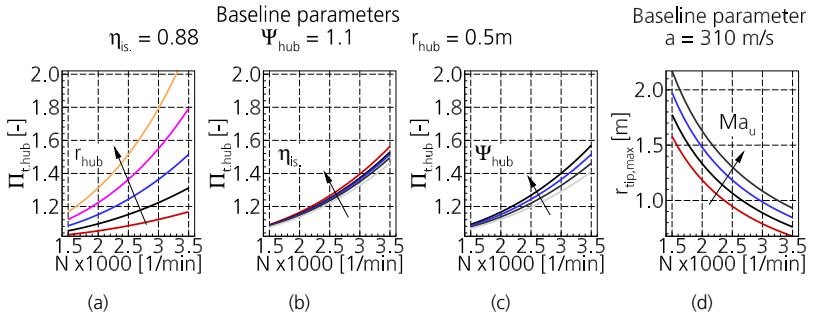

Figure 5.6.: Achievable fan pressure ratio near the hub with respect to hub radii variations (a), isentropic efficiency variations (b) and the velocity traingle shape (c). The tip radius estimation based on the blade tip Mach number is given in (d).

given in appendix A.7.1.

$$\Pi_{t,hub} = (\eta_{is} \cdot \frac{\Psi_{hub} \cdot (\frac{N \cdot \pi \cdot r_{hub,out}}{30})^2}{c_p \cdot T_{t,in}} + 1)^{\frac{\kappa}{\kappa-1}} \tag{5.5}$$

Equation 5.5 shows the dependence of the fan pressure ratio near the hub on the isentropic efficiency $\eta_{is.}$, the mechanical shaft speed N, the work input Ψ_{hub} and the hub radius at the fan rotor outlet $r_{hub,out}$. The mechanical shaft speed is rarely used in the aerodynamic analysis of turbomachinery flows. Typically, the corrected shaft speed is considered to achieve Mach similarity. However, in hybrid-electric propulsion units, the mechanical shaft speed is of interest because the performance of the electric motor depends on the mechanical shaft speed and is mainly independent of the ambient conditions. Further discussions on this topic can be found in the publications of Mennicken et al. (2022) or Vratny and Hornung (2018).

The fan pressure ratio near the hub is plotted against the mechanical shaft speed in fig. 5.6. In general, increasing the mechanical shaft speed leads to an increase in the fan pressure ratio. The most influential parameter to raise the fan pressure ratio is the hub radius, as can be clearly seen in fig. 5.6 (a). Increasing the hub radius results in increased blade speeds and a higher work input is achieved. In addition, increasing the hub radius allows the integration of an electric motor. The effect of the isentropic efficiency of the hub flow as well as the variation of the outflow velocity triangles is smaller, as shown by the narrow band in fig. 5.6 (b) and (c).

As a direct coupling of the electric motor and the fan stage is intended, the selection of the mechanical shaft speed must allow a good operating behaviour of both components. In contrast to the beneficial effect of increasing shaft speed on the hub flow, the mechanical shaft speed must be carefully balanced with respect to the tip flow. High blade speeds lead to high inflow Mach numbers and therefore the pre-shock Mach number is likely to increase and the associated shock losses are also likely to increase. Figure 5.6 (d) shows the resulting tip radius for different levels of tip Mach number. As the shaft speed increases, the specific tip Mach numbers are obtained at smaller tip radii.

Table 5.3.: Aft-fan design characteristics deduced from conceptual design.

N $[1/min]$	$r_{hub,out}$ [m]	httr [-]	D_{Fan} [m]	$u_{tip,corrected}$ [m/s]	Ψ_{hub} [-]	$p_{out,hub}/p_{out,midspan}$ [-]
2500	0.63	0.61	1.79	253.4	0.96	0.96

The power requirement of the electric motor is directly related to the torque of the electric motor, taking into account the shaft speed. In general, for a given power requirement, the electric motor torque increases as the shaft speed decreases and vice versa. In addition, it is easier to achieve a high electric motor torque as the electric motor diameter increases. Therefore, an increasing hub diameter is advantageous for direct coupled electrically driven fans.

5.3. Aft-Fan performance at design conditions - radial stagnation pressure distortion

This subsection deals with the design of the aft fan and the aerodynamic performance of the ADP. The results of the conceptual design study of section 5.2 are the basis for the two and three dimensional design of the fan stage. The design takes into account a radial stagnation pressure distortion introduced in section 5.1 and shown in fig. 5.2. Table 5.3 lists the specific design choices for the aft-propulsor design. As mentioned in the previous sections, the mechanical shaft speed of the rotor and the hub radius of the rotor trailing edge are important measures to achieve a high fan pressure ratio near the hub, which is required to attenuate the stagnation pressure distortion. Therefore, the fan shaft speed (which is automatically the electric motor shaft speed for a direct coupled drive train) is set at 2500 rpm and the hub radius at the rotor outlet is 0.63 m, which is relatively high compared to conventional fans. For the corrected mass flow and boundary layer profile, the hub-to-tip ratio and fan diameter are set to 0.61 and 1.79 m respectively. Consequently, the corrected blade tip speed is 253.4 m/s. Within the conceptual design, the work coefficient Ψ_{hub} is used to characterise the rotor outlet velocity triangle. The specific design has

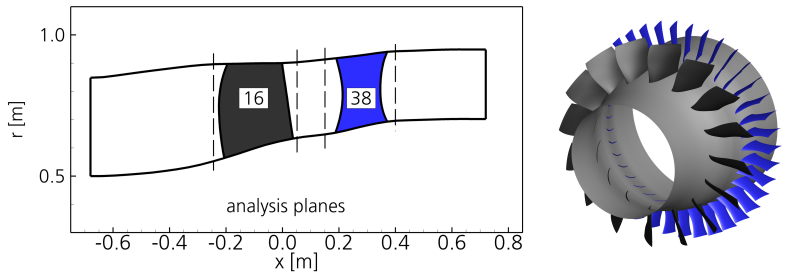

Figure 5.7.: Flow path, blade and vane count as well as analysis planes in (a). Full annulus propulsor (b). Adapted from Mennicken et al. (2022).

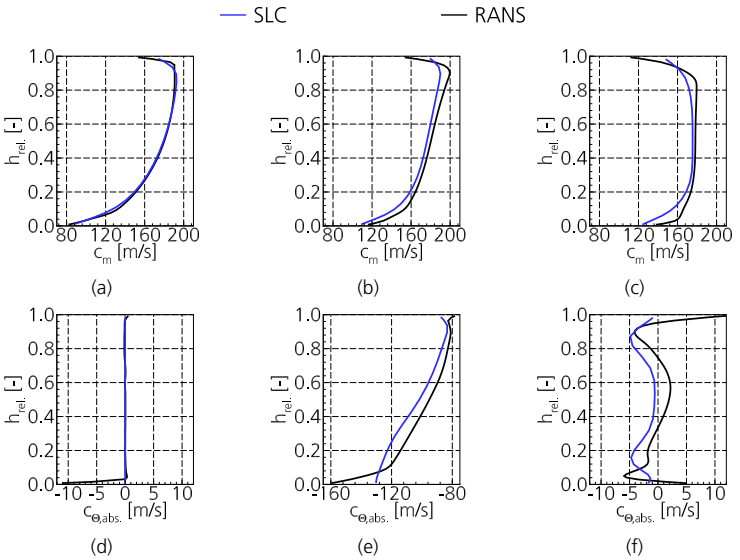

Figure 5.8.: Meridional and circumferential velocity at rotor inlet (a) and (d), rotor outlet (b) and (e) as well as at stator outlet (c) and (f).

a value of 0.96. At the rotor hub, the flow turning results in a velocity triangle where the velocity in the relative frame of reference is almost aligned with the axial direction. Figure 5.7 (a) shows the flow path of the aft fan, which consists of 16 blades and 38 vanes. The three-dimensional geometry is visualised in fig. 5.7 (b). The aft fan is designed using SLC and the associated airfoil database. As introduced in section 3.1.1, the SLC approach allows the seamless coupling of three-dimensional CFD calculations used to verify the fan performance.

Figure 5.8 shows the velocity distribution through the fan stage obtained from SLC and RANS. At the rotor inlet, the stagnation pressure profile translates directly into a low meridional velocity near the hub. This can be seen in fig. 5.8 (a) by the low meridional velocity levels in the lower 40% span. The design of the aft fan takes into account a non-swirling inflow. As intended, the hub section of the fan stage re-energises the boundary layer fluid. As a result, the velocity gradient through the fan stage decreases, as shown by the less steep meridional velocity profile in fig. 5.8 (b) compared to (a). Nevertheless, the difficult flow conditions near the fan root lead to fluid migration towards the midspan in the RANS calculations. This accounts for the very high magnitude of the circumferential velocity near the hub in fig. 5.8 (e). In addition, the spanwise distribution shows a lower magnitude of the circumferential velocity in the SLC, which is associated with a lower work input. Downstream of the fan, the meridional velocity distribution is characterised by low velocity gradients. In addition, the flow downstream of the fan stage is essentially free of swirl. The swirl angle is in the range of $\pm 2°$ in the lower 5% range, below 4° above 90% range and between 5-90% range between -1.5° and 0.7°. The flow conditions down-

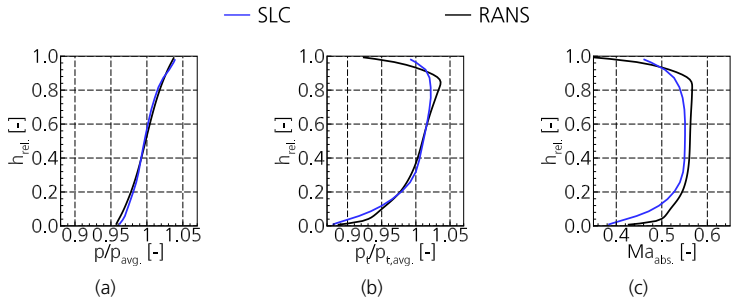

Figure 5.9.: Flow conditions downstream of the fan stage.

stream of the fan stage are complemented by the dimensionless static and stagnation pressures and the Mach number distribution shown in fig. 5.9. In the conceptual design, the static pressure is assumed to be homogeneous over the entire span, which directly translates into an axial outflow. As can be seen from fig. 5.9 (a), the static pressure near the hub is only 96% of the static pressure at midspan, driven by the residual swirl at the stator outlet (see fig. 5.8 (f)). This results in a lower fan pressure ratio requirement near the hub. The fan stage also reduces stagnation pressure distortion. The fuselage boundary layer shows a non-dimensional stagnation pressure variation of 20% with respect to the free stream stagnation pressure (see fig. 5.2). The high work input near the hub leads to a more homogeneous stagnation pressure distribution downstream of the fan stage and the spanwise variation of the stagnation pressure is about 13.7% as shown in fig. 5.9 (b). Corresponding to the homogeneous meridional velocity, a nearly constant Mach number of 0.56 is achieved over a wide portion of the span, as shown in fig. 5.9 (c). The Mach number distributions near the hub and casing show lower Mach numbers but remain above 0.36. In line with the explanations in section 5.1, these flow conditions are expected to be beneficial for the flow downstream of the fan.

Figure 5.10 shows the fan blade and vane performance data. The spanwise fan pressure distribution in fig. 5.10 clearly shows the design intent of a high fan pressure ratio near the hub. Below 5% span, the aforementioned three-dimensional fan root flow leads to an increase in fan pressure ratio as shown in fig. 5.10 (a). The blade loading increases significantly and the isentropic efficiency also shows an increase (see fig. 5.10 (b) and (c)). Therefore, this part of the spanwise distribution has to be treated carefully, as it is likely that the postprocessing routine will reach its limits due to the strong crossflow (see section 3.2). The upper part of the blade shows that the design philosophy of a descending fan pressure ratio distribution is well achieved. In addition, the figure shows a slightly lower fan pressure ratio in RANS than in SLC over a large part of the span. This is closely related to the higher efficiencies in SLC (see fig. 5.10 (c)) in the upper part of the blade. Therefore, the tip flow related loss mechanisms are not fully captured by SLC and a higher fan pressure ratio is provided in the SLC design to match the RANS specification data.

The blade is properly loaded over a wide portion of the span, resulting in DF<0.5 and 1-DH<0.3. As the fan pressure ratio decreases and with it the flow turning, the blade loading decreases in the spanwise direction. However, the trends and shape of the blade

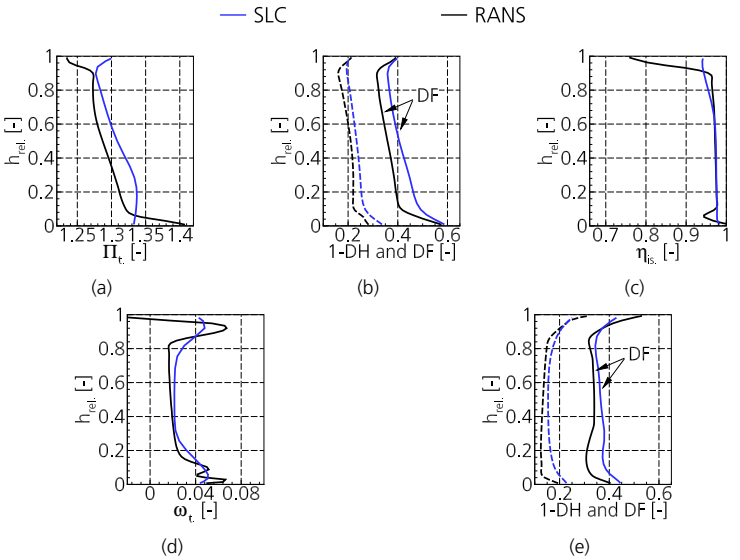

Figure 5.10.: Spanwise rotor performance in terms of fan pressure ratio (a), blade loading (b) and rotor isentropic efficiency (c). Spanwise vane losses in (d) and vane loading in (e).

load distributions are well captured by the SLC-based approach. The vane performance is assessed by considering the loss coefficient ω_t and the vane loading. The losses are well predicted over a large part of the vane. As already discussed, the flow is difficult to predict within the endwall boundary layers as well as the wake of the rotor tip gap. In these regions, SLC only considers simplified models. Therefore, the loss prediction below 10% and above 80% span differs between the two approaches. In addition, the blade loading prediction is in good agreement between the two approaches. The highest vane loading is obtained in the tip region. The flow path shows a slightly increasing casing radius in this particular region and no contraction is predicted. Therefore, the flow deceleration is high. In addition, the vane receives inflow from the upper part of the rotor blade. There, the fluid comes out of the tip gap and creates a more challenging flow condition within the vane.

Table 5.4.: Aerodynamic design point of the aft-propulsor.

	$\dot{m}$ [kg/s]	$\dot{m}_{corrected}$ [kg/s]	$Ma_{m,in}$ [-]	Π_t [-]	$\eta_{is.}$ [-]	SM [%]
Specification	99.5	294.0	-	1.27	>0.90	-
SLC	99.43	293.22	0.546	1.2926	0.936	12.9
RANS	99.28	291.69	0.543	1.2749	0.919	17.4

Table 5.4 summarises the aft fan specification and the results of the preliminary design. As discussed above, the SLC aft fan design required a slightly higher fan pressure ratio to meet the specification data. The specified minimum fan stage efficiency of 0.9 is exceeded by approximately 1.9% during fan stage design. Another important measure for fan stages is the margin to the stability limit. According to eq. (2.12), the stability margin is 12.9% and 17.4% from the SLC- and RANS-based assessment. The SLC-based figure is smaller, mainly due to the smaller corrected mass flow at the stability limit. As mentioned in the previous sections, the stability limit is reached when the stagnation-to-static characteristic peaks. Figure 5.11 (a) shows the comparison of the SLC- and RANS-based characteristics. It can clearly be seen that the fan pressure ratio is higher in SLC over the whole range of the fan map. The difference is due to lower predicted losses in SLC. However, the corrected mass flow related range of stable operating conditions is slightly lower in SLC than in RANS. Apart from these differences, the width of the fan map is well captured during preliminary design. Figure 5.11 (b) shows the fan map at cruise in terms of fan pressure ratio over corrected mass flow. The isentropic efficiency contour is also shown and the black square marks the aerodynamic design point which is well within the high efficiency region. The operating range of the electric motor is limited by the maximum torque shown by the solid grey line and the maximum power shown by the dashed grey line. The limits of the electric motor directly limit the operation of the fan. Consequently, the fan operates below both lines at cruising speed. It should be noted that the fan map is only valid for cruise conditions. On the one hand, varying ambient conditions will change the boundary layer properties and therefore the fan characteristics. On the other hand, the power requirement of the fan changes when cruise conditions change. Therefore,

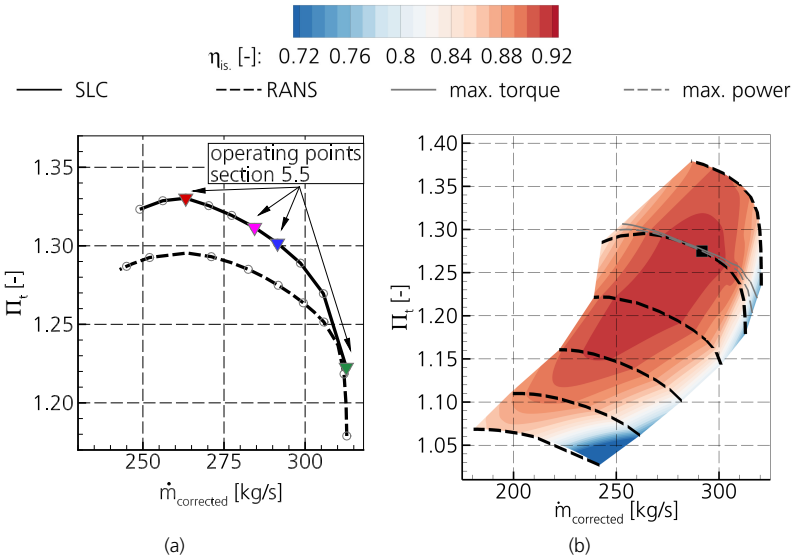

Figure 5.11.: SLC and RANS-based design speedlines in (a) and fan map for cruise operating conditions in (b).

the operating limits of the fan, which result from the operability of the electric motor, shift within the fan map. A comprehensive analysis of the above effects can be found in Mennicken et al. (2022). There, low altitude and low Mach number operation is examined.

5.4. Aft-Fan operation in realistic, two-dimensional fuselage boundary layer

In this section, the aft-fan design is subjected to a realistic two-dimensional fuselage boundary layer consisting of a stagnation pressure and a swirl distortion (see fig. 5.2 (b) and (c)). As the individual effect on fan performance is of interest, the analysis is split into two parts. Firstly, the isolated effect of stagnation pressure distortion is investigated. At this stage, the SLC-based assessment is used to identify the main changes in the operation of the aft fan. In addition, the results are verified by time-resolved calculations. Secondly, the effect of swirl distortion is analysed and compared to the fan performance in isolated stagnation pressure distortion.

5.4.1. Fan performance in stagnation pressure distortion

This subsection considers the assessment of fan performance under stagnation pressure distortion. On the one hand, the preliminary assessment is carried out taking advantage of the newly developed methodology. On the other hand, a time-resolved calculation is used as a verification dataset to show the applicability of the new methodology to a highly two-dimensional and therefore challenging boundary layer pattern. Figure 5.12 (a) shows the two-dimensional distribution of the non-dimensional stagnation pressure, while fig. 5.12 (b) shows the circumferential distribution at three spanwise positions. At 0° the VTP causes a decrease in the stagnation pressure. The upper part of the annulus shows high stagnation pressure values, while the fuselage upsweep causes a low stagnation pressure at ±90°. This results in a number of local maxima and minima. At this point it is helpful to recapitulate the idea of the preliminary fan assessment in the distorted inflow. When calculating

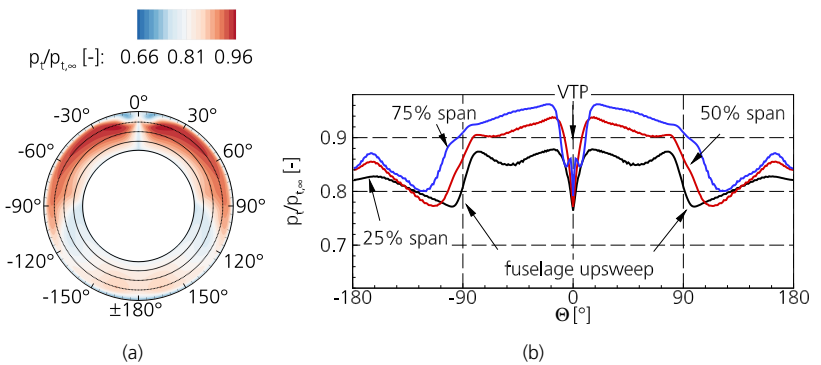

Figure 5.12.: Non-dimensional stagnation pressure distortion (a) and circumferential distribution at three spanwise positions (b) at intake inlet.

the flow redistribution, the maxima and minima of the stagnation pressure distribution need to be considered, as this is where the static pressure is expected to have its extremes. In addition, the stagnation pressure distortion is axisymmetric. Therefore, considering the stagnation pressure distribution shown in fig. 5.12 leads to the following selection: the stagnation pressure distribution is symmetric about the vertical axis. Thus only half of the annulus needs to be considered in the flow redistribution calculation. The ±180° position is included because it is a local maximum. At the -116° position, the upsweep of the fuselage causes the stagnation pressure minimum. At -48° the stagnation pressure is high and close to its maximum. In addition, the VTP wake causes a significant decrease in the stagnation pressure, which has a small circumferential extent compared to the rotor pitch. Depending on the circumferential position within the wake, the inflow boundary conditions for the SLC change and so does the flow field required to obtain the static pressure distribution at the AIP. To avoid this dependency, a 20° segment is circumferentially averaged to provide the inflow boundary condition for the SLC approach.

Flow redistribution

Figure 5.13 shows the dimensionless static pressure distribution at the aerodynamic interface plane. In general, the preliminary fan assessment methodology captures its main variations both qualitatively and quantitatively. The dimensionless SLC-based static pressure pattern is axisymmetric by definition, as can be seen in fig. 5.13 (a). In contrast, the time-resolved calculation in fig. 5.13 (b) shows a slightly asymmetric pressure field. Nevertheless, the main features within the static pressure distributions are similar. The higher static pressure at ±180° is captured as well as the local static pressure minimum at ±116°, which is slightly more smeared in the SLC-based analysis. The maximum static pressure in the upper part of the annulus between ±90° is also captured, but the static pressure is slightly higher in SLC than in the time-resolved calculation. Even in the VTP region the static pressure field is well captured within the flow redistribution calculation. The static pressure drop is slightly over predicted at 0°. Nevertheless, the general agreement of the dimensionless static pressure distributions is well achieved.

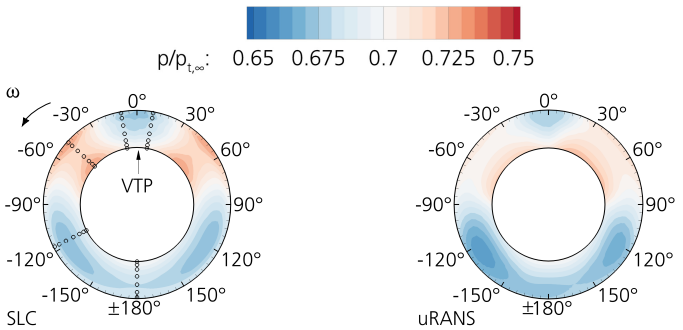

Figure 5.13.: Non-dimensional static pressure pattern at AIP.

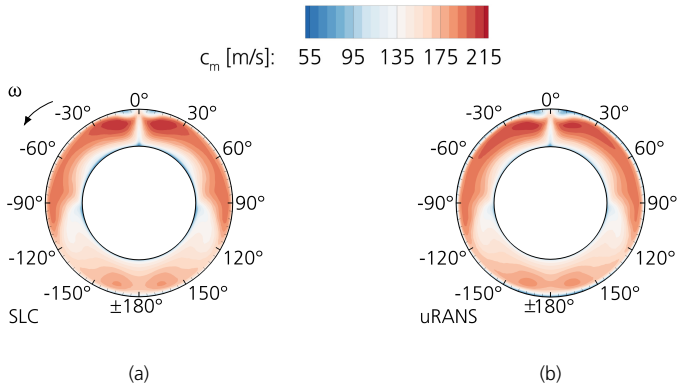

Figure 5.14.: Meridional velocity distribution at AIP.

As the meridional velocity distribution depends on the stagnation and static pressure distribution, the agreement between the preliminary assessment and the time-resolved data is expected, and the meridional velocity pattern is mainly driven by the stagnation pressure distribution. Figure 5.14 shows the two-dimensional meridional velocity at AIP and underlines the applicability of the preliminary design and assessment methodology to this integration scenario. The same applies to the circumferential velocity distribution in the absolute reference frame. This velocity component is closely related to the static pressure distribution and therefore the good agreement between fig. 5.15 (a) and (b) is expected, taking into account fig. 5.13.

The swirl pattern shows a complex distribution of co-swirl (blue) and counter-swirl (red) parts around the annulus. In the ±180° position the swirl is counterbalanced and leads to no swirl. The static pressure minimum is at ±116°. Consequently, between -116° and

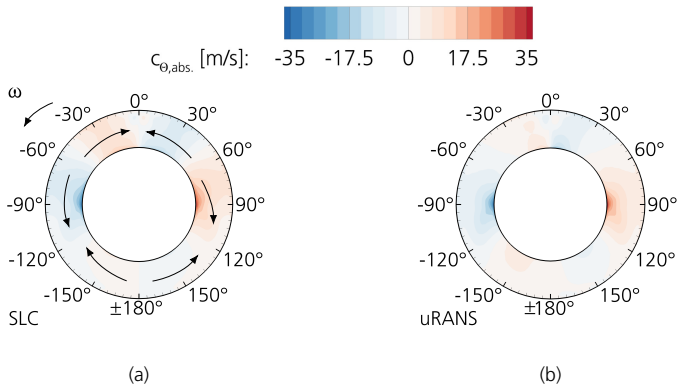

Figure 5.15.: Circumferential velocity distribution at AIP.

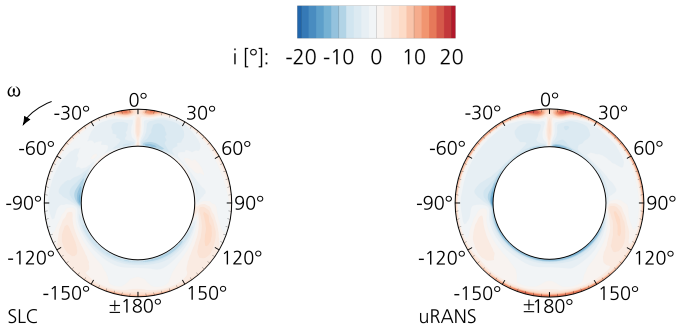

(a) (b)

Figure 5.16.: Incidence distribution at AIP.

±180° the static pressure field leads to counter-swirl, while between 116° and ±180° there is co-swirl. As mentioned above, the uRANS data show lower static pressure levels between -150° and -180°. There, the counter-swirl amplifies the tip gap flow leading to the lower static pressure level at midspan. In the opposite position, where the co-swirl is present, the tip gap flow is less severe and the static pressure level is higher. The same mechanism is already observed for the other integration scenario in section 3.3.4. From the ±116° to the ±48° position, the swirl distribution changes from co-swirl to counter-swirl and vice versa. The highest swirl velocities are in the hub region at ±90°. As the static pressure maximum is at ±48°, the swirl distribution changes from counter- to co-swirl and vice versa. The same explanation applies to the asymmetry along the vertical axis between ±30° and ±60°. The differences in static pressure are therefore closely linked to the variation in swirl at the rotor inlet. In the middle of the VTP wake, the swirl levels out and there is no swirl. The velocity distribution translates directly into the rotor incidence shown in fig. 5.16. First of all, the incidence patterns of both approaches match very well. Furthermore, the main incidence variations are associated with the meridional velocity distribution. Positive incidence is present at the ±116° position and negative incidence is located in the upper part of the annulus. The strong stagnation pressure decrease in the tip region of the VTP wake leads to a high positive incidence. Nevertheless, there are circumferential positions where the incidence distribution is dominated by the circumferential velocity. This is the case in the hub region at 10° and -90°. This feature is also captured by both approaches.

In this study, the incidence distribution is calculated with respect to the ADP. For ADP, the purely radial stagnation pressure distribution is derived from a simplified turbulent flat plate approach, while the two-dimensional distribution is derived from the distortion generator. The design condition shows a lower stagnation pressure near the hub than the higher fidelity distortion pattern. In addition, the stagnation point at the rotor leading edge is shifted to the pressure side below 5% span at ADP. This results in a highly negative incidence around the entire circumference, but the positioning of the stagnation point is better than the incidence distribution suggests.

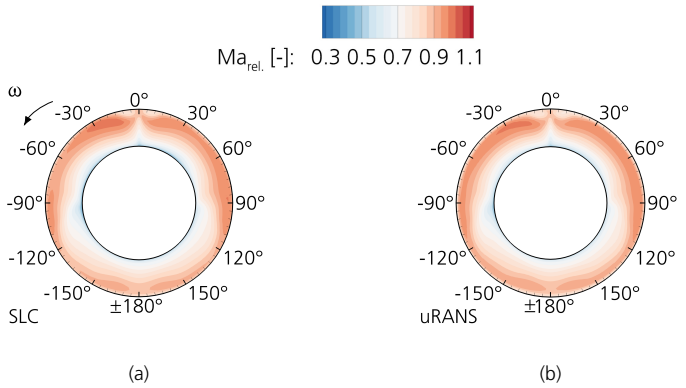

Figure 5.17.: Relative Mach number distribution at AIP. SLC (a) and uRANS (b).

Finally, the Mach number distribution in the relative frame of reference is shown in fig. 5.17. As already seen in the incidence distribution, the Mach number pattern depends mainly on the stagnation pressure and therefore on the meridional velocity pattern. Thus the upper part of the annulus shows high Mach numbers in the tip region, while the lower part of the annulus shows lower Mach numbers there. The peak Mach number occurs in the tip region at -20°. Close to the hub there are more homogeneous conditions around the circumference. This is associated with less variation in stagnation pressure around the circumference.

Averaged operating point

The fan performance of the fan stage in the presence of the two-dimensional stagnation pressure distortion is given in terms of (corrected) mass flow, fan pressure ratio and fan efficiency in table 5.5. The required mass flow is well matched by the preliminary fan assessment and the higher fidelity assessment using time-resolved calculations. The variation in the corrected mass flow is mainly due to a different stagnation pressure at the global inlet. Furthermore, the fan pressure ratio is higher in both calculations, as already observed and discussed in section 5.3. As presented in the previous chapters, the SLC-based prediction of isentropic efficiency is challenging as the loss prediction as well as the unsteady

Table 5.5.: Fan stage performance data stemming from the preliminary and time-resolved assessment of the aft-propulsor in stagnation pressure distortion.

	$\dot{m}$ [kg/s]	$\dot{m}_{corrected}$ [kg/s]	Π_t [-]	$\eta_{is.}$ [-]
Specification	99.5	294.0	1.27	>0.90
SLC	99.45	290.62	1.2958	0.9126
uRANS	100.35	293.14	1.2748	0.9074

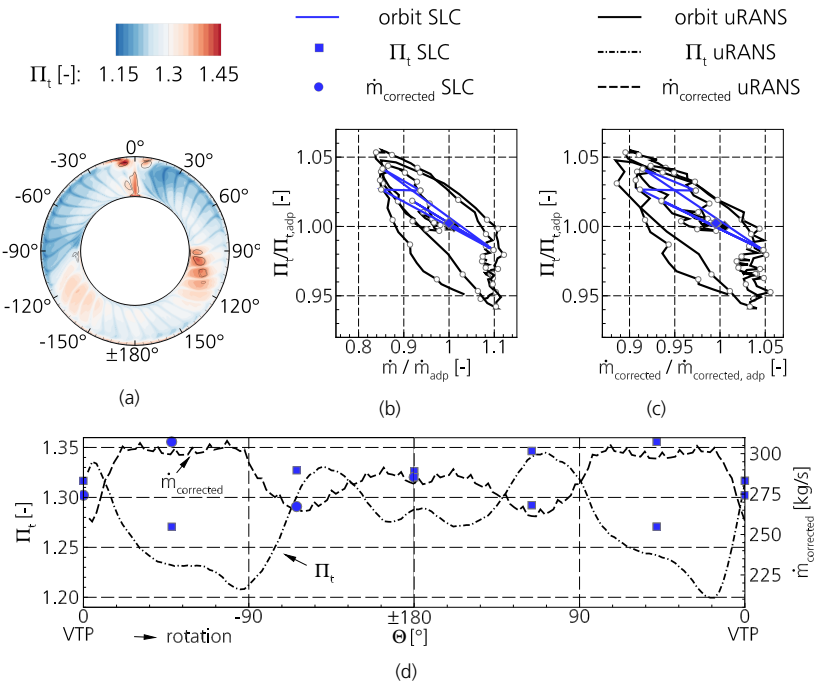

Figure 5.18.: Fan pressure ratio of the fan stage projected on the global inlet (a), local fan performance in terms of relative fan pressure ratio over non-dimensional mass flow (b) and corrected mass flow (c). Local fan performance around the circumference (d).

work input are not covered in SLC. This fact can be seen in the predicted fan efficiency drop of 2.34% in SLC. In contrast, the efficiency decrease due to stagnation pressure distortion in the time-resolved calculation is 1.16%. For the sake of completeness, the averaged fan efficiency within the SLC approach is included but not further investigated in this section. Figure 5.18 (a) shows the fan pressure ratio of the fan stage projected onto the fan inlet plane. As these results include the rotor and stator data, the vane wakes are present in the fan pressure ratio pattern. In addition, the positions are marked by the solid lines where the post-processing of local performance metrics within the time-averaged flow field is questionable. For example, such regions are near the VTP wake and near the hub at the 90° position. There the rotor inlet swirl is high and the particle path within the time-averaged calculation is not the same as the particle path in the time-resolved calculation. Therefore, any data that takes into account the relationships between different flow positions needs to be treated with caution at these circumferential positions. In particular, fan efficiency, which is sensitive to input variables, can be misleading. However, the flow kinematics, as well as quantities that are insensitive to input quantities, such as the fan pressure ratio, can be analysed and give an indication of the performance variations

around the circumference. The fan orbits are dimensionless with respect to ADP and show the local relative fan pressure ratio over the dimensionless mass flow (a) and the corrected mass flow (b), respectively. Compared to the orbit in the previous sections, the fan orbit in this integration scenario is much more complex. Therefore fig. 5.18 (d) shows the circumferential distribution of the fan pressure ratio derived from the orbits. It is mainly the low momentum fluid that causes the low (corrected) mass flow and high fan pressure ratio, while the high momentum fluid is associated with high (corrected) mass flow and low fan pressure ratio. The preliminary fan assessment covers the orbit in terms of relative mass flow. The mass flow variation is 25% between minimum and maximum. In addition, the SLC-based orbit consists of only a few passages around the circumference. Therefore, not every increase or decrease in the fan pressure ratio is covered. However, the main variation of this quantity between the high and low momentum fluid is accounted for. As seen in the other integration scenario, the time-resolved results show a slightly higher fan pressure ratio peak. The corrected mass flow differs due to the different consideration of the specific passage. Within the SLC-based approach, a specific infinitesimally thick circumferential extent is accounted for, whereas the passage extent of the time resolved result is approximately 9.5°. As the circumferential extent increases, the averaged stagnation pressure is likely to increase and therefore the corrected mass flow by definition will decrease. Nevertheless, the predicted local operating conditions of the aft-propulsor agree well with the higher fidelity data. A detailed analysis of the flow field and performance data is therefore carried out.

Rotor flow field and performance

The two-dimensional distributions discussed earlier show the correct calculation of flow redistribution within the intake. The spanwise distributions of the specific circumferential positions are given in fig. A.5, which can be found in appendix A.7. Slight differences appear in the passages not included in the flow redistribution calculation. The velocity components at the rotor outlet are shown in fig. 5.19. The circumferential variation due to BLI is well captured. However, there are differences between the two approaches for the meridional and circumferential velocity components. This is already observed for the other integration scenario and is related to the simplified modelling of the secondary flow, the simplified modelling of the stream tube contraction and the neglect of unsteady effects.

The circumferential velocity component is related to the specific work input. As the trends between the different circumferential positions are captured, it is expected that the differences in fan performance will also be well predicted. Figure 5.7 shows the positioning of the analysis planes and the stator inlet plane is slightly downstream of the rotor outlet. The good prediction of the stator incidence is therefore expected by judging the outflow velocity triangles and is visualised in fig. 5.19 (c) and (f). The trends around the circumference are well covered and the agreement at $\pm 180°$ and $\pm 48°$ between the two approaches is very good. Within the low momentum fluid, the differences between the two approaches are greater, mainly due to a difference in the static pressure rise. This in turn leads to differences in flow kinematics.

Figure 5.19 shows the rotor performance in terms of fan pressure ratio and blade loading. At the $\pm 180°$ position, the fan pressure ratio is overpredicted by the SLC approach compared to uRANS. In section 5.3 the designs are presented and still at ADP the SLC predicted fan pressure ratio was higher to meet the fan specification in RANS. So it is rea-

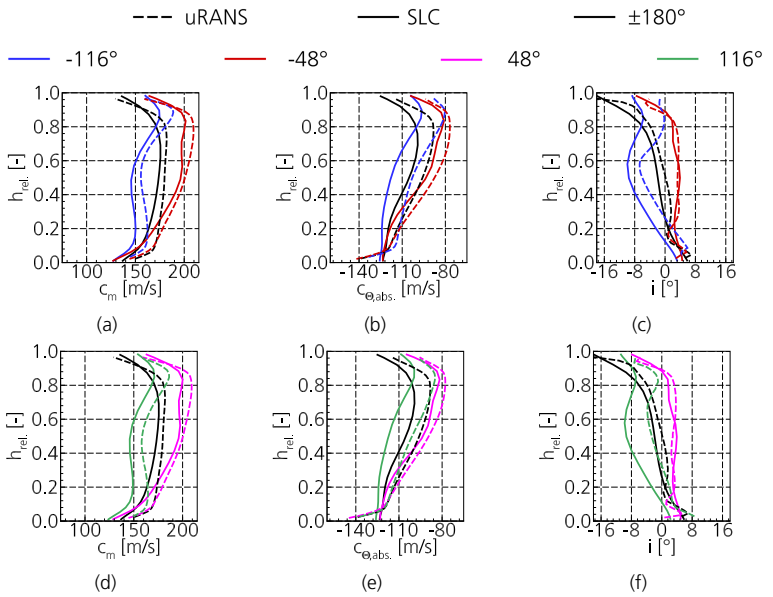

Figure 5.19.: Spanwise velocity components at rotor outlet in terms of meridional velocity (a) and (d), circumferential velocity (b) and (e). Stator incidence in (c) and (f).

sonable to expect the differences to appear in this position as well. The same applies to the blade loading at ±180°. Within the low momentum fluid, the fan pressure ratio distributions narrow between the two approaches. Thus, the lower work input in the SLC already identified for the other integration scenario in chapter 3 and chapter 4 remains for the rear integrated fuselage propulsor. At ±48°, the SLC predicted spanwise stagnation pressure rise is higher than in uRANS, except for the blade section at 70% span (see fig. 5.20 (a) and (d)). In addition, fig. 5.20 (b) and (e) show a higher full circumferential blade loading at SLC, mainly due to the differences in DeHaller number. There are therefore differences in terms of flow deceleration between the two approaches. In addition, the effect of the twist direction is visible in fig. 5.19. In particular, the counter-swirl leads to a higher flow deceleration and therefore a higher blade loading at +116°. Nevertheless, the newly developed methodology is able to capture the fan performance trends around the annulus, which is important in the preliminary design stage.

Rotor performance can also be translated into fan blade forces. Figure 5.21 shows the absolute and relative blade forces around the circumference. The absolute value of the resulting force shows a small offset over the entire circumference in fig. 5.21 (a). The blade force of the time-resolved data shows an increase in blade force as the blade passes through the VTP wake. In the high momentum fluid positions the blade force decreases and shows its minima, while in the low momentum fluid the blade force increases. It can be observed that the positions where the negative incidence peaks are found show the local minima of the blade force.

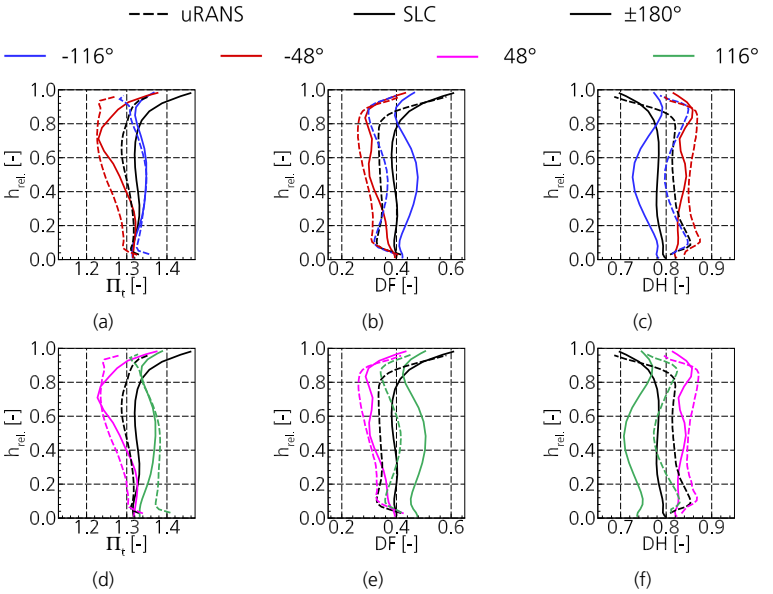

Figure 5.20.: Spanwise fan pressure ratio (a) and (d) and rotor blade loading in terms of the diffusion factor (b) and (e) and deHaller number (c) and (f).

The main trend is also covered within the preliminary fan assessment, but the maxima and minima are slightly shifted. In the SLC, the maximum fan blade is outside the minimum momentum fluid. So between 180° and 0° the fan blade forces are well matched. In

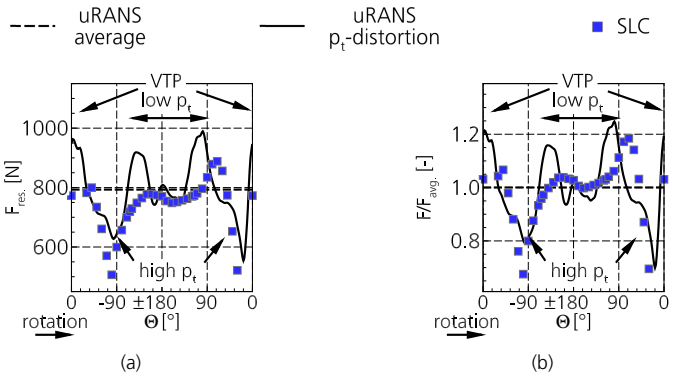

Figure 5.21.: Absolute and relative fan blade forces around the circumference.

particular, the relative fan blade force is well covered (see fig. 5.21 (b)). The peak at -135° is not captured by the SLC approach. As on the right side of the annulus, the peak on the left side of the annulus would be expected to be shifted more towards the high momentum. This is where the airfoil is operating in choked conditions and even the uRANS data shows a low blade force at -90°.

However, the increase in blade force within the low momentum fluid cannot be fully explained by the author and requires further investigation which is beyond the scope of this study. These variations are expected to be related to unsteady effects within the flow, which can quickly change the blade pressure distribution. In turn, the integrated blade force may show greater variations than those calculated using steady-state approaches. The unsteady effects on the blade forces are presented by Mailach (2010), Sanders et al. (2001) and Sanders and Fleeter (2001) and have already been briefly discussed in chapter 2. Nevertheless, the fan blade force variation is well covered and can be used in the preliminary fan design.

Stator flow field and performance

The stator performance is briefly discussed. The flow field downstream of the stator is shown in fig. 5.22. The SLC-based flow field is able to cover the circumferential variations in terms of meridional and circumferential velocities. The remaining swirl is low down-

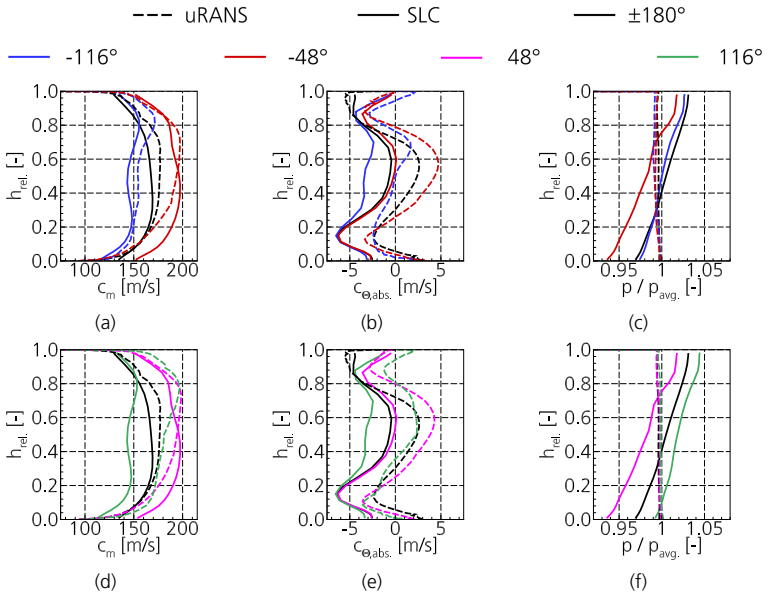

Figure 5.22.: Spanwise velocity components at stator outlet in terms of meridional velocity (a) and (d), circumferential velocity (b) and (e). Non-dimensional static pressure in (c) and (f).

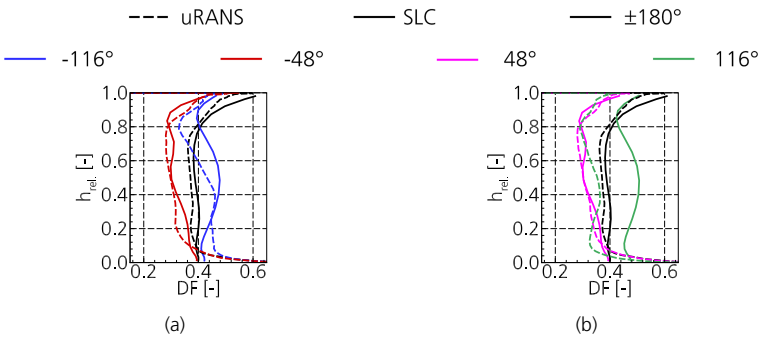

Figure 5.23.: Spanwise stator loading.

stream of the fan as shown in fig. 5.22 (b) and (e). As already seen at the rotor outlet, the 116° position shows the biggest difference between SLC and uRANS in terms of meridional velocity. This is due to the overpredicted pressure rise at this position as shown in fig. 5.22 (f). Another important aspect of the static pressure field downstream of the fan is the slightly different slope of the static pressure field. While the uRANS data are basically constant along the span, the SLC data show a radially increasing static pressure. As already seen and explained in chapter 3, the static pressure field can vary around the annulus when calculating the local fan performance due to the flow field coupling at the AIP. This difference needs to be carefully considered in the preliminary assessment of distortion tolerant fans. Figure 5.23 shows the corresponding vane loading. In general, the circumferential trends are captured by SLC with the exception of the 116° position. Furthermore, the shape of the spanwise variations is in good agreement with the uRANS data. However, the vane loading levels are slightly shifted.

5.4.2. Fan performance in stagnation pressure and swirl distortion

The previous subsection discusses fan performance within the isolated stagnation pressure distortion caused by the fuselage boundary layer. However, the BLI related inflow conditions also have a swirl distortion which is shown in fig. 5.24. The swirl distortion induces a deflection of the flow from the lower part of the fuselage to the upper part. As mentioned in section 5.1, co-swirl occurs mainly between 0° and 180° except for the tip region of the lower part of the annulus half and vice versa. Only the tip region between ±120° and ±180° shows the opposite swirl direction.

Swirl distortions are likely to have a detrimental effect on fan performance, which is addressed in SAE (2022). Castillo Pardo and Hall (2022) show that their aft-fan performance is sensitive to swirl, which significantly changes the blade loading and fan efficiency. Therefore, the aft-fan design is subjected to the swirl distortion to study the swirl-related differences within the flow field compared to the stagnation pressure-only operating conditions. Only time-resolved calculations are considered in this subsection.

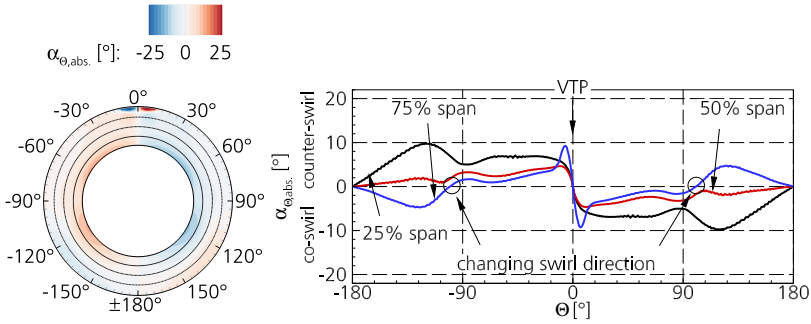

Figure 5.24.: Two-dimensional swirl angle distribution in (a) and at three different spanwise positions around the circumference in (b) at domain inlet.

Fan stage performance

Table 5.6 summarises the key fan performance metrics for both operating points and the specified performance requirements. As can be seen, both time-resolved operating points show slightly higher mass flows, while the corrected mass flow is slightly lower. This difference is due to the difference between the assumed stagnation pressure profile at specification and the two-dimensional stagnation pressure profile. The fan pressure ratio is slightly higher than specified and remains largely constant when the swirl distortion is superimposed. In addition, the fan efficiencies are above specification at both operating points. Swirl distortion causes an additional 0.35% reduction in fan efficiency. Figure 5.25 shows the fan pressure ratio projected onto the global inlet in (a) considering the combined distortion. The positions where the post-processing approach is questionable are marked by the black lines within the contour plot. Compared to the isolated stagnation pressure distortion, the regions near the VTP (0°) and between 90° and 120° increase. This is where the streamline tracking within the time-averaged flow field differs from the realistic time-resolved particle trajectory. Therefore, performance data relating inflow and outflow velocities should be treated with caution. Nevertheless, the time-averaged flow field data remain valid in terms of flow kinematics, and the performance data give an indication of the variations in fan performance. The orbit data shown in fig. 5.25 (b) and (c) show essentially the same complex behaviour and can be translated into a circumferential

Table 5.6.: Aft-fan performance in stagnation pressure distortion and a combined stagnation pressure and swirl distortion.

	$\dot{m}$ [kg/s]	$\dot{m}_{corrected}$ [kg/s]	Π_t [-]	$\eta_{is.}$ [-]
Specification	99.5	294.0	1.27	>0.90
pt-dist	100.35	293.14	1.2748	0.9074
pt- and swirl	100.07	292.36	1.2735	0.9039

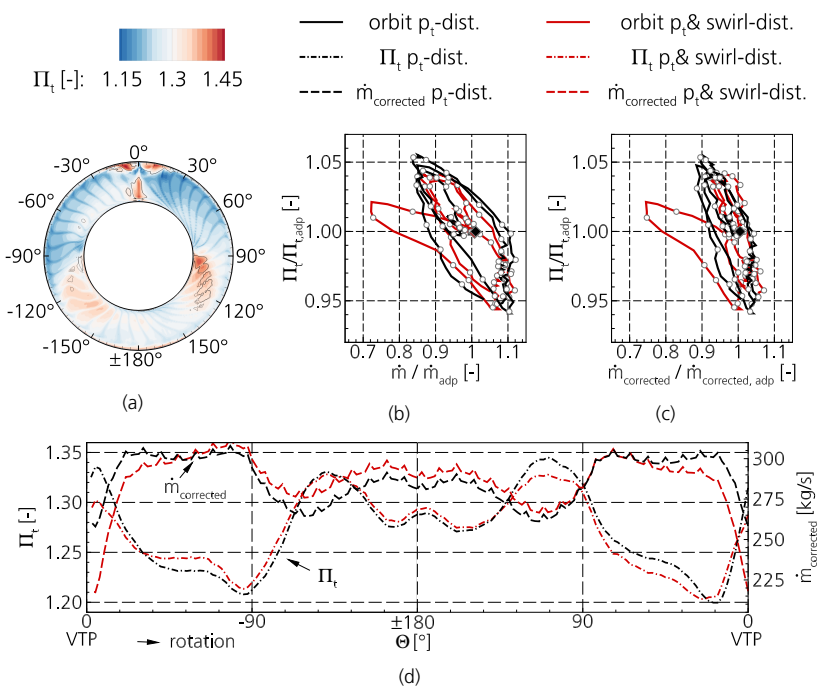

Figure 5.25.: Fan pressure ratio of the fan stage projected on the global inlet (a), local fan performance in terms of relative fan pressure ratio over non-dimensional mass flow (b) and corrected mass flow (c). Local fan performance around the circumference (d).

fan pressure ratio distribution shown in fig. 5.25 (d). The main difference in the superimposition of swirl distortion occurs close to the VTP. There is a large amount of swirling flow, resulting in lower axial velocities. This in turn reduces the relative mass flow. However, the VTP region covers only a small portion of the circumference and therefore this variation has only a small effect on the averaged mass flow as shown above.

Flow redistribution and rotor performance

In the following subsection, the changes in flow redistribution and local fan performance due to swirl distortion are discussed. Flow redistribution occurs upstream of the fan stage and affects the flow field at the AIP. Figure 5.26 shows the dimensionless static pressure distribution and shows that the static pressure pattern has similar characteristics for the isolated and combined distortions. There are only minor changes in the static pressure levels. Thus, the high static pressure regime remains in the combined distortion in the upper half of the annulus as well as the low static pressure regime in the lower half of the annulus. Furthermore, the effect of the VTP on the static pressure field at 0° is clearly visible. However, the high static pressure in the upper right part shows a slightly higher

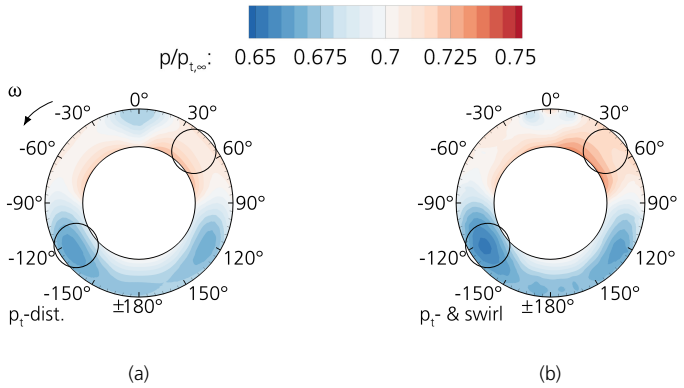

Figure 5.26.: Non-dimensional static pressure distribution stemming from the stagnation pressure distortion (a) and the combined stagnation pressure and swirl distortion (b) at AIP.

static pressure in fig. 5.26 (b) than in (a) and the low static pressure in the lower left part shows a slightly lower static pressure in fig. 5.26 (b) than in (a). These effects are caused by the swirl distortion, while the static pressure pattern is mainly driven by the stagnation pressure distortion.

Figure 5.27 shows the corresponding swirl distribution at the AIP. The upstream intake aims at decelerating the flow and attenuates the swirl velocity from the intake to the rotor inlet. In the vicinity of the VTP wake (at 0°) up to ±30°, the swirl entering the intake is mainly preserved as it flows towards the AIP. Between ±30° and ±75°, the swirl is slightly attenuated due to the flow redistribution, which causes an opposite swirl direction in the

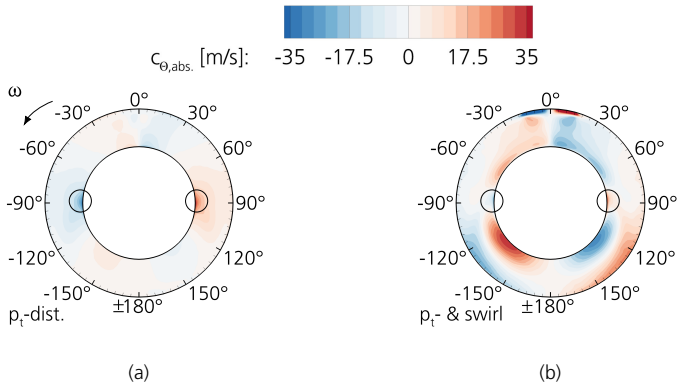

Figure 5.27.: Circumferential velocity distribution stemming from the stagnation pressure distortion (a) and the combined stagnation pressure and swirl distortion (b).

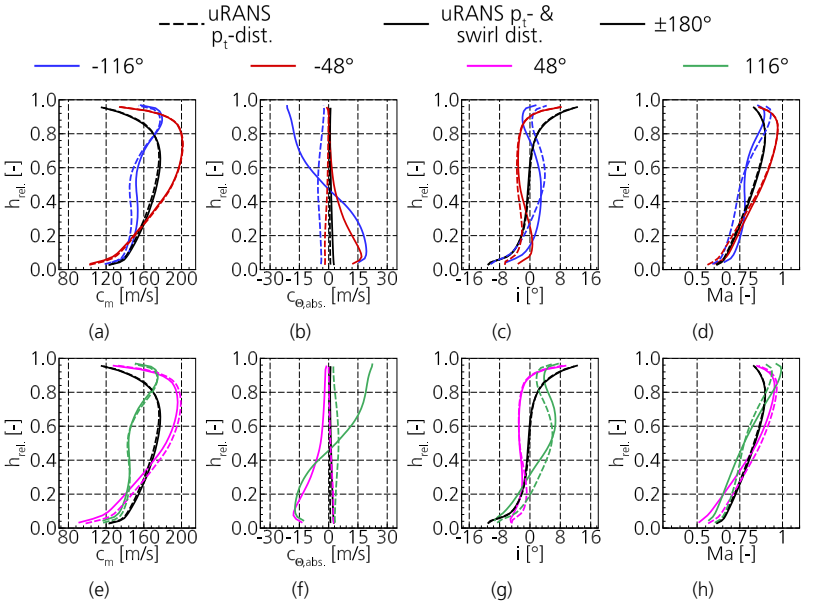

Figure 5.28.: Spanwise distribution of the meridional velocity (a) and (e), circumferential velocity (b) and (f), rotor incidence (c) and (g) as well as relative Mach number (d) and (h) at rotor inlet.

case of isolated stagnation pressure distortion. A significant change in the swirl occurs at ±90° where the low momentum fluid flow regime is located. There the flow redistribution changes the swirl direction from counter- to co-swirl and vice versa. In the lower part of the annulus between ±90° and ±180°, the flow redistribution of the isolated stagnation pressure distortion leads to a pre-swirl in the same direction as the incoming swirl. Consequently, the swirl is mainly preserved for the combined distortion. Thus, the swirl distortion pattern entering the engine remains mainly in the flow and the intake attenuates the swirl level only slightly. Nevertheless, the flow redistribution is able to change the swirl direction at ±90°.

In contrast to the swirl induced changes discussed at AIP, the stagnation pressure distortion mainly affects the flow field at AIP. As a result, the meridional velocity distribution remains essentially the same at AIP. Furthermore, the meridional velocity level is an order of magnitude larger than the circumferential velocity, which in turn leads to similar incidence and relative Mach number distributions. For the sake of completeness, these patterns are shown in fig. A.8, fig. A.9 and A.10.

Figure 5.28 depicts the spanwise flow kinematics around the circumference at the rotor inlet. As already seen in the dimensionless static pressure distribution, the swirl distortion causes a higher static pressure level in the upper right part of the annulus and a lower static pressure in the lower left part. Consequently, the meridional velocity components at

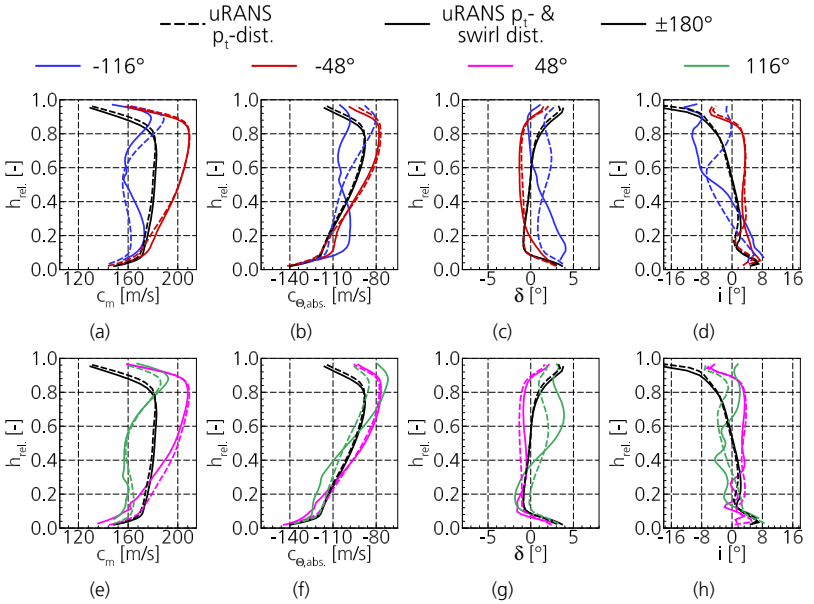

Figure 5.29.: Spanwise distribution of the meridional velocity (a) and (e), circumferential velocity (b) and (f) as well as deviation (c) and (g) at rotor outlet. Stator incidence in (d) and (h).

-116° and 48° in fig. 5.28 (a) and (e) show differences. In contrast, the spanwise distributions of the other circumferential positions are mainly on top of each other. The swirl distortion is the distinguishing flow feature between the two operating conditions. Consequently, the swirl distribution changes significantly between the two operating points in fig. 5.28 (b) and (f). On the one hand, the swirl mainly changes the circumferential velocity distribution below 50% span in the upper half of the annulus (at ±48°). On the other hand, the swirl causes a change in the swirl direction along the span in the lower part of the annulus at ±116°. The effect on the rotor incidence is shown in fig. 5.28 (c) and (g). As the meridional and circumferential velocities are essentially the same at ±180°, the incidence distributions are similar.

In the upper half of the annulus, the meridional velocity is mainly unaffected by the swirl distortion and the swirl changes the incidence levels below 35% span. At 48° the incidence is shifted towards positive incidence, while at -48° the incidence distribution is shifted towards negative incidence. At -116°, the lower 50% of the span is shifted towards positive incidence, while the upper part of the blade incidence is shifted towards negative incidence. Conversely, at 116°, the swirl shifts the incidence distribution towards negative incidence near the hub and towards positive incidence in the upper part of the blade. The relative Mach number distribution is also affected by the changes in the meridional and circumferential velocity distributions. In particular, the high swirl velocity near the hub leads to increasing Mach number levels at -116° and decreasing Mach number levels

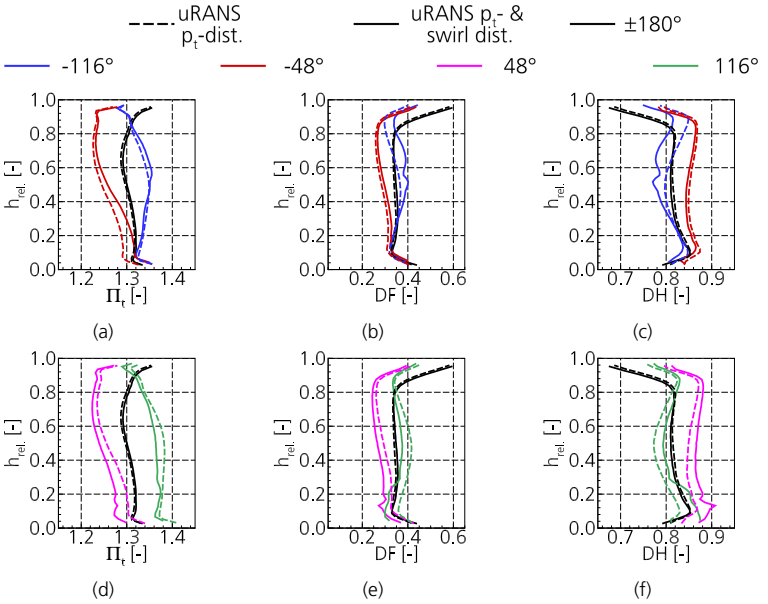

Figure 5.30.: Rotor pressure ratio (a) & (d), diffusion factor (b) & (e) and deHaller number (c) & (f).

at 48° and 116°. Consistent with the findings above, the variations are more pronounced in the lower part of the annulus than in the upper part. The varying flow kinematics at the rotor inlet change the blade aerodynamics and therefore the flow kinematics at the rotor outlet (cf. fig. 5.29). Within the ±180° position these changes are small and therefore the flow kinematics at the rotor outlet and stator inlet are similar. At ±48° there are small changes between the two operating points. The deviation shown in fig. 5.29 (c) and (g) causes the main differences there. In the vicinity of the hub, positive incidence results in a higher deviation, which means that the flow is not perfectly aligned with the direction of the blade trailing edge. This results in lower circumferential velocity levels in the absolute reference frame. The work input associated with the outflow velocity is therefore reduced. At -48°, the expected lower work input is compensated by additional work associated with the swirl velocity at the rotor inlet. The opposite is true at 48°.

The biggest difference in flow kinematics between the two cases occurs at ±116°. At -116°, the low momentum fluid near the hub combined with positive incidence leads to a deviation at the rotor outlet due to the swirl distortion. The lower circumferential velocity near the hub would lead to a lower work input, but is compensated by the swirl at the rotor inlet. As the inlet swirl direction, and therefore the rotor incidence distribution, changes along the span at -116°, the deviation in the spanwise direction also decreases. Above about 40% span, the combined distortion case shows less deviation and consequently the circumferential velocity increases and is higher than in the stagnation pressure distortion case. However, the upper part of the blade adds less work to the flow due to

the co-swirl at the rotor inlet. The corresponding stator incidence changes from positive to negative in the radial direction. The 116° position shows similar characteristics, but the swirl direction at the rotor inlet is in the opposite direction and therefore the opposite behaviour occurs compared to the -116° position. Rotor performance in terms of spanwise fan pressure ratio, diffusion factor and deHaller number is shown in fig. 5.30. As can be seen in this figure, the swirl distortion and associated work input changes the performance metrics compared to the isolated stagnation pressure distortion. Based on the flow kinematics, the work input changes only slightly between -116° and 116° and between -48° and 48°. Consequently, the spanwise fan pressure ratio is almost the same at ±116° and ±48°. Thus, the major variations along the circumference are due to the change in inflow momentum. As expected, the high inflow momentum has the lowest fan pressure ratio (see fig. 5.30 (a) and (d)). As a result, the blade load metrics show a low load in terms of flow deceleration in fig. 5.30(c), which is also reflected in a low diffusion factor. At ±180° the inflow conditions are comparable to the stagnation pressure profile of the aerodynamic design point. The fan pressure ratio and blade loading are therefore mainly comparable to those presented in section 5.3. The most demanding operating conditions for the fan stage occur within the low momentum fluid at ±116°. Within the isolated stagnation pressure distortion, the fan pressure ratio at 116° is higher than at the -116° position. This is mainly due to the lower deviation and higher work input. Within the combined distortion, below about 50% span, the fan pressure ratio at 116° remains higher than at -116°. Conversely, above 50% span, the fan pressure ratio of the -116° position exceeds that of the 116° position. Here, the inflow conditions due to the swirl distortion and the deviation at the rotor outlet lead to a higher work input and therefore a higher fan pressure ratio at the -116° position. The associated blade loading shows the same trend resulting from the above flow conditions. Within the isolated stagnation pressure distortion, the blade loading at 116° is more demanding than at -116°. Superimposing the swirl distortion results in a lower loading at 116°, mainly due to the lower flow deceleration.

The fan blade forces are shown in fig. 5.31. Both distributions show similar behaviour. In the low momentum fluid the blade forces are higher than in the high momentum fluid and the VTP causes a sharp force variation at 0°. However, the swirl distortion attenuates

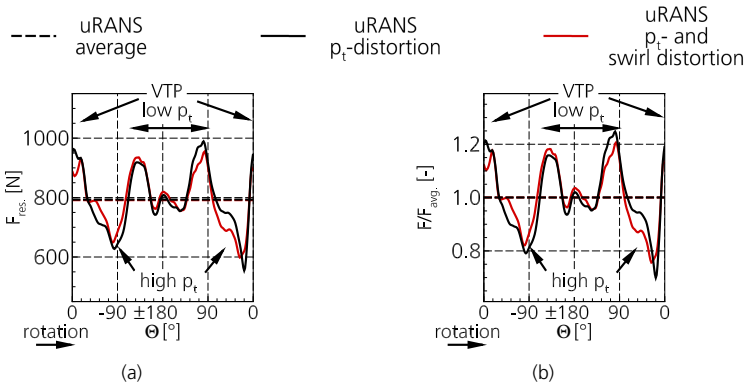

Figure 5.31.: Resulting blade forces around the circumference. Absolute (a), relative (b).

the blade force variation. The largest differences are in the range of 5% at 0°, 20°, 45° and 75°.

Stator flow and performance

Similar flow conditions are obtained downstream of the stator. Figure 5.32 (a) shows these conditions. The swirl distortion does not significantly alter the levels of the meridional velocity. Only small variations are visible in the 48° and 116° positions. The remaining swirl is of the same order of magnitude in the case of superimposed swirl distortion as in the case of isolated stagnation pressure distortion. Therefore, the fan is able to align the flow with the streamwise direction. Any remaining swirl downstream of the fan stage is a loss in terms of thrust generation. Furthermore, the static pressure field downstream of the vane shows higher variations for the combined distortion. However, the variation is relatively small and less than 1%. In line with the findings above, the swirl distortion causes variations in the vane loading which are mainly found below 50% span (see fig. 5.33). At -116° and ±180°, the additional swirl distortion leads to reduced vane loading. Conversely, higher vane loading is observed at 116° and 48°. This section discusses the circumferential variation of the fan pressure ratio and the associated distortion attenuation. Based on the overall efficiency of the fan stage, the swirl distortion showed only small variations. Downstream of the fan stage, the distortion intensity $DI_{60°}$ is evaluated for both distortions. The isolated stagnation pressure distortion shows a distortion intensity of 0.034, which is 30% lower than at the inlet. In contrast, the combined distortion has a distortion intensity of

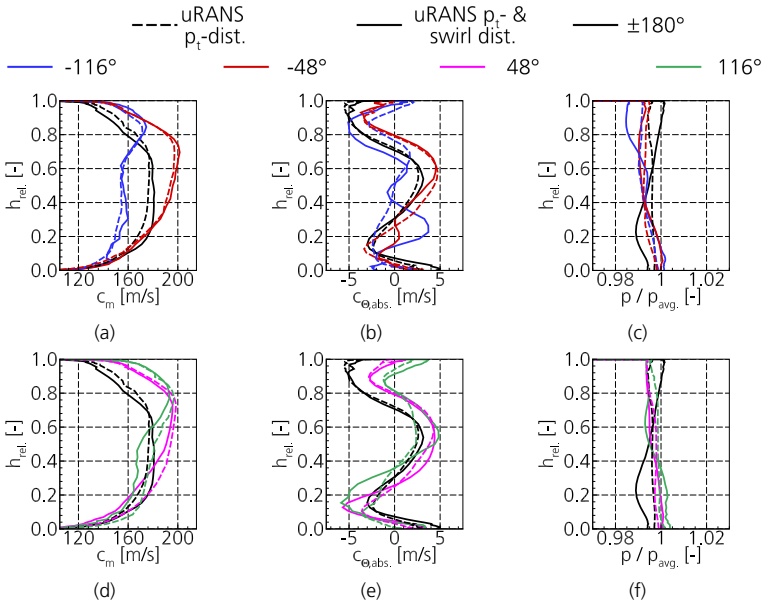

Figure 5.32.: Spanwise meridional velocity (a) & (d), circumferential velocity (b) & (e) and non-dimensional static pressure (c) & (f) downstream of the stator.

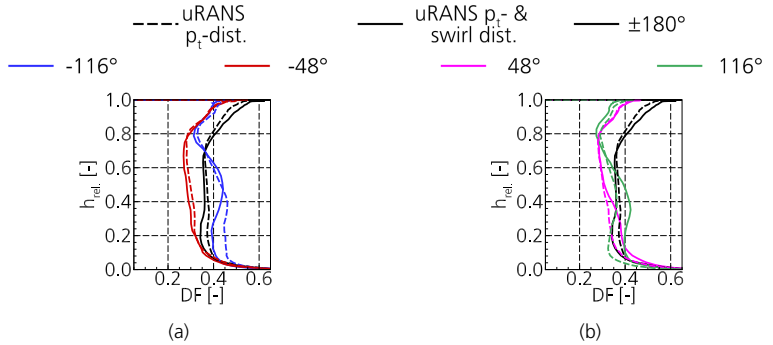

Figure 5.33.: Spanwise distribution of vane loading.

0.029. This is a reduction of 40% compared to the inlet distortion. Overall, the fan stage is able to significantly reduce the distortion and also homogenise the stagnation pressure distribution downstream of the fan stage. The intended aft-fan design therefore fulfils its intended purpose.

5.4.3. Entropy variation and associated loss generation through the fan stage

This subsection deals with convective entropy transport and entropy generation. Figure 5.34 shows the instantaneous entropy distribution at the rotor inlet in the top row, at the rotor mid-chord in the middle row and between the rotor and stator in the bottom row. At the rotor inlet, the entropy distribution is similar between the two operating points and is mainly associated with convective transport of the boundary layer fluid. Consequently, the high entropy region coincides with the low momentum fluid and vice versa. In addition, the VTP wake is present at the 0° position and passes through the rotor at this position. Within the blade row, the main loss generation is associated with the blade boundary layer and the tip gap flow. Downstream of the rotor blade, the fan blade wakes and the tip gap flow mixes with the surrounding fluid. Therefore, the distribution is more mixed compared to the mid-chord section. In addition, the VTP and blade wake merge to form a thicker combined wake. However, within the entropy distribution it is difficult to distinguish whether the high entropy level is due to convective transport of entropy or entropy generation. Therefore fig. 5.35 shows the entropy time rate $\dot{s}$ between rotor and stator of two consecutive time steps. High values of the time rate indicate a higher increase in entropy and therefore a higher loss generation and vice versa. The standard deviation is also evaluated. High values indicate that the entropy time rate of the wakes passing through a particular location is higher. This is associated with increased loss generation. Regions with low values of the standard deviation indicate lower loss generation.

In both flow fields the entropy time derivatives of the fan blade wakes are similar over a large part of the circumference as shown in fig. 5.35 (a) and (b). However, there are more pronounced rotor wakes between ±30° and ±80°. At 80° the wake has a different radial distribution, mainly related to the swirl distribution. Furthermore, the -150° to -180° region shows more pronounced wakes in the combined distortion case shown in fig. 5.35

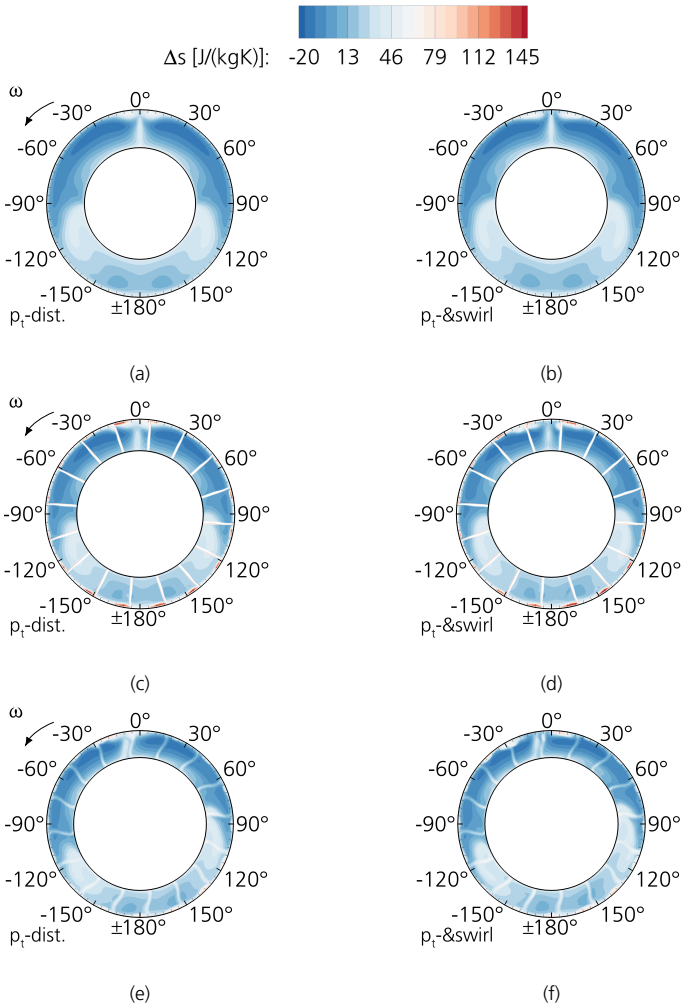

Figure 5.34.: Distribution of the entropy rise at rotor inlet in (a) and (b), rotor mid-chord in (c) and (d) and at rotor outlet (e) and (f). Left: stagnation pressure distortion. Right: stagnation pressure and swirl distortion.

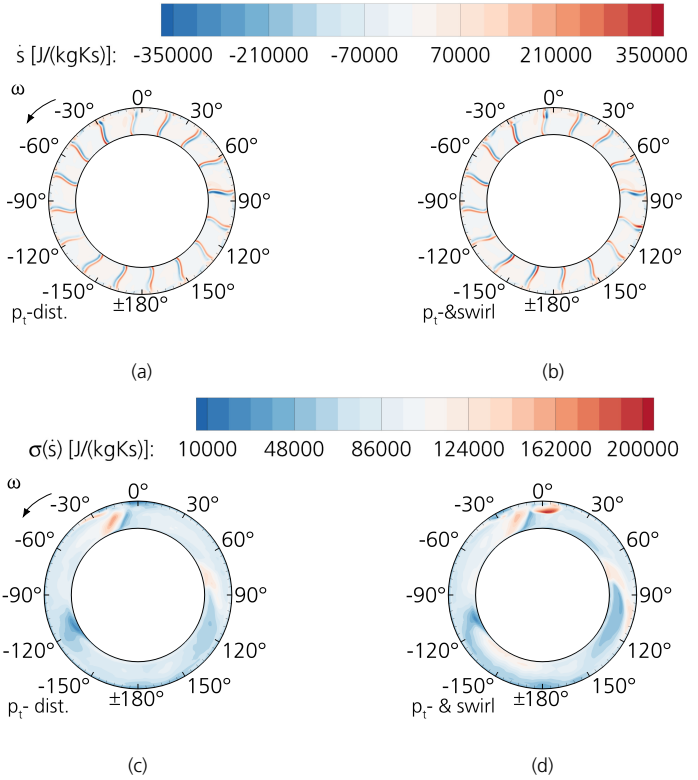

Figure 5.35.: Time derivative of the entropy between rotor and stator stemming from isolated stagnation pressure distortion (a) and combined distortion (b). Corresponding standard deviation of entropy time rate in (c) and (d).

(b). The same is true for the tip region between 90° and 120°.

The corresponding standard deviation of entropy shows essentially the same distribution for both distortions. There is a small variation in the co-swirl region between -90° and -120° near the hub. Furthermore, the hub region between 90° and 120° is also associated with lower time rates of entropy. Wake mixing leads to lower differences at -10° and higher variations at -20°. So the presence of the VTP wake causes more losses in the flow.

However, there are also differences in the standard deviation associated with swirl distortion. The VTP mixing in the upper part at 0° causes high values of the standard deviation. This is where the convective transport of co-swirl fluid into the counter-swirl inflow region takes place and is likely to produce higher losses leading to higher standard deviation. This flow feature would require further investigation beyond the scope of this work. Furthermore, the hub region showed the most significant swirl induced variations in the rotor

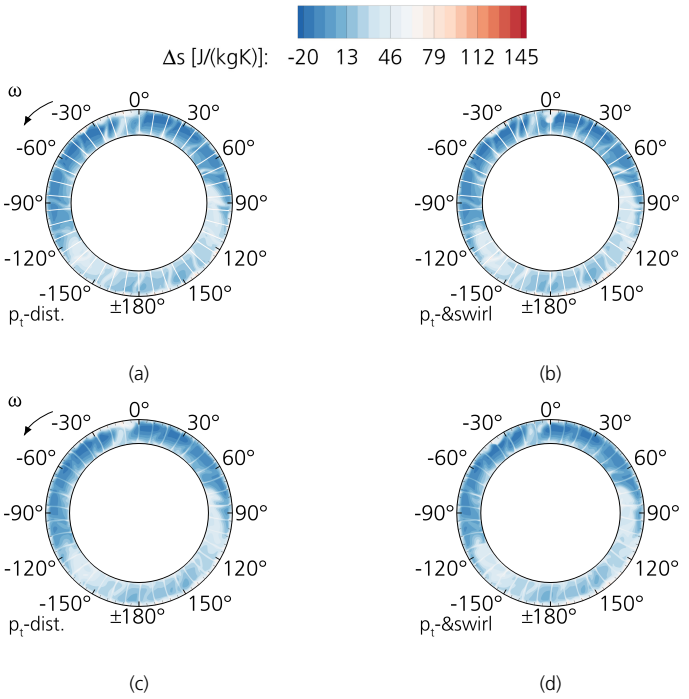

Figure 5.36.: Entropy distribution at stator mid-chord in (a) and (b) and stator outlet in (c) and (d). Left: stagnation pressure distortion. Right: stagnation pressure and swirl distortion.

inflow conditions at the positions between 30° and 60° and between -120° and -150°. In the co-swirl region (30° to 60°) the standard deviation and associated losses decrease, while the counter-swirl leads to higher standard deviation and therefore losses between -120° and -150°. In addition, the tip region between 90° and 120° and close to -30° shows swirl induced variations in the standard deviation of the entropy time rate associated with variations in the tip gap flow. Figure 5.36 shows the entropy distribution at the mid-chord of the stator (top row) and downstream of the stator (bottom row) of the isolated stagnation pressure distortion on the left and the combined distortion on the right. Between the rotor and stator, the flow contains swirl and entropy moves with the particles in a counterclockwise circumferential direction. Within the vane, losses are generated and entropy increases within the vane boundary layer. So the vane boundary layers are clearly visible in the top row of fig. 5.36. These are the sharp radial profiles, while the bended fan blade wakes are cut at the leading edge of the vanes and extend over at least two vane passages. Downstream of the vane row, the rotor and vane wakes remain in the flow but mix, resulting in a more mixed entropy pattern. The corresponding entropy time rate and standard deviation are given in fig. 5.37 downstream of the stator. It can be seen that the time derivative has lower values there. It can therefore be concluded that the main

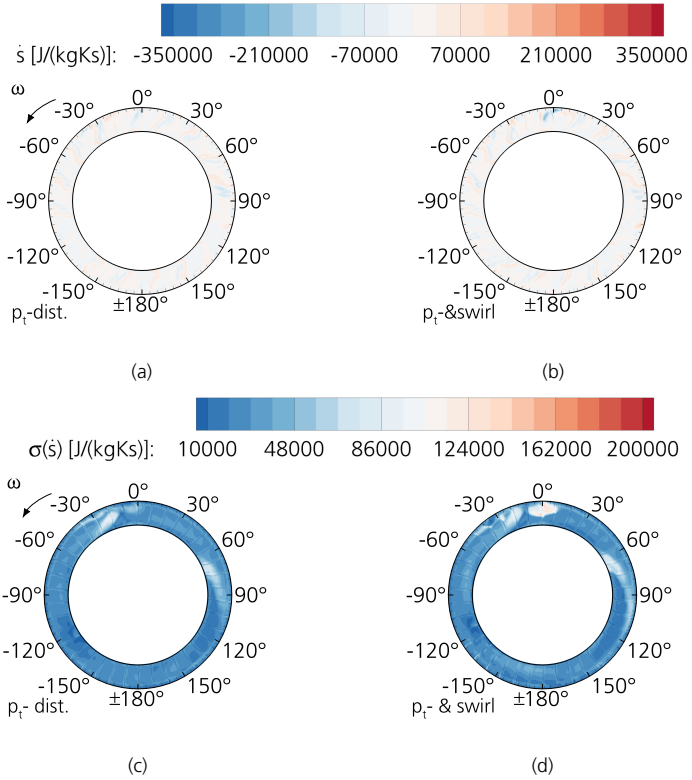

Figure 5.37.: Time derivative of the entropy at stator outlet stemming from isolated stagnation pressure distortion (a) and combined distortion (b). Corresponding standard deviation of entropy time rate in (c) and (d).

loss generation takes place in the rotor. Furthermore, the level of the standard deviation is lower downstream of the stator vane than in the upstream position. The main difference is related to the convective transport of the VTP related fluid. The standard deviation therefore peaks at 0° in the combined distortion.

To summarise the results presented in this subsection, the stagnation pressure distortion is the main driver of the fan performance and the main variations in the local flow characteristics, while the effect of the swirl distortion on the overall fan performance is small. The total mass flow decreases by about 0.2%, the fan pressure ratio is slightly lower and the fan efficiency decreases by about 0.4%. In addition, the interaction between the fan and the distortion leads to a change in the swirl direction in the hub region of $\pm 90°$, which is notable. However, the swirl distortion locally changes the inflow conditions in terms of incoming swirl and therefore incidence. Nevertheless, at an early stage of preliminary design, the effect of the fan response to the stagnation pressure distortion is of major

interest.

5.5. Fan operation along a fan iso-speedline

This subsection demonstrates an application of the newly developed methodology at an early preliminary design stage. As mentioned in the previous sections, the margin to the stability limit is crucial for assessing the fan stage operation. Therefore, the fan performance near the stability limit gives important insights into the distortion tolerance of the fan. In this subsection the fan performance along an iso speed line is investigated. The individual inlet boundary conditions along the speed line are derived from the distortion generator introduced in section 5.1. The main characteristic of the stagnation pressure distortion pattern remains within the individual distortions. Only minor variations occur in the VTP region. Figure 5.38 shows the specific orbits at different operating points within the fan map. The reference operating conditions are marked in fig. 5.11. The orbits show the variation in orbit width which increases from near choke to near stall conditions. In addition, the variation in fan pressure ratio is greater at near stall than at ADP. The near choke condition also shows a greater variation in fan pressure ratio than ADP. Table 5.7 contains data on the averaged operating point as well as the upper left and lower right points of the orbit. The observation of the orbits translates into the operating point variation listed in the three right columns of the table. These relative quantities take into account the variation between the left and right parts of the orbit in the nominator and are normalised by the averaged operating point. The real and corrected mass flow variations increase significantly from near choke to near stall. For example, the operating point variation increases from 8.49% at near choke to 22.88% at near stall in terms of corrected mass flow. In terms of fan pressure variation, there is an increase from 4.35% to 5.36% towards the stability limit. In addition, the fan pressure variation also increases towards the near stall conditions. The high variation of 7% is due to the choking of the high momentum fluid. There the fan pressure ratio drops as shown in table 5.7.

The application of the preliminary fan assessment over a wide range of operating conditions within the fan map underlines the beneficial use at an early design stage. The entire fan map calculation takes approximately four hours on a conventional workstation, so the off-design performance is quantified in a relatively short time and can be used to improve

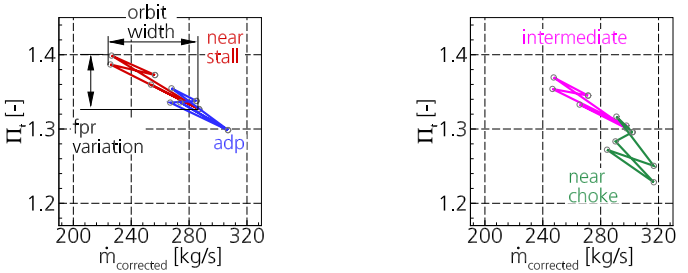

Figure 5.38.: Orbits of different operating conditions along an iso-speedline.

Table 5.7.: Fan operating points along an iso-speedline. Every operating point is characterized by the average performance data as well as the upper left and lower right point of the orbit.

		$\dot{m}$ [kg/s]	$\dot{m}_{corrected}$ [kg/s]	Π_t [-]	$\frac{\Delta\dot{m}}{\Delta\dot{m}_{avg.}}$ [-]	$\frac{\Delta\dot{m}_{corrected}}{\Delta\dot{m}_{corrected,avg.}}$ [-]	$\frac{\Delta\Pi_t}{\Delta\Pi_{t,avg.}}$ [-]
near stall	avg.	90.73	264.55	1.3486	0.3411	0.2288	0.0536
	left	71.32	226.4	1.3989			
	right	102.27	286.92	1.3266			
inter-mediate	avg.	95.25	277.96	1.323	0.2926	0.181	0.0518
	left	78.06	247.5	1.3694			
	right	105.93	297.82	1.3009			
adp	avg.	99.45	290.62	1.2958	0.2483	0.1377	0.0435
	left	84.51	267.29	1.3271			
	right	109.2	307.31	1.2707			
near choke	avg.	104.0	304.35	1.2634	0.1928	0.0849	0.0700
	left	92.26	290.89	1.3167			
	right	112.31	316.72	1.2283			

the fan design in a subsequent iteration. Nevertheless, the off-design performance assessment needs further verification with time-resolved calculations to increase the confidence level in the preliminary design and assessment methodology.

5.6. Summary and design suggestions for full annulus fuselage fans

This chapter presents and discusses the design of an aft-propulsor from concept through preliminary design to detailed fan assessment. In this integration scenario, a descending spanwise fan pressure ratio and a high hub-to-tip ratio fan stage are found to be beneficial in terms of distortion attenuation. The fan stage design meets all design specifications and even exceeds the required isentropic efficiency by 0.74% and 0.39% respectively. Furthermore, the design proves that the distortion intensity can be reduced by 30% and 40% respectively.

Nevertheless, the fan stage design can be improved by considering a more realistic stagnation pressure profile. The spanwise distribution available during preliminary design differs slightly from the circumferentially averaged stagnation pressure of the two-dimensional distortion. In particular, the hub and tip sections are subject to slightly different inflow conditions. This should be considered in future fan design and is expected to improve fan operation under realistic BLI conditions. In addition, the hub section of the rotor showed challenging flow conditions. A redesign of this specific blade section is expected to improve fan operation and efficiency.

This chapter also demonstrates the versatility of the new design and assessment methodology for distortion tolerant fans. The flow redistribution upstream of the fan as well as the fan performance metrics show that the methodology is able to cover the main BLI related

flow characteristics. Therefore, this methodology can be used in future design studies. Furthermore, the swirl distortion has only a small effect on the downstream fan performance and can therefore be neglected in the early stages of preliminary design.

However, the distortion pattern of a fuselage propulsor is much more complex and the data from the time-resolved calculations reveal more unsteady effects that need to be investigated in more detail in future studies.

6. Conclusion and way forward for distortion tolerant fan designs

Boundary layer ingestion is a thrust related technology for more fuel efficient engines for future aviation. In contrast to the beneficial influence on the engine cycle level, the inhomogeneous inflow poses a challenge for fan aerodynamics. In particular, the preliminary design of distortion tolerant fans is challenging because the approaches to account for BLI are either inaccurate in terms of aerodynamic flow calculation (i.e. compressors-in-parallel) or highly time-consuming and already require detailed geometric input, such as unsteady RANS approaches. Therefore, a design and assessment methodology for the preliminary aerodynamic design of distortion tolerant fans is required.

This thesis summarises the challenges for fan designs exposed to non-homogeneous inflow, introduces the BLI specific flow characteristics including flow redistribution upstream of the fan stage and the corresponding variations in fan performance. Based on these findings, the methodology for preliminary design and assessment of BLI fan stages is developed, which is numerically efficient and allows applicability during preliminary fan design. The results of the newly developed methodology are verified by time-resolved calculations and applied to the exploration of wide design spaces and fan performance along iso speed lines. The achievements of this work can be divided into achievements at the methodology level and for the fan design.

6.1. Achievements at methodology level

This study presents a new methodology that couples streamline curvature calculations with flow predictions from a RANS approach. The former is extended by a stream tube contraction model to include the BLI related flow redistribution. The determination of the stream tube contraction as a function of the radial stagnation pressure distribution is explained. Furthermore, the translation into a two-dimensional field as well as the influence of the stream tube contraction on the meridional velocity component is well demonstrated within chapter 3. The RANS approach is used to calculate the flow redistribution upstream of the fan stage. For this purpose, the radial static pressure distribution is extracted from the flow field obtained by the streamline curvature approach at specific circumferential positions. Two second and third order polynomials are then used to approximate the circumferential static pressure variation between local static pressure minima and maxima. The stacking of a number of circumferential static pressure distributions results in the two-dimensional static pressure field which serves as the outlet boundary condition within the flow redistribution calculations. Based on the flow redistribution, the local operating points around the circumference are calculated within SLC. The fan performance data of the newly developed methodology are comprehensively verified by time-resolved calculations and demonstrate its ability to calculate BLI flows in terms of (corrected) mass flow and fan pressure ratio variations. The accurate calculation of local operating points allows the assessment of local inflow conditions (i.e. blade incidence) and blade performance, which is related to

distortion attenuation. Furthermore, the design methodology is able to capture the effect of different radial fan pressure ratio distributions as well as a completely different fan integration scenario. Thus, aerodynamicists can use the methodology to accurately select a specific design philosophy for a given integration scenario. In addition, the methodology is also able to capture the blade force variations around the circumference, which is important for a preliminary aeromechanical evaluation of the blade. However, the limitations of the methodology, due to the neglect of unsteady work input and the limitations in terms of loss prediction, result in a rounder orbit than time-resolved calculations.

The entire fan assessment is less time-consuming than the calculation of the verification data. While the calculation of the uRANS flow field requires approximately 10000 CPUh, the preliminary design methodology requires only 3 CPUh. Therefore, the entire preliminary design and assessment of a distortion tolerant fan can be performed on a conventional workstation instead of a high performance computing cluster.

6.2. Achievements at fan design level

Fuselage embedded turbofans

This integration scenario shows a distortion pattern with low momentum fluid in the tip region, which also features radial distortion and extends approximately 120° in the circumferential direction. The rotor is therefore subjected to a one per revolution distortion. With the aim of maximising the boundary layer fluid fraction to minimise the power required for thrust generation, the fan pressure ratio of the fan stage should be slightly increased compared to a conventional underwing engine. Considering a 2035 technology level, the fan pressure ratio of conventional engines is expected to be between 1.3-1.32. A distortion tolerant fan is likely to be designed for a fan pressure ratio of 1.35 to 1.4. This will result in lighter engines, making engine integration easier. In addition, the intake geometry is expected to be highly three-dimensional at the inlet to increase the amount of boundary layer fluid ingested. However, the exact parameters will have to be determined in a joint design study taking into account the aircraft and the engine.

In terms of fan design parameters, the impact of the radial fan pressure ratio tends towards a constant or ascending distribution. These designs are able to re-energise the low momentum fluid, resulting in lower flow separations in the vane tip region. In accordance with the literature, the flow redistribution leads to positive incidence and high Mach number levels in the counter-swirl tip region. Such flow conditions result in amplified tip gap flow and hence increased losses. These increased losses due to off-design operation occur even when the losses at ADP are moderate. Consequently, the overall fan performance is adversely affected. One mitigation strategy is to unload the tip section of the blade to attenuate the tip gap flow and associated losses. The parameter space of meridional Mach number and blade tip speed showed no clear trend towards a distortion tolerant fan. At low meridional Mach numbers, the fan efficiency increases due to lower viscous losses. As the meridional Mach number increases, the flow deceleration at the inlet decreases, which also affects the flow redistribution. In the case of BLI, the blade incidence decreases with increasing meridional Mach number. Associated with the attenuated blade incidence, the blade force variation also decreases. These effects are a combination of the flow deceleration in the intake and the BLI related flow redistribution. As tip speed increases, work input

and blade force variation increase. In order to reduce the distortion, an increased tip speed appears to be advantageous, with the disadvantage of increased blade force amplitudes. The latter is expected to be detrimental to the aeromechanical performance of the fan. Therefore, an intermediate level of meridional Mach number and tip speed is expected to be beneficial for a distortion tolerant fan. The three-dimensional intake geometry in combination with the flow deceleration and the fan design parameters can be considered simultaneously by taking advantage of this design methodology.

Aft-propulsor

The integration of a propulsor that ingests the fuselage boundary layer over the entire circumference leads to an unconventional fan design. Due to the relatively low mass flow and the need to re-energise the low momentum fluid close to the fan hub, a fan with a high hub-to-tip ratio is designed with a decreasing radial fan pressure ratio. The fan stage meets the design specification and even exceeds the isentropic efficiency requirement by 0.74%. This design philosophy is able to reduce the distortion intensity downstream of the fan stage by 30% compared to the inflow conditions.

In addition, the effect of swirl distortion on flow redistribution and fan performance is identified. The flow redistribution is essentially unaffected by the swirl distortion. Thus, the static pressure field remains mainly the same compared to the isolated stagnation pressure distortion. The swirl distortion is attenuated over a large part of the annulus, but the swirl remains in the flow at the rotor inlet. However, the flow redistribution is able to change the swirl direction in the hub region at $\pm 90°$.

The fan performance in terms of corrected mass flow, fan pressure ratio and fan efficiency is only slightly reduced. The distortion attenuation increases compared to the isolated distortion and the distortion intensity downstream of the fan decreases by 40% compared to the inflow distortion. Based on these findings, it is sufficient to consider only the stagnation pressure distortion at an early design stage. As the design maturity increases, the combined distortion should be considered to include all relevant flow features.

6.3. Future work

In future studies, a deeper insight into the unsteady effects of boundary layer ingestion can improve the understanding of distortion tolerant fan design. The unsteady work input could be demonstrated by evaluating cascades with varying inflow conditions. These results would lead to a quantification of the unsteady stagnation temperature rise that occurs in BLI flows. Furthermore, the viscous loss generation due to non-homogeneous inflow needs to be studied in greater detail in order to understand the effect of lower loss generation in the co-swirl region, which is also characterised by positive incidence. Another effect expected to be caused by unsteadiness is the blade force variation of the aft-propulsor in chapter 5. Understanding all of these effects is necessary to further improve the aerodynamic and aeromechanical performance of distortion tolerant fans. Furthermore, this knowledge can be used to improve the specific loss and work input models within the preliminary design methodology.

As mentioned in the literature review in chapter 2, the loss generation associated with the tip gap flow in the counter-swirl region is the dominant loss mechanism that detrimentally affects BLI fan performance. Therefore, a distortion tolerant fan stage needs to attenuate this flow feature. On the one hand, this can be achieved by unloading the tip section of the blade. On the other hand, passive flow control devices could have a beneficial effect on the overall fan performance. Non-axisymmetric casing treatments or the use of brush seals could improve local flow conditions and lead to lower losses. Reducing loss generation at this specific location of the annulus is expected to significantly increase the efficiency of BLI fans.

References

Abbasi, S., Pirnia, A., & Taghavi Zenouz, R. (2018). Investigation of Inlet Distortion Effects on Axial Compressor Performance based on Streamline Curvature Method. *Journal of Theoretical and Applied Mechanics, Poland, Vol. 56, DOI: 10.15632/jtam-pl.56.4.1005*.

Adamczyk, J. J. (1984). Model Equation for Simulating Flows in Multistage Turbomachinery. *NASA Technical Report N85-12036*.

Arend, D. J., Wolter, J. D., Hirt, S. M., Provenza, A., Gazzaniga, J. A., Cousins, W. T., Hardin, L. W., & Sharma, O. (2017). Experimental Evaluation of an Embedded Boundary Layer Ingesting Propulsor for Highly Efficient Subsonic Cruise Aircraft. *53rd AIAA/SAE/ASEE Joint Propulsion Conference, ISBN: 978-1-62410-511-1, DOI: 10.2514/6.2017-5041*.

Bakhle, M., Reddy, T., Herrick, G., Shabbir, A., & Florea, R. (2012). Aeromechanics Analysis of a Boundary Layer Ingesting Fan. *AIAA 2012, Atlanta, Georgia, USA, ISBN: 978-1-60086-935-8, DOI: 10.2514/6.2012-3995*.

Bakhle, M. A., Reddy, T. S., Coroneos, R., Min, J. B., Provenza, A. J., Duffy, K. P., Stefko, G. L., & Heinlein, G. (2018). Aeromechanics Analysis of a Distortion-Tolerant Fan with Boundary Layer Ingestion. *AIAA Aerospace Sciences Meeting , 8–12 January, 2018, Kissimmee, Florida, DOI: 10.2514/6.2018-1891*.

Banjac, M., Petrovic, M. V., & Wiedermann, A. (2014). Secondary Flows, Endwall Effects and Stall Detection in Axial Compressor Design. *ASME Turbo Expo 2014: Turbomachinery Technical Conference and Exposition, GT2014-25115, June 16-20, 2014, Düsseldorf, Germany*.

Bardina, J., Ferziger, J. H., & Rogallo, R. S. (1985). Effect of Rotation on Isotropic Turbulence: Computation and Modelling. *Journal of Fluid Mechanics, Vol. 154*.

Becker, K., Heitkamp, K., & Kügeler, E. (2010). Recent Progress in a Hybrid-Grid CFD Solver for Turbomachinery Flows. *V European Conference on Computational Fluid Dynamics ECCOMAS CFD 2010, ISBN: 978-989-96778-1-4, DOI:*

Bräunling, W. J. G. (2009). Flugzeugtriebwerke. *Springer Berlin Heidelberg, Vol. , ISBN: 978-3-540-76368-0 978-3-540-76370-3*.

Cao, T., Vadlamani, N. R., Tucker, P. G., Smith, A. R., Slaby, M., & Sheaf, C. T. J. (2017). Fan–Intake Interaction Under High Incidence. *Journal of Engineering for Gas Turbines and Power, Vol. 139(4), 1528-8919, DOI: 10.1115/1.4034701*.

Castillo Pardo, A., & Hall, C. A. (2022). Effects of Sideslip Direction on a Rear Fuselage Boundary Layer Ingesting Fan. *Journal of Turbomachinery, Vol. 144, ISSN: 0889-504X, DOI: 10.1115/1.4055385*.

Castillo Pardo, A. C., & Hall, C. A. (2019). Aerodynamics of Boundary Layer Ingesting Fuselage Fans. *24th ISABE Conference, September 22-27, 2019 Canberra, Australia, ISABE-2019-24162*.

Cinquegrana, D., & Vitagliano, P. L. (2021). A reduced Order Model for Boundary Layer Ingestion Map Prediction at Fan Inlet of Rear-Mounted Engine Nacelle. *AIAA Scitech 2021 Forum, virtual, Vol. , ISBN: 978-1-62410-609-5, DOI: 10.2514/6.2021-0993*.

Comission, E. (2011). Flightpath 2050: Europe's vision for aviation: Maintaining global leadership and serving society's needs. *Publications Office of the European Union, Vol. , ISBN: 978-92-79-19724-6*.

Cousins, W. T., Voytovych, D., Tillman, G., & Gray, E. (2017). Design of a Distortion-Tolerant Fan for a Boundary-Layer Ingesting Embedded Engine Application. *53rd AIAA/SAE/ASEE Joint Propulsion Conference, DOI: 10.2514/6.2017-5042*.

Cumpsty, N. A. (2004). Compressor aerodynamics. *Krieger Pub., ISBN: 978-1-57524-247-7*.

Cumpsty, N. A. (2010). Some Lessons Learned. *Journal of Turbomachinery, Vol. 132, DOI: 10.1115/1.4001222*.

Day, I. J. (1991). Stall Inception in Axial Flow Compressors. *ASME Turbo Expo 1991: Turbomachinery Technical Conference and Exposition, DOI: 10.1115/91-GT-086*.

Day, I. J. (2016). Stall, Surge, and 75 Years of Research. *Journal of Turbomachinery, Vol. 138(1), ISSN: 0889-504X, 1528-8900, DOI: 10.1115/1.4031473*.

DeHaller, P. (1955). Das Verhalten von Tragflügeln in Axialverdichtern und im Windkanal. *VDI-Ber. 3 Probleme der Strömungstechnik im Maschinenbau*.

Denton, J. D. (1978). Throughflow Calculations for Transonic Axial Flow Turbines. *Journal of Engineering for Power, Vol. 100, ISSN: 0022-0825, DOI: 10.1115/1.3446336*.

Denton, J. D. (1993). Loss Mechanisms in Turbomachines. *ASME Journal of Turbomachinery, Vol. 115(4)*.

Drela, M. (2009). Power Balance in Aerodynamic Flows. *AIAA Journal, Vol. 47(7), ISSN: 0001-1452, 1533-385X, DOI: 10.2514/1.42409*.

Dunham, J. (1965). Non-Axisymmetric Flows in Axial Compressors. *Mechanical Engineering Science, Monograph No. 3*.

Eichner, F., & Belz, J. (2019). Application of the Modal Approach for Prediction of Forced Response Amplitudes for Fan Blades. *Journal of Engineering for Gas Turbines and Power, Vol. 141(3), ISSN: 0742-4795, 1528-8919, DOI: 10.1115/1.4041453*.

Eichner, F., Belz, J., Winkelmann, P., Schnell, R., & Lengyel-Kampmann, T. (2019). Prediction of Aerodynamically Induced Fan Blade Vibration due to Boundary Layer Ingestion. *Proceedings of 13th European Conference on Turbomachinery Fluid Dynamics and Thermodynamics, ETC2019-370, April 8-12, 2019, Lausanne, Switzerland*.

Fidalgo, V. J., Hall, C. A., & Colin, Y. (2012). A Study of Fan-Distortion Interaction within the NASA Rotor 67 Transonic Stage. *Journal of Turbomachinery, Vol. 134(5), ISSN: 0889-504X, DOI: 10.1115/1.4003850*.

Florea, R. V., Matalanis, C., Hardin, L. W., Stucky, M., & Shabbir, A. (2015). Parametric Analysis and Design for Embedded Engine Inlets. *Journal of Propulsion and Power, Vol. 31, ISSN: 0748-4658, 1533-3876, DOI: 10.2514/1.B34804*.

Frey, C., Ashcroft, G., Kersken, H.-P., Schönweitz, D., & Mennicken, M. (2017). Simulation of Indexing and Clocking with Harmonic Balance. *International Journal of Turbomachinery, Propulsion and Power, Vol. 3, ISSN: 2504-186X, DOI: 10.3390/ijtpp3010001*.

Gallimore, S. J., & Cumpsty, N. A. (1986). Spanwise Mixing in Multistage Axial Flow Compressors: Part I - Experimental Investigation. *ASME Journal of Turbomachinery, Vol. 108*.

Giesecke, D., & Friedrichs, J. (2019). Aerodynamic Comparison Between Circumferential and Wing-Embedded Inlet Distortion for an Ultra-High Bypass Ratio Fan Stage. *ASME Turbo Expo 2019: Turbomachinery Technical Conference and Exposition, GT2019-90425, June 17-21, 2019, Phoenix, AZ, USA*.

Giesecke, D., Friedrichs, J., & Stark, U. (2017). Preliminary Aerodynamic Design of a Fan Stage for an Ultra High Bypass Ratio Engine. *24th ISABE Conference, September 3-8, 2017, Manchester, UK, ISABE-2017-2253*.

Godard, B., De Jaeghere, E., & Gourdain, N. (2019). Efficient Design Investigation of a Turbofan in Distorted Inlet Conditions. *ASME Turbo Expo 2019: Turbomachinery Technical Conference and Exposition, GT2019-90471, June 17-21, 2019, Phoenix, AZ, USA*.

Goulos, I., Otter, J., Stankowski, T., MacManus, D., Grech, N., & Sheaf, C. (2018). Design Optimisation of Separate-Jet Exhausts for the Next Generation of Civil Aero-Engines. *The Aeronautical Journal, Vol. 122, ISSN: 0001-9240, 2059-6464, DOI: 10.1017/aer.2018.95*.

Greitzer, E. M., & Griswold, H. R. (1976). Compressor-Diffuser Interaction with Circumferential Flow Distortion. *Journal of Mechanical Engineering Science, ISSN: 0022-2542, 2058-3389*.

Grieb, H., Schill, G., & Gumicio, R. (1975). A Semi-Empirical Method for the Determination of Multistage Axial Compressor Efficiency. *ASME Turbo Expo 1975: Gas Turbine Conference, Houston, Texas, Paper 75-GT-11*.

Gummer, V., & Wenger, U. (2000). Using Sweep and Dihedral to Control Three-Dimensional Flow in Transonic Stators of Axial Compressors. *ASME Turbo Expo 2000: Turbomachinery Technical Conference and Exposition, 2000-GT-0490, May 8-11, 2000, Munich, Germany*.

Gunn, E. J., & Hall, C. A. (2014). Aerodynamics of Boundary Layer Ingesting Fans. *ASME Turbo Expo 2014: Turbomachinery Technical Conference and Exposition, GT2014-26142, June 16-20, 2014, Düsseldorf, Germany*.

Gunn, E. J., & Hall, C. A. (2017). Non-Axisymmetric Stator Design for Boundary Layer Ingesting Fans. *ASME Turbo Expo 2017: Turbomachinery Technical Conference and Exposition, GT2017-63082, June 26-30, 2017, Charlotte, NC, USA*.

Gunn, E. J., Tooze, S. E., Hall, C. A., & Colin, Y. (2013). An Experimental Study of Loss Sources in a Fan Operating with Continuous Inlet Stagnation Pressure Distortion. *Journal of Turbomachinery, Vol. 135(5), DOI: 10.1115/1.4007835*.

Habermann, A. L., Bijewitz, J., Seitz, A., & Hornung, M. (2020). Performance Bookkeeping for Aircraft Configurations with Fuselage Wake-Filling Propulsion Integration. *CEAS Aeronautical Journal, Vol. 11, ISSN: 1869-5582, 1869-5590, DOI: 10.1007/s13272-019-00434-w*.

Hah, C., Rabe, D. C., Sullivan, T. J., & Wadia, A. R. (1998). Effects of Inlet Distortion on the Flow Field in a Transonic Compressor Rotor. *ASME Journal of Turbomachinery, Vol. 120(2), ISSN: 0889-504X, DOI: 10.1115/1.2841398*.

Hall, D. K. (2015). Analysis of Civil Aircraft Propulsors with Boundary Layer Ingestion. *Ph.D. Thesis, Massachusetts Institute of Technology, USA*.

Hall, D. K., Greitzer, E. M., & Tan, C. S. (2017). Analysis of Fan Stage Conceptual Design Attributes for Boundary Layer Ingestion. *ASME Journal of Turbomachinery, Vol. 139(7), ISSN: 0889-504X, 1528-8900, DOI: 10.1115/1.4035631*.

Hall, D. K., Greitzer, E. M., & Tan, C. S. (2022). Mitigation of Boundary Layer Ingestion Circumferential Distortion Using Nonaxisymmetric Fan Exit Guide Vanes. *Journal of Turbomachinery, Vol. 145, ISSN: 0889-504X, DOI: 10.1115/1.4055645*.

Heinlein, G. S., Bakhle, M. A., & Chen, J. P. (2019). Aeromechanic Response of a Coupled Inlet-Fan Boundary Layer Ingesting Distortion-Tolerant Fan. *ASME Turbo Expo 2019: Turbomachinery Technical Conference and Exposition, GT2019-91866, June 17-21, 2019, Phoenix, AZ, USA, DOI: 10.1115/GT2019-91866*.

Hergt, A., Meyer, R., Liesner, K., & Nicke, E. (2011). A New Approach for Compressor Endwall Contouring. *ASME 2011 Turbo Expo: Turbine Technical Conference and Exposition, GT2011-45858, Vancouver, British Columbia, Canada*.

Huppert, M. C., & Benser, W. A. (1953). Some Stall and Surge Phenomena in Axial-Flow Compressors. *Journal of the Aeronautical Sciences, Vol. 20, DOI: 10.2514/8.2871*.

Hynes, T. P., & Greitzer, E. M. (1987). A Method for Assessing Effects of Circumferential Flow Distortion on Compressor Stability. *Journal of Turbomachinery, Vol. 109(3), ISSN: 0889-504X, DOI: 10.1115/1.3262116*.

Inoue, M., Kuroumaru, M., Yoshida, S., Minami, T., Yamada, K., & Furukawa, M. (2004). Effect of Tip Clearance on Stall Evolution Process in a Low-Speed Axial Compressor Stage. *ASME Turbo Expo 2004: Turbomachinery Technical Conference and Exposition, DOI: 10.1115/GT2004-53354*.

Iura, T., & Rannie, W. D. (1954). Experimental Investigations of Propagating Stall in Axial-Flow Compressors. *Transactions of the American Society of Mechanical Engineers, ISSN: 0097-6822, DOI: 10.1115/1.4014879*.

Junge, L. K. (2023). A new Harmonic Balance Approach using Multidimensional Time. *Dissertation Ruhr-Universität Bochum*.

Kaplan, B., Nicke, E., & Voss, C. (2006). Design of a Highly Efficient Low-Noise Fan for Ultra-High Bypass Engines. *ASME Turbo Expo 2006: Turbomachinery Technical Conference and Exposition, GT2006-90363, May 8-11, 2006, Barcelona, Spain*.

Kato, M., & Launder, B. (1993). The Modeling of Turbulent Flow around Stationary and Vibrating Square Cylinders. *9th Symposium on Turbulent Shear Flows*.

Kožulović, D. (2010). Propulsive Efficiency of Plane and Axisymmetric Nozzles with Non-Uniform Velocity Distributions. *ASME Turbo Expo 2010: Turbomachinery Technical Conference and Exposition, GT2010-22074, June 14-18, 2010, Glasgow, UK*.

Lakshminarayana, B. (1970). Methods of Predicting the Tip Clearance Effects in Axial Flow Turbomachinery. *Journal of Basic Engineering, Vol. 92, DOI: 10.1115/1.3425036*.

Lecht, M. (1987). Improvement of the Parallel Compressor Model by Consideration of Unsteady Blade Aerodynamics. *AGARD Lecture Series*.

Lee, B. J., Liou, M.-F., & Liou, M.-S. (2018). Aerdynamic Conceptual Design of Boundary Layer Ingestion Propulsor Systems: A quasi-2d Through Flow Analysis Method and Multi-Fidelity Propulsor Design Framework. *ASME Turbo Expo 2018: Turbomachinery Technical Conference and Exposition, GT2018-75861, June 11-15, 2018, Oslo, Norway*.

Lengyel-Kampmann, T. (2016). Vergleichende aerodynamische Untersuchungen von gegenläufigen und konventionellen Fanstufen für Flugtriebwerke. *Dissertation Ruhr-Universität Bochum*.

Lieblein, S., Schwenk, F. C., & Broderick, R. L. (1953). Diffusion Factor Estimating Losses and Limiting Blade Loadings in Axial Flow Compressor Blade Elements. *NACA Research Memorandum*.

Longley, J. P., & Greitzer, E. M. (1992). Inlet Distortion Effects in Aircraft Propulsion System Integration. *AGARD Lecture Series*.

Mailach, R. (2010). Unsteady Flow in Turbomachinery. *TUDpress, Dresden, ISBN: 978-3-941298-92-7*.

Mårtensson, H., Ellbrant, L., & Lundbladh, A. (2019). Design Conditions for an Aft Mounted Fan with Boundary Layer Ingestion. *24th ISABE Conference, September 22-27, 2019 Canberra, Australia, ISABE-2019-24258*.

Mårtensson, H., & Laban, M. (2020). Design and Performance of a Boundary Layer Ingesting Fan. *ASME Turbo Expo 2020: Turbomachinery Technical Conference and*

Exposition, GT2020-15479, September 21 – 25, 2020, online, ISBN: 978-0-7918-8406-5, DOI: 10.1115/GT2020-15479.

Mårtensson, H., Lejon, M., Ghosh, D., Åkerblom, M., Rasimarzabadi, F., & Neuteboom, M. (2022). Design Conditions for an Aft Mounted Fan with Boundary Layer Ingestion. *25th ISABE Conference, September 25-30, 2022 Ottawa, Canada*.

Max, P., Stößel, M., Kožulovic, D., Krummenauer, M., & Niehuis, R. (2022). Comparison of Active Flow Control Measures in an Advanced S-Shaped Engine Intake by using a Turbo- Compressor. *25th ISABE Conference, September 25-30, 2022 Ottawa, Canada*.

Mazzawy, R. S. (1977). Multiple Segment Parallel Compressor Model for Circumferential Flow Distortion. *Journal of Engineering for Power, DOI: 10.1115/1.3446288*.

Melick Jr., H., & Simpkin, W. (1972). A unified Theory of Inlet/Engine Compatibility. *AIAA 8th Joint Propulsion Specialist Conference, Vol. , ISSN: , DOI: 10.2514/6.1972-1115*.

Mennicken, M., Arzberger, M., & Schnell, R. (2022). Exploring the Operational Strategy of an Electrically-Driven Variable Pitch BLI-Fan. *25th ISABE Conference, September 25-30, 2022 Ottawa, Canada, ISABE-2022-217*.

Mennicken, M., Hollmann, C., Staggat, M., Schnell, R., Silberhorn, D., Arzberger, M. J., Eichner, F., & Winkelmann, P. (2020). Preliminary Fan Design for a Full Annulus BLI Propulsor. *Deutscher Luft- und Raumfahrtkongress 2020, online, oral presentation*.

Mennicken, M., Schoenweitz, D., Schnoes, M., & Schnell, R. (2019). Conceptual Fan Design for Boundary Layer Ingestion. *ASME Turbo Expo 2019: Turbomachinery Technical Conference and Exposition, GT2019-90257, June 17-21, 2019, Phoenix, AZ, USA*.

Mennicken, M., Schoenweitz, D., Schnoes, M., & Schnell, R. (2021). Fan Design Assessment for BLI Propulsion Systems. *CEAS Aeronautical Journal, Vol. 13, ISSN: 1869-5582, 1869-5590, DOI: 10.1007/s13272-021-00532-8*.

Migliorini, M., Zachos, P. K., & MacManus, D. G. (2022). Novel Method for Evaluating Intake Unsteady Flow Distortion. *Journal of Propulsion and Power, Vol. 38, ISSN: 1533-3876, DOI: 10.2514/1.B38127*.

Ordaz, I., Rallabhandi, S. K., Nielsen, E. J., & Diskin, B. (2017). Mitigation of Engine Inlet Distortion through Adjoint-Based Design. *35th AIAA Applied Aerodynamics Conference, ISSN: 978-1-62410-501-2, DOI: 10.2514/6.2017-3410*.

Page, J. H., Hield, P., & Tucker, P. G. (2017). Effect of Inlet Distortion Features on Transonic Fan Rotor Stall. *ASME Turbo Expo 2017: Turbomachinery Technical Conference and Exposition, GT2017-64612, June 26-30, 2017, Charlotte, NC, USA*.

Perovic, D., Gunn, E. J., & Hall, C. A. (2015). Stall Inception in a Boundary Layer Ingesting Fan. *ASME Turbo Expo 2015: Turbomachinery Technical Conference and Exposition, GT2015-43025 , June 15-19, 2015, Montréal, Canada*.

Peters, A. (2014). Ultra-short Nacelles for Low Fan Pressure Ratio Propulsors. *Ph. D. Thesis, Massachusetts Institute of Technology, USA*.

Peters, A., Spakovszky, Z. S., Lord, W. K., & Rose, B. (2015). Ultrashort Nacelles for Low Fan Pressure Ratio Propulsors. *ASME Journal of Turbomachinery, Vol. 137(2), ISSN: 0889-504X, 1528-8900, DOI: 10.1115/1.4028235*.

Plas, A. (2006). Performance of a Boundary Layer Ingesting Propulsion System. *Master Thesis, Massachusetts Institute of Technology, USA*.

Pullan, G., Young, A. M., Day, I. J., Greitzer, E. M., & Spakovszky, Z. S. (2015). Origins and Structure of Spike-Type Rotating Stall. *Journal of Turbomachinery, VOl. 137(5), ISSN: 0889-504X, DOI: 10.1115/1.4028494*.

Rasimarzabadi, F., Clark, C., Neuteboom, M., Orchard, D., & Martensson, H. (2022). An Altitude Capable Rig for Studying Engine Inlet Velocity Profile Effects: Boundary Layer Generator. *The Aeronautical Journal, Vol. 126, ISSN: 0001-9240, 2059-6464, DOI: 10.1017/aer.2022.67*.

Reid, C. (1969). The Response of Axial Flow Compressors to Intake Flow Distortion. *ASME Turbo Expo 1969: Turbomachinery Technical Conference and Exposition, 69-GT-29, DOI: 10.1115/69-GT-29*.

Reutter, O., Enders, G., Dabrock, T., & Peters, A. (2020). Experimental Investigation of Inlet Distortion in a 4.5-Stage Axial Compressor. *ASME Turbo Expo 2020: Turbomachinery Technical Conference and Exposition, GT2020-16201, September 21 – 25, 2020, online, ISBN: 978-0-7918-8406-5, DOI: 10.1115/GT2020-16201*.

Roberts, W. B., Serovy, G. K., & Sandercock, D. M. (1986). Modeling the 3-D Flow Effects on Deviation Angle for Axial Compressor Middle Stages. *Journal of Engineering for Gas Turbines and Power, Vol. 108, ISSN: 0742-4795, DOI: 10.1115/1.3239859*.

SAE. (2011). Gas Turbine Engine Inlet Flow Distortion Guidelines. *SAE International ARP1420 Rev. B*.

SAE. (2017). Assessment of the Inlet/Engine Total Temperature Distortion Problem. *SAE International AIR5867, DOI: 10.4271/AIR5867*.

SAE. (2022). A Methodology for Assessing Inlet Swirl Distortion. *SAE International AIR5686*.

Sanders, A. J., & Fleeter, S. (2001). Multi-Blade Row Interactions in a Transonic Axial Compressor: Part II — Rotor Wake Forcing Function and Stator Unsteady Aerodynamic Response. *ASME Turbo Expo 2001: Turbomachinery Technical Conference and Exposition, 2001-GT-0269, DOI: 10.1115/2001-GT-0269*.

Sanders, A. J., Papalia, J., & Fleeter, S. (2001). Multi-Blade Row Interactions in a Transonic Axial Compressor: Part I - Stator Particle Image Velocimetry (PIV) Investigation. *ASME Turbo Expo 2001: Turbomachinery Technical Conference and Exposition*.

Saravanamuttoo, H., Rogers, G., Cohen, H., Straznicky, P., & Nix, A. (2017). Gas Turbine Theory. *Pearson Education Limited, 7th Edition*.

Sato, S. (2012). The Power Balance Method for Aerodynamic Performance Assessment. *Ph. D., Massachusetts Institute of Technology, USA*.

Satyanarayana, B., Gostelow, J. P., & Henderson, R. E. (1974). A Comparison Between Experimental and Theoretical Fluctuating Lift on Cascades at Low Frequency Parameters. *ASME Turbo Expo 1978: Turbomachinery Technical Conference and Exposition, DOI: 10.1115/74-GT-78*.

Schmitz, A., Aulich, M., Schönweitz, D., & Nicke, E. (2012). Novel Performance Prediction of a Transonic 4.5 Stage Compressor. *ASME Turbo Expo 2012: Turbomachinery Technical Conference and Exposition, GT2012-69003, June 11-15, 2012, Copenhagen, Denmark*.

Schnell, R., Giebmanns, A., Nicke, E., & Dabrock, T. (2009). Aerodynamic Analysis of a Fan for Future Ultra-High-Bypass-Ratio Aero Engines. *19th ISABE Conference, ISABE-2009-1149, September 7-11, 2009, Montreal, Canada*.

Schnell, R., Zhao, X., Rallis, E., Kavvalos, M., Sahoo, S., Schnoes, M., & Kyprianidis, K. (2019). Assessment of a Turbo-Electric Aircraft Configuration with Aft-Propulsion Using Boundary Layer Ingestion. *MDPI Aerospace Journal, Vol. 6, ISSN: 2226-4310, DOI: 10.3390/aerospace6120134*.

Schnös, M. (2020). Eine Auslegungsmethodik für mehrstufige Axialverdichter auf Basis einer Profildatenbank. *Dissertation Ruhr-Universität Bochum, ISSN: 1434-8454*.

Schoenweitz, D., & Schnell, R. (2016). Development and Evaluation of a Performance Estimation Methodology for Fans Operating within Non-Homogeneous Inflow. *ASME*

Turbo Expo 2016: Turbomachinery Technical Conference and Exposition, GT2016-57095, June 13-17, 2016, Seoul, South Korea, ISBN: 978-0-7918-4972-9, DOI: 10.1115/GT2016-57095.

Schoenweitz, D., Theune, M., & Schnell, R. (2015). Inlet Distortion Sensitivity of Fans with Different Pressure Ratios. *22nd ISABE Conference, October 25-30, 2015 Phoenix, AZ, USA, ISABE-2015-22008*.

Schönweitz, D., Nicke, E., Schnell, R., & Mennicken, M. (2017). Fan Design for Boundary Layer Ingestion. *New Engine Integration Concepts Symposium, Braunschweig, oral presentation*.

Schönweitz, D., Trailovic, A., & Schnell, R. (2013). Vortical Inflow Distortion in a Jet Engine Intake During Take-Off. *62. Deutscher Luft- und Raumfahrtkongress 2013*.

Schröder, W. (2010). Fluidmechanik, 3. auflage. *Wissenschaftsverlag Mainz, Aachen, Germany, ISBN: 3-86130-371-X*.

Seitz, A., Habermann, A. L., Peter, F., Troeltsch, F., Castillo Pardo, A., Della Corte, B., van Sluis, M., Goraj, Z., Kowalski, M., Zhao, X., Grönstedt, T., Bijewitz, J., & Wortmann, G. (2021). Proof of Concept Study for Fuselage Boundary Layer Ingesting Propulsion. *MDPI Aerospace, Vol. 8, ISSN: 2226-4310, DOI: 10.3390/aerospace8010016*.

Silberhorn, D., Arzberger, M. J., Mennicken, M., Wolters, F., Hollmann, C., & Iwanizki, M. (2020). Multidisciplinary Investigation of Partially Turboelectric, Boundary Layer Ingesting Aircraft Concepts. *AIAA Scitech 2020 Forum, Orlando, FL, USA, ISBN: 978-1-62410-595-1, DOI: 10.2514/6.2020-0504*.

Silberhorn, D., Hollmann, C., Mennicken, M., Wolters, F., & Eichner, F. (2019). Overall Design and Assessment of Aircraft Concepts with Boundary Layer Ingesting Engines. *DLRK, 2019, Darmstadt, Germany*.

Smith, L. H. (1993). Wake Ingestion Propulsion Benefit. *Journal of Propulsion and Power, Vol. 9, ISSN: 0748-4658, 1533-3876, DOI: 10.2514/3.11487*.

Stenning, A. H. (1980). Inlet Distortion Effects in Axial Compressors. *Journal of Fluids Engineering, DOI: 10.1115/1.3240630*.

Storer, J. A., & Cumpsty, N. A. (1991). Tip Leakage Flow in Axial Compressors. *Journal of Turbomachinery, Vol. 113(2), ISSN: 0889-504X, DOI: 10.1115/1.2929095*.

Sulam, J. T., D. H., Keenan, M. J., & Flynn, J. T. (1970). Single-stage Evaluation of Highly-Loaded High Mach-number Compressor Stages. 2 - Data and Performance, Multiple-Circular-Arc Rotor. *NASA Technical Report PWA-3772*.

Taylor, J. V., & Miller, R. J. (2016). Competing Three-Dimensional Mechanisms in Compressor Flows. *Journal of Turbomachinery, Vol. 139, DOI: 10.1115/1.4034685*.

Thollet, W., Dufour, G., Carbonneau, X., & Blanc, F. (2016). Assessment of Body Force Methodologies for the Analysis of Intake-Fan Aerodynamic interactions. *ASME Turbo Expo 2016: Turbomachinery Technical Conference and Exposition, GT2016-57014, June 13-17, 2016, Seoul, South Korea*.

Vinz, A., & Raichle, A. (2022). Investigation of the Effects of BLI Engine Integration on Aircraft Thrust Requirement. *Deutscher Luft- und Raumfahrtkongress 2022, Dresden, Germany*.

Vo, H. D., Tan, C. S., & Greitzer, E. M. (2008). Criteria for Spike Initiated Rotating Stall. *Journal of Turbomachinery, Vol. 130(1), ISSN:0889-504X, DOI: 10.1115/1.2750674*.

Voigt, J., & Friedrichs, J. (2021). Development of a Multi-Segment Parallel Compressor Model for a Boundary Layer Ingesting Fuselage Fan Stage. *Energies Vol. 14, ISSN: 1996-1073, DOI: 10.3390/en14185746*.

Vratny, P. C., & Hornung, M. (2018). Sizing Considerations of an Electric Ducted Fan for Hybrid Energy Aircraft. *Transportation Research Procedia, Vol. 29, ISSN: 23521465, DOI: 10.1016/j.trpro.2018.02.037*.

Wartzek, F. (2017). Zum aerodynamischen Verhalten des Transsonikverdichters bei gestörter Zuströmung. *Shaker Verlag, Aachen*.

Weingold, H. D., & Behlke, R. F. (1987). The Use of Surface Static Pressure Data as a Diagnostic Tool in Multistage Compressor Development. *Journal of Turbomachinery, Vol. 109(1), ISSN: 0889-504X, DOI: 10.1115/1.3262057*.

Welstead, J., & Felder, J. L. (2016). Conceptual Design of a Single-Aisle Turboelectric Commercial Transport with Fuselage Boundary Layer Ingestion. *54th AIAA Aerospace Sciences Meeting, 2016, San Diego, California, USA, ISBN: 978-1-62410-393-3, DOI: 10.2514/6.2016-1027*.

Wilcox, D. C. (1988). Reassessment of the Scale-Determining Equation for Advanced Turbulence Models. *AIAA Journal, Vol. 26, ISSN: 0001-1452, DOI: 10.2514/3.10041*.

Williams, D. D. (1986). Review of Current Knowledge on Engine Response to Distorted Inflow Conditions. *AGARD Lecture Series CPP-400/401*.

Yang, H., Nürnberger, D., & Weber, A. (2002). A Conservative Zonal Approach with Applications to Unsteady Turbomachinery Flows. *Deutscher Luft- und Raumfahrtkongress 2002*.

Yang, Z., Lu, H., Pan, T., & Li, Q. (2021). Numerical Investigation on the Influences of Boundary Layer Ingestion on Tip Leakage Flow Structures and Losses in a Transonic Axial-Flow Fan. *Journal of Fluids Engineering, Vol. 143, ISSN: 0098-2202, 1528-901X, DOI: 10.1115/1.4051403*.

Yao, J., Gorrell, S. E., & Wadia, A. R. (2008). High-Fidelity Numerical Analysis of Per-Rev-Type Inlet Distortion Transfer in Multistage Fans: Part II - Entire Component Simulation and Investigation. *ASME Turbo Expo 2008: Turbomachinery Technical Conference and Exposition, GT2008-50813, June 9-13, 2008, Berlin, Germany*.

A. Appendix

A.1. Velocity triangle definition

Figure A.1 shows the velocity triangle definition

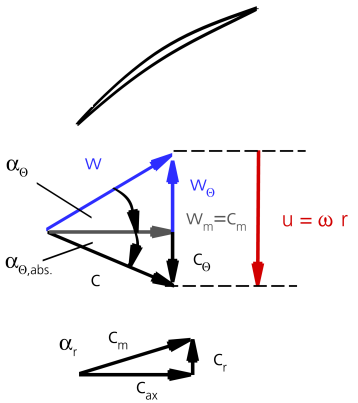

Figure A.1.: Velocity triangle and flow angle definition.

A.2. Favre and Reynolds-averaged Navier-Stokes equations

$$\frac{\partial \rho}{\partial t} + \frac{\partial}{\partial x_i}(\rho u_i) = 0 \tag{A.1}$$

$$\frac{\partial}{\partial t}(\rho u_i) + \frac{\partial}{\partial x_j}(\rho u_i u_j) = -\frac{\partial p}{\partial x_i} + \frac{\partial \tau_{ij}}{\partial x_j} \tag{A.2}$$

$$\frac{\partial}{\partial t}[\rho(\varepsilon + \frac{\partial u_i u_j}{2})] + \frac{\partial}{\partial x_j}[u_j \rho(\frac{\partial u_i u_j}{2})] = \frac{\partial}{\partial x_j}[-q_j + u_i \tau_{ij}] \tag{A.3}$$

A.3. Generic boundary layer description

In chapter 1 the advantages of BLI engines are introduced and the BLI related flow features are comprehensively described in chapter 2. This subsection describes the generic boundary layer description which is taken advantage of in this study. The boundary layer modelling assumes a fully turbulent flat plate as described in Schröder (2010). The flat plate has an infinite extension in the direction of the z coordinate. Thus, the boundary layer profile is dependent on the x and y coordinate Schröder (2010). All flow features which are associated with curved surfaces are neglected. As boundary layer properties are dependent on the Reynolds number, the definition of the Reynolds number is given in eq. (A.4). The nominator represents inertial forces and the denominator accounts for viscous forces.

$$Re(x) = \frac{\rho \cdot u_\infty \cdot x}{\eta} = \frac{u_\infty \cdot x}{\nu} \tag{A.4}$$

According to the boundary layer model the boundary layer thickness δ increases in dependence on the axial length of the plate x and the axial Reynolds number.

$$\delta(x) = x \cdot \frac{0.37}{Re(x)^{1/5}} \tag{A.5}$$

Turbulent velocity profiles u can be divided into a time-averaged velocity component $\overline{u}$ and a fluctuating velocity u'. Figure A.2 shows the non-dimensional velocity profile within a boundary layer. Due to the slip condition at the surface, there the flow satisfies eq. (A.6).

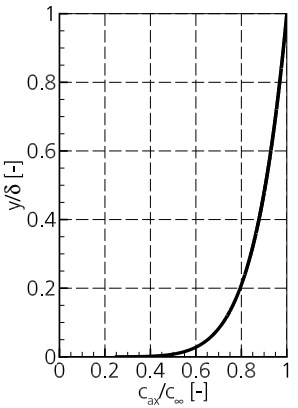

Figure A.2.: Non-dimensional velocity profile within a fully turbulent flat plate boundary layer according to Schröder (2010).

$$u(y = 0) = 0. \tag{A.6}$$

Then the averaged velocity profile is only dependent on the freestream velocity u_∞, the boundary layer thickness δ and the position perpendicular to the flow.

$$\overline{u}(y) = u_\infty \cdot \left(\frac{y}{\delta}\right)^{1/7} \tag{A.7}$$

Under the consideration of ideal gas, the definition of the flight Mach number and the Sutherland-law, the calculation of the stagnation pressure profile can be performed.

A.4. Blade forces

Within RANS the blade force vector is given by:

$$\vec{F} = (p_w \vec{n} + \tau_w \vec{u_t}) \cdot A \tag{A.8}$$

where p_w is the pressure at the face, $\vec{n}$ is the outward pointing unit face normal, τ_w is the wall shear stress, $\vec{u_t}$ is the part of the normalized velocity at the inner cell next to the face parallel to the face, and A is the face area.

Within SLC the momentum balance around the blade is solved in the axial and circumferential direction.

$$\iint_A \rho \vec{c}(\vec{c} \cdot \vec{n}) dA = \iint_A p \cdot \vec{n} dA + \sum \vec{F}_{external} \tag{A.9}$$

Within SLC F_r is neglected.

$$F_{res} = \sqrt{F_x^2 + F_\Theta^2 + F_r^2} \tag{A.10}$$

A.5. Entropy related analysis

Entropy is a quantity which is related to the static pressure, static temperature and a specific reference state.

$$\Delta s = s - s_{ref.} = c_p \cdot ln(\frac{T}{T_{ref.}}) - R \cdot ln(\frac{p}{p_{ref.}}) \tag{A.11}$$

Throughout this study the reference pressure p_{ref} is 35000Pa and the reference temperature T_{ref} is 250K.

The formula for the time derivative of the entropy is:

$$\dot{s} = \frac{\partial s}{\partial t} = \frac{s_{t,2} - s_{t,1}}{\Delta t} \tag{A.12}$$

The standard deviation of the time derivative of the entropy is:

$$\sigma(\dot{s}) = \sqrt{\frac{1}{N}\sum_{1}^{N}(\dot{s} - \dot{s}_{avg})^2} \tag{A.13}$$

A.6. Fuselage embedded turbofan

A.6.1. Spanwise fan pressure ratio

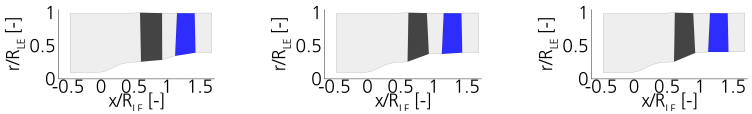

Figure A.3.: Flow path. From left to right: ascending, constant, descending.

Table A.1.: Operating points at ADP.

		$\dot{m}$ [kg/s]	$\dot{m}_{corrected}$ [kg/s]	Π_t [-]	$\eta_{is.}$
ascending	SLC	256.7	685.2	1.3093	0.9246
	RANS	256.5	684.3	1.3020	0.9017
constant	SLC	252.9	677.7	1.3172	0.9161
	RANS	253.1	675.3	1.3102	0.8996
descending	SLC	250.5	668.7	1.3180	0.9205
	RANS	250.7	668.8	1.3131	0.8907

Table A.2.: Operating points in case of BLI.

		$\dot{m}$ [kg/s]	$\dot{m}_{corrected}$ [kg/s]	Π_t [-]
ascending	BLI SLC	253.24	682.67	1.3074
	BLI uRANS	252.88	680.59	1.3021
constant	BLI SLC	249.86	673.60	1.3212
	BLI uRANS	248.57	668.93	1.3138
descending	BLI SLC	247.97	668.69	1.3107
	BLI uRANS	245.99	661.94	1.3187

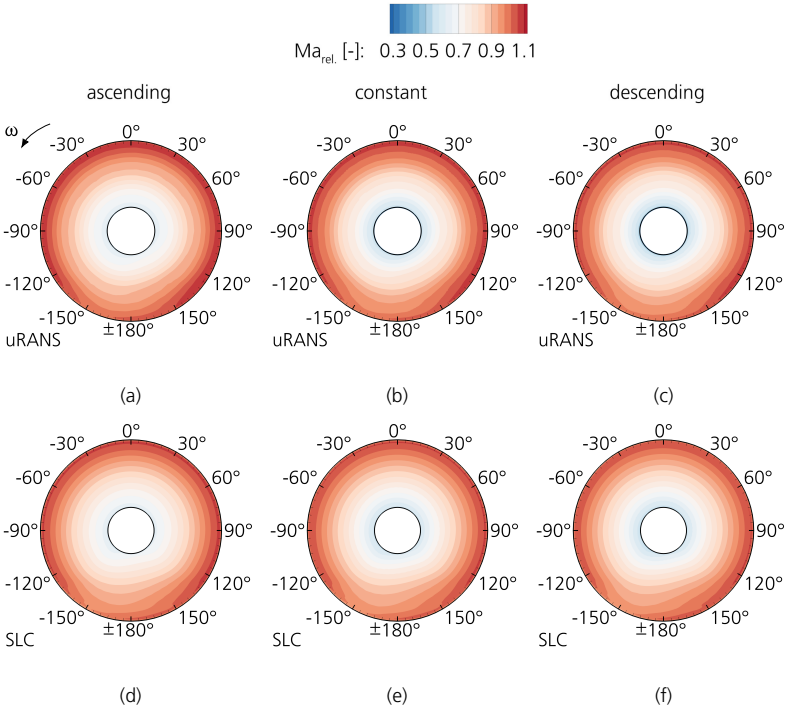

Figure A.4.: Relative Mach number at the aerodynamic interface plane.

A.7. Aft-propulsor

A.7.1. Derivation of the formula of the achievable fan pressure ratio near the hub

$$\eta_{is} = \frac{\Pi_t^{(\kappa-1)/\kappa} - 1}{\tau_t - 1} \tag{A.14}$$

Solving for Π_t gives:

$$\Pi_t = (\eta_{is} \cdot (\tau_t - 1) + 1)^{\kappa/(\kappa-1)} \tag{A.15}$$

The definition of the stagnation temperature ratio τ_t is:

$$\tau_t = \frac{T_{t,out}}{T_{t,in}} = \frac{T_{t,in} + \Delta T_t}{T_{t,in}} = 1 + \frac{\Delta T_t}{T_{t,in}} \tag{A.16}$$

The Euler work equation for non-swirling inflow leads to the product of the blade velocity u_2 times the circumferential velocity component in the absolute frame of reference $c_{\theta,abs.,2}$. In adiabatic flow this is equal to the stagnation enthalpy rise.

$$a = u_{out} \cdot c_{\theta,abs.,out} - u_{in} \cdot c_{\theta,abs.,in} = u_{out} \Delta c_{\theta,abs.,out} = c_p \cdot (T_{t,out} - T_{t,in}) = c_p \cdot \Delta T_t \tag{A.17}$$

Applying the definition in eq. (A.16) and eq. (A.17) to eq. (A.15) leads to:

$$\Pi_t = (\eta_{is} \cdot (\frac{\Delta T_t}{T_{t,in}}) + 1)^{\kappa/(\kappa-1)} = (\eta_{is} \cdot (\frac{u_{out} \cdot c_{\theta,abs.,out}}{c_p \cdot T_{t,in}}) + 1)^{\kappa/(\kappa-1)} \tag{A.18}$$

The definition of the blade velocity is given in eq. (A.19).

$$u = \omega \cdot r = \frac{N \cdot \pi}{30} \cdot r \tag{A.19}$$

A simplification of the downstream velocity triangle can be introduced by considering the work coefficient near the hub, which relates both velocities.

$$\Psi_{hub} = \frac{c_{\theta,out}}{u_{out}} \tag{A.20}$$

Replacing the velocity $c_{\theta,out}$ by $x \cdot u_{out}$ and introducing the definition of the blade velocity which is given in eq. (A.19) leads to:

$$\Pi_{t,hub} = (\eta_{is} \cdot \frac{\Psi_{hub} \cdot u_{out} \cdot u_{out}}{c_p \cdot T_{t,in}} + 1)^{\frac{\kappa}{\kappa-1}} = (\eta_{is} \cdot \frac{\Psi_{hub} \cdot (\frac{N \cdot \pi \cdot r_{hub}}{30})^2}{c_p \cdot T_{t,in}} + 1)^{\frac{\kappa}{\kappa-1}} \tag{A.21}$$

A.7.2. Stagnation pressure distortion

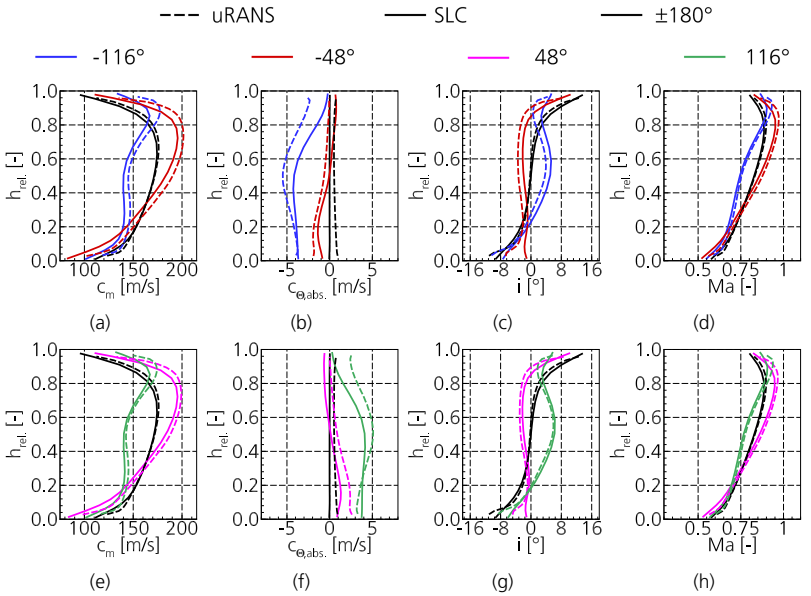

Figure A.5.: Spanwise inflow conditions at rotor inlet in terms of meridional velocity (a) and (e), circumferential velocity (b) and (f), incidence (c) and (g) and relative Mach number (d) and (h).

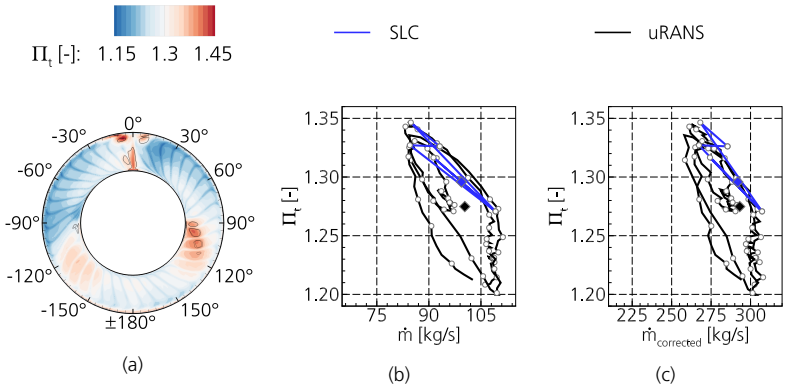

Figure A.6.: Fan pressure ratio projected on fan inlet plane (a), and local operating points stemming from SLC (blue) and uRANS (black) in (b) and (c).

A.7.3. Stagnation pressure and swirl distortion

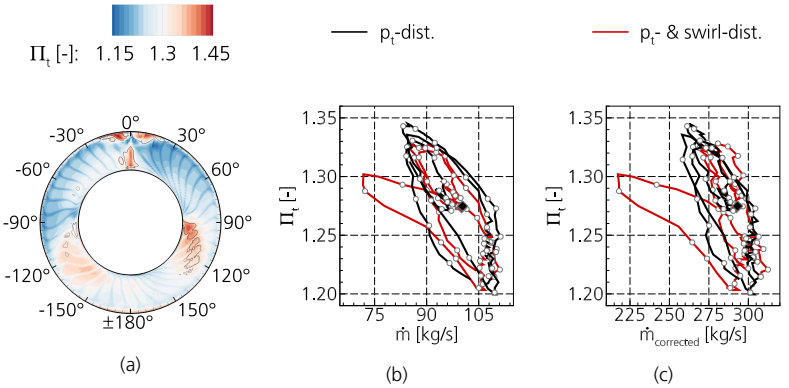

Figure A.7.: Fan pressure ratio projected on fan inlet plane of the combined distortion (a), and local operating points stemming from the stagnation pressure (black) and combined distortion (red) in (b) and (c)

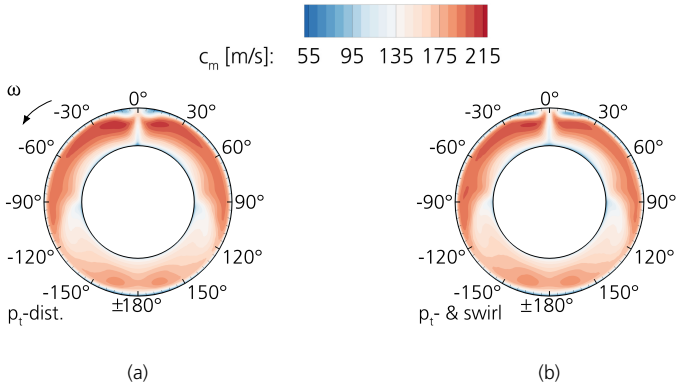

Figure A.8.: Meridional velocity distribution stemming from the stagnation pressure distortion (a) and the combined stagnation pressure and swirl distortion (b).

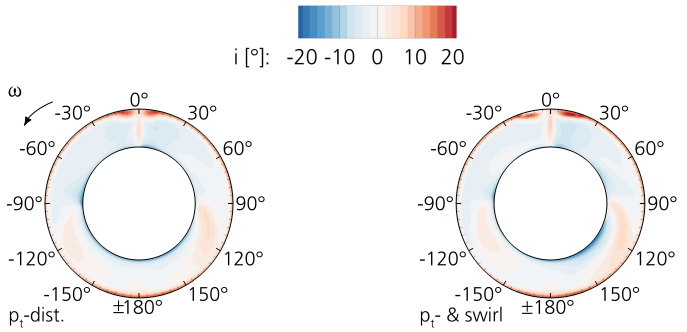

Figure A.9.: Incidence distribution stemming from the stagnation pressure distortion (a) and the combined stagnation pressure and swirl distortion (b).

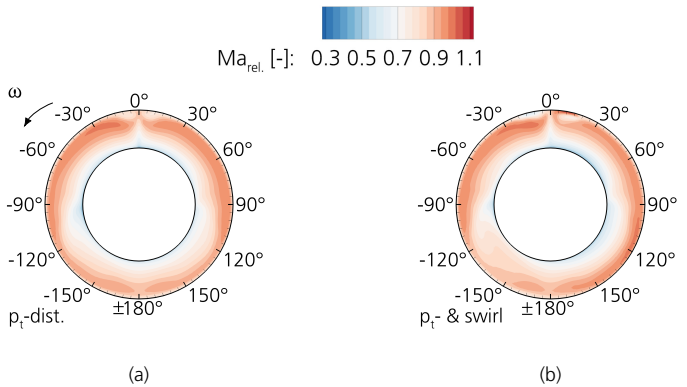

Figure A.10.: Mach number distribution stemming from the stagnation pressure distortion (a) and the combined stagnation pressure and swirl distortion (b).